Structural and Thermal Performance of Cold-Formed Steel Studs with Slits

A thesis

submitted in fulfilment

of the requirements for the degree of

Doctor of Philosophy in Engineering

at

The University of Waikato

by

Kushal Ghosh

Chief Supervisor- Dr. Krishanu Roy

Co Supervisors- Dr. James Lim, Dr. James Carson and Dr. Ray Hudd

THE UNIVERSITY OF
WAIKATO
Te Whare Wānanga o Waikato

2025

To
Ma & Baba,
My wife,
My sister,
And my entire family

Abstract

Cold-formed steel (CFS) studs in lightweight construction increasingly incorporate web slits to limit thermal bridging, yet these openings can reduce axial strength. This thesis integrates structural and thermal assessments through validated non-linear elasto-plastic finite element analysis (FEA) and complementary heat-transfer modelling. Shell-element FEA models were developed and validated against tests, then used in a 960-case parametric study spanning section dimensions, slit geometry, thickness, and member length to establish the influence of slits on concentric axial capacity. The results were evaluated against the Direct Strength Method (DSM) in AS/NZS 4600, leading to strength-reduction recommendations and modified DSM expressions that achieve reliability indices $\beta \geq 2.5$. The programme was extended to combined axial compression and minor-axis bending using 1,134 FEA models with six eccentricities, demonstrating a systematic discrepancy in current AS/NZS 4600 interaction checks: strengths are generally underestimated at eccentricities of 10–25 mm and overestimated at 50 mm. A new interaction equation incorporating element and web slenderness ratios is proposed and verified within the AISI S100 reliability framework. Subsequently, a parametric three-dimensional heat-transfer study quantified the dependence of heat flux on geometry and slit parameters, providing a quantitative basis for thermal performance gains and their balance with strength. The thesis proposes design recommendations and revised equations for slitted CFS studs that satisfy codified reliability targets and support informed selection of slit configurations to balance energy efficiency and structural capacity in practice.

Preface

This thesis is submitted to the University of Waikato, New Zealand in fulfilment of the requirement for the degree of Doctor of Philosophy. The work contained in this thesis has not been previously submitted for a degree or diploma in any other higher educational institution. To the best of my knowledge and belief, the thesis contains no material previously published or written by another person except where due reference is made.

Journal Publications:

1. Ghosh, K., Roy, K., Tiwari, S., Fang, Z., Paul, B., & Lim, J. B. (2025). Axial capacity of cold-formed steel channel sections with slits. *Engineering Structures*, 322, 119094.

2. Ghosh, K., Tiwari, S., Roy, K., Paul, B., Fang, Z., & Lim, J. B. (2026). Axial capacity of cold-formed steel channel sections with slits subjected to axial compressive load with eccentricity. *Structures* (Revision stage).

Acknowledgements

It is my great pleasure to take this opportunity to express my sincere gratitude to my supervisor, Dr. Krishanu Roy. He has not only guided me technically but has also taken every step to ensure my overall well-being, for which I shall remain deeply indebted to him. His extreme commitment to his students is a trait which I hope to emulate in the future. His efficient guidance, continuous encouragement and great patience constitute the most essential foundation of this thesis.

I would also like to thank my co-supervisor, Dr. James Lim, for being a constant source of inspiration. His visits to the laboratory and his encouraging conversations were always a great source of motivation and energy. His help, along with that of Dr. Roy, in the meticulous planning of numerical studies played a pivotal role in the timely completion of this thesis. Dr. Roy and Dr. Lim form a remarkable team who ensure that no one in their research group is left behind, irrespective of their skill level.

My sincere thanks also go to my co-supervisor, Dr. James Carson, who has been nothing but kind and supportive throughout my research journey. My brief encounters with him on campus always had a calming and reassuring effect on me.

I am equally grateful to my co-supervisor, Dr. Ray Hudd, for his constant encouragement and for giving me the opportunity to assist him in teaching papers on the design of reinforced concrete.

I would also like to express my sincere thanks to Dr. Arthur Fang for his continued technical support and valuable guidance.

My heartfelt thanks to Dr. Kim de Graaf for her continuous support and encouragement. I have learnt a great deal from her while working on various projects with her and Dr. Roy.

I also wish to extend my gratitude to the staff of the School of Engineering, University of Waikato, for their tireless assistance and round-the-clock support to all PhD students.

I would like to thank Shubham Tiwari and Bikram Paul, who played an integral role in helping me complete my numerical simulations. Their contributions are invaluable. I would also like to thank Yazeed Al Radhi for his valuable feedback. Special thanks also to Dinesh Lakshaman for offering his suggestions whenever I needed them.

I would like to express my deep appreciation to Balasubramanian Elankumaran for being a true friend, supporting me wholeheartedly during this journey, and always being there in my times of need.

My family has been the backbone of my journey. My parents, Somnath Ghosh and Shaswati Ghosh, have made countless sacrifices to help me reach this stage. They have taught me the virtues, ethics, and moral values of life by living and embodying them. A few lines in this section can hardly do justice to their immense contribution. No event in my life is complete without my sister Madhurima, who I see as an

extension of myself but with a higher IQ. I am also deeply thankful to my grandparents, Late Anil Kumar Ghosh, Surama Ghosh, Late Nirmalya Dutta Majumdar, and Late Surabhi Dutta Majumdar, for the time, wisdom, and experiences they shared to prepare us for life's unexpected challenges. I also wish to thank my aunt Mitali Rudra, uncle Ashok Rudra, and cousin Ruchi Rudra for their unwavering support and their everlasting confidence in me.

I would also like to thank my wife, Ishita Roy Choudhury, for being there at all times and for walking the difficult road beside me without complaint. She has been my friend, philosopher, and guide, and has acted as a perpetual fountain of optimism throughout this journey. I would also like to thank my parents-in-law, Amit Roy Choudhury and Kajal Roy Choudhury, for their steadfast encouragement and cheerful presence, even during trying times, which brought me great comfort.

I would like to express my gratitude to Mrs. Tapati Chatterjee, my teacher during middle school, who had faith in me even when I doubted myself. Any milestone in my life feels incomplete without her mention.

Finally, I wish to thank Partha Ghosh, my supervisor, during my research at Jadavpur University, for always encouraging me to pursue further studies. I would also like to thank Vishal Patil and Sandeep Mali, my teachers at Pune University for their constant support. I am also grateful to Arun Deb Gupta and Pradip Sen of Skematic Consultants, who gave me my first opportunity as a design engineer and thus launched my professional journey into the world of civil engineering.

Table of Contents

List of Figures

List of Tables

Abbreviations:

Notation	Description
CFS	Cold-formed steel
D	Section depth (mm)
Bf	Flange width (mm)
t	Thickness of the section (mm)
L	Length of the studs (mm)
L_{sl}	Slit length (mm)
W_{sl}	Slit width (mm)
B_l	Lip width (mm)
f_y	Yield strength (MPa)
E	Young's modulus (GPa)
FEA	Finite Element Analysis
ABAQUS	Software used for finite element modelling
S4R	Shell elements used in finite element modelling
RP	Reference point for applying boundary and loading conditions
Eigen value analysis	Used to identify the critical buckling mode
P	Axial capacity (kN)
P_{FEA}	Axial capacity from FEA results (kN)

Notation	Description
P_{test}	Axial capacity from experimental tests (kN)
P_{DSM}	Axial capacity predicted by the Direct Strength Method (kN)
$P_{AISI\&AS/NZS}$	Design strength as per AISI and AS/NZS standards (kN)
λ_c	Column slenderness ratio as per DSM method, defined as the square root of the ratio of the yield stress to the elastic compression buckling stress in flexural, torsional, and flexural–torsional buckling ($\lambda c = \sqrt{(Fy/Fcre)}$)
σ_{true}	True stress (MPa)
ε_{true}	True strain
σ	Engineering stress (MPa)
ε	Engineering strain
DSM	Direct Strength Method
P_n	Nominal axial strength (kN)
P_{nl}	Local buckling strength (kN)
P_{nd}	Distortional buckling strength (kN)
P_{ne}	Global buckling strength (kN)
P_{prop}	Proposed design axial capacity (kN)
D/t	Ratio of section depth to thickness
B_f/t	Ratio of flange width to thickness
W_{sl}/t	Ratio of slit width to thickness
L_{sl}/W_{sl}	Ratio of slit length to slit width
φ	Resistance factor
β	Reliability index
COV	Coefficient of variation
R	Axial capacity reduction factor
λ_l	Slenderness ratio for local buckling
λ_d	Slenderness ratio for distortional buckling
P_{crl}	Critical local buckling load (kN)
P_{crd}	Critical distortional buckling load (kN)
P_{cre}	Critical elastic buckling load (kN)
M_m	Mean of the material factor for CFS section (1.1)
F_m	Mean of the fabrication factor for CFS section (1.0)

Notation	Description
V_m	COV of the material factor for CFS section (0.1)
V_f	COV of the fabrication factor for CFS section (0.05)
C_p	Correction factor
C_c	Correlation coefficient
V_p	Coefficient of variation of the proposed equation
P_m	Mean value of the proposed equation
V_q	COV of the load effect for CFS section (0.21)

Chapter 1 Introduction

1.1. Background and problem statement

Cold-formed steel (CFS) structural members are widely used in residential construction. With advancements in manufacturing technologies and the need for more efficient building systems, there have been continuous developments in their shapes and configurations. However, one of their disadvantages is thermal efficiency. To help overcome this, slits (refer to Fig. 1-1) can be included in the webs of the channel sections [1], [2], [3], [4]. Fig. 1-2 illustrates that introducing slits extends the heat flow path, resulting in improved thermal efficiency compared to a similar section with an equivalent solid web. Although the thermal benefits of slits have been highlighted in previous studies, little attention has been given in literature to quantifying the reduced axial strength due to such slits.

Fig.1- 1. Cold-formed steel stud with slits after Laboube [4]

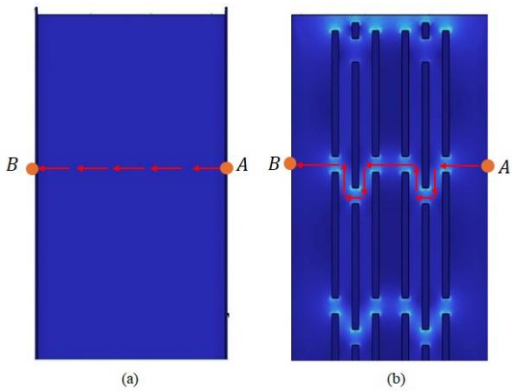

Fig.1- 2. Heat flow paths through studs: (a) Plain web, (b) Slits in web

The Direct Strength Method (DSM), adopted in the North American Specification (2004) [5] and AS/NZS 4600 (2005) [6], is a modern design approach that predicts ultimate strength using elastic buckling loads, primarily for non-perforated cold-formed steel members. Moen and Schafer [7] extended DSM to perforated columns by introducing design equations that account for the effects of perforations on local, distortional, and global buckling. Subsequent studies have expanded on perforated section behaviour, including simplified equations for edge-stiffened circular holes [8][9], comparisons of unstiffened and stiffened elongated holes [10], the influence of perforation width [11], behaviour under pinned–pinned boundary conditions [12], local–distortional interaction [13], and high-strength perforated channel sections [14]. Overall, these studies consistently reported reductions in axial capacity due to perforations; however, the focus has largely been on slots (refer to Fig. 1-3) rather than slits.

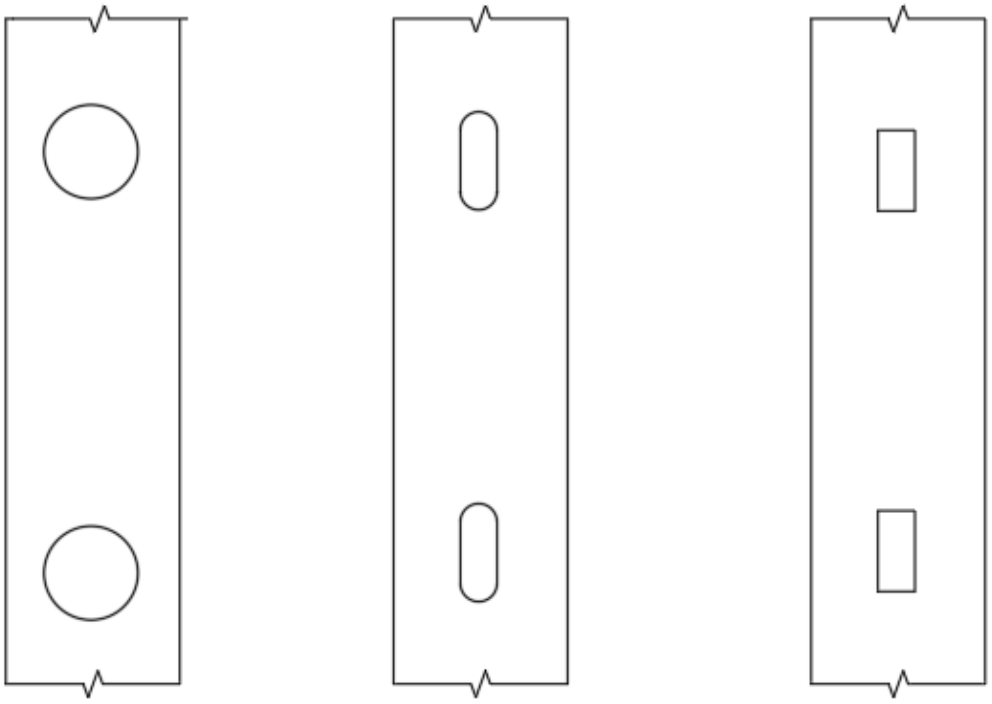

(a) Chen et al [9] (b) Chandramohan et al [10] (c) Zhao et al [11]

Fig.1- 3. Types of slots reported in literature on sections with perforations

Eccentric loads in stud-based wall systems commonly arise from ledger framing connections [15], [16]. Perimeter studs [4] and moment-resisting frame columns are also subjected to

combined axial compression and lateral pressure or bending [17], [18]. However, most previous studies have focused on shear behaviour rather than axial strength under eccentric loading. Höglund [1], [19] proposed an analytical method, based on the Swedish Code, to estimate the shear strength of slitted webs, which was later validated experimentally by others [20], [21]. Salmi [22] further identified shear-related failure modes in perforated studs. Nevertheless, these studies did not quantify axial capacity loss under eccentric loading using numerical or finite element methods. In addition, although previous studies have examined the thermal performance of wall panels with slitted CFS sections [4], they did not quantify how thermal efficiency depends on geometric or slit parameters. Thus, further research is needed on the structural behaviour of CFS sections under concentric axial compression as well as combined axial compression through eccentric loading and the quantification of the influence of slit parameters on the thermal performance of the wall panels with CFS sections with slits.

1.2 Objective of the study

The objective of this research is to investigate the behaviour of cold-formed steel (CFS) sections with web slits under concentric axial compression and combined axial compression due to eccentric loading, and to quantify the influence of slit parameters on the thermal performance of wall panels incorporating such sections.

1. To develop non-linear FE models for slitted and plain CFS studs and validate them using the available experimental datasets, namely slitted sections under concentric loading and plain sections under eccentric loading, using previously reported experimental results.
2. To perform comprehensive parametric analyses using the validated FE models to examine how channel dimensions, slit geometry, section thickness, and stud length influence axial capacity under concentric and eccentric loading.

3. To assess the applicability and accuracy of existing DSM-based design provisions (AS/NZS 4600) for predicting the strength of slitted CFS members and to propose improved DSM equations where required.
4. To evaluate the reliability of the proposed design equations in accordance with AISI S100 criteria.
5. To quantify the effect geometric parameters of slits on the total heat flux of wall panels with slitted CFS studs.

1.3 Thesis outline

This thesis comprises six chapters, as outlined below:

Chapter 1: Provides an introduction to the research topic, including problem statement, background, limitations in existing research, objectives and the overall methodology adopted in the study.

Chapter 2: Presents a comprehensive literature review on cold-formed steel (CFS) members, the use of slits and perforations, axial and eccentric loading behaviour, and current design approaches such as the Direct Strength Method (DSM). Previous experimental and numerical studies are reviewed, and research gaps are highlighted.

Chapter 3: Focuses on developing and validating non-linear elasto-plastic finite element (FE) models of CFS studs with slits using experimental results. The validated models are then used in a parametric study to examine the effects of channel geometry, slit configuration, thickness, and stud length on axial capacity. The FE results are compared with Direct Strength Method (DSM) predictions from AS/NZS 4600. Based on the findings, strength reduction factors and modified DSM design equations are proposed and calibrated through reliability analysis.

Chapter 4: Focuses on extending the investigation to the behaviour of slitted CFS studs subjected to combined axial compression and minor-axis bending through eccentric loading. A comprehensive parametric study is conducted using finite element models to examine the influence of member length, thickness, cross-sectional dimensions, and varying eccentricities on axial capacity. The FE results are compared with the general interaction equation in AS/NZS 4600, revealing limitations in existing design provisions. Based on the findings, a new design interaction equation is proposed, incorporating element and web slenderness ratios. The accuracy of the proposed equations is then assessed through reliability analysis in accordance with the AISI-S100 framework.

Chapter 5: Investigates the thermal performance of wall panels incorporating CFS studs with slits. Finite element thermal simulations are conducted to quantify the influence of geometric and slit parameters on heat flow and thermal efficiency.

Chapter 6: Provides a summary of the research findings, draws key conclusions, and outlines directions for future research.

Chapter 2 Literature review

2.1 Introduction

Cold-formed steel (CFS) channel sections are integral to modern lightweight structural systems, including pallet storage racks and light-gauge steel-framed buildings. These thin-walled members offer high strength-to-weight ratios, but they often incorporate web perforations to accommodate services (e.g. wiring, plumbing) or connections. Such openings, however, can significantly reduce the member's load-bearing capacity and alter its buckling behavior. For example, studies on perforated rack upright columns (common in warehouse storage racks) have reported strength reductions on the order of 10–30% due to the presence of web holes, along with changes in stiffness and failure modes. Given that CFS columns and beam-columns in practice may be subject to axial compression as well as combined bending loads, understanding the structural implications of these perforations is critical for safe design. Within this broader context of perforations, slits, which are continuous and narrow openings introduced along the web, represent a distinct class of web modifications. Slits are increasingly used for purposes such as improving thermal performance by interrupting heat-flow paths in wall studs. However, despite their growing relevance in energy-efficient wall systems, limited research has been conducted on the structural behaviour of slitted CFS members, particularly under combined loading. The presence of slits introduces unique geometric discontinuities that differ from conventional service holes, and their influence on buckling modes, axial strength, and load interaction behaviour remains insufficiently understood. Therefore, while this thesis focuses specifically on CFS channel sections with web slits, a comprehensive review of the broader literature on CFS members with perforations, including unstiffened holes, stiffened openings, slots, and slits, is essential. This literature review therefore examines the state of knowledge on the axial and combined loading performance of perforated CFS channel sections including sections with slits, with an emphasis on current applications and experimental findings, in order

to identify research gaps and limitations of existing design methods.

2.2 Axial compression behavior of CFS sections with openings

2.2.1 Single lipped channel sections with web openings

Cold-formed steel (CFS) structural members are increasingly popular in light-gauge construction due to their high strength-to-weight ratio and ease of fabrication. However, the introduction of web openings or slotted holes for practical purposes (e.g., plumbing or electrical conduits) significantly affects the axial load capacity of these sections. This section provides a comprehensive review of studies focusing on the axial compression behaviour of single lipped channel sections with unstiffened or slotted web holes.

Sivakumaran [23] carried out early investigations into the influence of web openings on axial compression strength and web crippling of CFS members. His findings demonstrated that while hole shape had negligible influence, the size of openings substantially reduced axial capacity, particularly for $a/W > 0.6$. Moen and Schafer [24] through experimental testing of slotted web holes in short and intermediate-length columns. They observed only a limited strength reduction of up to 2.7 percent, but significant changes in buckling mode and post-peak ductility. Guo and Yao [3], [4] proposed effective width-based methods and finite element models to predict the axial capacity of lipped channel sections with rectangular web openings. They conducted 44 axial compression tests, revealing that distortional or combined local-distortional buckling dominated failure modes. The capacity was found to reduce consistently with increased hole size, and their FE simulations using ABAQUS closely matched experimental results. A refined design method was proposed based on distortional buckling coefficients. Zhao et al. [5] conducted a study involving 20 experimental tests and 412 finite element simulations across a range of hole sizes. They reported that axial capacity reductions ranged between 11.7% and 31.5% as the hole width-to-web width ratio increased. They developed a modified Direct Strength Method (DSM) that does not require explicit calculation of elastic buckling stresses. Kulatunga and Macdonald

[25] (refer to Fig. 2-1) conducted finite element investigation using ANSYS to examine how the position of perforations in cold-formed lipped channel columns influences axial strength. Their numerical models, validated through both experimental and theoretical comparisons, revealed a notable sensitivity to perforation location, especially near the ends of slender members, leading to capacity reductions of up to 19%. They emphasized that local buckling was the dominant failure mechanism, and sections with perforations near the supports showed more pronounced weakness. Furthermore, they found that the load capacity was generally lower than the capacity calculated from net sectional area alone, and that British design standards (BS 5950) were conservative in strength estimation. Kulatunga et al. [26] (refer to Fig. 2-1) conducted both experimental and numerical studies on perforated columns, highlighting the interaction of local and distortional buckling modes near the perforation zones. Reductions in axial capacity were shown to correlate with increased perforation size and length, with up to 34.43% reduction in load capacity observed. Their comparison with FE analysis validated the performance of ANSYS models. Loov [27] focused on stub columns with punched webs, establishing effective width equations based on 36 tests. Although supporting CSA S136 yield stress provisions, Loov found existing code equations overly conservative for webs adjacent to openings.

Pu et al. [28] proposed a formulation for predicting strength of symmetrically perforated channels, using unstiffened strip models and a modified Perry-Robertson approach. Their test results (63 stub columns) showed that the size and position of holes strongly influenced strength, while aspect ratio had marginal impact. Yao and Rasmussen [29], [30] presented studies on inelastic buckling of perforated C-sections using advanced isoparametric spline finite strip methods. They evaluated different hole geometries and material models, identifying that hole width had the most significant influence on strength, followed by length and spacing. A parametric DSM design method was proposed based on the results. Expanding on the understanding of buckling and interaction modes, Yao and Rasmussen [31] carried out a

comprehensive parametric study using ABAQUS to simulate 146,207 column configurations across five different cross-section types and a variety of perforation geometries. Their study focused on capturing interactions between local, distortional, and global buckling (L, D, G) as well as combined modes (LD, LG, DG, LDG), offering a broad understanding of how multiple buckling mechanisms occur in the presence of holes.

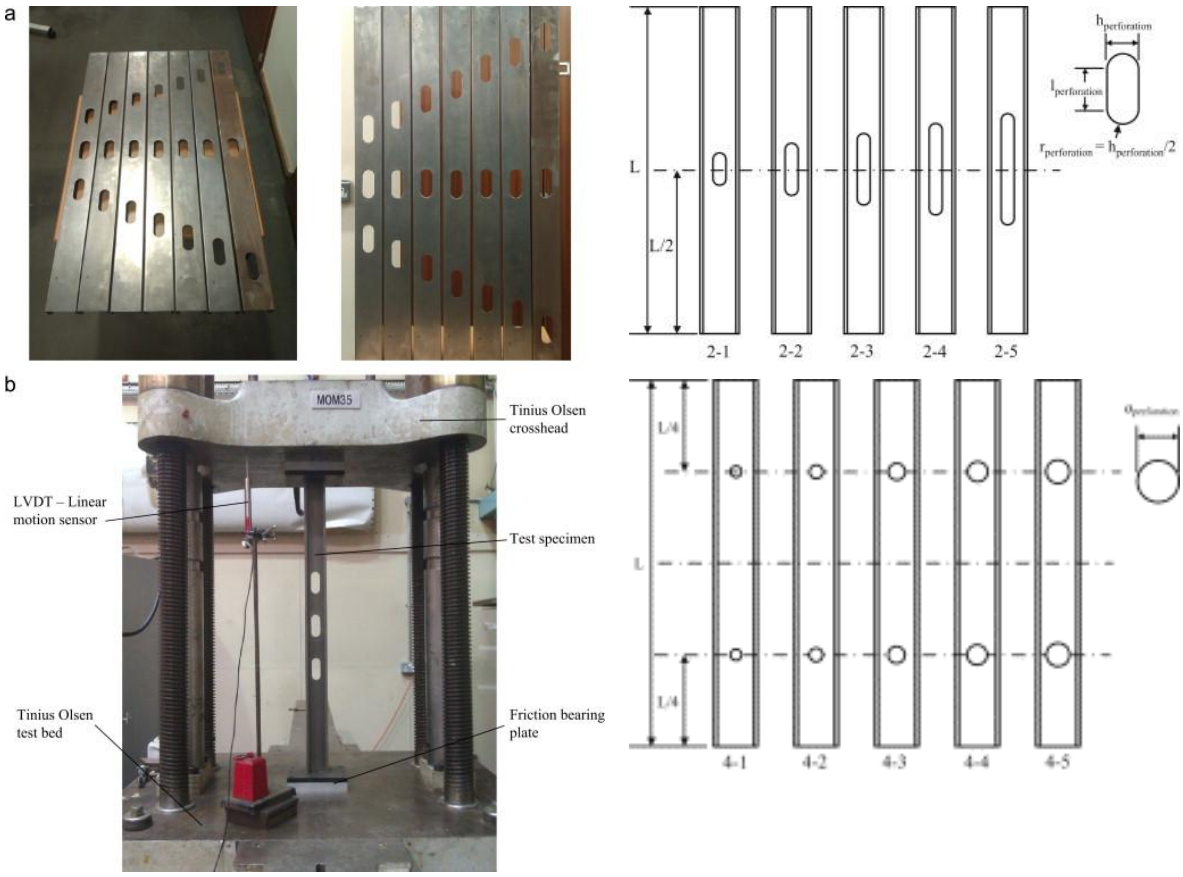

(a) [25] (b) [26]

Fig. 2- 1. Experimental test setup and specimen configurations from Kulatunga and Macdonald [25]and Kulatunga et al. [26]

They found that code specified guidelines based on the Direct Strength Method (DSM) significantly overestimated capacity in many cases, particularly when interaction between buckling modes was prominent. The study also showed that column length, material properties, and even centroid shift due to hole geometry altered strength outcomes, suggesting the necessity for a refined DSM formulation for perforated sections. The buckling shapes and failure

progressions are presented in their Fig.2-2 and Fig.2-3.

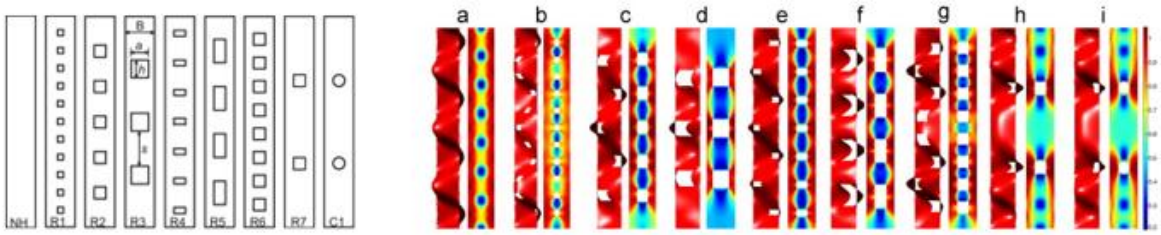

Fig. 2- 2. Failure modes and normalised von Mises membrane stress distributions for perforated plates studied by Yao and Rasmussen [29].

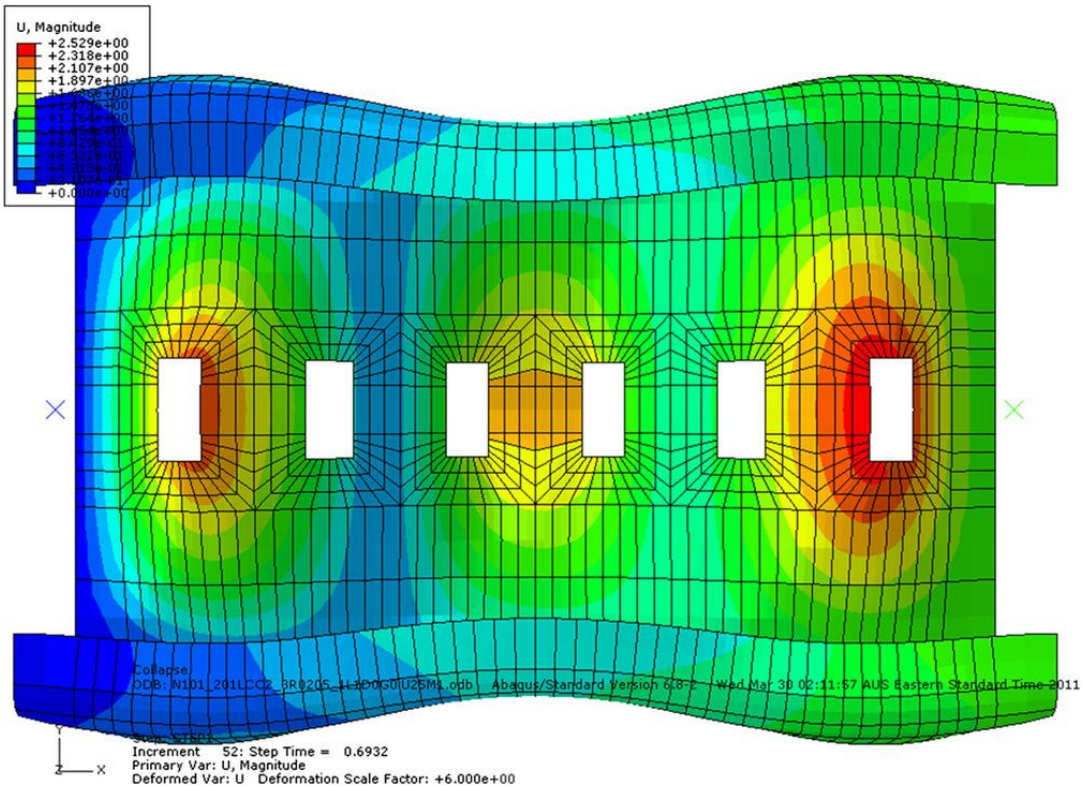

(a)

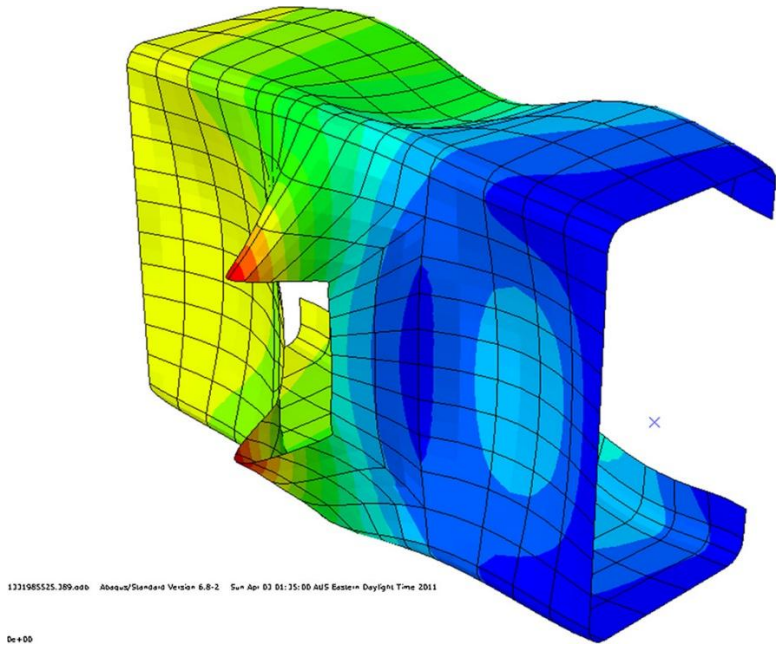

(b)

Fig. 2- 3. Buckling modes and stress contour plots from the finite element simulations as reported by Yao and Rasmussen [31], illustrating the local buckling (a) as well as the interactions of local, distortional, and global buckling (b) in perforated cold-formed steel columns with rectangular holes.

Singh and Singh [32] studied rectangular hollow sections (RHS) and square hollow sections (SHS) stub columns with centrally placed circular perforations. A non-linear drop in strength was observed with increasing perforation diameter, reaching a 44% reduction at d/w = 0.9. Although most code predictions were conservative, the authors recommended refined equations for better accuracy. Sivakumaran [33], [34] also provided additional experimental and finite element insights into lipped channel members with various hole geometries. These studies reaffirmed the inadequacy of existing design codes in capturing the effects of different hole shapes and sizes on local buckling behaviour. Yao [35] tested 26 intermediate-length lipped channel columns with slotted web holes, observing distortional buckling dominance. FE analysis confirmed the impact of hole dimensions on both elastic buckling stress and ultimate strength. A modified effective width method was proposed for design applications. Moen et al. [36] (refer to Fig. 2-4) investigated cold-formed steel C-section joists with unstiffened rectangular web holes, showing that such perforations reduce flexural capacity and intensify distortional buckling. As

hole depth approached web depth, sudden flange and web buckling occurred above the opening. Strip buckling in the compressed web also accompanied distortional modes. Critical elastic buckling moments were calculated using finite strip methods and new engineering expressions. Preliminary DSM equations incorporating web holes showed good agreement with experimental results, demonstrating their potential for reliable flexural capacity prediction.

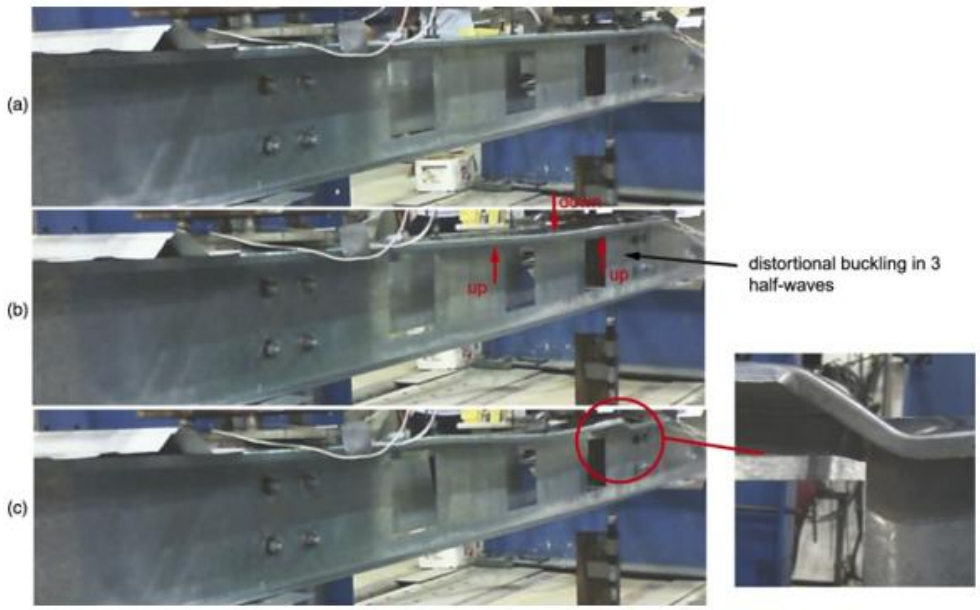

Fig. 2- 4. Experimental observation of distortional buckling in cold-formed steel C-section joists with unstiffened rectangular web holes, as reported by Moen et al. [36].

A consistent set of observations can be drawn from the reviewed studies. Most failures were governed by distortional buckling or combined local-distortional buckling, heavily influenced by hole placement and dimensions [26], [29], [35], [37], [38]. Axial strength was consistently reduced by web perforations, with reductions up to 44% depending on hole width-to-web width ratio [11], [32]. Finite Element Analysis using tools such as ABAQUS and ANSYS was critical in simulating buckling behaviour, validating experiments, and developing prediction models [26], [34], [38]. Modified DSM and effective width-based approaches have been proposed to address the limitations of conventional codes [11], [30], [35], [38].

2.2.2 Channel sections with stiffened web holes

Recent research has introduced edge-stiffened web holes as a strategy to mitigate the detrimental

effects of perforations under axial loading. This review analyses experimental and numerical research focused on the structural behaviour associated with this hole configuration.

Chandramohan et al. [10] and Chen et al. [39] found improvements of up to 14% and 21% respectively in axial strength when comparing edge-stiffened configurations to unstiffened specimens. Their work was supported by extensive parametric FE simulations and experimental testing, all pointing to the enhanced load bearing capacity provided by stiffened edges. Fig. 2-5. and Fig. 2-6. show the post-buckling configurations and deformation patterns in stiffened specimens. In contrast, unstiffened openings led to strength reductions of up to 20%, mainly due to premature local or distortional buckling.

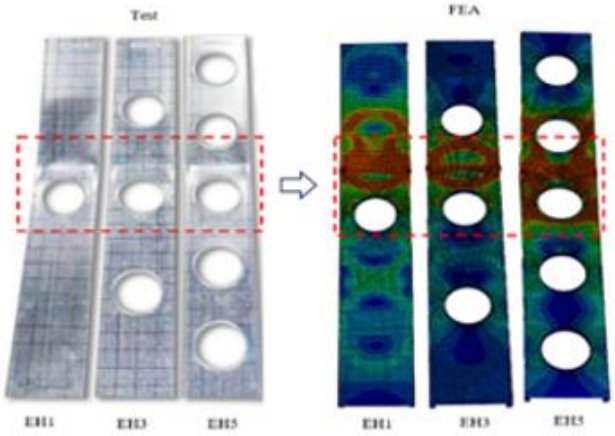

Fig. 2- 5. Failure modes of unstiffened and edge-stiffened CFS sections with circular web openings under axial compression as reported by Chandramohan et al. [1].

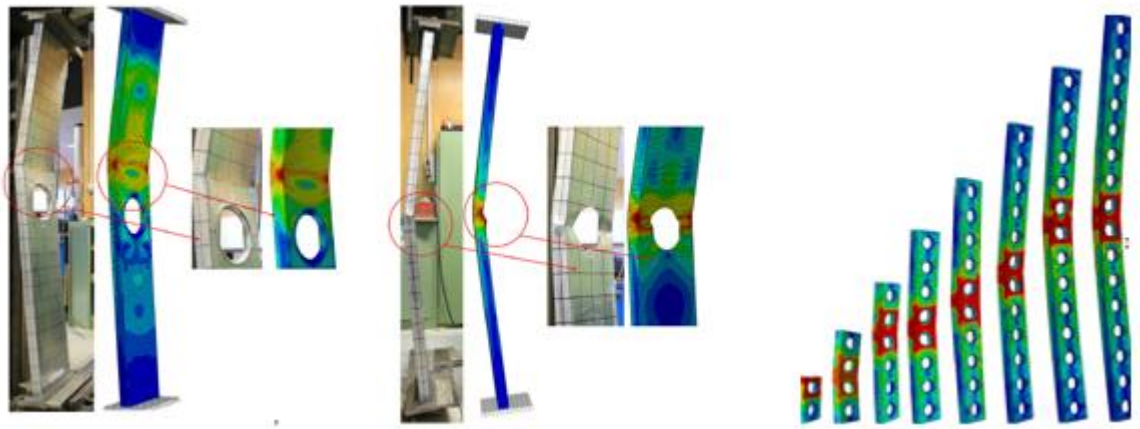

Fig. 2- 6. Experimental and numerical failure modes of edge-stiffened CFS sections under axial loading as reported by Chen et al. [2].

Numerical investigations by Chen et al. [8] and Osgouei et al. [40], further demonstrated that the

axial capacity of members with edge-stiffened holes is strongly influenced by section slenderness and hole dimensions. Chen et al. [8] proposed bivariate regression-based DSM modifications to address this sensitivity. Osgouei et al. [40] (see Fig.2-7) validated their analytical model based on polynomial deflection functions, achieving less than 5% error.

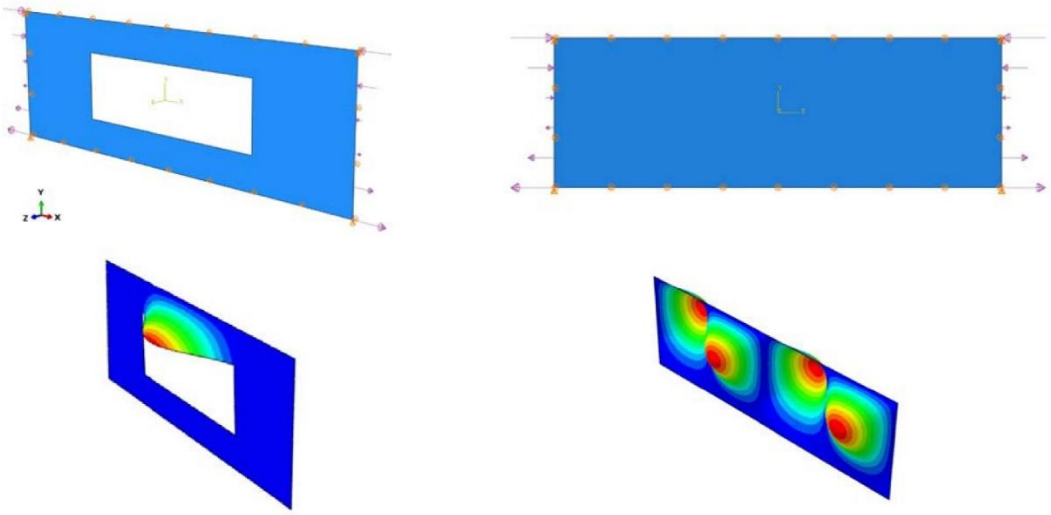

(a) Plate with and without opening under pure bending.

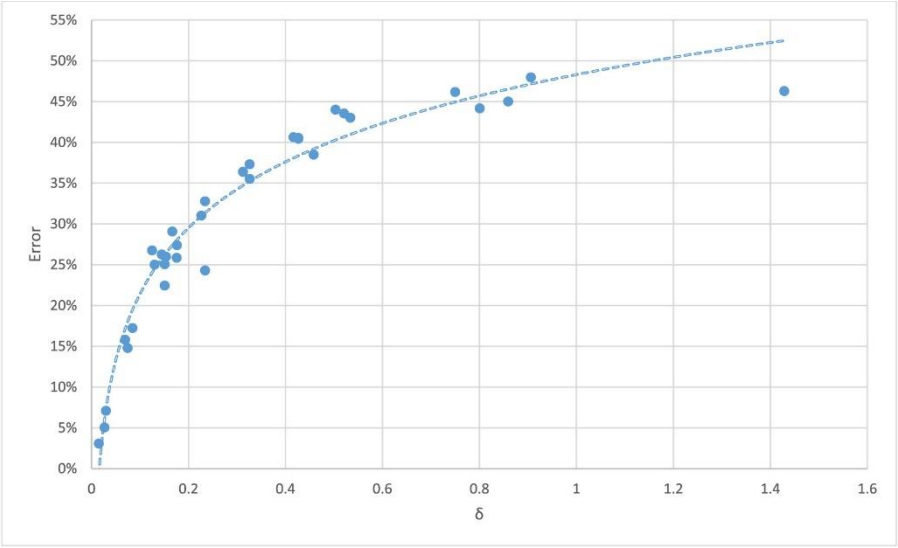

(b) k_5 error for plate above or below the opening.

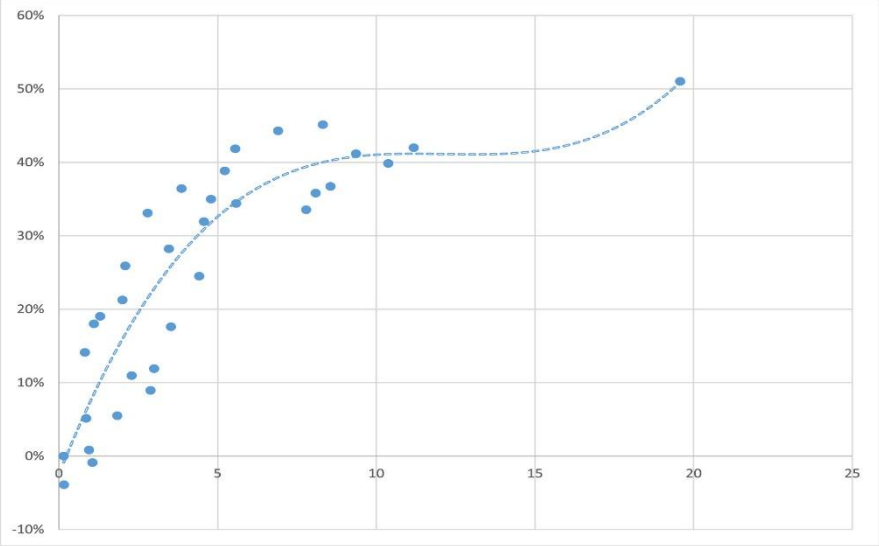

(c) k_5 error for stiffened plate with opening under pure bending.

Fig. 2- 7. Finite element and analytical comparison for plates with and without openings under pure bending as reported by Osgouei et al.[40]

Design standards such as AISI and AS/NZS were found to be overly conservative or inaccurate in predicting the axial strength of perforated sections with edge-stiffened holes. Chen et al. [8] and Shaker et al. [41] (see Fig.2-8) highlighted that these standards could underestimate capacity by up to 66%. Even the DSM, though improved when modified, struggled to account for local-distortional and global interaction effects observed in tests by He et al. [13] and Chen et al. [42].

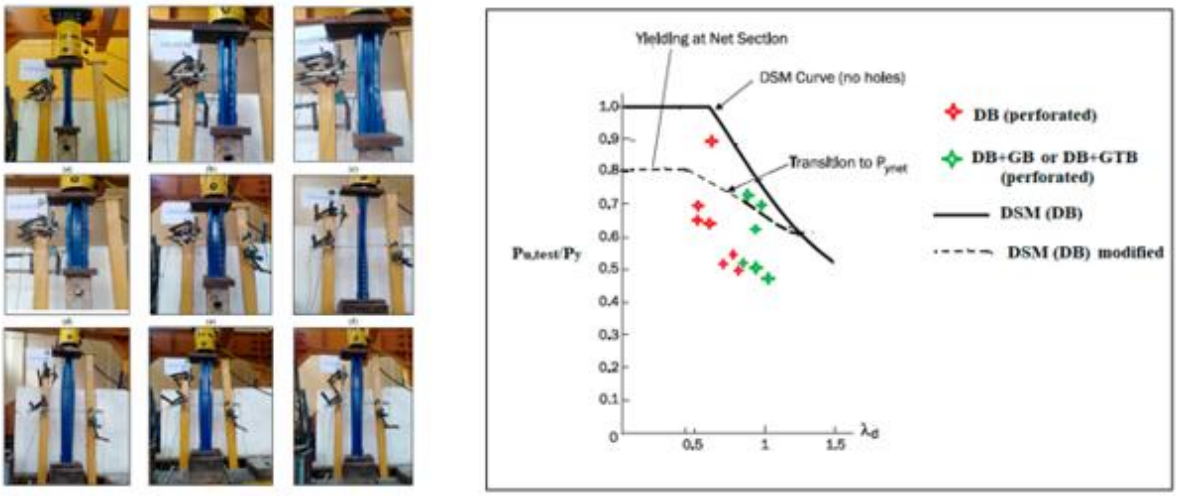

Fig. 2- 8. Test setup and comparison of predicted and observed strengths for perforated, stiffened rack uprights under distortional–global interaction as reported by Shaker et al. [41]

In summary, a consistent observation across literature is that edge-stiffening significantly improves the axial performance of CFS sections with web perforations. The integration of

stiffening at the hole boundary proves to be an effective and practical design strategy. However, accurate prediction of this behaviour remains a challenge under current design provisions.

2.2.3 Back-to-back (built-up) channel sections with web openings

Cold-formed steel (CFS) back-to-back (B2B) channel assemblies are increasingly used in structural applications due to their enhanced axial and flexural strength. These built-up sections often incorporate web perforations for service installations, which may either weaken or enhance structural performance depending on hole geometry, placement, and stiffening measures. Recent investigations have focused on evaluating the axial and flexural behavior of such B2B sections through experimental, numerical, and data-driven modeling techniques.

Chen et al. [9] (refer to Fig. 2-9) conducted an extensive experimental and finite element study on the axial strength of B2B CFS channels featuring edge-stiffened holes, unstiffened holes, and plain webs. Through 27 compression tests and 135 FE analyses, they found that edge-stiffened holes increased axial strength by 6.6% over plain channels, while unstiffened holes reduced capacity by 12.4%. Composite action due to the built-up nature of the sections was observed to enhance capacity in longer columns (e.g., 1420 mm) but was negligible for stub columns. Their validated nonlinear FE model showed strong agreement with test results and served as the basis for a comprehensive parametric study, highlighting the effects of hole diameter, screw spacing, and stiffener geometry. In a subsequent study, Chen et al. [43] (refer to Fig. 2-9) evaluated the moment capacity of B2B channels under four-point bending. Test results from 14 specimens indicated that edge-stiffened holes increased flexural strength by 15.4%, while unstiffened holes caused a 15.1% reduction. Finite element simulations were validated against experimental results, and subsequent parametric studies and design strength comparisons showed that existing design codes such as AISI and AS/NZS conservatively estimated the strength of perforated channels by 23–49%.

[9] [43]

Fig. 2- 9. Comparison of experimental and FE results for B2B CFS channels with web holes under (a) axial compression [9] and (b) four-point bending [43]

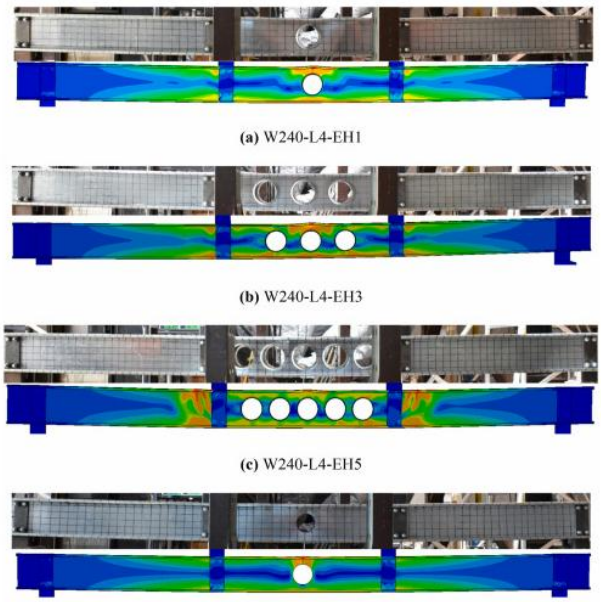

[44]

Fig. 2- 10. Experimental and FE comparison of CFS channel beams with varying edge-stiffened hole configurations under four-point bending [44].

Dai et al. [44] (refer to Fig. 2-10) proposed a novel machine learning framework using the eXtreme Gradient Boosting (XGBoost) algorithm to predict moment capacity of CFS channel beams with both edge-stiffened and unstiffened holes. The model, trained on 1620 data points from validated FE simulations, achieved an R^2 score near 99%. Compared to Moen and Schafer's equations (for unstiffened holes) and Yu's equations (for stiffened holes), the XGBoost model offered significantly improved accuracy. New design equations derived from the model showed

average absolute errors as low as 8.78%, with reliability indices above 2.5, aligning with AISI standards. Chi et al. [45] focused specifically on the axial capacity of B2B channels with edge-stiffened holes, exploring the effect of hole spacing. Using 29 compression tests and 44 FE simulations, they observed a 19.2% increase in axial capacity relative to plain sections. Their findings confirmed that AISI and AS/NZS standards are reasonably conservative (9%) for plain channels, but Moen and Schafer's design equations were conservative by 47% for channels with stiffened holes.

Recent studies indicate that edge-stiffened web holes, when appropriately dimensioned and positioned, can improve both axial and flexural strength of back-to-back cold-formed steel channel sections relative to unstiffened or plain-web sections. The influence of built-up action between paired channels increases with member length, particularly in slender columns where interactions between local and global buckling are more prevalent. Existing design equations, including those in AISI and AS/NZS standards do not consistently capture the structural response of sections with perforations. To address this limitation, recent work has incorporated nonlinear finite element analysis and data-driven methods such as eXtreme Gradient Boosting, which have shown high predictive accuracy and can support the development of updated design provisions.

2.2.4 Perforated cold-formed steel rack upright members

Recent investigations into perforated cold-formed steel rack uprights under axial compression have provided insights into the effects of perforations and complex buckling interactions. Baldassino et al. [46] (refer to Fig. 2-11) conducted a study involving 72 tests on solid and perforated thin-walled cold-formed profiles commonly used as uprights in pallet rack systems. Their findings revealed that perforations significantly influence both strength and stiffness, with capacity reductions ranging from 10% to 30% depending on specimen length and failure mode. Moreover, their bending tests indicated that relying on equivalent solid sections to evaluate second moments of area may not yield accurate results, highlighting the need for revised

provisions in current rack design codes. Neiva et al. [47] (refer to Fig. 2-12) carried out 18 physical tests and 64 numerical simulations of uprights with rectangular web perforations, indicating that existing Direct Strength Method (DSM) formulations do not adequately predict the strength of members with perforations. Subsequently, they proposed modified distortional mode coefficients tailored for rack members with perforations.

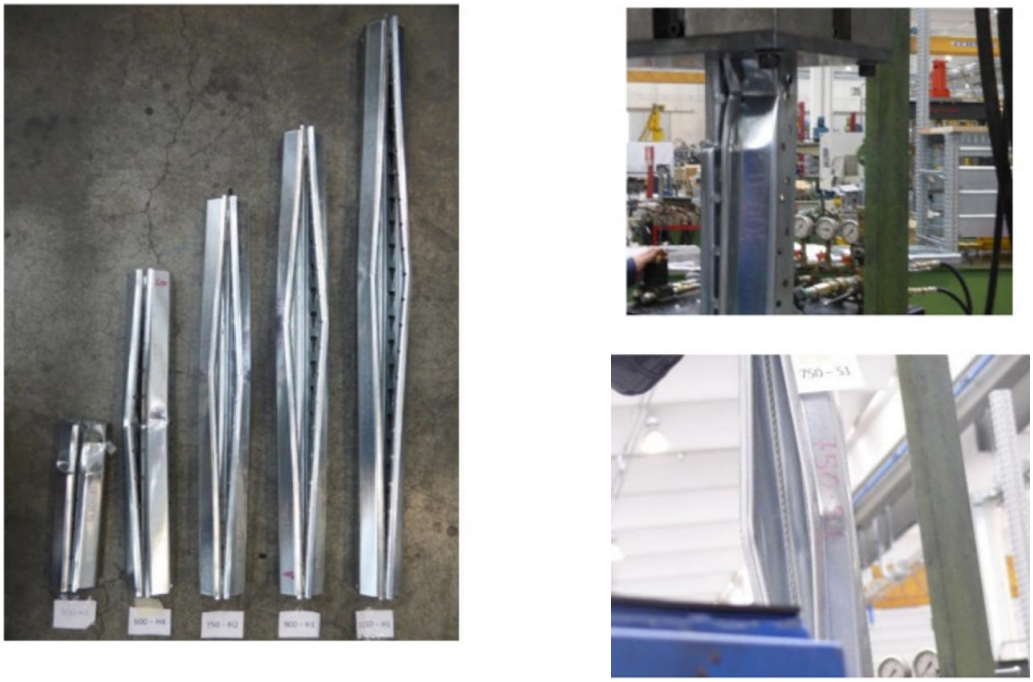

Fig. 2- 11. Various failure modes observed in profiles of different lengths,as reported by Baldassino et al. [46]

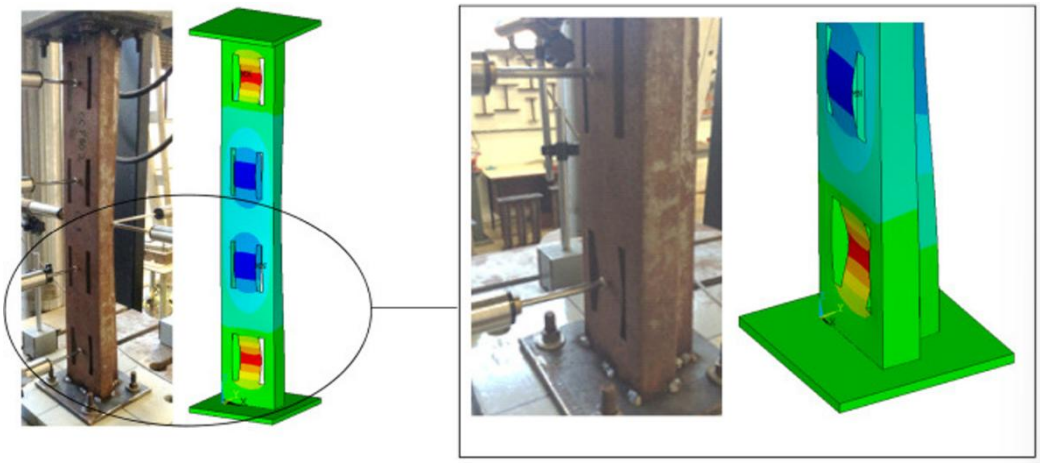

Fig. 2- 12. Comparison between experimental and numerical failure modes as reported by Neiva et al. [47]

Focusing on mode interactions, Miyazaki et al. [48] (refer to Fig. 2-13) explored distortional and global buckling interactions through over 3000 numerical simulations using ABAQUS. Their

study highlighted that boundary conditions critically affect failure loads and that conventional DSM equations lack consistency under this type of interaction. To address this, new DSM-based formulations were proposed, specific to support configurations. Casafont et al. [49] similarly examined perforated rack columns with a range of lengths and confirmed that distortional and global buckling interaction occurs in commonly used column sizes. Their experimental results showed that including such interaction in strength predictions using the DSM significantly improves accuracy. The study suggested two approaches to account for interaction effects: either using a lower-bound estimate of distortional buckling strength or applying an interaction formula, with the latter yielding better alignment with observed behavior. Moreover, their findings demonstrated that excluding this interaction could lead to strength overestimation of 10 to 20 percent, reinforcing the need for its inclusion in design methodologies.

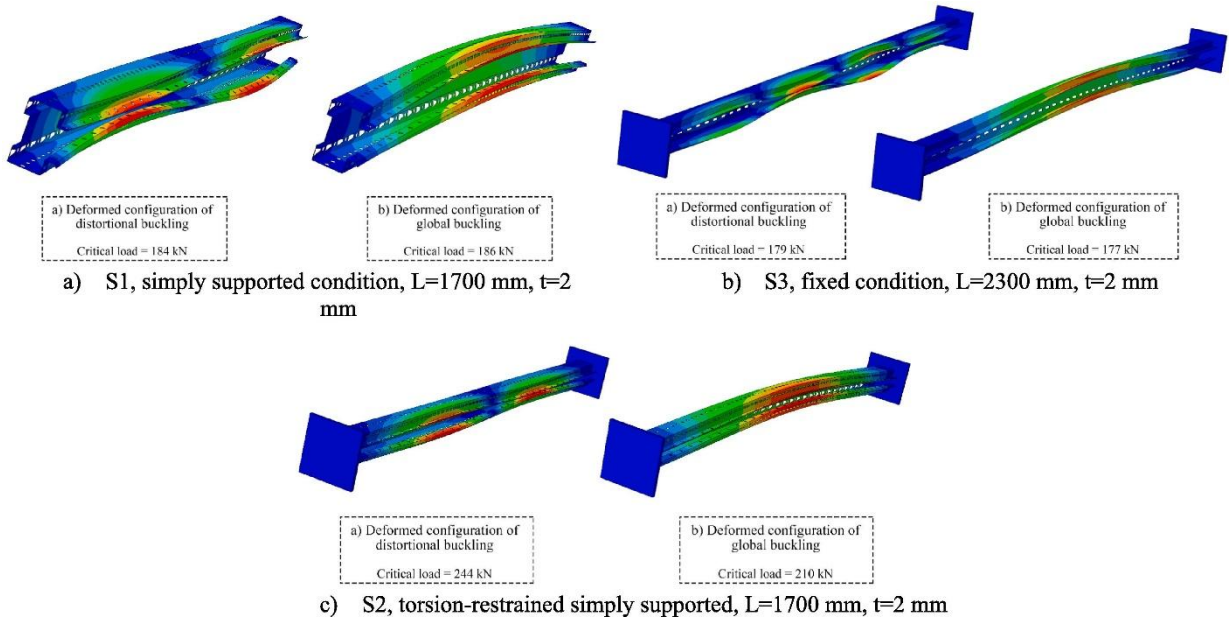

a) S1, simply supported condition, L=1700 mm, t=2 mm

b) S3, fixed condition, L=2300 mm, t=2 mm

c) S2, torsion-restrained simply supported, L=1700 mm, t=2 mm

[48]

Fig. 2- 13. Numerical deformation profiles showing distortional and global buckling interaction under different boundary conditions, as reported by Miyazaki et al. [48]

Bertocci et al. [50] (refer to Fig. 2-14) conducted an extensive campaign involving 128 tests on mono-symmetric perforated profiles and supplemented their findings with nonlinear finite element analyses to develop three-dimensional compression-biaxial bending strength domains.

Their results revealed discrepancies between experimental behavior and EN 15512 predictions, especially for bending about the weak axis and under seismic-like load trajectories. Bonada et al. [51] (refer to Fig. 2-15) investigated the influence of bending moments on the load-carrying capacity of uprights and showed that distortional buckling becomes critical when induced by axial eccentricity. Their validated finite element models demonstrated the significance of incorporating residual stress and strength enhancement to achieve accurate predictions.

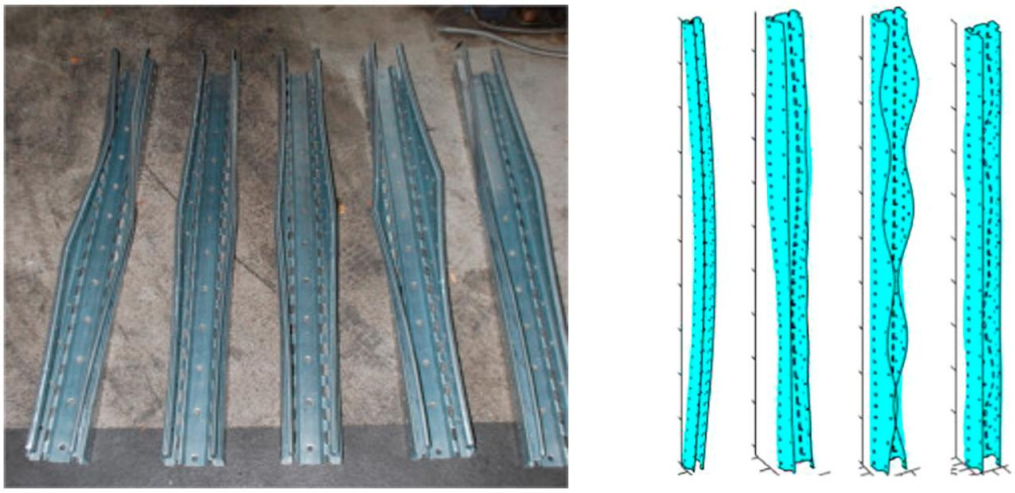

Fig. 2- 14. Experimental and numerical buckling modes of 2000 mm long perforated profiles, illustrating global and various local failure mechanisms as reported by Bertocci et al. [50]

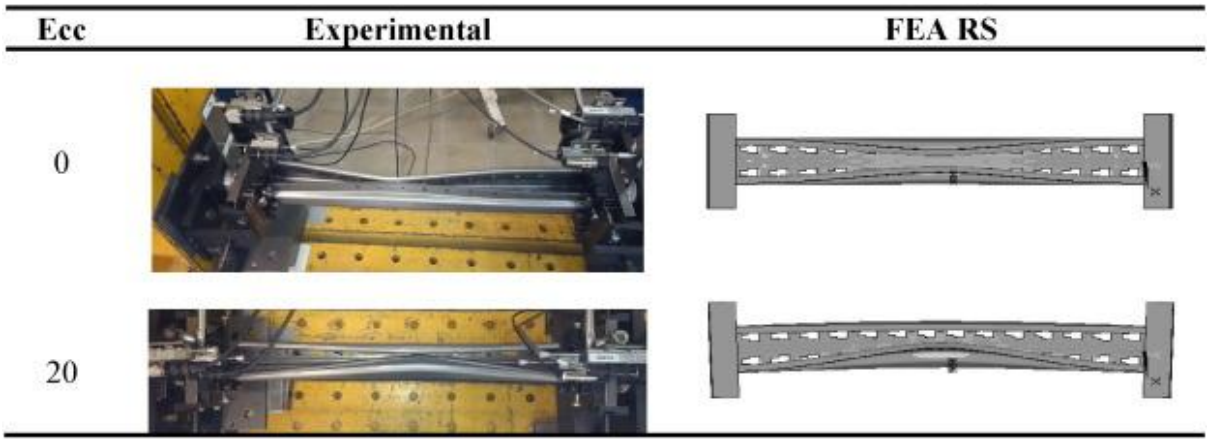

Fig. 2- 15. Comparison of experimental and numerical failure modes under axial load with 0 mm and 20 mm eccentricities, illustrating the effect of residual stresses and strain hardening, as reported by Bonada et al..[51]

Orlando et al. [52] evaluated the reliability of current European codes by testing slender open-section perforated columns under varying eccentricities. Their findings indicated that existing formulations might underestimate the collapse load, especially in cases of high eccentricity.

Pastor et al. [53] (refer to Fig. 2-16) examined uprights subjected to combined bi-axial bending and compression and compared experimental and numerical results with EN 15512. They observed up to a 53% reduction in load capacity under combined eccentricities and noted that the standard underestimates the strength in cases of negative bending about the minor axis.

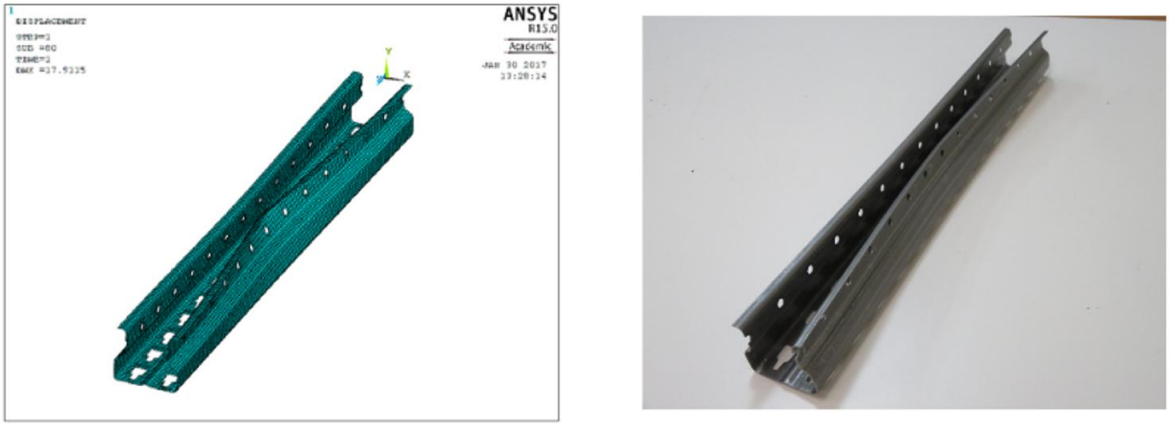

(a) (b)

Fig. 2- 16. a) Numerical failure mode under bi-axial eccentric loading (ey = 0 mm, ez = 20 mm); b) Corresponding experimental failure mode for ey = 0 mm, ez = 20 mm [53]

Smith and Moen [54] developed approximate finite strip solutions to predict elastic buckling loads of thin-walled perforated columns. The methods accounted for reductions in plate stiffness due to perforations, affecting local, distortional, and global modes. A comprehensive validation against over 1,200 finite element models confirmed the accuracy of these approaches for perforated pallet rack columns, providing the basis for extending the DSM to include such sections.

Expanding the scope to full upright frames, Dai et al. [55] performed axial compression tests and nonlinear simulations on cold-formed thin-walled rack upright frames. They identified global buckling and distortional-global buckling interactions as dominant failure modes. Their findings demonstrated that frame boundary conditions and slenderness significantly impact ultimate load capacity. They also confirmed that while the global DSM curve reasonably predicts strength, the distortional DSM curve requires modification. Consequently, they proposed an improved distortional buckling DSM formulation that accounts for buckling interactions specific to upright

frames. Taranu et al. [56] (refer to Fig. 2-17) conducted full-scale experiments and FEM simulations on cold-formed steel uprights with central stiffeners and perforated webs. The failure modes transitioned from local buckling in short columns to distortional–flexural interaction and global flexural buckling in longer specimens. DSM yielded predictions within 2 to 7 percent of experimental values, particularly when using the full net section. The study emphasized DSM's reliability for moderately slender, stiffened perforated sections, while also identifying EWM as a conservative alternative.

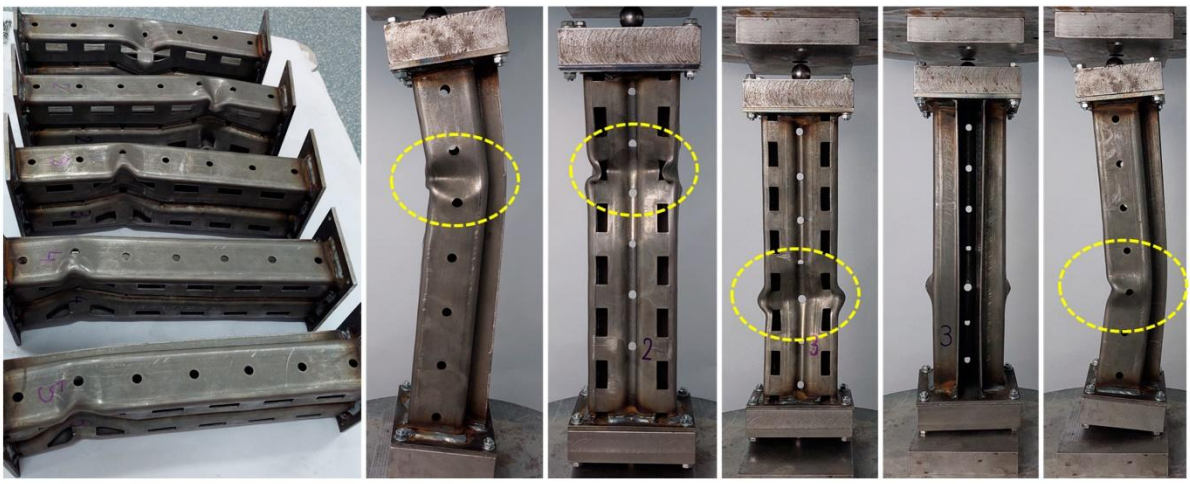

Fig. 2- 17. Influence of the perforation location on the local buckling mode as reported by Xiang et al. [56]

These studies underline the critical role of perforation geometry, boundary conditions, and buckling mode interactions in the structural performance of cold-formed steel rack uprights and emphasize the necessity for experimentally validated updates to the DSM and racking standards to enhance safety and accuracy in practical design applications.

2.2.5 Channel sections with edge-stiffened or complex stiffeners

Wang et al. [57] investigated axially loaded cold-formed perforated columns featuring complex edge stiffeners and web stiffeners. Their experimental and numerical results showed that Σ-type web stiffeners improved load efficiency by 30 to 50 percent when compared to simpler channels. However, the presence of web holes reduced axial capacity, approximately 6 percent for channels and 25 percent for Σ-section specimens. The study also confirmed that the Direct Strength

Method (DSM) could be reliably applied to such complex perforated profiles. Another study by Wang et al. [58] involved a parametric finite element analysis on perforated lipped channel columns, examining the effects of hole height, width, shape, and spacing. Hole height had the most significant impact on axial capacity, while width, spacing, and shape mainly influenced the buckling mode. A modified DSM approach suited to Chinese specifications was proposed and validated, demonstrating its applicability to channels with complex edge stiffeners. Wang et al. [59] (refer to Fig. 2-18) also tested perforated built-up I-section columns with web and edge stiffeners under axial and eccentric loads. Web stiffeners notably improved ultimate strength, particularly in stub and medium-length columns. While the stiffeners effectively limited local deformation around perforations, they were found to reduce composite action between adjacent webs. The DSM formulations provided good agreement with both experimental and numerical results for these complex configurations. Xiang et al. [60] (refer to Fig. 2-19) examined G-section columns, which are channels with complex edge stiffeners, with and without perforations under axial loading. A test series of 36 specimens, supported by validated ABAQUS models, showed that larger perforation dimensions resulted in greater strength reduction, while changes in perforation location had a stronger influence on deformation shape. To mitigate strength loss and prevent web instability, circular hole spacing between three and six times the hole diameter was recommended.

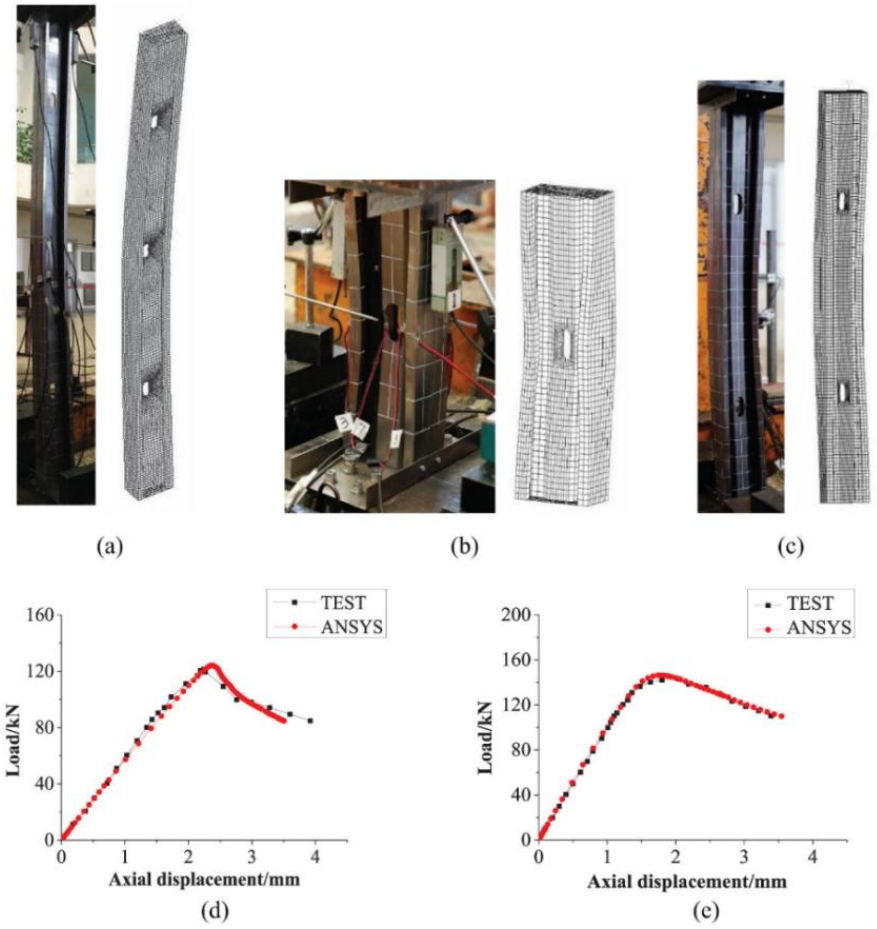

Fig. 2- 18. Experimental and numerical comparison of perforated built-up I-section columns with stiffeners, including (a–c) failure mode comparisons and (d–e) load–displacement responses for selected specimens, as reported by Wang et al.[59]

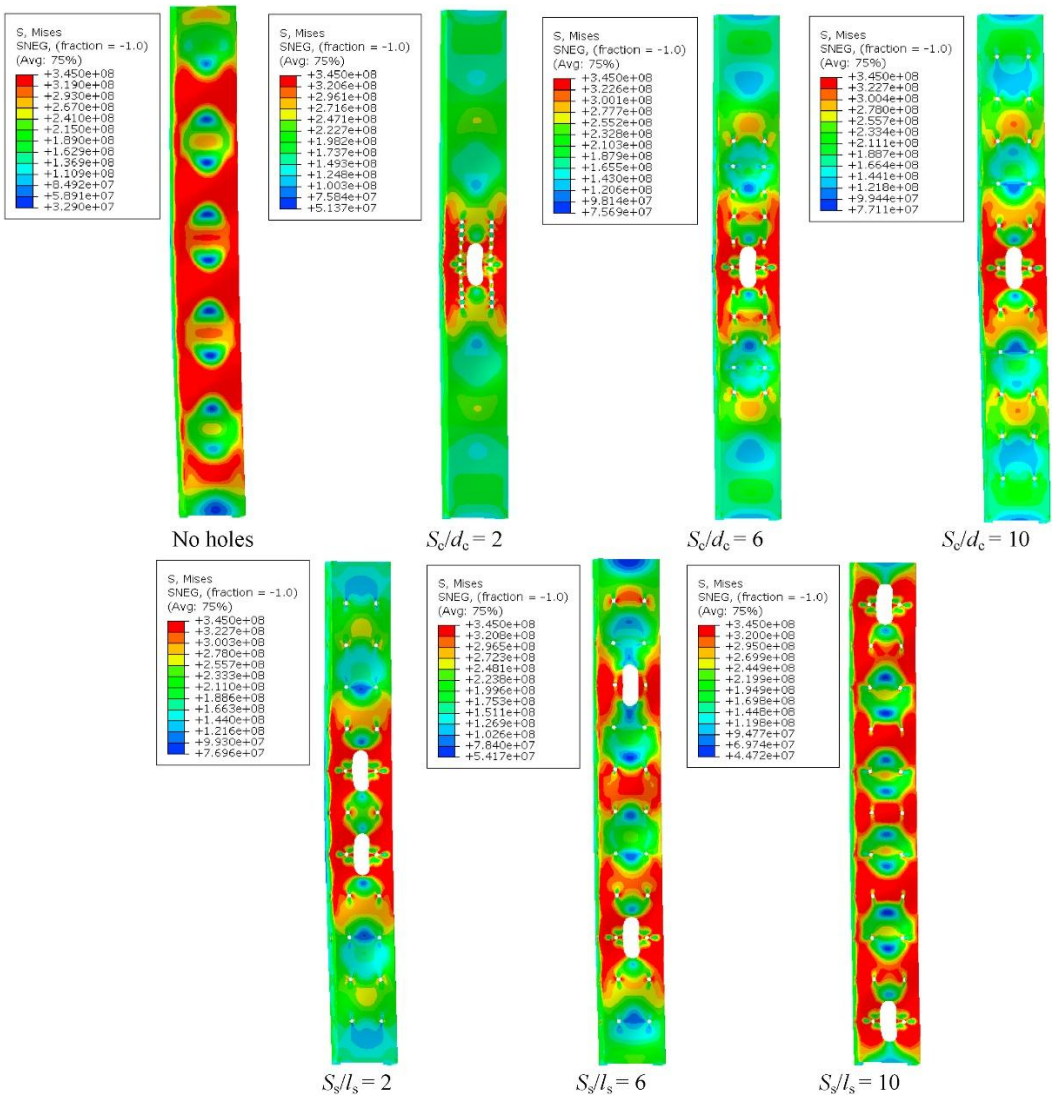

Fig. 2- 19. Influence of the perforation location on the local buckling mode as reported by Xiang et al.[60]

2.2.6. Non-channel perforated sections

Recent investigations into perforated cold-formed steel (CFS) and aluminium alloy members have focused on their axial capacity and buckling behavior under compression. Singh and Singh [32] experimentally studied CFS stub columns with centrally located circular perforations and found that perforation ratios up to 0.1 had negligible influence on axial strength. However, increasing the perforation size ratio to 0.9 led to a strength reduction of up to 44%. Although most existing design equations provided conservative estimates, their predictions were scattered. Feng et al. [61] conducted a finite element study on aluminium alloy circular hollow sections

(CHSs) with circular holes. Their parametric study involving 300 validated models showed that existing design rules for perforated CFS sections were unsuitable for aluminium CHSs. As a result, new design equations were proposed based on the effective area method and demonstrated strong predictive accuracy through reliability analysis. Fang et al. [62] investigated aluminium alloy back-to-back (BTB) channels with web holes. Based on 14 experimental tests and 720 parametric FE models, they concluded that section thickness had a strong effect on axial strength, while modified slenderness had minimal impact for stub and short columns. Existing AISI and AS/NZS standards were conservative by about 10%. Axial strength reduction factor equations were proposed and validated using reliability analysis. Further work by Fang et al. [63] focused on intermediate and slender BTB columns with centred web holes. The results showed that distortional buckling was the dominant failure mode, and axial strength was sensitive to hole size and screw spacing. Increasing the hole size reduced strength by 15–20%, and screw spacing affected whether the channels remained integrated or separated at failure. While AISI and AS/NZS guidelines were found to be conservative by about 15%, the authors proposed refined strength reduction factors. Fig.2-20 shows the failure pattern of the sections used in the above-mentioned studies.

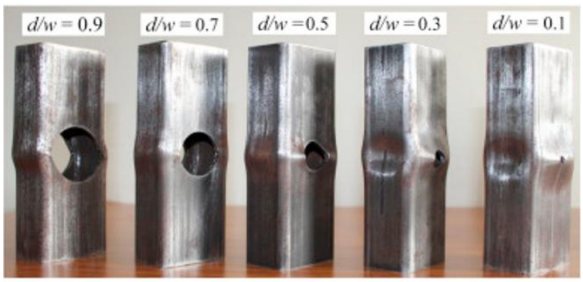

[32]

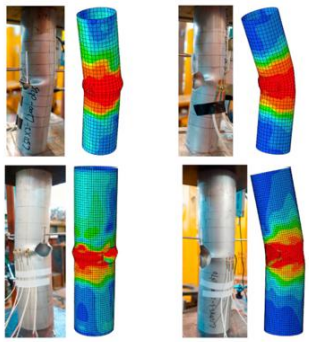

[61]

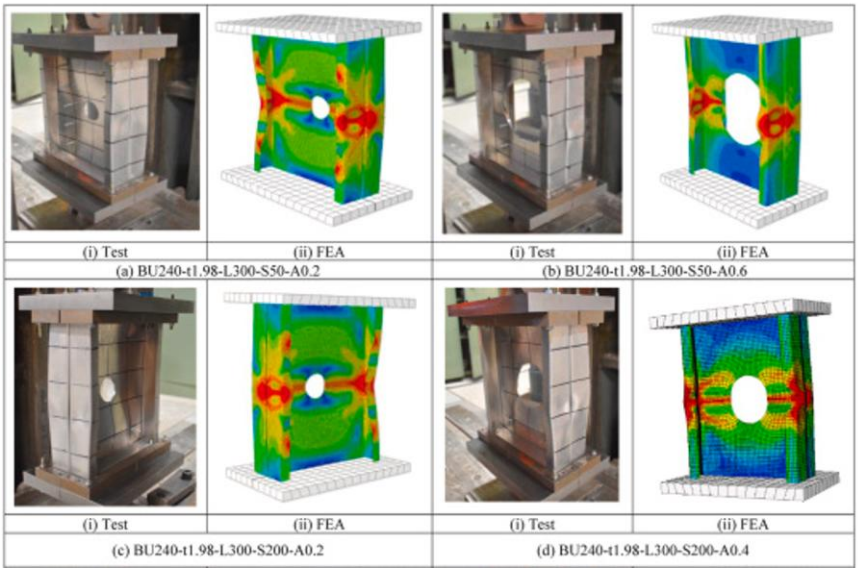

[63]

Fig. 2- 20. Experimental and numerical buckling modes as reported by Singh and Singh [32], Feng et al. [61] and Fang et al. [62]

2.2.7 Design methods and code provisions

Cold-formed steel (CFS) members with web or flange perforations experience complex buckling interactions under combined axial compression and bending. Abdel-Rahman and Sivakumaran [64] developed effective width equations based on finite element models to estimate the ultimate strength of such members, accounting for various perforation geometries and configurations. Davis and Yu [65] experimentally established that holes reduce buckling capacity, with square holes inducing greater reductions than circular ones, though post-buckling strengths were comparable. They proposed modified effective width equations to better reflect these effects. Grey and Moen [66] proposed simplified elastic buckling methods incorporating edge-stiffened holes, demonstrating that global buckling predictions can be reliably extended using classical equations with adjusted section properties. Extending the Direct Strength Method (DSM), Moen and Schafer [7] validated DSM predictions for columns with holes using over 200 nonlinear FE models, suggesting that elastic buckling properties and net-section limits can effectively capture strength reduction in the inelastic regime. Smith and Moen [54] advanced finite strip analysis by introducing reduced thickness models that simulate the stiffness loss from perforations. Yao and Rasmussen [67] conducted a comparative study of 19 DSM-based methods using a dataset of

over 60,000 points and proposed a regression-enhanced approach that includes global–distortional (DG) interaction, demonstrating strong accuracy for stiffened C-sections and rack profiles. Earlier work by Yu and Davis [68] highlighted the need for new design provisions due to the inadequate performance of existing standards when applied to perforated thin-walled members. Moen's doctoral thesis [69] detailed how large or closely spaced holes initiate mixed-mode buckling. Moen and Schafer [70] further explored the introduction of local, distortional, and global mode interactions, showing that failure often occurs prematurely at the net section. Yao and Rasmussen [71] validated ABAQUS-based FE models for a wide range of geometries and showed that mode interactions (LD, DG, LDG) critically affect capacity. Finally, Schafer and Peköz [72] demonstrated that numerically obtained elastic buckling solutions from tools such as CUFSM and ABAQUS can streamline DSM-based capacity estimates without relying on iterative effective width calculations.

2.3 Perforated CFS sections under combined axial compression and bending

Multiple studies have been conducted on perforated cold-formed steel (CFS) sections used in pallet racking systems, which have already been discussed in the earlier section. This section focuses on other studies involving CFS members with perforations subjected to combined axial compression and bending. Ren et al. [73] experimentally and numerically evaluated lipped CFS channel members with circular web openings under minor-axis bending and axial load. Their findings revealed dominant distortional-global buckling mode interactions and showed that the current Direct Strength Method (DSM) overestimates capacity. A modified DSM curve was proposed to improve strength predictions. Chen et al. [43] studied back-to-back channels with and without web perforations under four-point bending. Results indicated that edge-stiffened holes enhanced capacity by 15.4%, while un-stiffened holes reduced it by 15.1%, with distortional buckling as the predominant failure mode. The current AISI and AS/NZS design equations were found to be conservative by 23%–49%. Dai et al. [44] developed a machine

learning model using XGBoost trained on 1620 validated finite element simulations to predict moment capacities. The model achieved high accuracy ($R^2 \approx 0.99$) and was used to propose new design equations with reliability indices above 2.5. Davies et al. [74] employed a modified Generalized Beam Theory (GBT) to account for local, distortional, and global buckling in singly symmetric perforated sections under axial and biaxial bending. Their approach allowed for conservative strength predictions that reduced the reliance on extensive physical testing. Casafont et al. [49] also emphasized the significance of including distortional-global buckling interaction in design formulations, showing that neglecting it could lead to strength overestimation by up to 20%. Their work supported modifications to the DSM framework to better reflect interaction effects in perforated members. Collectively, these studies highlight the need for refined analytical or data-driven design models to accurately capture the complex buckling and failure behaviour of CFS sections with web openings under combined loading. Pham [75] examined the effects of web holes on the elastic global buckling loads of cold-formed steel channel members under compression and bending. Using validated finite element models, the study found that holes positioned at mid-length caused a noticeable reduction in global buckling capacity, especially when the hole depth was large relative to the section depth. Although the AISI S100 “weighted average” method remained suitable for estimating flexural-torsional buckling under compression, the study highlighted the importance of hole size and location in design. Earlier, Shan, LaBoube, and Yu [76], [77] conducted a series of experimental investigations to study the behaviour of cold-formed steel members with web openings under bending, shear, and combined loading. Based on 202 test specimens, they concluded that the AISI interaction equation could adequately predict member capacity if the nominal shear and bending strengths were modified to reflect the presence of web openings.

In conclusion, these studies highlight that web perforations significantly affect the buckling behavior and strength of CFS members under combined loading. Standard design methods often

overestimate capacity, emphasizing the need for refined models that account for perforation effects, especially distortional-global interactions, hole geometry, and placement.

2.4 Shear and web crippling behavior of perforated CFS sections

Keerthan and Mahendran [78] began this line of investigation by conducting 26 shear tests on LiteSteel Beams (LSBs) with web openings using a three-point loading configuration. The specimens, with an aspect ratio of 1.5, were tested to determine the impact of web openings on shear performance. Results indicated that the AS/NZS 4600 and AISI design provisions were conservative. Based on these findings, the authors proposed modified shear capacity reduction factors tailored to LSBs with web openings. In a subsequent study [79], they developed and validated nonlinear finite element models to replicate the observed shear behavior and failure modes. A parametric study was then performed, covering variations in hole geometry and beam dimensions. The results supported an alternative shear design method based on an equivalent reduced web thickness. The authors concluded that shear design rules applicable to LSBs without web openings could be extended to those with openings by adopting this equivalent thickness approach. Keerthan and Mahendran [80] (refer to Fig. 2-21) expanded their research to include cold-formed lipped channel beams (LCBs), conducting 40 shear tests under mid-span loading for beams with aspect ratios of 1.0 and 1.5. The experimental results revealed that existing code provisions were conservative for LCBs with small openings but unconservative for those with large ones. A combined failure mode involving shear and flange distortion was identified in short-span LCBs without flange restraints. Modified reduction factors were proposed to address these behaviors. In a follow-up study [81](refer to Fig. 2-22), finite element models of LCBs with unreinforced circular web openings were developed and validated against experimental data. These models accurately predicted shear capacity and failure modes. A detailed parametric study led to improved shear design equations, which the authors recommended for future inclusion in design codes. Shan et al.[76], [77] performed an extensive series of 202 tests on

standard cold-formed steel C-sections to examine the effects of web openings under pure bending, pure shear, and combined bending and shear. They found that the interaction equations in the AISI Specification could be adapted to predict member strength if the nominal shear and bending capacities were adjusted to reflect the influence of web openings. Uzzaman et al.,[82], [83] investigated the web crippling strength of cold-formed channel sections with unstiffened and edge-stiffened circular web holes under end-two-flange (ETF) and interior-two-flange (ITF) loading. They conducted 60 laboratory tests and developed validated finite element models. A parametric study involving 1116 FEA for each loading condition was carried out, considering variables such as hole diameter, edge-stiffener length, fillet radius, hole position, and bearing plate length. Based on the findings, web crippling strength reduction factors were proposed.

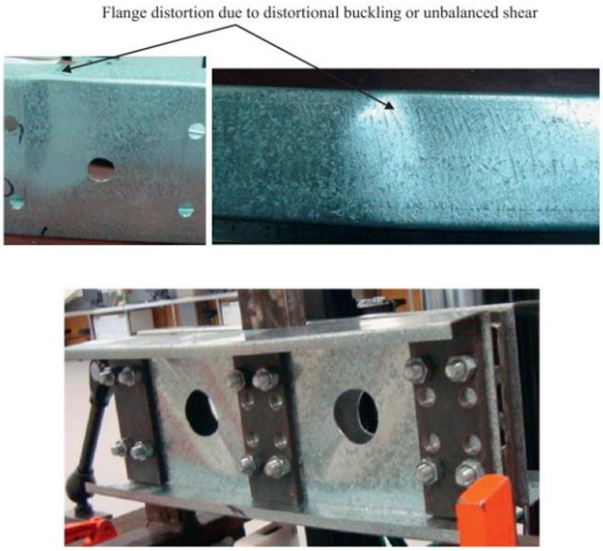

Fig. 2- 21. Failure modes of LCBs with web openings and no straps as reported by Keerthan and Mahendran [80]

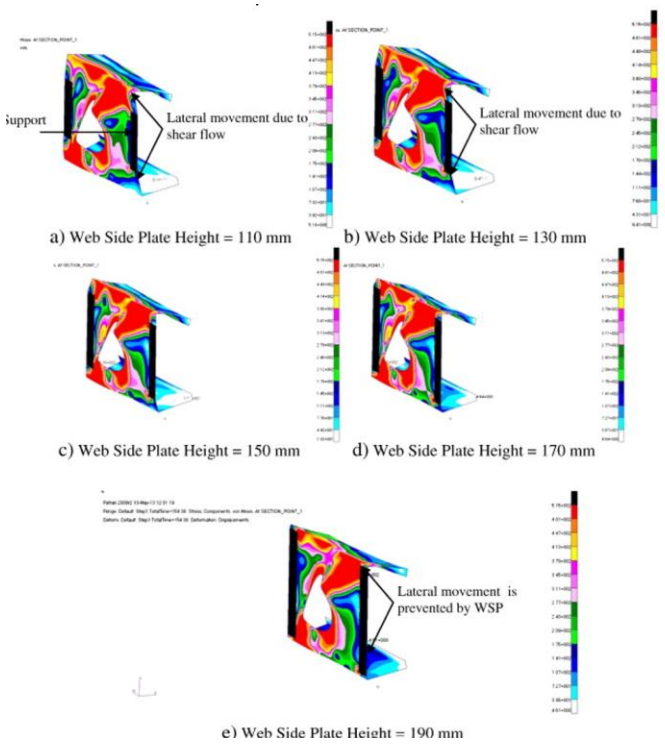

Fig. 2- 22. Failure modes of LCBs as reported by Keerthan and Mahendran [81]

These factors were found to be conservative when validated against both experimental and numerical results. Chen et al. [84] extended this work by focusing on the effect of fastening flanges in cold-formed steel channel sections with web holes. A total of 36 web crippling tests were conducted under ETF and ITF loading, and a parametric study using 912 finite element models was performed. The results showed that flange fastening significantly improved web crippling capacity, by approximately 71 percent for ETF and 33 percent for ITF loading. The authors validated their models against experimental data and confirmed the reliability of the reduction factors proposed by Uzzaman et al. when applied to fastened configurations. In summary, these studies clearly demonstrate the significant influence of web openings on the shear and web crippling performance of cold-formed steel members. While current design codes are generally conservative for small openings, they tend to be unconservative for larger or unreinforced holes. Extensive experimental and numerical investigations have led to the development of refined reduction factors and alternative design methods, such as the use of

equivalent web thickness and improved shear and crippling equations. These findings highlight the need to update existing design provisions to ensure accurate and reliable predictions for perforated cold-formed steel members.

2.5 Structural behavior of CFS sections with slits

The introduction of slitted web studs originated from the need to reduce thermal bridging in light steel framing systems used in cold climates. Höglund and Burstrand [1] (refer to Fig. 2-23) demonstrated that slitting the web significantly increased the heat flow path through steel studs, leading to notably improved thermal resistance. Their work enabled the use of steel studs in external walls in countries such as Sweden and contributed to the development of Light Steel Framing systems. They also highlighted that slitted studs influence not only thermal performance but also serviceability-related aspects such as sound insulation, fire performance, vibration, and construction processes.

LaBoube [4] through hot-box thermal tests reported that slit-web studs improved overall wall R-values by approximately 17% compared to solid-web studs. When combined with angle tracks or thin external insulation, further enhancements up to 28% were achieved.

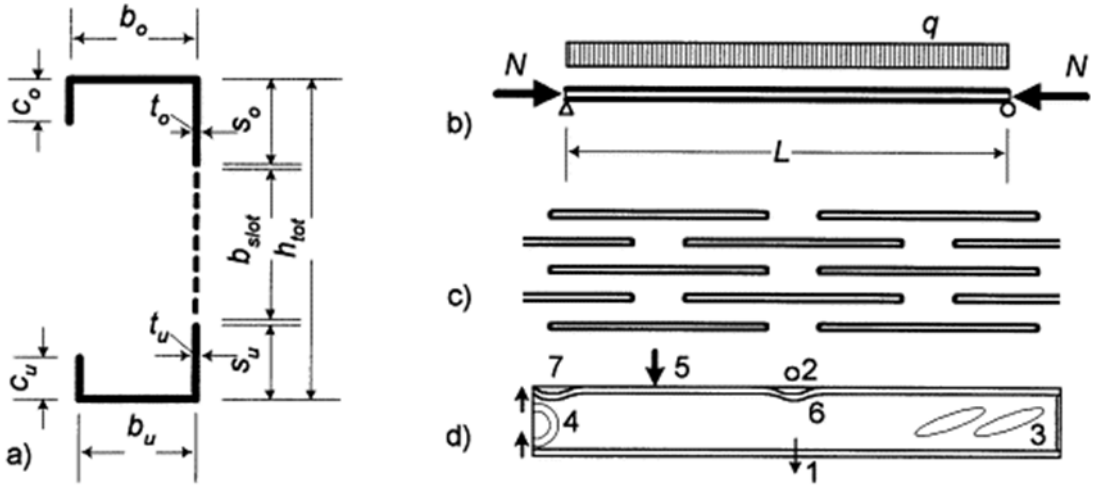

Fig. 2- 23. Slitted stud. a) cross section, b) loading, c) slits, d) failure modes [1].

2.5.1 Axial behaviour

Andreassen and Jönsson [3] (refer to Fig. 2-24) conducted compression tests on slitted load-bearing studs connected to tracks. They examined different column lengths (500–1000 mm), thicknesses (0.7–1.0 mm), and the presence or absence of web stiffeners. Interestingly, web stiffeners provided almost no improvement to ultimate capacity. Failure modes were dominated by global–distortional interaction, even in relatively short columns, confirming that slits significantly influence buckling behaviour. For some configurations, failure included both end crushing and distortional-local interaction, indicating complex mode coupling.

Fig. 2- 24. Test setup: front view [3]

Kesti [85] performed an extensive combined numerical and experimental study on perforated steel wall studs under concentric compression. The study demonstrated that perforations reduce perpendicular flexural stiffness and significantly decrease distortional buckling strength. The European code (Eurocode 3) was shown to produce inaccurate elastic distortional buckling predictions. Methods by Lau and Hancock, and Schafer and Peköz, were found to be more accurate.

Kesti [85] also reported that gypsum sheathing provides significant rotational restraint to the stud, which can double the distortional buckling stress. In some cases, even a minimal level of

restraint was sufficient to eliminate flexural buckling, highlighting the importance of sheathing–stud interaction. Screw pitch was also identified as a critical factor, reducing the screw spacing from 600 mm to 200 mm doubled the distortional buckling stress. Based on these findings, Kesti proposed design equations for perforated studs and provided practical guidelines for incorporating sheathing restraint and web stiffening to enhance buckling resistance.

2.5.2 Behaviour of slitted CFS members under other load combinations

Although axial studies are scarce, relatively more but still limited research has been conducted on slitted or perforated CFS members under shear, bending, combined loading, and web crippling.

(a) Shear Behaviour

Degtyarev and Degtyareva [86] (refer to Fig. 2-25) used validated FE models to examine the shear buckling and ultimate shear strength of slitted channels. They found that changing boundary conditions from test setups to realistic restraints had minimal effect (1–4%) on solid webs but caused 52% reductions in elastic shear buckling load and 39% reductions in ultimate shear strength in slitted webs. This shows slitted webs are highly sensitive to realistic boundary conditions, and design based on idealised test conditions may be unconservative. They concluded that future parametric studies must consider realistic boundary conditions.

In another experimental study by the same authors [87](refer to Fig. 2-26), 15 slitted and 10 solid channels were tested. Slitted webs caused 50–71% strength reduction, decreasing with thicker or deeper sections. Slitted members exhibited more ductile behaviour due to plastic deformation of web strips. Reinforcing flanges improved shear strength by up to 31% due to Vierendeel action. Tentative shear design equations were proposed, and the inclusion of tension field action resulted in good agreement with test results.

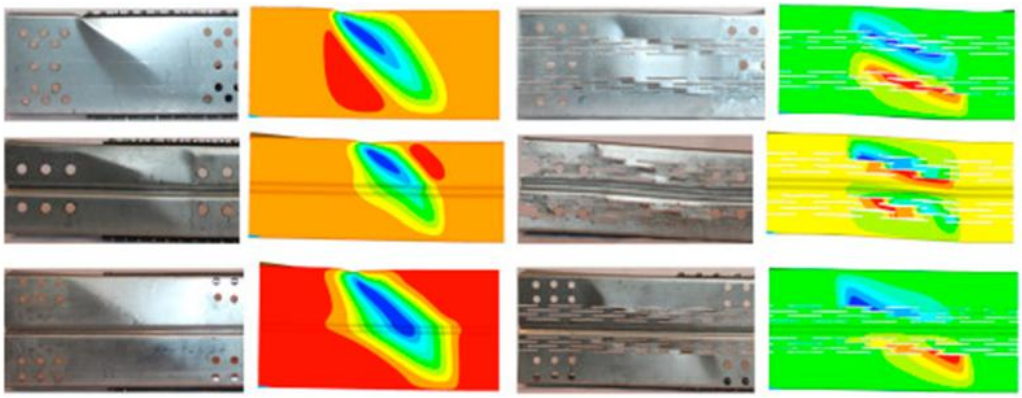

Fig. 2- 25. Failure mode shapes of tested specimens (left column) and FE models (right column) [86].

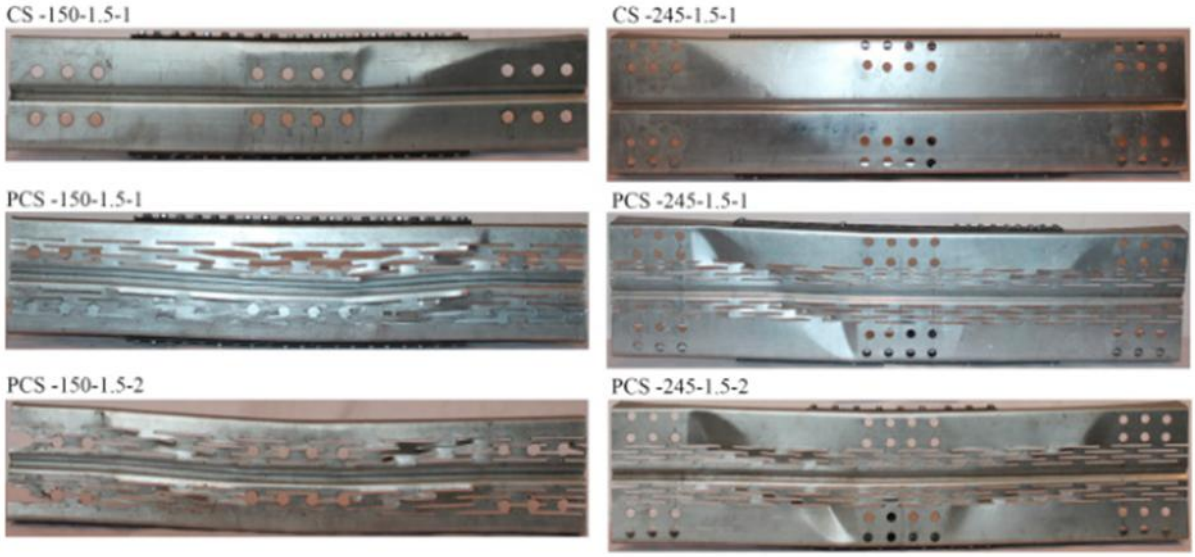

Fig. 2- 26. Failure modes of test specimens with stiffened webs [87].

(b) Flexural behaviour

Degtyareva et al. [88] (refer to Fig. 2-27) investigated local buckling strength of CFS beams with staggered slitted perforations. A validated 3D FE model formed the basis of 432 parametric models. Results showed that staggered slitted perforations caused up to 11% reduction in bending capacity due to local buckling. Modified DSM-based design equations were developed and shown to provide good agreement with FE results, improving accuracy compared to existing DSM formulations.

In another study [89], the same authors focused on distortional buckling under bending, which was not previously addressed. Up to 23% reduction in bending capacity was reported. The

current DSM provisions in AISI S100 (2016) and AS/NZS 4600 (2018) were found inadequate for predicting distortional buckling in slitted beams. New design rules were proposed, with modified DSM slenderness formulations, which significantly improved accuracy and reliability.

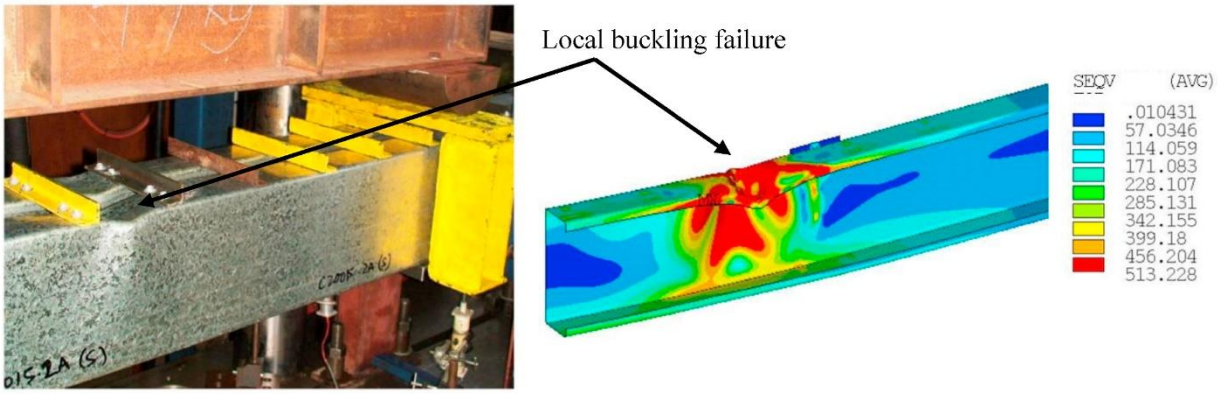

Fig. 2- 27. Failure mode comparison between test and FE model of the Specimen [88].

(c) Combined bending and shear

Degtyareva et al. [90] (refer to Fig. 2-28) conducted a numerical study on slitted CFS channels subjected to combined bending and shear. The parametric study varied depth (d), thickness (t), slot length and width, number of rows, yield strength, and aspect ratio. Staggered slitted perforations caused significant reductions in combined capacity. New empirical interaction equations were proposed, improving prediction accuracy. However, the study did not consider axial forces or eccentric loading.

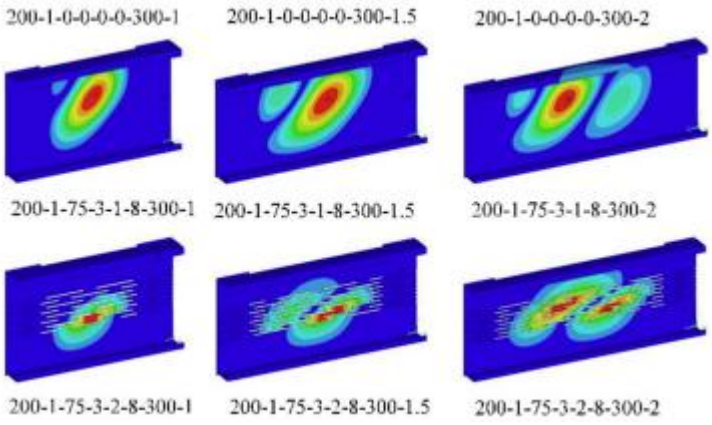

Fig. 2- 28. Critical buckling mode of solid and slitted channels subjected to combined bending and shear [90]

(d) Web crippling

Several recent studies have investigated the web crippling behaviour of slitted perforated CFS sections under different loading conditions. Under the Interior-One-Flange (IOF) load case, Gatheeshgar et al. [91] (refer to Fig. 2-29) reported that staggered slitted perforations resulted in reductions of up to 49% in web crippling strength. Based on their findings, reduction factor-based equations were proposed, which showed good agreement with finite element (FE) predictions. Under the End-One-Flange (EOF) load case, Gatheeshgar et al. [92] tested 48 specimens with solid and slitted webs and observed even more severe strength reductions, reaching up to 74%. They also demonstrated that existing design provisions in AISI S100, AS/NZS 4600, and EN 1993-1-3 were unable to accurately predict the capacity of slitted sections, leading to the development of a new design equation that significantly improved prediction consistency. Furthermore, Degtyareva et al. [93] experimentally validated web crippling design equations and confirmed that current code provisions often underestimate or overestimate the capacity of slitted members. They proposed modified equations that explicitly account for slitted effects and achieved strong agreement with experimental results. Overall, these studies establish that web perforations can severely compromise web crippling capacity and necessitate modified design rules; however, they primarily focus on local bearing failures and do not address global buckling or axial–bending interaction.

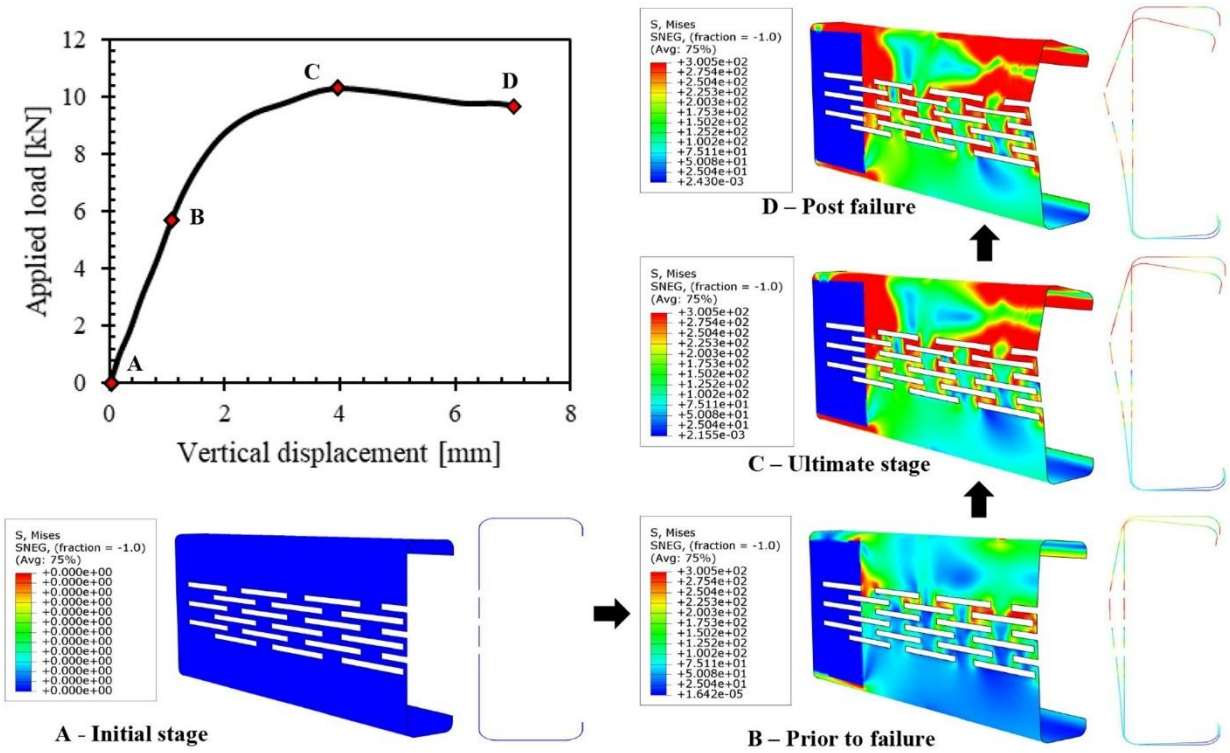

Fig. 2- 29. Failure mode progression of specimen in conjunction with applied load vs vertical displacement plot [91].

2.6 Thermal performance of CFS sections with slits

Liu et al. [2] investigated the fire performance of non-load-bearing slitted steel stud walls using full-scale ISO-834 standard fire tests. Temperatures were recorded at the exposed surface, unexposed surface, and within the stud cross-section. The study analysed the influence of web height, number of slot rows, number of gypsum board layers, and the application of mortar on the unexposed side. Increasing stud height, slot density, and gypsum layers reduced heat transfer, while spalling of the gypsum board during fire increased temperatures in the steel components. A three-dimensional finite element (FE) model was developed in ABAQUS and validated against experimental data. Parametric analysis confirmed the influence of geometric and material parameters on temperature distribution. However, the timing and extent of gypsum spalling could not be predicted, indicating the need for further investigation of thermal degradation.

Lipták-Váradi [94] examined the thermal behaviour of slitted steel girders and introduced the concept of equivalent thermal conductivity to simplify modelling. Finite element simulations

using ANSYS and HEAT3 were used to analyse heat transfer through various slot geometries. Equivalent thermal conductivity values were calculated so that a solid section could replicate the heat transfer of a slitted section. The comparison showed agreement between the original slitted models and the equivalent solid models. The study showed that slot geometry has a direct effect on heat flow and proposed modified slot configurations to reduce thermal conductance. The equivalent conductivity approach reduces computational time in multi-dimensional thermal modelling and can be used in facade and thermal bridge simulations. Martins et al. [95] conducted a parametric study on thermal bridge mitigation strategies in lightweight steel-framed wall systems. The study examined insulation materials, air layers, and geometric modifications to steel components. Conventional mitigation strategies reduced U-values, while further reductions were achieved through the use of advanced insulation materials such as aerogel and vacuum insulation panels. The study proposed design rules for the thermal improvement of lightweight steel-framed elements. Although slitted studs were not the main focus, the work showed that geometric modifications to steel profiles are an effective method for reducing heat transfer and can be combined with material-based strategies. Li et al. [96] analysed a lightweight assembled exterior wall panel (LAEWP) system incorporating steel studs and insulation using experimental testing and three-dimensional FE modelling. The FE model showed agreement with experimental results and was used for parametric analyses. The study evaluated the effects of changing insulation material, reducing the number or size of studs, introducing web openings, and combining multiple strategies. Changing insulation material reduced the U-value by 13.2%, while combining geometric and material changes reduced the U-value by 23.7%. Web openings were shown to decrease heat transfer and improve insulation efficiency. The authors noted that environmental factors such as moisture content may affect thermal performance and require further study through in-situ monitoring. Alekperov and Aksenov [97] focused on modifying slot shape to improve thermal performance while maintaining structural capacity. Finite element

simulations in COMSOL Multiphysics were used to analyse steel studs with different web hole geometries. Experimental testing was used to compare the thermal performance of prototype studs with standard slitted studs. The results showed a 9–19% reduction in heat conduction for modified slot shapes, with triangular slots performing best. The proposed slot configurations reduced thermal bridging without requiring additional insulation layers. A new manufacturing method was also suggested, where slot patterns are interrupted at billet cutting locations to preserve web shear resistance near supports.

2.7 Summary of literature review

Extensive research to date has established that the introduction of web perforations in CFS channels generally diminishes member strength and can precipitate complex buckling mode interactions (local, distortional, and global). Strengthening measures such as adding edge stiffeners around holes have been shown to partially recover lost capacity, yet accurately predicting the load resistance of perforated sections remains challenging under current design provisions. Existing design specifications and classical calculation methods often do not fully capture the observed behavior of members with web holes, tending to be conservative in some instances and unconservative in others when critical buckling interactions are present. This highlights significant limitations in present design methods and underscores the need for continued research. Also, existing studies show that slotted or slitted CFS studs reduce thermal bridging and improve energy performance. Experimental and numerical evidence confirms that web geometry, stud height, insulation configuration, and facing materials affect temperature distribution. Slitted studs have also been observed to exhibit reductions in axial capacity, altered stiffness characteristics, and shifts in governing failure modes, effects that differ from those associated with conventional service holes. Despite these observations, only limited studies have explored the structural performance of slitted CFS members, and even fewer have examined behaviour under combined axial and bending actions.

Future studies are required to develop refined analytical models and structural design approaches that account for perforation geometry, stiffening strategies, and combined loading effects. While the thermal efficiency benefits of slits have been acknowledged, previous studies have not quantified how geometric and slit parameters influence thermal performance. Addressing these gaps will improve the reliability of strength thermal performance predictions and facilitate the safe, economical use of perforated CFS channel sections in structural applications.

Tables 2-1 and 2-2 are provided subsequently summarise the major experimental, numerical, and analytical findings from the reviewed literature, providing a consolidated overview of perforation types, methods, structural as well as thermal responses.

2.8 Research gaps

From the comprehensive literature review presented in this chapter, several critical research gaps have been identified:

- Although numerous studies have investigated perforated and slotted CFS members, research specifically focused on CFS studs with slits in the web is extremely limited, particularly in relation to their structural performance.
- Existing studies on slitted CFS sections have primarily considered concentric axial loading, and no systematic investigation has been conducted on the behaviour of slitted members under eccentric or combined axial–bending loads, which are common in practical wall systems.
- The current Direct Strength Method (DSM) and codified design provisions (AS/NZS 4600 and AISI S100) do not accurately predict the axial strength of slitted members, especially when buckling mode interactions or eccentric loading are involved.
- While the thermal efficiency benefits of slits have been acknowledged, previous studies have not quantified how geometric and slit parameters influence thermal performance.

Table 2- 1:Summary of Previous Studies on the Axial Behaviour of Perforated Cold-Formed Steel Members

Ref. No.	Authors	Method	Loading Type	Section Type	Hole Type	Key Findings
[23]	Sivakumaran	Experimental	Axial compression	Lipped channel	Unstiffened web holes	Hole shape negligible, size affects strength; significant reduction for a/W > 0.6
[24]	Moen & Schafer	Experimental + FEM	Axial compression	Short/intermediate lipped channels	Slotted web holes	Modest strength reduction (up to 2.7%); changes in buckling mode and ductility
[37]	Guo & Yao	Experimental + FEM (ABAQUS)	Axial compression	Lipped channels	Rectangular holes	Distortional or combined buckling dominant; refined design method proposed
[11]	Zhao et al.	Experimental + FEM	Axial compression	CFS channels	Various rectangular holes	Capacity reduction (11.7–31.5%) with hole width; modified DSM proposed
[25]	Kulatunga & Macdonald	FEM (ANSYS)	Axial compression	Lipped channels	Hole position variation	Strength sensitive to hole location; lower than net section predictions
[26]	Kulatunga et al.	Experimental + FEM	Axial compression	Perforated columns	Various hole sizes	Up to 34.43% reduction; interaction of local & distortional buckling
[27]	Loov	Experimental	Axial compression	Stub columns	Punched webs	Proposed effective width; existing code conservative
[28]	Pu et al.	Experimental	Axial compression	Symmetrically perforated channels	Unstiffened holes	Hole size & position affect strength; aspect ratio negligible
[29]	Yao & Rasmussen	Spline FSM + ABAQUS	Axial compression	C-sections	Various holes	Hole width most critical; proposed parametric DSM
[31]	Yao & Rasmussen	FEM (ABAQUS)	Axial compression	Various cross-sections	Multiple geometries	Interaction of L, D, G buckling; DSM overestimates; centroid shift critical
[33]	Sivakumaran	Experimental + FEM	Axial compression	Lipped channel	Various holes	Local buckling dominant; codes inadequate
[34]	Sivakumaran	FEM	Axial compression	Lipped channel	Various holes	Reinforces effect of geometry on buckling; confirms prior experiments
[35]	Yao	Experimental + FEM	Axial compression	Lipped channel	Slotted holes	Distortional buckling mode; effective width method suggested
[36]	Moen et al.	Experimental + FSM	Flexural (linked to compression)	C-section joists	Unstiffened rectangular holes	Distortional & web buckling; preliminary DSM equations

Ref. No.	Authors	Method	Loading Type	Section Type	Hole Type	Key Findings
[32]	Singh & Singh	Experimental	Axial compression	RHS & SHS	Centrally placed circular holes	Up to 44% loss at d/w = 0.9; new equations recommended
[10]	Chandramohan et al.	Experimental + FEA	Axial Compression	Lipped Channel	Edge-stiffened Rectangular	Edge-stiffening improved axial strength by up to 14%
[39]	Chen et al.	Experimental + FEA	Axial Compression	Lipped Channel	Edge-stiffened Rectangular	Edge-stiffening improved axial capacity by 21%, more uniform deformation
[40]	Osgouei et al.	Analytical + FEA	Axial Compression	Lipped Channel	Edge-stiffened Circular	Analytical model with <5% error; polynomial deflection functions accurate
[8]	Chen et al.	FEA + Regression	Axial Compression	Lipped Channel	Edge-stiffened Rectangular	Proposed DSM modifications, captured sensitivity to slenderness and hole size
[41]	Shaker et al.	FEA	Axial Compression	Lipped Channel	Edge-stiffened Rectangular	Design codes underestimate strength by up to 66%
[13]	He et al.	Experimental	Axial Compression	Lipped Channel	Slotted (Edge-stiffened)	Observed buckling interaction modes not captured by existing codes
[42]	Chen et al.	Experimental + FEA	Axial Compression	Lipped Channel	Slotted (Edge-stiffened)	Complex buckling interaction, recommended design considerations
[45]	Chi et al.	Experimental	Axial Compression	Back-to-Back Channels	Multiple Edge-stiffened Circular	19.2% strength gain, conventional equations inadequate
[9]	Chen et al.	Experimental + Finite Element Analysis (27 tests + 135 FE simulations)	Axial compression	Back-to-back cold-formed steel channels	Edge-stiffened, unstiffened, plain	Edge-stiffened holes increased axial strength by 6.6%, unstiffened reduced by 12.4%. Composite action enhanced capacity in longer columns. Validated FE model used for parametric study.
[43]	Chen et al.	Experimental + Finite Element Analysis (14 tests)	Four-point bending	Back-to-back cold-formed steel channels	Edge-stiffened, unstiffened	Edge-stiffened holes increased flexural strength by 15.4%, unstiffened reduced by 15.1%. Distortional buckling dominated. Design codes conservative by 23–49%.

Ref. No.	Authors	Method	Loading Type	Section Type	Hole Type	Key Findings
[44]	Dai et al.	Machine Learning (XGBoost model with 1620 FE data points)	Moment capacity prediction	Cold-formed steel channel beams	Edge-stiffened, unstiffened	XGBoost model achieved R^2 ~99%, outperforming Moen & Schafer and Yu's equations. New design equations showed 8.78% error, reliability indices >2.5.
[45]	Chi et al.	Experimental + Finite Element Analysis (29 tests + 44 simulations)	Axial compression	Back-to-back cold-formed steel channels	Edge-stiffened	19.2% axial capacity increase with stiffened holes. AISI and AS/NZS conservative by 9% for plain channels. Moen & Schafer's equations overly conservative by 47%.
[50]	Bertocci et al.	Experimental and FEA	Combined Axial and Bending	Mono-symmetric perforated profiles	Perforated	Identified discrepancies with EN 15512, especially under weak axis bending and seismic loading; developed 3D strength domains.
[51]	Bonada et al.	Experimental and FEA	Axial and Eccentric Bending	Perforated Uprights	Perforated	Distortional buckling critical due to axial eccentricity; validated FE models highlight role of residual stresses and strength enhancement.
[52]	Orlando et al.	Experimental	Combined Axial and Bending	Slender open-section columns	Perforated	Current codes underestimate strength under high eccentricity.
[53]	Pastor et al.	Experimental and FEA	Bi-axial Bending and Compression	Uprights	Perforated	Observed up to 53% capacity reduction under combined eccentricities; EN 15512 overly conservative in some cases.
[55]	Dai et al.	Experimental and FEA	Axial Compression	Rack Upright Frames	Perforated	Global and distortional-global buckling dominant; proposed improved DSM for distortional buckling in upright frames.
[57]	Wang et al.	Experimental and numerical	Axial compression	CFS channels with edge and web stiffeners	Web holes	Σ-type web stiffeners increased axial strength by ~30–50%. Web holes reduced strength by ~6% for channels and ~25% for Σ-sections. DSM applicable to these profiles.
[58]	Wang et al.	Parametric FEA	Axial compression	Perforated lipped channels	Rectangular holes (varied height, width)	Hole height was most influential on axial capacity; width, shape, and spacing affected buckling modes. Modified DSM validated.
[59]	Wang et al.	Experimental and FEA	Axial and eccentric compression	Built-up I-sections with web and edge stiffeners	Rectangular web holes	Web stiffeners improved strength, particularly in short and medium columns. Composite action slightly reduced. DSM aligned with test data.

Ref. No.	Authors	Method	Loading Type	Section Type	Hole Type	Key Findings
[60]	Xiang et al.	Experimental and ABAQUS FEA	Axial compression	G-section channels with complex stiffeners	Circular holes	Larger holes reduced strength; hole location influenced deformation. Recommended spacing of 3–6 times the hole diameter to prevent web instability.
[24]	Moen and Schafer	Experimental + FE	Axial Compression	CFS columns	Slotted web holes	Ultimate strength slightly affected; post-peak ductility influenced; interaction between local and distortional buckling observed; friction-bearing ends viable.
[54]	Smith and Moen	Analytical + FE Validation	Buckling Analysis	Perforated pallet rack columns	Various perforations	Finite strip solutions validated against 1200+ FE models; provided basis for DSM extension to perforated sections.
[56]	Taranu et al.	Experimental + FE	Axial Compression	CFS uprights with stiffeners	Perforated webs	Failure modes shifted with length; DSM accurate within 2–7% for full net section; EWM conservative for stiffened sections.
[32]	Singh and Singh	Experimental	Axial Compression	CFS Stub Columns	Circular Perforations	Perforation ratios up to 0.1 had negligible effect; strength reduced up to 44% at 0.9 ratio; conservative but scattered code predictions.
[61]	Feng et al.	Finite Element Study	Axial Compression	Aluminium Alloy CHSs	Circular Holes	300 validated models; existing CFS design rules unsuitable; new equations based on effective area method proposed and validated.
[62]	Fang et al.	Experimental + FE Modelling	Axial Compression	Aluminium BTB Channels	Web Holes	Thickness influenced strength, modified slenderness had limited impact; AISI/AS-NZS conservative by ~10%; strength reduction factor equations proposed.
[63]	Fang et al.	Experimental + FE Modelling	Axial Compression	Intermediate and Slender BTB Channels	Centred Web Holes	Distortional buckling dominant; strength reduced by 15–20% with increased hole size; screw spacing influenced failure mode; refined reduction factors proposed.
[64]	Abdel-Rahman & Sivakumaran	FE Modelling	Axial + Bending	CFS with Perforations	Various	Developed effective width equations for strength prediction considering hole geometry
[65]	Davis & Yu	Experimental	Axial + Bending	CFS with Square/Circular Holes	Square, Circular	Square holes reduce capacity more than circular ones; post-buckling comparable
[66]	Grey & Moen	Analytical	Elastic Buckling	Edge-Stiffened CFS	Edge-Stiffened	Proposed simplified methods for global buckling prediction using adjusted properties
[28]	Moen & Schafer	Nonlinear FE	Axial + Bending	CFS Columns with Holes	Slotted, Round	DSM extended to include holes; net-section limits and elastic properties suffice
[54]	Smith & Moen	Finite Strip Analysis	Compression	Thin-Walled Perforated CFS	Central Perforation	Introduced reduced-thickness FSA to simulate stiffness loss from holes
[67]	Yao & Rasmussen	Comparative Study	Compression	Stiffened C-Sections & Racks	Circular	Regression DSM approach including DG interaction gave strong accuracy

Ref. No.	Authors	Method	Loading Type	Section Type	Hole Type	Key Findings
[68]	Yu & Davis	Experimental	Compression	Perforated Thin-Walled	Slotted	Current standards underperform for perforated thin-walled members
[69]	Moen	Thesis	Compression	CFS with Large Holes	Closely Spaced	Large holes initiate mixed buckling; detailed nonlinear behavior
[70]	Moen & Schafer	FE Study	Compression	Perforated CFS Columns	Mixed-Mode	Studied interaction of local, distortional, global modes with holes
[71]	Yao & Rasmussen	FE Validation	Compression	Various CFS Sections	Various	Mode interactions (LD, DG, LDG) critically affect strength
[72]	Schafer & Peköz	Numerical	Compression	General CFS Sections	NA	Elastic buckling tools (CUFSM, ABAQUS) support streamlined DSM use
[73]	Ren et al.	Experimental + Numerical (FE)	Combined axial + bending	Lipped channel	Circular web openings	DSM overestimated capacity; proposed modified DSM curve; distortional-global buckling dominant
[43]	Chen et al.	Experimental + FE	Four-point bending	Back-to-back channels	Edge-stiffened and unstiffened web holes	Edge-stiffened holes increased strength by 15.4%; un-stiffened reduced it by 15.1%; distortional buckling dominant
[44]	Dai et al.	Machine Learning (XGBoost) + FE	Moment capacity prediction	Back-to-back channels	Stiffened and unstiffened	High predictive accuracy ($R^2 \approx 0.99$); proposed new design equations; reliability index > 2.5
[74]	Davies et al.	Analytical (Modified GBT)	Axial + biaxial bending	Singly symmetric sections	Web perforations	Incorporated buckling interactions (L, D, G); conservative strength predictions
[49]	Casafont et al.	Experimental + Numerical	Combined loading	Perforated rack columns	Web openings	Neglecting distortional-global interaction overestimates strength by up to 20%
[75]	Pham	Finite Element Modelling	Compression + bending	CFS channel	Web holes	Mid-length holes reduce global buckling capacity; hole size and position critical
[76], [77]	Shan, LaBoube & Yu	Experimental	Bending, shear, combined	CFS with web openings	Web openings	AISI interaction equations adequate with adjusted nominal strengths for openings
[78]	Keerthan and Mahendran	Experimental	Shear	LiteSteel Beams (LSBs)	Web openings	AS/NZS 4600 and AISI provisions conservative; modified reduction factors proposed for LSBs.
[79]	Keerthan and Mahendran	FE + Parametric Study	Shear	LSBs	Web openings	Developed and validated FE models; introduced equivalent reduced web thickness for design.

Ref. No.	Authors	Method	Loading Type	Section Type	Hole Type	Key Findings
[80]	Keerthan and Mahendran	Experimental	Shear	Lipped Channel Beams (LCBs)	Web openings	Conservatism varies with hole size; combined shear and flange distortion failure; modified reduction factors.
[81]	Keerthan and Mahendran	FE + Parametric Study	Shear	LCBs	Circular web openings	Accurate predictions of capacity; improved shear design equations proposed.
[76], [77]	Shan et al.	Experimental	Shear + Bending	C-sections	Web openings	AISI interaction equations adaptable with adjusted nominal capacities.
[82], [83]	Uzzaman et al.	Experimental + FE + Parametric	Web Crippling (ETF, ITF)	Channel sections	Circular web holes	Reduction factors proposed and validated; conservative predictions.
[84]	Chen et al.	Experimental + FE + Parametric	Web Crippling (ETF, ITF)	Channel sections with fastened flanges	Web holes	Fastening increased web crippling capacity by ~71% (ETF) and ~33% (ITF); validated Uzzaman et al.'s reduction factors.
[1]	Höglund & Burstrand	Conceptual / System Development	Thermal	Slitted Studs	Slits	Slits increase heat flow path; improved thermal resistance; enabled light steel framing; affects sound, fire, vibration, construction
[4]	LaBoube	Experimental (Hot-box tests)	Thermal	Slit-Web Stud Walls	Slits	~17% increase in R-value; up to 28% improvement with angle tracks or insulation
[3]	Andreassen & Jönsson	Experimental	Compression	Load-bearing Slitted Studs	Slits	Web stiffeners had minimal effect; failure dominated by global–distortional interaction; complex buckling
[85]	Kesti	Numerical + Experimental	Compression	Perforated Wall Studs	Holes	Perforations reduced flexural stiffness and distortional strength; Eurocode 3 inaccurate; alternative methods more accurate
[86]	Degtyarev & Degtyareva	Numerical (validated)	Shear	Slitted Channels	Slits	Boundary conditions had minimal effect on solid webs (1–4% change), but a substantial effect on slitted webs, reducing shear buckling loads by 52% and ultimate shear strength by 39%, and realistic boundary conditions are therefore required.
[87]	Degtyarev & Degtyareva	Experimental	Shear	Slitted Channels	Slits	Slitted webs resulted in 50–71% strength reduction, exhibited ductile behaviour, flange reinforcement increased strength by up to 31%, and shear design equations incorporating tension field action were proposed.
[88]	Degtyareva et al.	Numerical + Parametric Study	Bending (Local Buckling)	CFS Beams with Staggered Slits	Slits	Staggered slitted perforations resulted in up to 11% reduction in bending capacity, and modified DSM equations improved prediction accuracy.
[89]	Degtyareva et al.	Numerical + Parametric Study	Bending (Distortional Buckling)	Slitted Beams	Slits	Up to 23% reduction in bending capacity, DSM (AISI/AS/NZS) provisions were inadequate, and new DSM rules with modified slenderness improved reliability.

Ref. No.	Authors	Method	Loading Type	Section Type	Hole Type	Key Findings
[90]	Degtyareva et al.	Numerical + Parametric Study	Combined Bending & Shear	Slitted Channels	Staggered Slits	Combined bending and shear caused significant reduction in capacity, interaction equations were proposed, and axial or eccentric effects were not considered.
[91]	Gatheeshgar et al.	Numerical + Experimental	Web Crippling (IOF)	Slitted Channels	Staggered Slits	Up to 49% reduction in web crippling capacity, a reduction factor-based equation was proposed, and good agreement with numerical results was observed.
[92]	Gatheeshgar et al.	Experimental	Web Crippling (EOF)	Slitted & Solid Channels	Staggered Slits	Up to 74% reduction in web crippling capacity, existing code provisions were inaccurate, and the new design equation improved prediction consistency.
[93]	Degtyareva et al.	Experimental	Web Crippling	Slitted Channels	Staggered Slits	Existing design codes often underestimated or overestimated capacity, and modified equations incorporating slot effects achieved high accuracy.

Table 2-2: Summary of Previous Studies on the Thermal Behaviour of Perforated Cold-Formed Steel Members

Ref. No.	Authors	Method	Type of Study	Section Type	Hole Type	Key Findings
[2]	Liu et al.	Experimental + Numerical (3D FE)	Fire (ISO-834)	Slitted stud walls	Slits	Stud height, slot rows, gypsum layers reduce heat transfer.
[94]	Lipták-Váradi	Numerical (ANSYS + HEAT3)	Thermal conduction	Slitted steel girders	Slits	Equivalent thermal conductivity was introduced, slit geometry affected heat flow, and equivalent solid models matched the performance of slitted sections.
[95]	Martins et al.	Parametric study	Thermal bridge mitigation	Lightweight steel-framed walls	Not specific	Geometric and material modifications reduced the U-value, advanced insulation produced further reductions,

Ref. No.	Authors	Method	Type of Study	Section Type	Hole Type	Key Findings
						and design rules were proposed.
[96]	Li et al.	Experimental + 3D FE	Thermal insulation wall panels (LAEWP)	Steel studs in panels	Web openings	Changing insulation reduced the U-value by 13.2%, combining web openings with material changes reduced the U-value by 23.7%, and moisture effects were noted.
[97]	Alekperov & Aksenov	Numerical (COMSOL) + Experimental	Thermal conduction	Slitted CFS studs	Modified slit shapes	Modified slit shapes reduced heat conduction by 9–19%, triangular slits performed best, and slot interruption preserved shear resistance near supports.

Chapter 3 Axial capacity of cold-formed steel channel sections with slits

3.1 Introduction

As mentioned, the literature reports limited experimental tests on the axial capacity of CFS studs with slits (refer to Fig. 3-1). In 2016, an experimental study was conducted by Andreasson and Jönsson [3] (refer to Fig. 3-1a). However, equivalent tests on CFS studs with solid webs were not conducted, and no design recommendations were provided. Furthermore, no comparison with non-linear elasto-plastic finite element models was presented. In 2006, Laboube [4] reported an experimental study (refer to Fig. 3-1b). While the sections included slits, web opening was also included for services. Laboube reported that, in terms of thermal performance, slit-web studs performed 17% better than solid-web studs, achieving an overall R-value of 10.4 [4]. Furthermore, slit-web studs outperformed solid-web studs in bending and axial capacity, with increases of 50% and 45%, respectively. Part of this improvement was attributed to the higher yield and ultimate strengths of the slit-web studs, which were 27% and 30% greater, respectively [4]. Finally, in 2000, Kesti [85] reported an experimental study (refer to Fig. 1c). Again, while the sections included slits, they also included an intermediate stiffener in the web. The experimental test results reported by Andreasson and Jönsson [3] are thus the most relevant for the study reported in this chapter. It should also be noted that none of the studies reported a direct comparison of axial capacities between a solid stud and a stud with slits of the same specification.

In terms of shear, more recent numerical work has been reported in the literature. Using non-linear elasto-plastic finite element analysis, Degtyareva et al. [86], [87], [88], [89], [90] (refer to Fig. 3-1d) investigated the reduced shear capacity of CFS beams with slits. They reported a 71% reduction in shear strength due to the inclusion of slits. Additionally, the local buckling flexural capacity is decreased by up to 67% [88], the distortional buckling capacity by up to 23% [90], and the capacity for combined shear and bending by up to 11% [89]. It should

be noted that while other loading conditions, such as web crippling, were also considered by the same authors [91], [92], [93], no work has been reported on compression.

Other studies in literature have focused solely on the thermal performance of perforated studs [2][94], [95], [96], [97]. These studies demonstrated a correlation between the perforation geometry and the heat flow through the element [94]. Additionally, the presence of slits in the web increases the heat path length within the steel elements, resulting in reduced thermal bridging compared to studs with standard solid geometry [96].

Recent research on perforated sections has addressed multiple aspects, such as developing simplified design formulations for edge-stiffened circular openings [8], [9], evaluating differences between unstiffened and edge-stiffened elongated holes [10], examining the impact of perforation width [11], investigating the response of slotted sections under pinned–pinned boundary conditions [12], analysing local–distortional interactive effects [13], and assessing the structural behavior of perforated high-strength steel channel sections [14].

The average reduction in axial capacity due to circular holes was reported as 19% [8] and 14% [9], while for elongated holes, it was 18% [10]. Zhao et al. [11] found a reduction of 11.7% when the hole width-to-web width ratio increased from 0 to 0.4, and 31.5% for an increase from 0.4 to 0.8. Under pinned-pinned boundary conditions, axial capacity was reduced by an average of 2.4% for specimens primarily failing due to distortional buckling, and by 6.4% for those failing due to local buckling [12]. Ziqi et al. [13] observed a 2.74% reduction due to the introduction of slots. Zhang et al. [14] reported significant reductions in axial capacity for web-stiffened high-strength steel members: 28.9%, 17.5%, 23.1%, and 11.5% for member lengths of 300, 900, 1500, and 2000 mm, respectively, compared to smaller reductions of 6.8%, 3.7%, 2.8%, and 1.1% for non-perforated members of the same lengths. However, these studies primarily addressed slots rather than slits.

In this chapter, the axial capacity of CFS studs with slits was studied. Firstly, Finite

Element (FE) models were developed and validated against those of Andreasson and Jönsson [3]. Using the validated FE models, a parametric study was conducted, considering the effects of section depth (D), flange width (B_f), thickness (t), slit length (L_{sl}), slit width (W_{sl}), and length (L) of the studs (refer to Fig.3- 2). Finally, design recommendations in the form of strength reduction factors were proposed, and based on these, modified design DSM equations are presented.

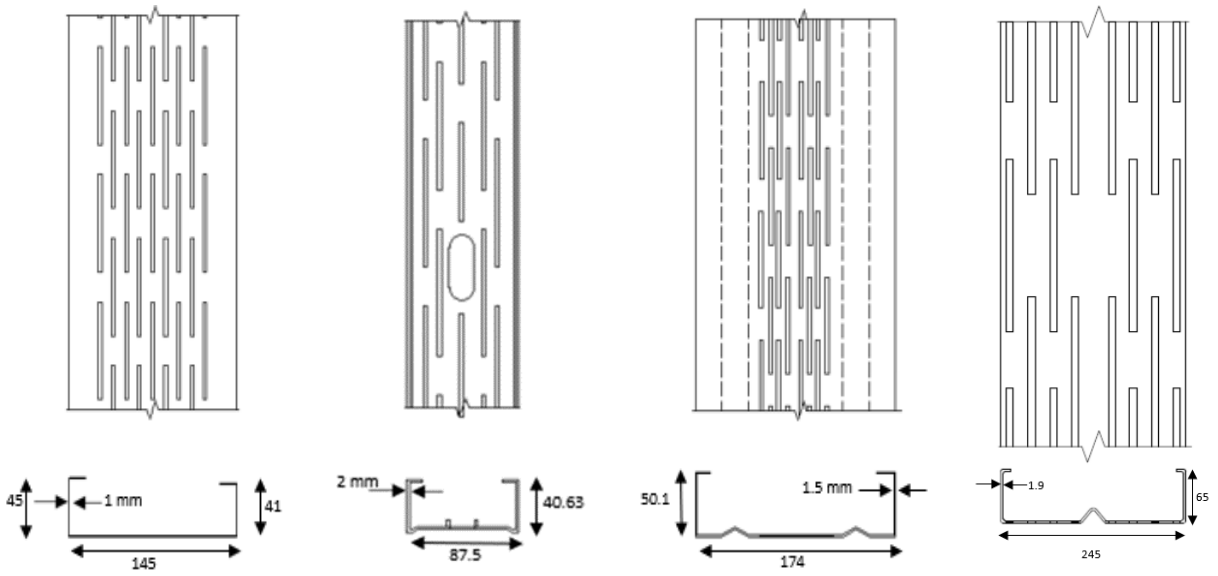

(a) Andreasson et al. [3] (b) LaBoube [4] (c) Kesti et al. [7] (d) Degtyarev et al. [8]

Fig.3- 1 Summary of experimental tests reported in literature on sections with slits

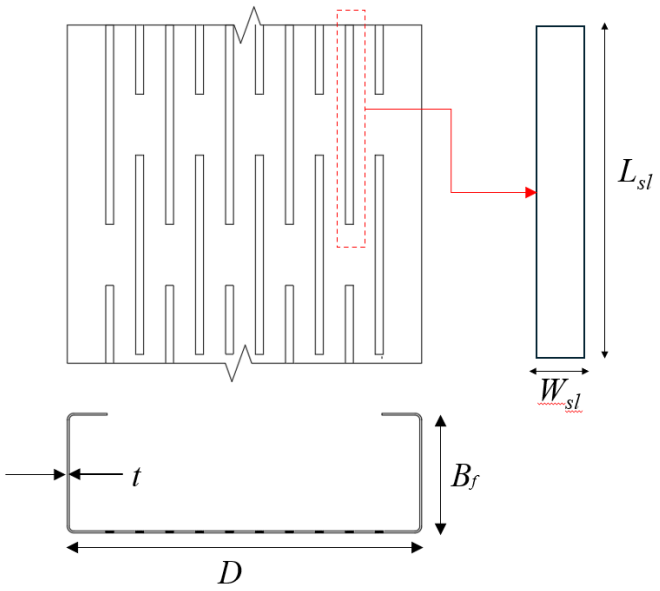

Fig.3- 2 Parameters used to describe cold-formed steel channels with slits

3.2. Summary of test results by Andreassen and Jönsson [3]

As mentioned in the introduction, the only experimental tests reported in the literature considering the compressive strength of unstiffened CFS studs with slits are those by Andreassen and Jönsson [3]. Fig. 3-3 (a) shows a photograph of the experimental tests as well as details of the dimensions of the sections (refer Fig. 3-3 (b) and Fig. 3-3 (c)) used in the tests. The tested studs had heights of 500 mm and 1000 mm, having a thickness of either 0.7 mm or 1.0 mm.

As can be seen from Fig. 3-3 (a), track sections, denoted as U-sections, were securely fastened to a support block at both the top and bottom of the specimen, employing two bolts in each U-section. These prevented any dislodging of the assembly from the experimental setup. The decision to employ a fixed support condition was driven by the typical scenario where an external wall connects the lower and upper floor levels.

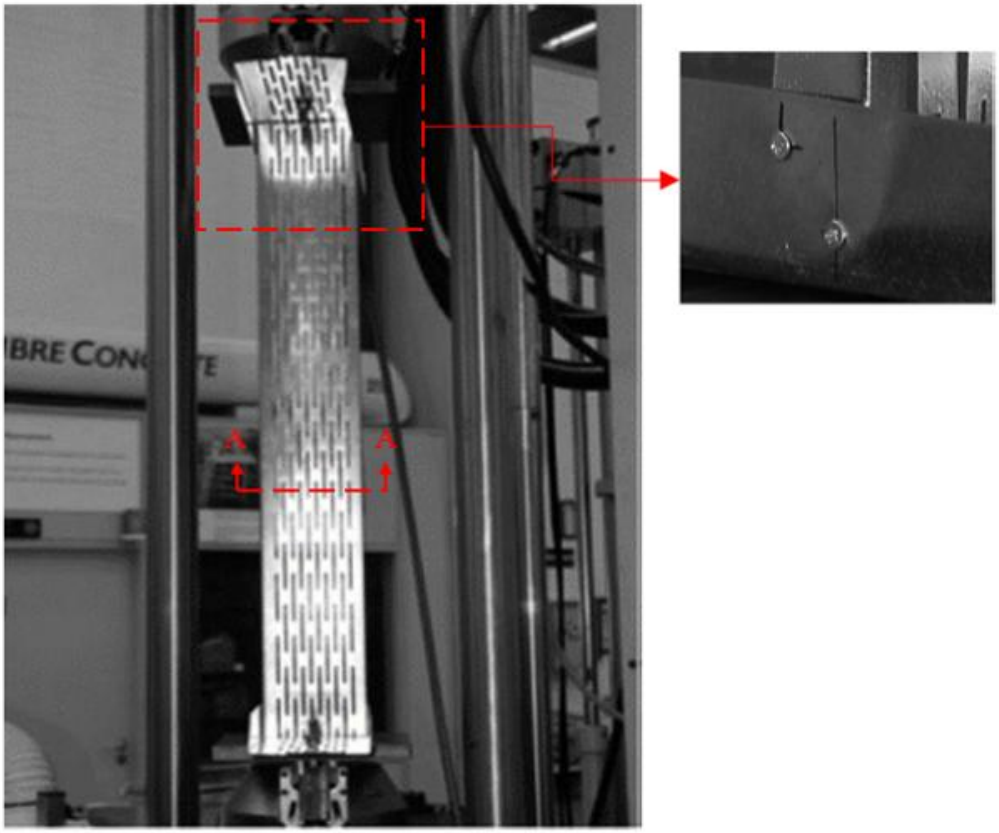

(a) Experimental Set up

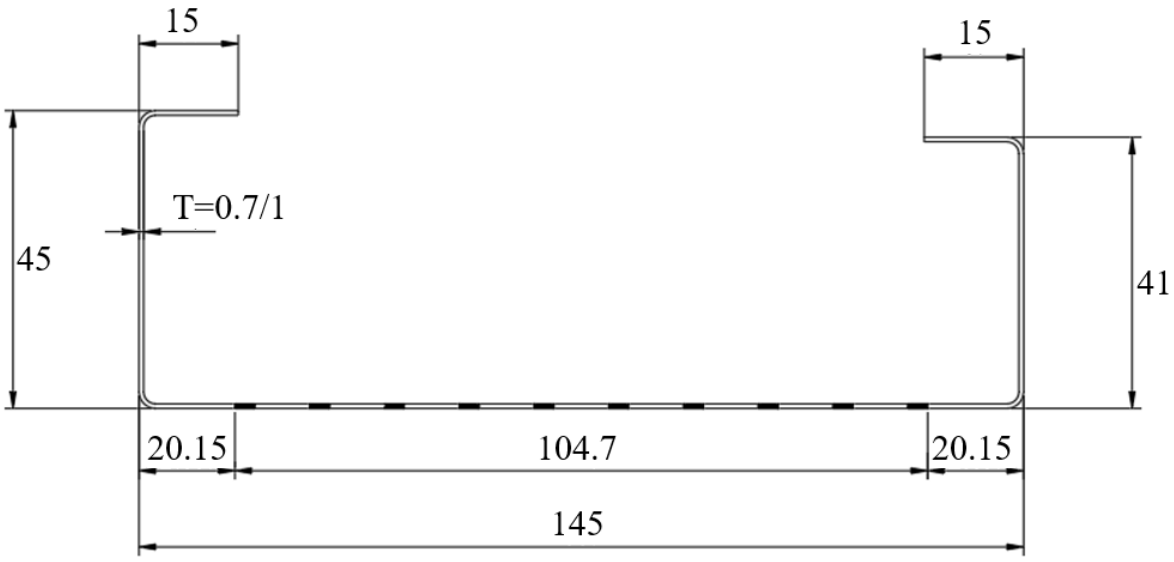

(b) SEC A-A

(c)

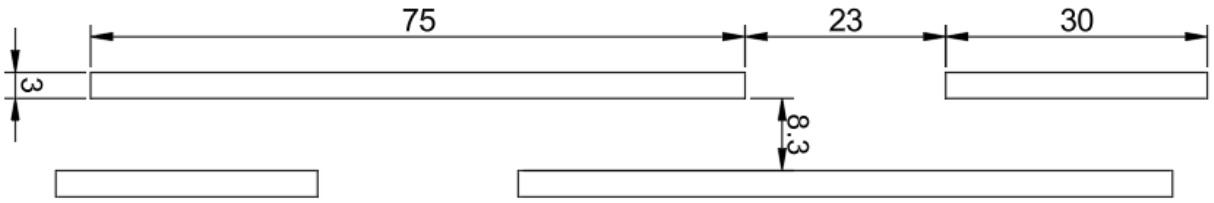

(c) Distance between slits

Fig.3- 3 Experimental test setup and dimensions of test specimens after Andreassen and Jönsson [3]- outer to outer dimensions (in mm) have been used

3.3 Description of the finite element modelling

3.3.1 General

An elastic-plastic model was used for modeling the channel sections with slits and without slits. ABAQUS [98] was used to analyse channel sections with slits and without slits. The FE modeling accounted for the geometric imperfections initially present in the CFS channel sections. The modeling techniques used in this study are elaborated upon in the following sections.

3.3.2 Material properties

The material properties with a yield strength and Young's modulus of 360.8 MPa and 192 GPa, respectively, was used in the validation for the FEA models as per Andreassen and Jönsson [3]. For the parametric study a higher yield strength of 500 MPa was used. By adopting the material models that Gardner and Yun [99] and Rossi et al. [100] had proposed, the CFS sections' stress-strain behaviour was evaluated. The following equations were used to convert the engineering stress-strain curve into a true stress-strain curve:

$$\sigma_{true} = \sigma\,(1+\varepsilon) \quad (1)$$

$$\varepsilon_{true} = ln\,(1+\varepsilon) - \frac{\sigma_{true}}{E} \quad (2)$$

Wherein E represents the modulus of elasticity, σ denotes the engineering stress, ε signifies the engineering strain, σ_{true} indicates the true stress and ε_{true} refers to the true strain.

3.3.3 Meshing

The mesh for the CFS channel sections was created through S4R shell elements, each having six degrees of freedom per node. A mesh size of 1 mm × 1mm (refer to Fig. 3-4) has been selected as the channel sections have multiple slits and finer mesh size was required to truly capture the behaviour of the channel section with multiple slits.

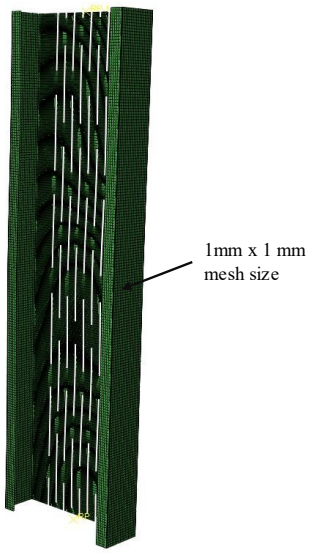

Fig.3- 4 Details of the FE meshing

3.3.4 Boundary and loading conditions

Two reference points (RP-1, RP-2) were placed at the ends of the channel sections on centre of gravity of the column cross-section of both plain sections and sections with slits. Rigid body tie constraints have been used to simulate experimental boundary conditions.

One reference point (RP-1) was restrained against all translational movement, except in the z-direction. The axial compression load was applied using this reference point in the z-direction. The other reference point (RP-2) was restrained against all translational movements. Additionally, both reference points restrained against rotation in major axis (y) and torsion (z), respectively. However, the reference points were permitted to rotate about the minor axis. Fig. 3-5 shows the channel section with slits's boundary conditions.

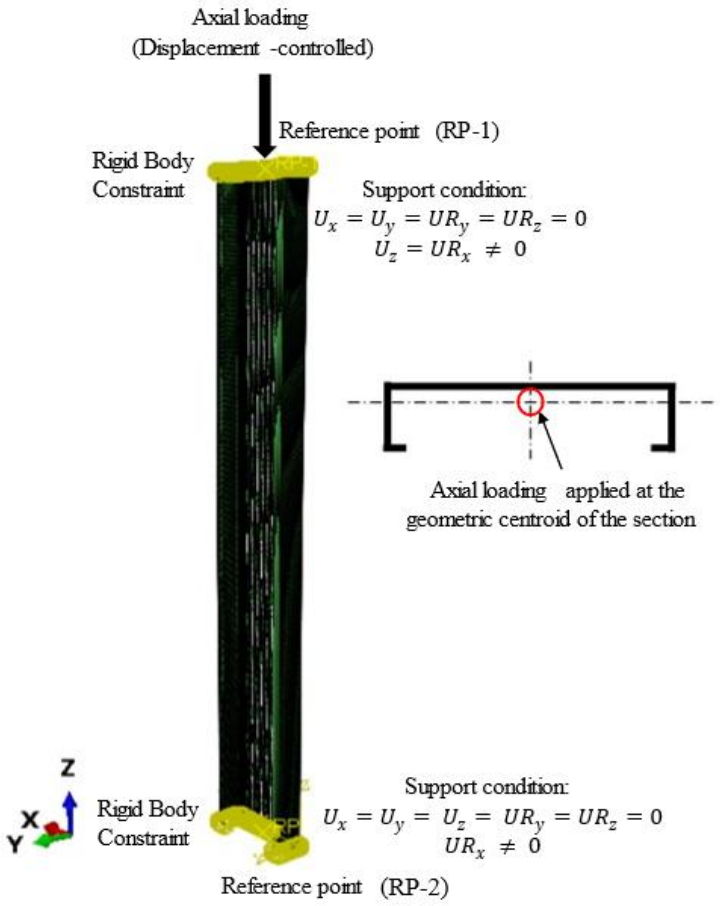

Fig.3- 5 Boundary and loading conditions applied in FE models

3.3.5 Geometrical imperfections

CFS sections often exhibit geometric imperfections due to fabrication and transportation processes, and these imperfections were incorporated into the FE models. To determine the shapes of imperfection, eigenvalue analyses were performed. Lowest eigenmodes corresponding to the local, distortional, and global buckling modes were considered. The combined effects of local, distortional, and global geometric imperfections were accounted for. The magnitudes of these imperfections followed the guidelines specified in AS/NZS-4600 [101].

3.3.6 Sensitivity Analysis

A detailed mesh sensitivity analysis was performed to assess the influence of mesh density on the numerical predictions. The predicted compressive strength of a representative CFS member,

specifically the cross-section from test series 8 with a length of 500 mm and thickness of 0.7 mm adopted from Andreassen and Jönsson [3], was determined using different mesh sizes, and the corresponding results are summarised in Table 1. The results indicate that mesh refinement beyond an element size of 1 × 1 mm² produced only a negligible change in the predicted compressive capacity. Accordingly, an element size of 1 × 1 mm² was selected for modelling the slitted CFS sections in this study.

Table 3- 1 Mesh sensitivity analysis for the CFS member from test series 8 (L = 500 mm, t = 0.7 mm) adopted from Andreassen and Jönsson [3]

Element Size	P_{FEA}
mm^2	kN
0.5 X 0.5	31.27
1 X 1	31.29
2.5 x 2.5	31.88
5 x 5	32.29

3.4 Validation of finite element models

Regarding ultimate loads and failure modes (refer to Fig. 3-6), the FE analysis results demonstrated close agreement with the experimental findings of Andreasson and Jönsson [3]. Table 3-2 presents a comparison between the test results (P_{Test}) of test series 1,3,4,5,7 and numerical results (P_{FEA}) for C145 × 45 × 15 channel sections. Photographs of the experimental failure modes for the entire sections in test series 1 and 3 were unavailable. However, the failure modes for all specimens in test series 3 and for 4 out of 5 specimens in test series 1 were reported as distortional buckling, similar to the failure mode observed in test series 4. The mean value of the P_{Test}/P_{FEA} ratio is 0.92, with a corresponding coefficient of variation (COV) of 0.05.

Fig. 3-6 illustrates the failure mode observed in both experiments and FEA. The observed failure mode primarily entails distortional buckling of the flanges coupled with global buckling,

with a few instances of local buckling. Specifically, the sections showed distortional buckling, accompanied by the closure of the lipped section. It's important to note that Andreasson and Jönsson did not report load-deflection results. It should also be noted that the experimental study reported average peak loads for grouped specimens rather than individual test results. Consequently, validation of the finite element (FE) models is limited to comparisons of average ultimate load and reported failure modes.

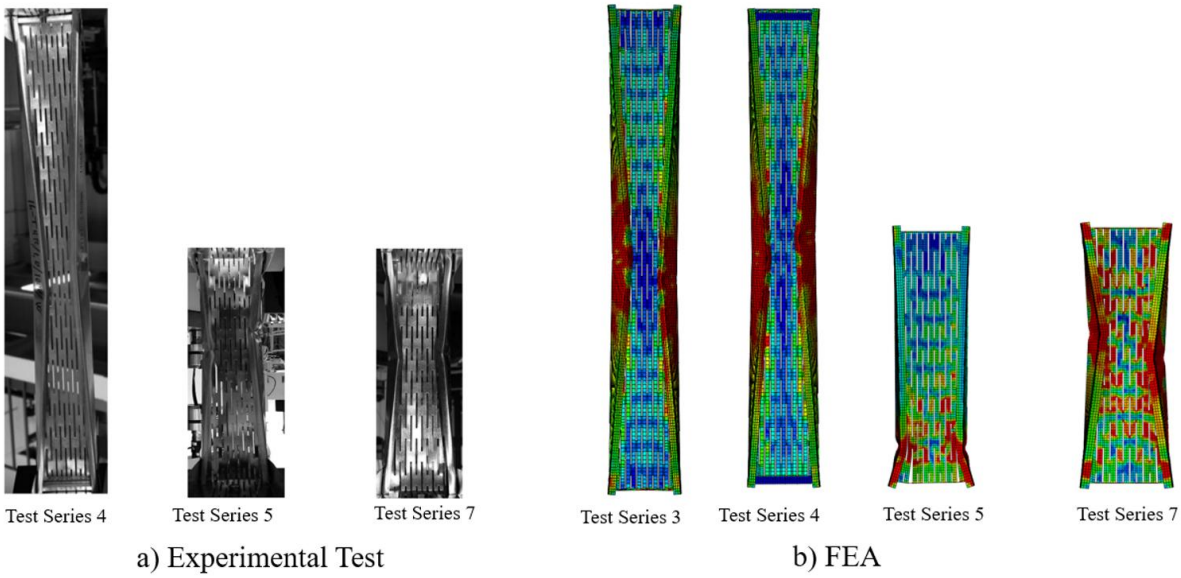

Fig.3- 6 Comparison of failure modes obtained from the test after Andreassen and Jönsson [3]

The standard deviation values for the experimental results [3] range from 0.5 kN to 2.0 kN. When expressed as coefficients of variation (COV), the values range approximately from 2.1% to 12.0%. The lowest COV occurs in test series 4, while the highest value is observed in test series 1. For the remaining test series, the COV values lie between approximately 3.8% and 6.4%. Each test series consisted of five specimens, and therefore the statistical measures reported for each configuration are based on a sample size of five tests. As shown in Table 3-1, the overestimation is more pronounced for thinner (0.7 mm) sections. Given that only average peak forces were available, the variability within each test group could not be explicitly assessed. Furthermore,

the absence of full force–displacement curves limits the ability to evaluate the accuracy of the predicted elastic stiffness and post-buckling response.

Table 3- 2 Comparisons of ultimate load between numerical and experimental investigations C145 × 45 × 15 after Andreassen and Jönsson [3]

Test Series	Length	Thickness	Test	P_{FEA}	P_{Test}/P_{FEA}
			kN	kN	
1	1000	0.7	11.7	13.2	0.88
3	1000	1	23.5	24.10	0.98
4	1000	1	23.4	25.4	0.92
5	500	0.7	14.1	16.2	0.87
7	500	1	29.9	31.29	0.96
				Mean	0.92
				COV	0.05

3.5 Parametric study

3.5.1 General, chosen parameters and labelling of specimens

The validated Finite Element (FE) model, confirmed by experimental results, was used for a thorough parametric analysis. A total of 900 FE models with slits and 60 without were employed to study how different factors affect the axial capacity of CFS sections with slits. Parameters considered in the study included channel dimensions, slit width, slit length, section thickness, yield strength, and stud length. The dimensional parameters varied during the analysis included section depth (D), flange width (B_f), thickness (t), slit length (L_{sl}), slit width (W_{sl}) and length (L), the details of which are given in Table 3-3.

The material properties for the parametric analyses were yield strength of 500 MPa, Young's modulus of 192 GPa, and a Poisson ratio of 0.3.

The results of the parametric study are given in Tables (3-5)-(3-7). The ratio of net area (A_n) to gross area (A_g) is provided in Tables (3-5)-(3-7). The description of the specimen

labelling used in the parametric study is shown in Fig.3-7. Each web depth featured 10 rows of equally spaced slits, spanning the full width of the section. The transverse distance between the slits varied with both the web depth and the slit dimensions. However, the transverse distance from one edge of the web to the nearest slit was consistently 25 mm across all sections. The longitudinal distance between the slits remained constant across all cross sections and was the same as used by Andreasson and Jönsson [3] . The details are provided in Fig.3-8 and Table 3-4.

Table 3- 3 Parametric study details

f_y	D	B_f	B_l	t	L_{sl}	W_{sl}	L	No of models
(MPa)	(mm)	(mm)	(mm)	(mm)	(mm)	(mm)	(mm)	
500	145	45	15	0.6,1,1.2, 1.6, 2	60, 75,90	3, 4,5,6,7	500,1000, 1500,2000	300
	200	45	15	0.6,1,1.2, 1.6, 2	60, 75,90	3, 4,5,6,7	500,1000, 1500,2000	300
	250	65	15	0.6,1,1.2, 1.6, 2	60, 75,90	3, 4,5,6,7	500,1000, 1500,2000	300
	145/200/250	45/65	15	0.6,1,1.2, 1.6, 2	0	0	500,1000, 1500,2000	60
							Total	960

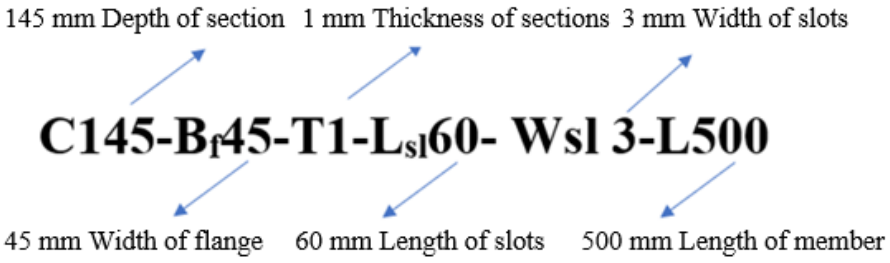

Fig.3- 7 Specimen labelling

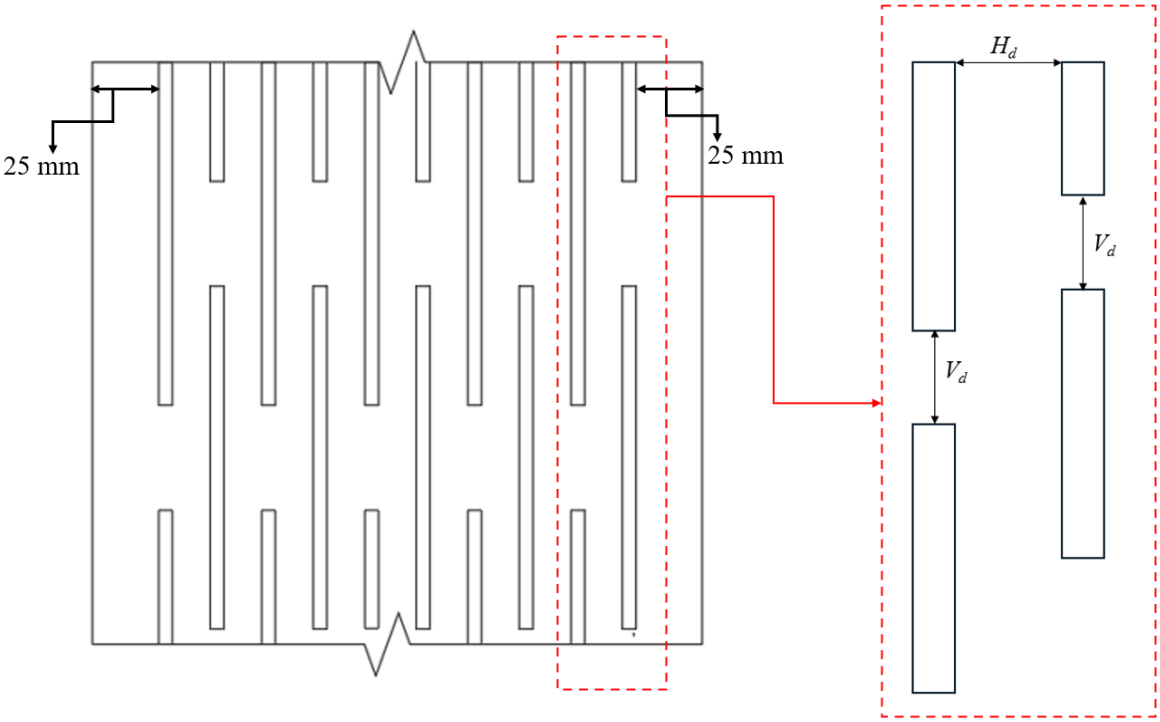

Fig.3- 8 Details of distance between slits used for parametric analysis

Table 3- 4 Details of distance between slits used for parametric analysis

Specimen	H_d *(in mm)*	V_d *(in mm)*
C145-B_f45-W_{sl}3	7.22	23
C145-B_f45-W_{sl}4	6.11	23
C145-B_f45-W_{sl}5	5.00	23
C145-B_f45-W_{sl}6	3.89	23
C145-B_f45-W_{sl}7	2.78	23
C200-B_f45-W_{sl}3	13.33	23
C200-B_f45-W_{sl}4	12.22	23
C200-B_f45-W_{sl}5	11.11	23
C200-B_f45-W_{sl}6	10.00	23
C200-B_f45-W_{sl}7	8.89	23
C250-B_f45-W_{sl}3	18.88	23
C250-B_f45-W_{sl}4	17.77	23
C250-B_f45-W_{sl}5	16.66	23
C250-B_f45-W_{sl}6	15.55	23
C250-B_f45-W_{sl}7	14.44	23

Table 3- 5 Results of the Parametric Study for C145 Channel Sections with Plain Webs and Slits

Axial capacity results of channel sections from FEA, P_{FEA}/ P_{DSM} (kN)																
Specimen	Plain web (kN)	L_{sl}60					L_{sl}75					Lsl90				
		W_{sl} 3	W_{sl} 4	W_{sl} 5	W_{sl} 6	W_{sl} 7	W_{sl} 3	W_{sl} 4	W_{sl} 5	W_{sl} 6	W_{sl} 7	W_{sl} 3	W_{sl} 4	W_{sl} 5	W_{sl} 6	W_{sl} 7
		A_n/A_g- 0.89	A_n/A_g- 0.85	A_n/A_g- 0.81	A_n/A_g- 0.77	A_n/A_g- 0.73	A_n/A_g- 0.89	A_n/A_g- 0.85	A_n/A_g- 0.81	A_n/A_g- 0.77	A_n/A_g- 0.73	A_n/A_g- 0.89	A_n/A_g- 0.85	A_n/A_g- 0.81	A_n/A_g- 0.77	A_n/A_g- 0.73
L500- P_{FEA} (kN)																
C145-Bf45-T0.6	18.47	18.28	18.14	17.99	17.63	17.34	17.61	17.13	17.01	16.77	16.93	17.44	17.37	17.31	17.18	16.99
C145-Bf45-T1.0	48.98	42.71	41.84	41.50	40.63	39.97	41.80	40.97	40.16	38.80	37.92	40.83	41.05	39.22	37.85	37.08
C145-Bf45-T1.2	66.02	57.49	56.28	55.06	54.14	53.77	54.95	53.14	52.99	51.48	52.07	54.43	52.81	52.23	50.77	49.77
C145-Bf45-T1.6	103.89	87.18	85.63	86.33	82.88	82.31	84.44	81.69	82.65	80.09	80.14	83.91	81.55	82.15	80.18	78.93
C145-Bf45-T2.0	146.86	118.10	116.83	114.73	112.90	112.13	115.73	113.39	111.53	107.86	108.97	114.71	112.36	112.00	109.08	107.59
L500-P_{DSM} (kN)																
C145-Bf45-T0.6	18.66	22.02	21.95	21.94	21.83	21.77	19.84	19.58	19.44	19.09	18.91	18.25	18.03	18.01	17.65	17.35
C145-Bf45-T1.0	45.44	45.48	45.02	44.63	44.12	43.59	40.98	40.37	39.81	39.13	38.46	37.84	37.11	36.49	35.57	34.73
C145-Bf45-T1.2	62.39	59.33	58.67	58.04	57.31	56.49	53.58	52.76	51.95	51.05	50.10	49.40	48.42	47.52	46.33	45.19
C145-Bf45-T1.6	102.48	91.44	90.31	89.12	87.85	86.32	82.91	81.59	80.22	78.78	77.19	76.35	74.79	73.27	71.46	69.64
C145-Bf45-T2.0	149.72	126.81	124.99	123.00	120.91	118.25	115.40	113.38	111.24	109.02	106.43	106.33	104.03	101.70	99.04	96.25
L1000- P_{FEA} (kN)																
C145-Bf45-T0.6	16.10	14.58	14.40	14.35	14.34	14.24	14.34	14.42	14.25	14.32	13.83	14.11	14.27	14.16	14.23	13.60
C145-Bf45-T1.0	39.29	32.40	33.22	32.49	31.69	30.85	32.14	31.38	30.77	29.62	29.35	31.78	30.95	30.27	29.77	29.06
C145-Bf45-T1.2	53.11	43.56	42.77	42.06	41.08	40.29	41.72	40.90	40.32	39.92	40.25	41.15	40.30	40.32	40.02	39.85
C145-Bf45-T1.6	85.44	64.40	63.17	62.16	60.83	59.66	62.22	61.72	61.27	60.17	58.54	62.12	61.34	60.43	59.25	57.41
C145-Bf45-T2.0	124.14	86.79	84.48	82.61	80.44	78.71	84.08	82.51	81.01	78.88	76.91	82.54	80.97	79.68	77.96	75.56
L1000- P_{DSM} (kN)																
C145-Bf45-T0.6	15.57	17.27	17.06	16.78	16.42	16.01	16.12	15.94	15.69	15.51	15.24	15.08	14.87	14.59	14.36	14.02
C145-Bf45-T1.0	37.73	38.43	37.89	37.23	36.51	35.62	35.26	34.76	34.14	33.66	33.01	32.73	32.17	31.51	30.93	30.11
C145-Bf45-T1.2	51.79	51.64	50.90	50.02	49.08	47.91	47.18	46.48	45.63	44.97	44.08	43.70	42.93	42.02	41.22	40.12
C145-Bf45-T1.6	85.08	82.68	81.49	80.08	78.67	76.82	75.28	74.12	72.72	71.60	70.12	69.61	68.35	66.88	65.56	63.80
C145-Bf45-T2.0	124.43	107.19	104.99	102.51	99.99	96.79	97.62	95.50	93.05	90.87	88.13	90.32	88.13	85.64	83.32	80.42
L1500- P_{FEA} (kN)																
C145-Bf45-T0.6	12.47	10.87	10.77	10.63	10.50	10.30	10.55	10.36	10.25	10.21	9.99	10.42	10.33	10.20	10.10	9.91
C145-Bf45-T1.0	28.78	27.80	27.80	27.80	27.80	27.80	27.80	27.80	27.80	27.80	27.80	27.80	27.80	27.80	27.80	27.80
C145-Bf45-T1.2	38.52	27.62	27.23	26.76	26.36	25.56	26.69	26.57	26.11	25.43	24.47	28.42	26.08	25.32	24.81	23.87

Axial capacity results of channel sections from FEA, P_{FEA}/ P_{DSM} (kN)																
Specimen	Plain web (kN)	L_{sl}60					L_{sl}75					Lsl90				
		W_{sl} 3	W_{sl} 4	W_{sl} 5	W_{sl} 6	W_{sl} 7	W_{sl} 3	W_{sl} 4	W_{sl} 5	W_{sl} 6	W_{sl} 7	W_{sl} 3	W_{sl} 4	W_{sl} 5	W_{sl} 6	W_{sl} 7
		A_n/A_g- 0.89	A_n/A_g- 0.85	A_n/A_g- 0.81	A_n/A_g- 0.77	A_n/A_g- 0.73	A_n/A_g- 0.89	A_n/A_g- 0.85	A_n/A_g- 0.81	A_n/A_g- 0.77	A_n/A_g- 0.73	A_n/A_g- 0.89	A_n/A_g- 0.85	A_n/A_g- 0.81	A_n/A_g- 0.77	A_n/A_g- 0.73
C145-Bf45-T1.6	61.26	41.93	39.91	38.80	37.79	36.54	38.73	37.97	36.89	36.12	34.82	38.35	37.59	36.81	35.45	34.22
C145-Bf45-T2.0	92.66	57.09	54.99	53.01	50.67	48.79	52.55	51.23	49.28	48.34	46.37	50.73	49.76	48.53	47.32	45.32
L1500- P_{DSM} (kN)																
C145-Bf45-T0.6	11.51	14.29	14.06	13.83	13.58	13.30	12.92	12.70	12.46	12.27	12.03	11.78	11.54	11.28	11.03	10.73
C145-Bf45-T1.0	27.80	34.58	34.05	33.51	32.93	32.29	31.23	30.69	30.12	29.63	28.95	28.46	27.88	27.25	26.66	25.95
C145-Bf45-T1.2	38.24	47.32	46.60	45.87	45.09	44.20	42.75	42.01	41.24	40.55	39.73	38.98	38.18	37.33	36.51	35.55
C145-Bf45-T1.6	63.24	77.30	76.14	74.96	73.68	72.18	69.96	68.73	67.49	66.30	64.89	63.87	62.56	61.18	59.83	58.25
C145-Bf45-T2.0	93.40	83.77	81.39	78.93	76.34	73.41	76.11	73.75	71.35	68.94	66.23	69.72	67.37	64.94	62.49	59.81
L2000- P_{FEA} (kN)																
C145-Bf45-T0.6	9.21	7.48	7.21	7.08	6.92	6.75	7.08	6.95	6.84	6.85	6.49	6.82	6.74	6.61	6.54	6.39
C145-Bf45-T1.0	20.05	15.03	14.33	13.93	13.51	13.06	13.86	13.54	13.25	12.87	12.39	13.34	13.34	12.82	12.51	12.08
C145-Bf45-T1.2	26.49	19.70	18.69	17.86	17.25	16.53	17.86	17.14	16.72	16.19	15.58	17.00	16.62	16.21	15.78	15.31
C145-Bf45-T1.6	45.70	29.61	28.48	27.21	25.77	24.36	27.23	26.05	24.75	23.80	22.74	25.47	24.53	23.72	22.93	22.02
C145-Bf45-T2.0	64.29	40.69	39.13	37.13	35.24	33.00	37.22	35.88	34.17	32.52	30.59	35.25	33.92	32.56	31.15	29.57
L2000-P_{DSM} (kN)																
C145-Bf45-T0.6	8.09	13.71	13.50	13.30	13.08	12.83	12.50	12.29	12.10	11.90	11.71	11.47	11.23	11.00	10.75	10.49
C145-Bf45-T1.0	19.53	33.05	32.55	32.06	31.55	30.95	29.96	29.44	28.97	28.48	28.00	27.35	26.78	26.22	25.61	25.00
C145-Bf45-T1.2	26.91	45.19	44.52	43.84	43.15	42.32	40.95	40.23	39.59	38.90	38.23	37.37	36.59	35.83	34.99	34.15
C145-Bf45-T1.6	44.87	73.75	72.67	71.57	70.43	69.01	66.88	65.71	64.65	63.47	62.29	61.09	59.82	58.59	57.21	55.82
C145-Bf45-T2.0	67.12	58.96	56.86	54.76	52.67	50.38	53.78	51.71	49.76	47.75	45.72	49.38	47.34	45.38	43.34	41.33

Table 3- 6 Results of the Parametric Study for C200 Channel Sections with Plain Webs and Slits

Specimen	Plain web (kN)	Lsl60					Lsl75					Lsl90				
		W_{sl} 3	W_{sl} 4	W_{sl} 5	W_{sl} 6	W_{sl} 7	W_{sl} 3	W_{sl} 4	W_{sl} 5	W_{sl} 6	W_{sl} 7	W_{sl} 3	W_{sl} 4	W_{sl} 5	W_{sl} 6	W_{sl} 7
		A_n/A_g- 0.91	A_n/A_g- 0.87	A_n/A_g- 0.84	A_n/A_g- 0.81	A_n/A_g- 0.78	A_n/A_g- 0.91	A_n/A_g- 0.87	A_n/A_g- 0.84	A_n/A_g- 0.81	A_n/A_g- 0.78	A_n/A_g- 0.91	A_n/A_g- 0.87	A_n/A_g- 0.84	A_n/A_g- 0.81	A_n/A_g- 0.78
Axial capacity results of channel sections from FEA, P_{FEA}/ P_{DSM} (kN)																
L500- P_{FEA} (kN)																
C200-Bf45-T0.6	17.50	16.33	16.45	16.29	16.15	16.12	16.10	16.16	16.24	16.19	16.11	15.93	16.07	15.95	15.69	15.59
C200-Bf45-T1.0	46.25	41.43	41.06	40.24	39.87	39.53	39.86	39.50	39.02	38.91	38.45	39.16	38.97	38.15	38.04	37.34
C200-Bf45-T1.2	62.70	54.31	53.88	52.98	52.78	52.05	53.05	52.70	52.11	51.58	50.50	51.73	51.35	50.45	50.15	49.35
C200-Bf45-T1.6	100.81	82.85	82.60	81.29	80.45	79.38	80.64	80.38	79.39	78.72	76.55	77.37	77.77	76.60	75.74	74.89
C200-Bf45-T2.0	142.82	114.19	113.17	110.88	109.51	106.96	109.79	109.74	107.86	106.19	104.64	106.76	106.35	104.36	103.92	101.63
L500- P_{DSM} (kN)																
C200-Bf45-T0.6	17.92	20.08	19.87	19.66	19.45	19.23	19.13	18.93	18.71	18.50	18.27	18.03	17.82	17.57	17.34	17.07
C200-Bf45-T1.0	44.12	43.57	43.01	42.49	41.93	41.38	41.60	41.03	40.47	39.90	39.33	39.46	38.86	38.27	37.66	37.04
C200-Bf45-T1.2	60.71	58.06	57.28	56.57	55.79	55.06	55.35	54.57	53.80	53.02	52.24	52.54	51.72	50.93	50.08	49.26
C200-Bf45-T1.6	100.06	92.12	90.84	89.70	88.43	87.26	87.64	86.36	85.13	83.86	82.61	83.26	81.93	80.68	79.31	78.02
C200-Bf45-T2.0	146.65	132.26	130.40	128.80	126.95	125.29	125.72	123.87	122.12	120.29	118.50	119.50	117.59	115.84	113.88	112.08
L1000- P_{FEA} (kN)																
C200-Bf45-T0.6	15.23	13.91	13.87	13.85	13.69	13.67	13.82	13.37	14.52	13.33	13.29	13.34	13.85	13.32	13.12	13.09
C200-Bf45-T1.0	36.79	31.59	31.20	30.98	30.47	30.08	31.11	30.64	30.48	29.85	30.24	30.76	30.24	30.50	30.41	30.08
C200-Bf45-T1.2	49.67	41.63	40.87	40.35	39.82	40.45	40.08	39.58	40.01	39.93	39.36	40.20	40.00	39.44	39.19	38.53
C200-Bf45-T1.6	79.09	63.41	62.56	61.59	60.84	60.08	60.68	60.14	59.39	58.92	58.12	59.43	58.88	58.29	57.84	57.22
C200-Bf45-T2.0	114.36	85.58	84.43	83.03	81.72	80.08	82.37	81.48	80.13	79.21	78.04	80.09	79.33	78.40	77.68	76.48
L1000- P_{DSM} (kN)																
C200-Bf45-T0.6	15.27	18.41	18.22	18.03	17.84	17.64	17.67	17.45	93.42	17.04	16.85	16.84	16.61	16.43	16.21	16.02
C200-Bf45-T1.0	37.54	40.53	40.04	39.59	39.08	38.60	38.52	37.95	37.49	36.95	36.46	36.69	36.14	35.64	35.09	34.58
C200-Bf45-T1.2	51.65	54.31	53.63	52.99	52.31	51.67	51.45	50.71	50.04	49.31	48.63	48.92	48.17	47.49	46.73	46.04
C200-Bf45-T1.6	85.10	86.77	85.65	84.62	83.52	82.47	81.94	80.74	79.65	78.46	77.36	77.75	76.53	75.42	74.21	73.07
C200-Bf45-T2.0	124.75	125.05	123.45	121.96	120.37	118.86	117.97	116.25	114.67	112.96	111.36	111.88	110.12	108.52	106.77	105.13
L1500- P_{FEA} (kN)																
C200-Bf45-T0.6	11.81	10.59	10.57	10.50	10.42	10.37	10.46	11.32	10.23	10.40	10.05	10.28	10.32	10.13	10.47	11.79
C200-Bf45-T1.0	26.99	22.66	22.54	22.25	21.82	21.40	21.93	21.71	21.41	20.98	20.76	21.12	20.80	20.74	20.57	20.41
C200-Bf45-T1.2	35.63	29.21	28.66	28.22	27.85	27.38	28.22	27.23	26.94	26.74	26.51	26.74	26.64	26.36	26.25	25.89

Axial capacity results of channel sections from FEA, P_{FEA}/ P_{DSM} (kN)

Specimen	Plain web (kN)	Lsl60					Lsl75					Lsl90				
		W_{sl} 3	W_{sl} 4	W_{sl} 5	W_{sl} 6	W_{sl} 7	W_{sl} 3	W_{sl} 4	W_{sl} 5	W_{sl} 6	W_{sl} 7	W_{sl} 3	W_{sl} 4	W_{sl} 5	W_{sl} 6	W_{sl} 7
		A_n/A_g- 0.91	A_n/A_g- 0.87	A_n/A_g- 0.84	A_n/A_g- 0.81	A_n/A_g- 0.78	A_n/A_g- 0.91	A_n/A_g- 0.87	A_n/A_g- 0.84	A_n/A_g- 0.81	A_n/A_g- 0.78	A_n/A_g- 0.91	A_n/A_g- 0.87	A_n/A_g- 0.84	A_n/A_g- 0.81	A_n/A_g- 0.78
C200-Bf45-T1.6	55.84	43.68	43.17	42.71	40.27	39.63	40.27	39.79	39.32	38.83	38.21	39.01	38.63	38.17	37.71	37.22
C200-Bf45-T2.0	79.54	61.03	60.50	56.54	54.18	52.85	54.06	53.21	52.39	51.56	50.67	52.21	51.97	50.77	50.10	49.27
L1500- P_{DSM} (kN)																
C200-Bf45-T0.6	11.69	16.45	16.26	16.07	15.88	15.68	15.66	15.47	15.27	15.09	14.88	14.97	14.79	14.58	14.39	14.17
C200-Bf45-T1.0	28.75	37.91	37.46	36.98	36.53	36.05	35.75	35.28	34.78	34.32	33.82	33.91	33.43	32.92	32.43	31.92
C200-Bf45-T1.2	39.58	51.36	50.74	50.09	49.48	48.83	48.34	47.70	47.02	46.37	45.69	45.77	45.10	44.42	43.74	43.04
C200-Bf45-T1.6	65.41	83.06	82.06	81.01	80.02	78.98	78.04	77.00	75.90	74.86	73.75	73.78	72.70	71.59	70.50	69.37
C200-Bf45-T2.0	96.35	120.43	118.99	117.49	116.06	114.56	113.12	111.63	110.05	108.55	106.95	106.92	105.36	103.75	102.20	100.56
L2000- P_{FEA} (kN)																
C200-Bf45-T0.6	8.87	7.83	7.83	7.72	7.68	7.61	7.60	7.51	8.26	7.43	7.29	7.44	7.38	6.65	7.01	6.90
C200-Bf45-T1.0	19.27	15.95	15.77	15.63	15.59	15.43	15.86	15.44	15.38	14.51	13.64	15.66	14.13	14.03	13.42	13.33
C200-Bf45-T1.2	25.27	20.49	20.23	19.91	19.57	19.54	20.98	19.74	18.96	17.74	17.33	19.40	17.53	17.19	16.96	16.79
C200-Bf45-T1.6	39.18	29.90	29.39	30.96	29.57	28.70	29.93	28.46	27.57	26.11	25.01	27.24	26.21	24.96	24.36	24.04
C200-Bf45-T2.0	56.63	42.19	41.65	41.15	39.49	38.41	38.95	38.28	37.02	35.56	33.67	36.75	35.54	33.94	32.86	32.12
L2000- P_{DSM} (kN)																
C200-Bf45-T0.6	8.34	15.08	14.89	14.70	14.51	14.32	14.24	14.05	13.86	13.67	13.48	13.54	13.34	13.15	12.94	12.75
C200-Bf45-T1.0	20.51	35.84	35.37	34.93	34.48	34.04	33.64	33.18	32.71	32.25	31.79	31.77	31.27	30.81	30.32	29.85
C200-Bf45-T1.2	28.27	48.90	48.27	47.67	47.05	46.46	45.85	45.22	44.58	43.96	43.33	43.24	42.57	41.94	41.27	40.63
C200-Bf45-T1.6	46.96	79.69	78.68	77.72	76.71	75.77	74.69	73.67	72.64	71.62	70.60	70.40	69.32	68.29	67.20	66.17
C200-Bf45-T2.0	69.75	115.96	114.54	113.16	111.72	110.36	108.78	107.31	105.82	104.35	102.88	102.58	101.02	99.54	97.97	96.48

Table 3- 7 Results of the Parametric Study for C250 Channel Sections with Plain Webs and Slits

Specimen	Plain web (kN)	Lsl60					Lsl75					Lsl90				
		W_{sl} 3	W_{sl} 4	W_{sl} 5	W_{sl} 6	W_{sl} 7	W_{sl} 3	W_{sl} 4	W_{sl} 5	W_{sl} 6	W_{sl} 7	W_{sl} 3	W_{sl} 4	W_{sl} 5	W_{sl} 6	W_{sl} 7
		A_n/A_g- 0.93	A_n/A_g- 0.90	A_n/A_g- 0.88	A_n/A_g- 0.85	A_n/A_g- 0.83	A_n/A_g- 0.93	A_n/A_g- 0.90	A_n/A_g- 0.88	A_n/A_g- 0.85	A_n/A_g- 0.83	A_n/A_g- 0.93	A_n/A_g- 0.90	A_n/A_g- 0.88	A_n/A_g- 0.85	A_n/A_g- 0.83
Axial capacity results of channel sections from FEA, P_{FEA}/ P_{DSM} (kN)																
L500- P_{FEA} (kN)																
C250-Bf65-T0.6	19.92	19.82	18.86	18.80	18.70	18.18	18.48	18.55	18.47	18.20	17.85	18.32	18.59	18.52	18.45	17.73
C250-Bf65-T1.0	50.13	44.28	43.94	43.56	43.22	41.88	43.34	42.90	42.56	42.42	43.63	42.00	41.62	41.44	41.25	42.40
C250-Bf65-T1.2	71.55	61.85	61.31	60.48	60.44	60.74	60.84	60.42	59.70	59.30	60.27	58.94	58.54	57.77	57.72	58.76
C250-Bf65-T1.6	120.82	99.50	98.68	97.74	97.29	99.02	96.73	96.59	95.74	95.08	97.36	94.20	94.06	93.24	92.94	94.46
C250-Bf65-T2.0	176.47	141.22	140.23	138.44	137.42	139.68	135.34	134.39	132.50	131.40	135.93	132.35	131.78	130.04	128.80	132.21
L500- P_{DSM} (kN)																
C250-Bf65-T0.6	19.72	20.84	20.60	20.37	20.13	20.05	20.16	19.92	19.68	19.44	19.38	19.46	19.22	18.98	18.74	18.70
C250-Bf65-T1.0	48.71	47.74	47.16	46.63	46.05	45.80	45.98	45.40	44.85	44.28	44.06	44.33	43.76	43.20	42.64	42.44
C250-Bf65-T1.2	67.15	64.43	63.68	62.95	62.20	61.89	62.04	61.29	60.54	59.79	59.51	59.94	59.20	58.45	57.70	57.41
C250-Bf65-T1.6	111.13	103.53	102.33	101.14	99.94	99.43	99.59	98.37	97.16	95.94	95.43	96.13	94.93	93.69	92.49	91.94
C250-Bf65-T2.0	163.63	150.18	148.43	146.72	144.97	144.20	144.44	142.67	140.90	139.13	138.34	139.40	137.64	135.85	134.09	133.22
L1000- P_{FEA} (kN)																
C250-Bf65-T0.6	16.87	16.01	15.45	15.28	15.18	14.96	15.06	14.99	14.93	14.87	14.29	14.96	14.84	14.85	14.80	14.30
C250-Bf65-T1.0	45.67	40.30	39.89	39.56	39.13	39.10	38.95	38.92	38.41	38.79	39.37	38.34	38.09	37.93	38.55	38.49
C250-Bf65-T1.2	64.83	55.55	55.08	54.67	54.22	54.81	54.75	54.01	53.64	53.20	53.99	53.21	52.80	52.54	52.41	52.87
C250-Bf65-T1.6	107.11	87.42	86.49	85.77	84.98	86.50	84.30	83.61	83.13	82.43	84.60	81.92	81.38	80.34	80.56	82.48
C250-Bf65-T2.0	154.18	121.63	119.98	118.68	117.24	119.47	115.92	114.73	113.59	113.01	115.72	112.30	111.47	110.61	109.91	112.83
L1000- P_{DSM} (kN)																
C250-Bf65-T0.6	18.03	19.92	19.71	19.50	19.30	19.27	19.13	18.92	18.71	18.49	18.48	18.42	18.21	18.00	17.78	17.79
C250-Bf65-T1.0	44.52	44.92	44.44	43.94	43.45	43.32	42.99	42.48	41.98	41.46	41.36	41.30	40.78	40.28	39.77	39.67
C250-Bf65-T1.2	61.35	60.65	59.99	59.32	58.66	58.46	57.99	57.29	56.62	55.92	55.76	55.67	54.97	54.29	53.59	53.42
C250-Bf65-T1.6	101.48	97.96	96.89	95.80	94.73	94.37	93.57	92.45	91.36	90.23	89.92	89.76	88.64	87.53	86.41	86.09
C250-Bf65-T2.0	149.37	142.27	140.75	139.18	137.64	137.09	135.85	134.25	132.67	131.06	130.55	130.32	128.71	127.11	125.50	124.98
L1500- P_{FEA} (kN)																
C250-Bf65-T0.6	15.63	13.74	13.72	13.71	13.56	13.04	13.46	13.48	13.50	13.41	12.81	13.15	13.78	13.22	13.29	12.81
C250-Bf65-T1.0	39.76	34.84	34.62	34.32	33.65	33.06	33.70	33.33	32.96	32.88	33.28	33.30	32.99	32.46	32.48	32.56
C250-Bf65-T1.2	54.93	46.18	45.86	45.48	42.11	46.29	44.49	44.32	43.91	43.76	44.38	43.92	43.91	43.28	43.45	43.41

Axial capacity results of channel sections from FEA, P_{FEA}/ P_{DSM} (kN)

Specimen	Plain web (kN)	Lsl60					Lsl75					Lsl90				
		W_{sl} 3	W_{sl} 4	W_{sl} 5	W_{sl} 6	W_{sl} 7	W_{sl} 3	W_{sl} 4	W_{sl} 5	W_{sl} 6	W_{sl} 7	W_{sl} 3	W_{sl} 4	W_{sl} 5	W_{sl} 6	W_{sl} 7
		A_n/A_g- 0.93	A_n/A_g- 0.90	A_n/A_g- 0.88	A_n/A_g- 0.85	A_n/A_g- 0.83	A_n/A_g- 0.93	A_n/A_g- 0.90	A_n/A_g- 0.88	A_n/A_g- 0.85	A_n/A_g- 0.83	A_n/A_g- 0.93	A_n/A_g- 0.90	A_n/A_g- 0.88	A_n/A_g- 0.85	A_n/A_g- 0.83
C250-Bf65-T1.6	88.12	71.74	71.22	70.28	69.11	70.98	67.84	67.43	66.89	66.36	68.00	66.48	66.16	65.66	64.68	67.19
C250-Bf65-T2.0	127.11	100.44	95.32	97.64	96.19	97.54	94.97	93.80	92.88	91.57	94.21	90.43	89.62	88.64	88.27	90.72
L1500- P_{DSM} (kN)																
C250-Bf65-T0.6	15.54	18.14	17.98	17.71	17.50	17.39	17.36	17.14	94.18	16.71	16.61	16.67	16.46	16.24	16.03	15.91
C250-Bf65-T1.0	38.33	42.59	42.11	41.60	41.13	40.91	40.67	40.16	39.67	39.16	38.96	38.90	38.41	37.90	37.41	37.19
C250-Bf65-T1.2	52.81	58.00	57.35	56.67	56.02	55.76	55.36	54.69	54.01	53.34	53.08	52.92	52.25	51.56	50.89	50.62
C250-Bf65-T1.6	87.33	94.55	93.50	92.43	91.39	91.01	90.20	89.11	88.02	86.95	86.57	86.24	85.15	84.05	82.97	82.54
C250-Bf65-T2.0	128.56	137.98	136.48	134.94	133.46	132.94	131.65	130.09	128.52	126.97	126.43	125.95	124.38	122.79	121.23	120.60
L2000- P_{FEA} (kN)																
C250-Bf65-T0.6	13.29	11.98	11.86	11.85	11.76	11.57	11.72	12.10	11.61	11.56	11.47	11.58	11.38	11.40	11.32	11.33
C250-Bf65-T1.0	33.91	28.58	28.34	28.27	28.21	28.12	28.47	28.07	27.78	27.51	27.54	27.29	27.12	27.00	26.80	27.03
C250-Bf65-T1.2	45.97	38.43	37.14	36.51	36.39	36.89	37.56	36.26	36.12	35.20	33.29	35.29	35.03	34.88	34.65	35.27
C250-Bf65-T1.6	72.43	56.15	55.55	54.97	54.15	55.72	53.77	53.16	52.78	52.17	53.34	52.44	52.09	51.62	51.32	52.66
C250-Bf65-T2.0	104.83	78.24	77.03	75.71	74.37	75.98	74.70	73.41	72.47	71.42	73.04	71.77	71.25	70.18	69.23	71.37
L2000- P_{DSM} (kN)																
C250-Bf65-T0.6	12.61	19.26	19.06	18.87	18.67	18.68	18.52	18.32	18.12	17.91	17.94	17.85	17.64	17.45	17.23	17.27
C250-Bf65-T1.0	31.10	43.33	42.86	42.42	41.94	41.90	41.36	40.88	40.42	39.94	39.91	39.68	39.18	38.73	38.23	38.20
C250-Bf65-T1.2	42.85	58.44	57.81	57.20	56.56	56.48	55.73	55.08	54.46	53.80	53.73	53.41	52.73	52.12	51.44	51.37
C250-Bf65-T1.6	70.94	94.26	93.23	92.25	91.21	91.03	89.82	88.76	87.76	86.69	86.51	86.01	84.92	83.92	82.83	82.64
C250-Bf65-T2.0	104.64	136.81	135.33	133.91	132.42	132.10	130.38	128.86	127.40	125.86	125.53	124.87	123.29	121.84	120.26	119.91

3.6 Results and discussion

Tables (3-5)-(3-7) show the axial capacity of CFS channel sections with plain webs and slits as calculated from the FEA results. The influence of λ_c , D/t, B_f/t, W_{sl}/t, D/B_f, and L_{sl}/W_{sl} on the axial capacity of sections are analyzed in the following sub-sections, with insights drawn from the results of the parametric study.

3.6.1 Influence of column slenderness (λ_c) on the axial capacity for sections with slits

The column slenderness (λ_c) was adjusted between 0.36 and 2.13 to study its effect on the axial capacity of CFS channel sections with slits. Failure modes for varying section lengths are shown in Figs. 3-9 (a), (b), and (c). It should be noted that, for simplicity, the column slenderness of the corresponding plain sections was considered. Figs. 3-9 (a) and (b) illustrate how local buckling was the prevalent mode across sections from 500 mm-1500 mm. For sections with a length of 2000 mm, both global and local buckling were observed. Figs. 3-10 (a), (b) and (c) display the load-displacement curves for these sections. Tables (3-5)–(3-7) show that the axial capacity of the CFS channel with slits decreased progressively with increasing slenderness from 0.36 to 2.13. Specifically, an increase in λ_c from 0.36 to 0.53 led to a 17.03% average reduction in axial capacity. Further increases from 0.72 to 1.06, from 1.08 to 1.60, and from 1.94 to 2.13 resulted in average reductions of 20.95%, 24.31%, and 31.43% in axial capacity, respectively.

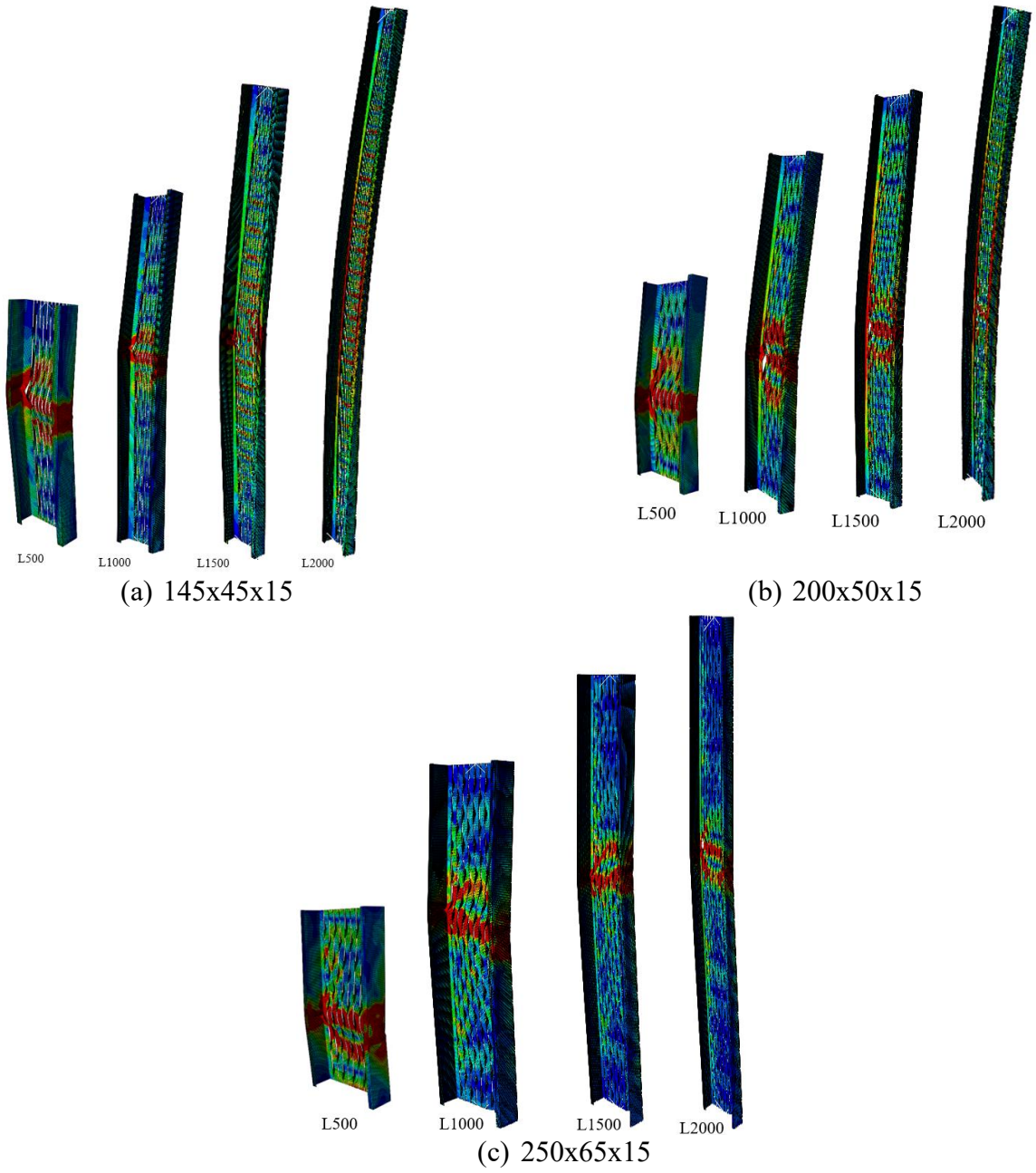

Fig.3- 9 Failure modes for varying section lengths of different CFS channel sections

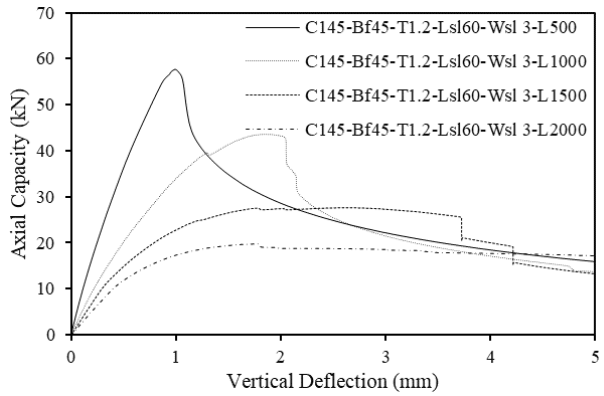

(a) 145x45x15

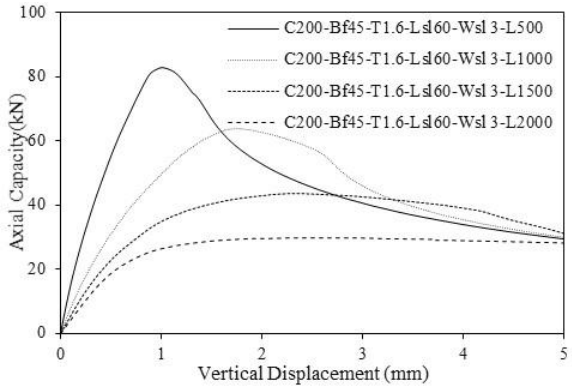

(b) 200x50x15

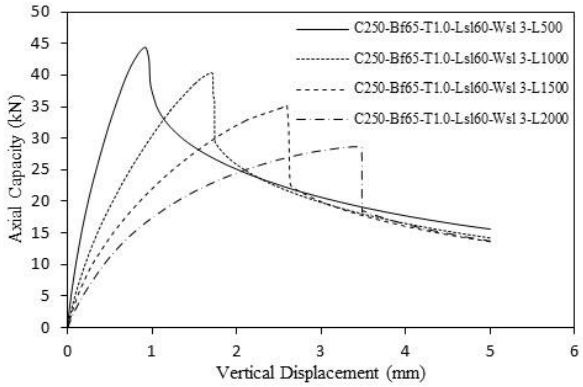

(c) 250x65x15

Fig.3- 10 Axial capacity- vertical displacement of different CFS channel sections

3.6.2 Influence of D/t on the axial capacity for sections with slits

The effect of the *D/t* ratio on the axial capacity of CFS channel sections with slits is detailed in Tables (3-5)–(3-7) and results are depicted in Fig. 3-11. FEA (Fig. 3-11) revealed that the axial capacity of these sections decreased by an average of 4.93% when the *D/t* ratio increased from 241.67 to 333.33. Conversely, when the *D/t* ratio further increased from 333.33 to 416.67, the axial capacity of the sections with slits saw an average increase of 29.83%. As per Fig. 3-11, the average overall capacity reductions for the section with slits, compared to the plain section, are 10.52%, 9.37%, and 6.89% for D/t ratios of 241.67, 333.33, and 416.67, respectively. The sections with D/t ratios of 241.77, 333.33, and 416.67 had corresponding D/B_f ratios of 3.22, 4.44, and 3.85, respectively. The variation in axial capacity with the D/t ratio can be attributed

to the section depth-to-flange width ratio(D/B_f), as detailed in Section 4.2.4.

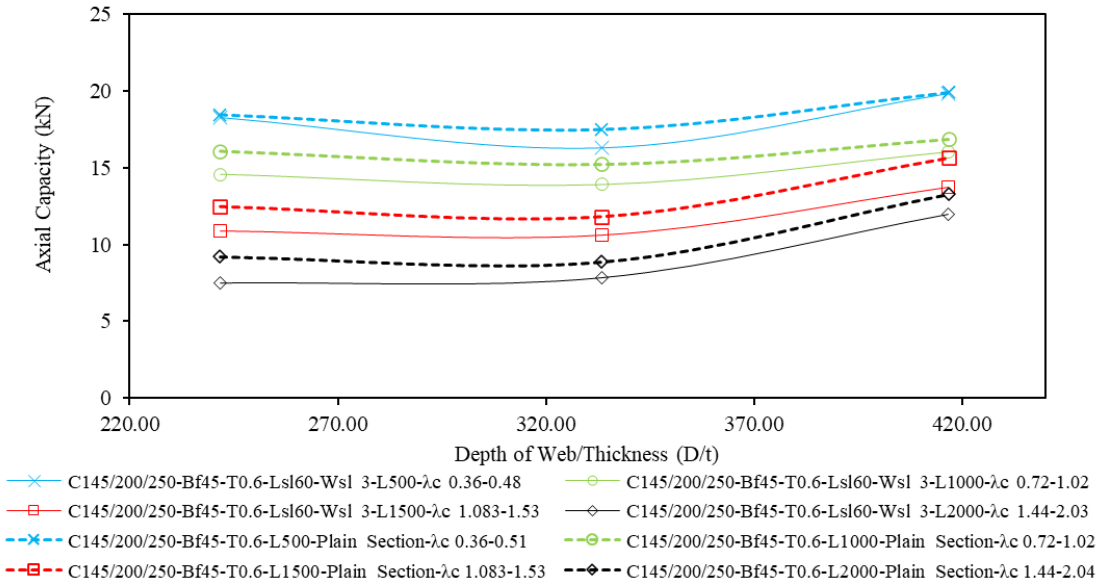

Fig.3- 11 Effect of D/t on the CFS channel sections with slits' axial capacity

3.6.3 Effect of B_f/t on the axial capacity (P) for sections with slits

The effect of the B_f/t on the axial capacity of CFS channel sections with slits is detailed in Tables (3-5)–(3-7) and results are shown in Fig. 3-12, according to results obtained from FEA. The data (Fig. 3-12) shows a series of increments in axial capacity associated with an increase in the B_f/t ratio from 75 to 108.33 across varying levels of column slenderness (λ_c). Specifically, for λ_c values between 0.36 and 0.48, there was an 8.41% increase in axial capacity. This rise was slightly higher, at 9.85%, for λ_c values between 0.72 and 0.97. A more substantial increase of 26.41% was observed for λ_c values between 1.08 and 1.45. The most significant increase, at 60.18%, occurred when the λ_c was between 1.44 and 1.93, highlighting a pronounced sensitivity of axial capacity to changes in the B_f/t ratio as column slenderness increases. In addition, it can be seen that as per Fig. 3-12, the average overall capacity reductions for the section with slits, compared to the plain section, are 10.52% and 6.89% for B_f/t ratios of 75 and 108.33, respectively.

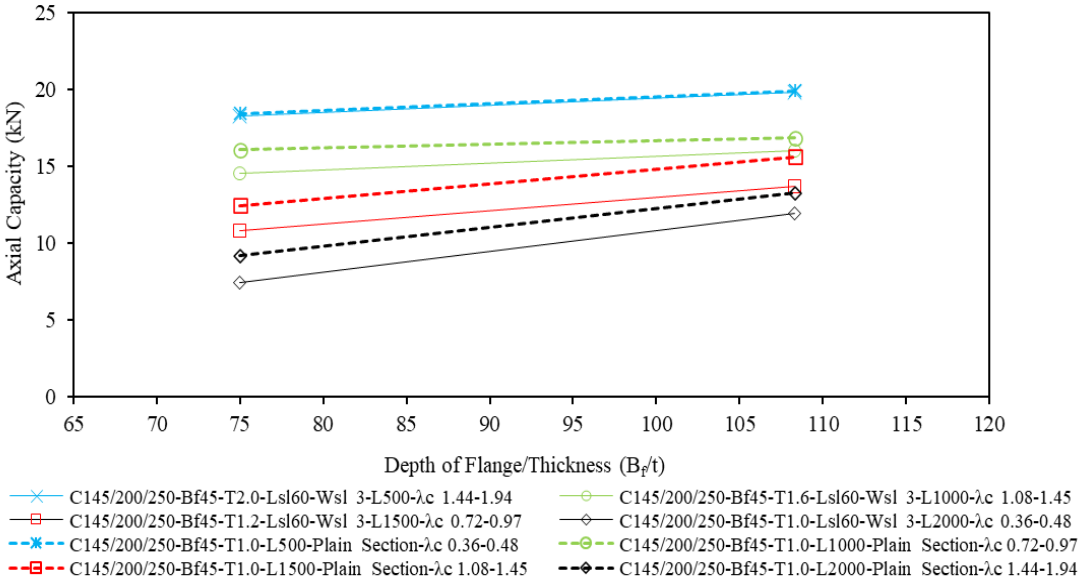

Fig.3- 12 Effect of B_f/t on the axial capacity of CFS channel sections with slits

3.6.4 Effect of D/B_f on the axial capacity (P) for sections with slits

The effect of the D/B_f ratio on the axial capacity of CFS channel sections with slits is shown in Tables (3-5)–(3-7) and depicted in Fig. 3-13. It showed that the axial capacity of these sections increased by an average of 26.22% when the D/B_f ratio increased from 3.22 to 3.85. As the flange width ratio decreases, the fixity of the web becomes less restrained thus reducing the web buckling coefficient. This lower coefficient indicates that the section is more prone to buckling at lower loads, explaining the decrease in the local buckling moment [102]. Conversely, when the D/B_f ratio further increased from 3.85 to 4.44, the axial capacity of the sections with slits saw an average decrease of 22.09%. A more favorable flange-to-web width ratio, achieved by having a wider flange, results in the web being more effectively restrained by the flanges. This increased restraint enhances the web's resistance to local buckling, leading to higher local buckling moments [13]. This trend is consistent with the findings of Degtyareva et al. [88], who observed a decrease in buckling moment when the section depth increased from 145 mm to 200 mm, while maintaining a flange width of 45 mm. They also reported an increase in buckling moment when the section size was further increased from a depth of 200 mm and flange width of 45 mm to a

depth of 250 mm and flange width of 65 mm. In terms of overall capacity reduction for the section with slits compared to the plain section, the values are 10.52%, 6.89%, and 9.37% for D/B_f ratios of 3.22, 3.85, and 4.44, respectively.

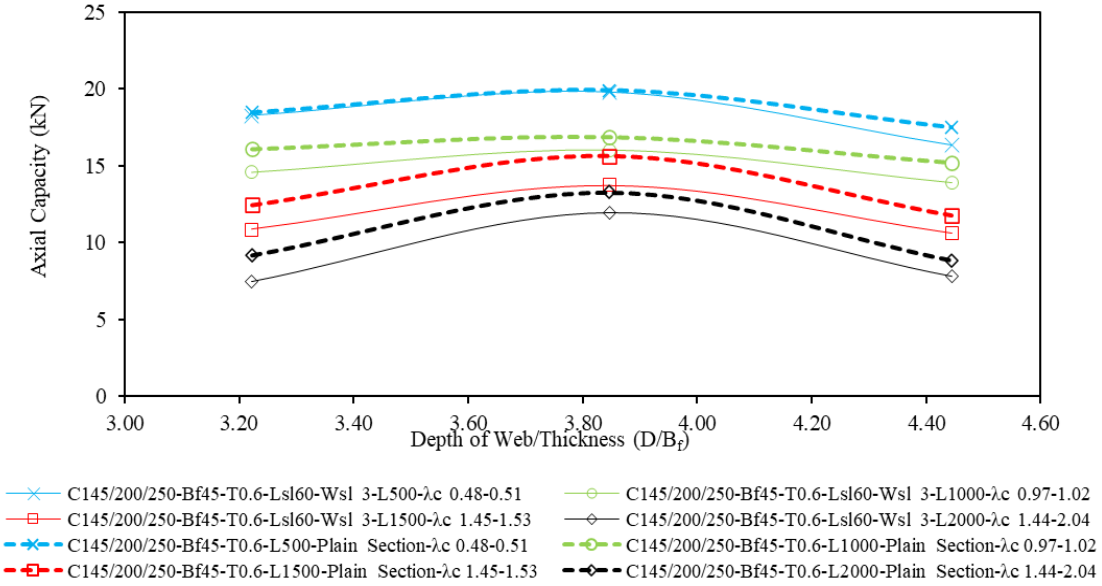

Fig.3- 13 Effect of D/B_f on the axial capacity of CFS channel sections with slits

3.6.5 Effect of width of slot Wsl/t on the axial capacity (P) for sections with slits

Tables (3-5)–(3-7) and Figs. 3-14 (a), (b), and (c) collectively depict the effects of the W_{sl}/t ratio on the axial capacity of various CFS channel sections with slits, as derived from FEA results. For the C145X45X15 sections (Fig. 3-14 (a)), the axial capacity decreased by 5.15% when the W_{sl}/t ratio was varied from 5 to 11.66, for λ_c value of 0.48. The decrease in axial capacity was further observed as follows: by 2.298% for λ_c value of 0.97, by 5.25% for λ_c value of 1.46, and significantly by 9.83% for λ_c value of 1.94. The C200X45X15 sections (Fig. 3-14 (b)) showed a more gradual decrease, with reductions of 1.23%, 1.71%, 2.12%, and 2.81% for λ_c values of 0.51, 1.02, 1.53, and 2.04, respectively, as the W_{sl}/t ratio varied from 5 to 11.66. In contrast, the C250X65X15 sections (Fig. 3-14 (c)) experienced reductions of 5.43%, 2.96%, 5.12%, and 1.60% for λ_c values of 0.36, 0.73, 1.09, and 1.46, respectively, as the W_{sl}/t ratio varied from 5 to 11.66. These results highlight a decreasing trend of axial capacity as the W_{sl}/t ratio

increases across different levels of column slenderness. The overall capacity reduction for the section with slits compared to the plain section, as the W_{sl}/t ratio varied from 5 to 11.66, varied depending on the section type. For the C145X45X15 section, the reductions were 3.2%, 10.65%, 14.89%, and 23.04% for λ_c values of 0.36, 0.73, 1.09, and 1.46, respectively. For the C200X45X15 section, the reductions were 7.05%, 9.38%, 11.17%, and 12.86% for the same λc values. Similarly, for the C250X65X15 section, the reductions were 13.46%, 13.30%, 14.25%, and 16.53% for the corresponding λ_c values.

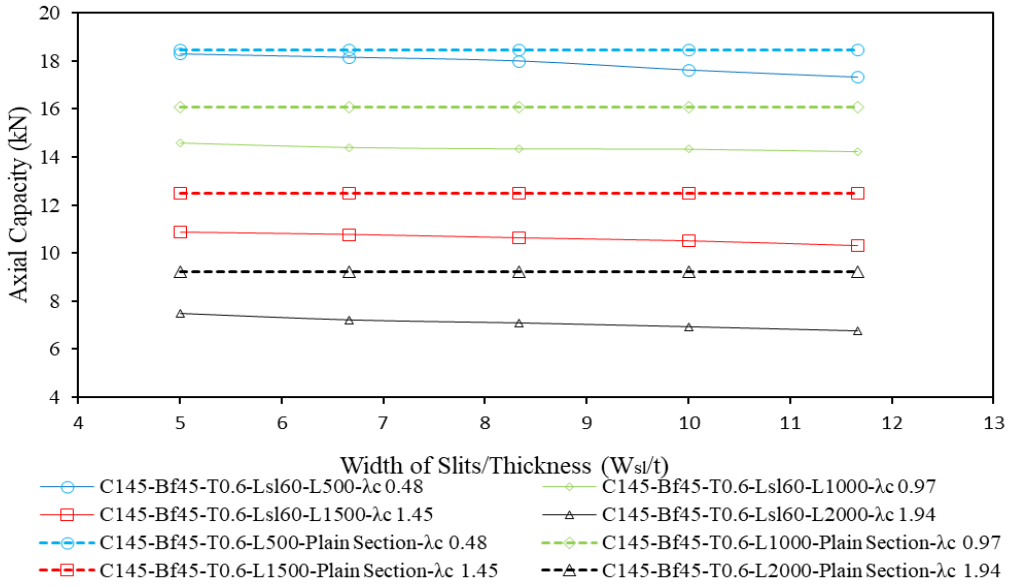

(a) 145x45x15

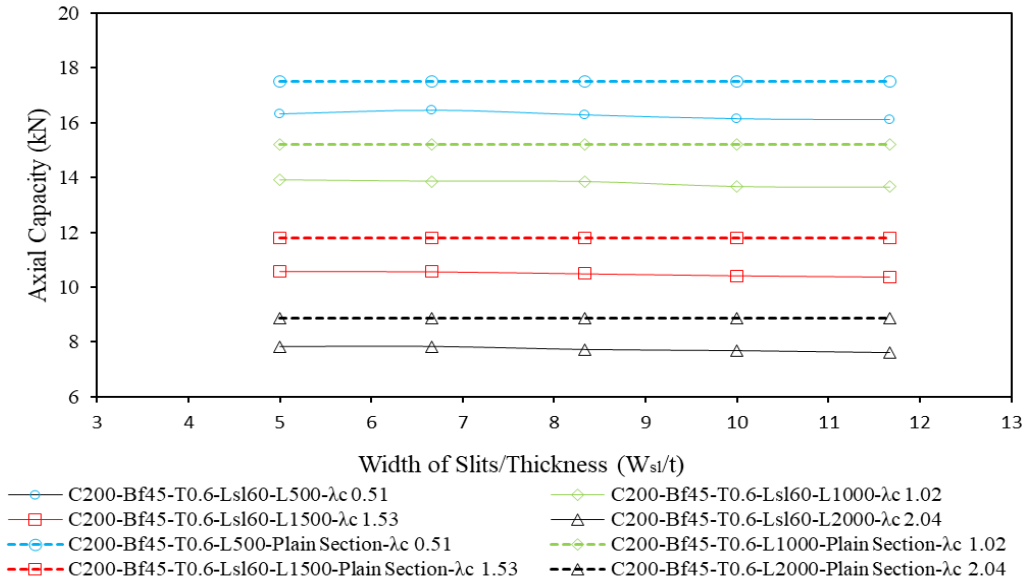

(b) 200x45x15

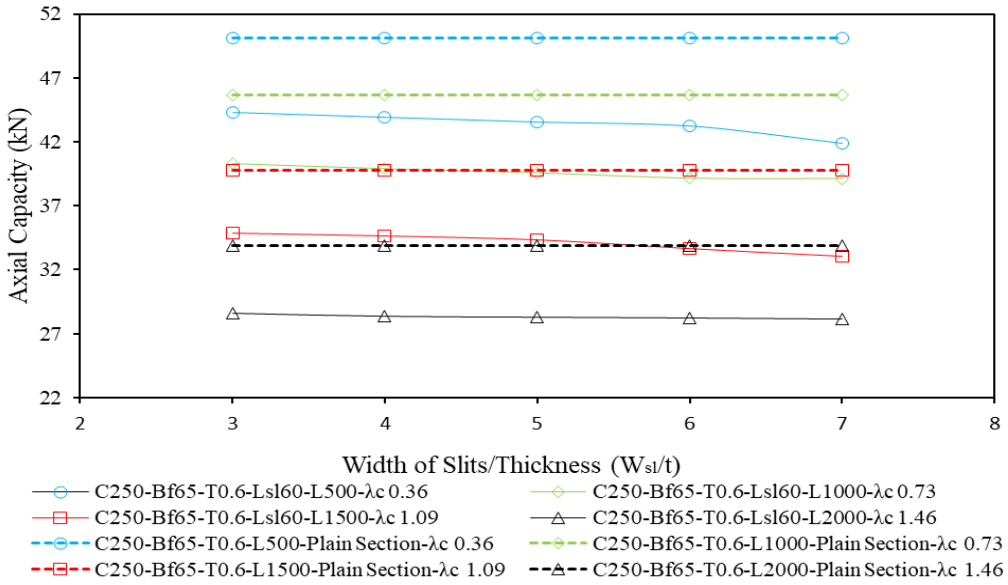

(c) 250x65x15

Fig.3- 14 Effect of W_{sl}/t on the CFS channel sections with slits' axial capacity

3.6.7 Effect of L_{sl}/W_{sl} on the axial capacity (P) for sections with slits

Tables (3-5)–(3-7) and Figs. 3-15 (a), (b), and (c) collectively show the effects of the L_{sl}/W_{sl} ratio on the axial capacity of various CFS channel sections with slits, according to FEA results. For the C145X45X15 sections (Fig. 3-15 (a)), axial capacity decreased by 4.57% when the L_{sl}/W_{sl}

ratio increased from 20 to 30 for a λ_c value of 0.48, by 3.21% for 0.97, by 4.08% for 1.45, and significantly by 8.77% for 1.94. The C200X45X15 sections (Fig. 3-15 (b)) experienced decreases of 2.42%, 4.11%, 2.89%, and 4.97% for λ_c values of 0.51, 1.02, 1.53, and 2.04, respectively, as the L_{sl}/W_{sl} ratio increased from 20 to 30. In contrast, the reductions in the C250X65X15 sections (Fig. 3-15 (c)) were 5.15%, 4.86%, 4.43%, and 4.51% for λ_c values of 0.36, 0.97, 1.08, and 1.44, respectively, as the L_{sl}/W_{sl} ratio increased from 20 to 30.

These results demonstrate a consistent trend of decreasing axial capacity with increasing L_{sl}/W_{sl} ratios across different column section dimensions. The overall capacity reduction for the section with slits compared to the plain section, as the L_{sl}/W_{sl} ratio varied from 20 to 30, varied depending on the section type. For the C145X45X15 section, the reductions were 3.74%, 10.89%, 14.89%, and 22.59% for λ_c values of 0.48, 0.96, 1.45, and 1.94, respectively. In the case of the C200X45X15 section, the reductions were 7.91%, 10.11%, 11.56%, and 14.11% for the same λc values. Similarly, for the C250X65X15 section, the reductions were 13.79%, 14.19%, 14.63%, and 17.09% for the corresponding λ_c values.

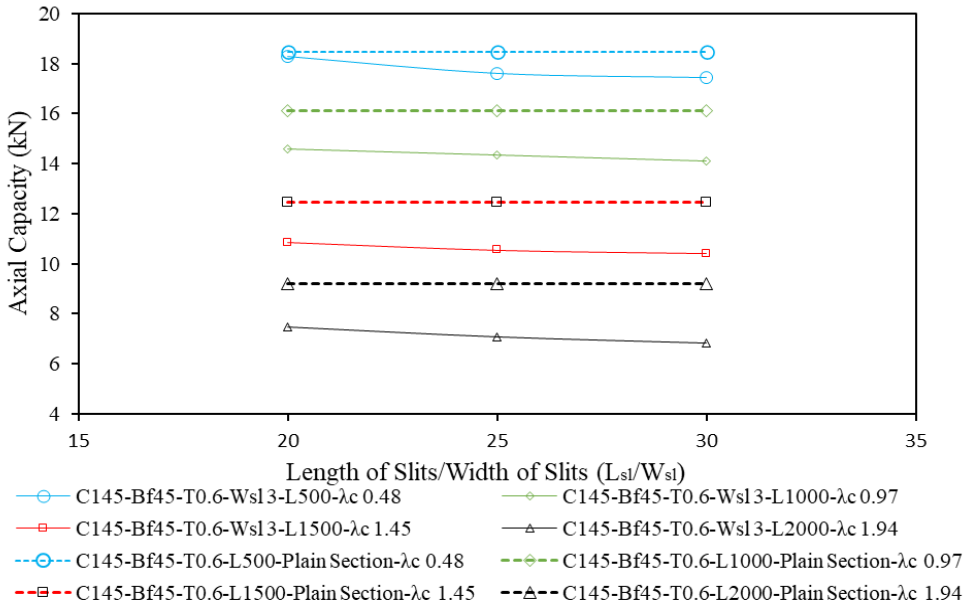

(a) 145x45x15

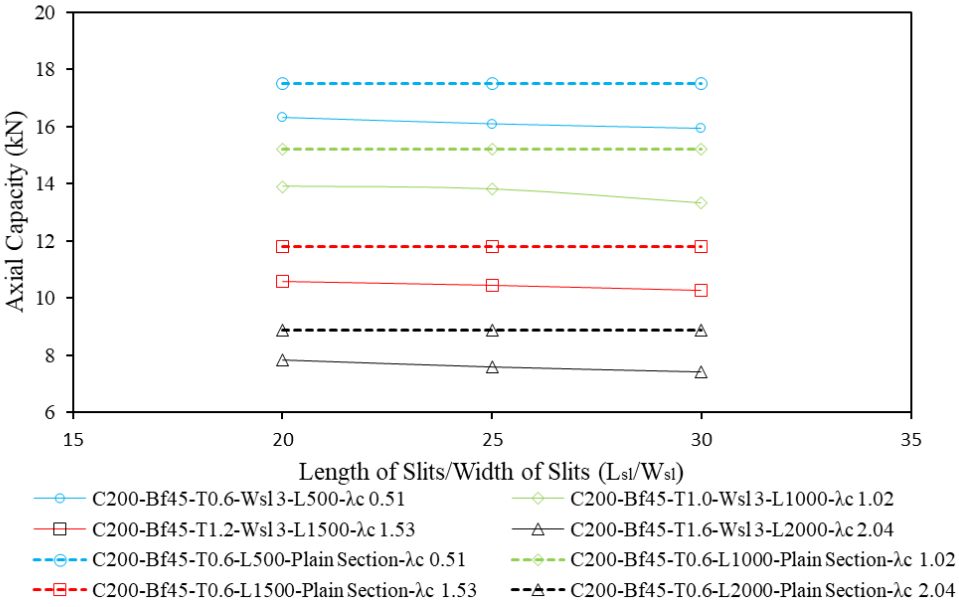

(b) 200x45x15

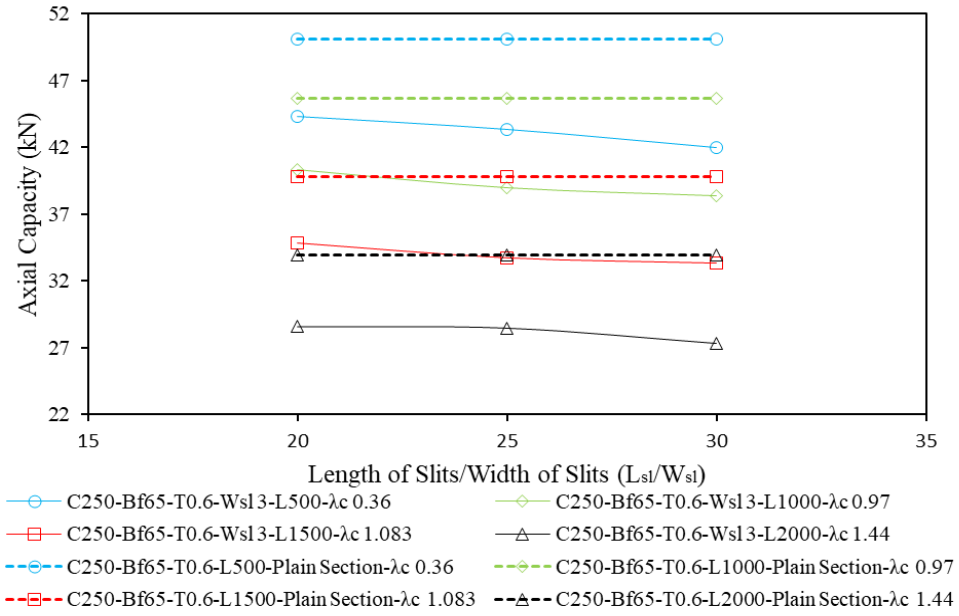

(c) 250x65x15

Fig.3- 15 Effect of L_{sl}/W_{sl} on the CFS channel sections with slits' axial capacity

3.7 Design rules for axial strength of cold-formed steel sections with slits

Existing standards do not provide design guidelines for determining the axial strengths of studs with slits. However, design guidelines outlined in AISI S100-2016 [103] and AS/NZS

4600-2018 [101] for carbon steel columns with centred web holes were used. The Direct Strength Method (DSM) was used to determine the design capacities of these CFS sections, aligning with specified design guidelines. The design rules for assessing the axial capacity of CFS channels with holes are detailed in Sections 3.8.

3.8 Current design rules

3.8.1 General

The minimum value of the global buckling strength (P_{ne}), local buckling strength (P_{nl}), and distortional buckling strength (P_{nd}) yields the un-factored design strength ($P_{AISI\&AS/NZS}$) for CFS channels without holes [1–10].

$$P_{AISI\&AS/NZ} = \min(P_{nl}, P_{nd}, P_{ne}) \quad (1)$$

The design formula for calculating the global buckling (P_{ne}) are given in Equations (2) and (3):

$$For\ \lambda_c < 1.5\ ; P_n = \left(0.658^{\lambda_c{}^2}\right) f_y \quad (2)$$

$$For\ \lambda_c > 1.5\ ; P_n = \left(\frac{0.877}{\lambda_c{}^2}\right) f_y \quad (3)$$

$$\lambda_c = \sqrt{\frac{P_y}{P_{cre}}} \quad (4)$$

Equations (4) and (5) provide the design formula for computing the local buckling (P_{nl}) :

$$\lambda_l \leq 0.776, P_{nl} = P_{ne} \quad (5)$$

$$\lambda_l > 0.776, P_{nl} = \left[1 - 0.15\left(\frac{P_{crl}}{P_{ne}}\right)^{0.4}\right]\left(\frac{P_{crl}}{P_{ne}}\right)^{0.4} P_{ne} \quad (6)$$

$$\lambda_l = \sqrt{\frac{P_{ne}}{P_{crl}}} \quad (7)$$

Equations (6) and (7) give the design formula for determining the distortional buckling (P_{nd}):

$$\lambda_d \leq 0.561, P_{nd} = P_y \quad (8)$$

$$\lambda_d > 0.561, P_{nd} = \left[1 - 0.25\ \left(\frac{P_{crd}}{p_y}\right)^{0.6}\right]\left(\frac{P_{crd}}{p_y}\right)^{0.6} P_y \quad (9)$$

$$\lambda_d = \sqrt{\frac{P_y}{P_{crd}}} \tag{10}$$

It should be mentioned that the signature curves produced by finite strip analysis can be used to determine P_{crl}, P_{crd} and P_{cre}.

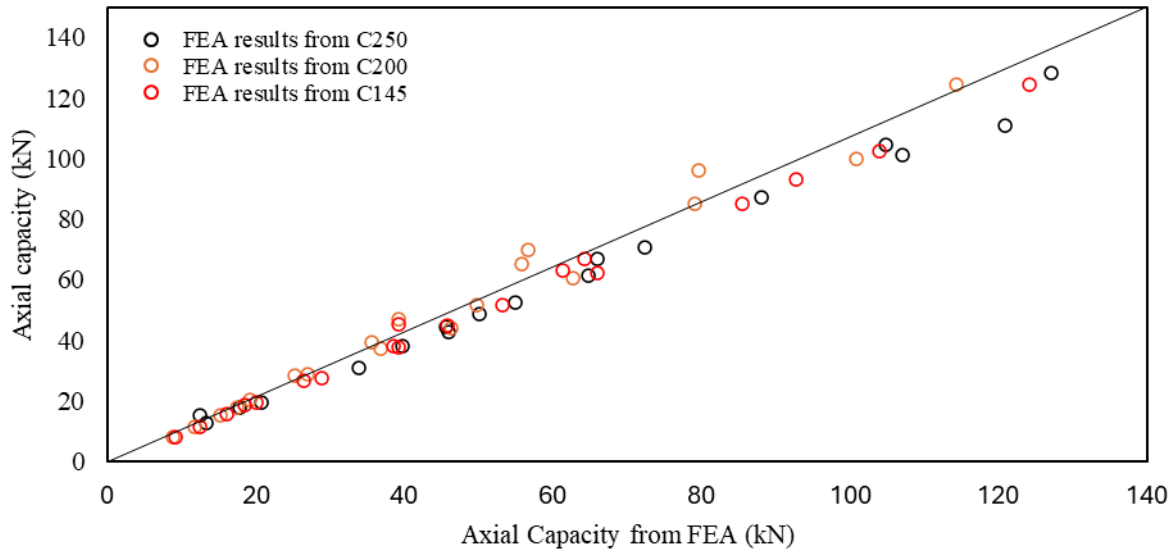

Fig.3- 16 Comparison of the FEA findings for CFS channel sections with plain webs with the results using DSM equations [Eqs 1-10]

3.9 Comparison of design strengths with the FEA results

Fig. 3-16 compares the axial capacity of CFS channel sections with plain webs which was predicted from the FE model and DSM equations [Eq 1-10]. The average P_{FEA}/P_{DSM} ratios are 0.99 and the COV is 0.072 for CFS channels with plain webs, as shown in Table 3-8. Consequently, the DSM equations from the AISI [103] and AS/NZS [32] standards provide an accurate prediction of the axial capacity of CFS channel sections with plain webs.

Table 3- 8 FEA results compared with predicted capacities using current design equations

Design guidelines	Design equations	Type of section	Equations	Comparison	Mean	COV
AS/NZS [101] & AISI [103]	DSM	Plain webs	Eqs. 1-10	$P_{FEA}/P_{DSM\ [32,34]}$	0.99	0.072

3.10 Proposed design equations

As mentioned previously, no design rules are available in the literature for determining the axial capacity of CFS channels with slits. When comparing the numerical simulation results with the design strengths calculated using equations from the American Iron and Steel Institute (AISI 2016) and the Australia/New Zealand Standards (AS/NZS 2018), it was found that for CFS channel sections with slits, the Direct Strength Method (DSM) equations overestimated the strengths by an average of 24.9% (refer Tables (3-5)–(3-7)).

The results from the parametric study suggest that the ratios D/t, B_f/t, W_{sl}/t, D/B_f and L_{sl}/W_{sl} are the main factors influencing the axial capacity of these sections under compression. The modified design equations for calculating the axial capacity (P_{prop}) of CFS channels with slits are given in Equations (11)-(16). For CFS channel sections with slits, parametric results indicated that columns with λ_c ranging from 0.36 to 1.60 underwent local buckling, whereas columns with a slenderness value exceeding 1.60 exhibited a combination of local and global buckling failure. Thus, modified DSM equations [Eqs. 11-16] were introduced to calculate the nominal axial capacity (P_{prop}) of CFS channels with slits, derived from the design strength of CFS channel plain sections.

For CFS channel sections with slits,

$$P_{Prop} = \left[0.659 - 0.0002\left(\frac{D}{t}\right) + 0.004\left(\frac{Bf}{t}\right) - 0.0017\left(\frac{Wsl}{t}\right) + 0.0105\left(\frac{D}{Bf}\right) + 0.0004\left(\frac{Lsl}{Wsl}\right)\right] \times P_{DSM} \quad for\ 0.36 < \lambda_c < 0.53 \quad (11)$$

$$P_{Prop} = \left[0.323 - 0.0012\left(\frac{D}{t}\right) + 0.0072\left(\frac{Bf}{t}\right) + 0.0004\left(\frac{Wsl}{t}\right) + 0.00866\left(\frac{D}{Bf}\right) + 0.0002\left(\frac{Lsl}{Wsl}\right)\right] \times P_{DSM} \quad for\ 0.72 < \lambda_c < 1.06 \quad (12)$$

$$P_{Prop} = \left[0.187 - 0.00089\left(\frac{D}{t}\right) + 0.007249\left(\frac{Bf}{t}\right) - 0.005\left(\frac{Wsl}{t}\right) + 0.11\left(\frac{D}{Bf}\right) - 0.0008\left(\frac{Lsl}{Wsl}\right)\right] \times P_{DSM} \quad for\ 1.08 < \lambda_c < 1.56\ and\ 0.6\,mm < t < 1.2\,mm \quad (13)$$

$$P_{Prop} = \left[0.574 - 0.0005\left(\frac{D}{t}\right) + 0.0149\left(\frac{Bf}{t}\right) - 0.069\left(\frac{Wsl}{t}\right) + 0.001\left(\frac{D}{Bf}\right) - 0.007\left(\frac{Lsl}{Wsl}\right)\right] \times P_{DSM} \quad for\ 1.08 < \lambda_c < 1.60\ and\ 1.6\,mm < t < 2\,mm \qquad (14)$$

$$P_{Prop} = \left[0.194 - 0.0004\left(\frac{D}{t}\right) + 0.006\left(\frac{Bf}{t}\right) - 0.017\left(\frac{Wsl}{t}\right) + 0.11\left(\frac{D}{Bf}\right) - 0.0027\left(\frac{Lsl}{Wsl}\right)\right] \times P_{DSM} \quad for\ 1.94 < \lambda_c < 2.08\ and\ 0.6\,mm < t < 1.2\,mm \qquad (15)$$

$$P_{Prop} = \left[0.49 - 0.0006\left(\frac{D}{t}\right) + 0.013\left(\frac{Bf}{t}\right) - 0.075\left(\frac{Wsl}{t}\right) + 0.002\left(\frac{D}{Bf}\right) - 0.007\left(\frac{Lsl}{Wsl}\right)\right] \times P_{DSM} \quad for\ 1.94 < \lambda_c < 2.13\ and\ 1.6\,mm < t < 2\,mm \qquad (16)$$

Fig. 3-17 and Fig. 3-18 compare the FEA results with the predictions made by the proposed DSM-based equations for CFS channel sections with slits. Generally, the proposed DSM-based design equations correspond well with the FE results in predicting the axial capacity of CFS channel sections with slits. Fig. 3-18 shows that the equations are more accurate for slenderness values less than 1. The scope of the proposed design equations is restricted to the ranges $0.36 < \lambda_c < 0.53$, $0.72 < \lambda_c < 1.06$, $1.08 < \lambda_c < 1.60$, $1.94 < \lambda_c < 2.13$ and $0.6\,mm < t < 2\,mm$.

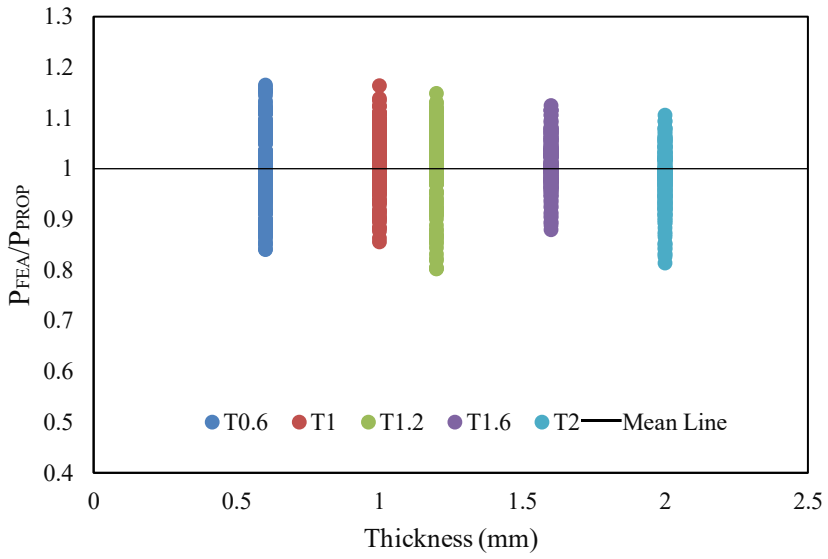

Fig.3- 17 Comparison of FEA results with predictions from proposed DSM equations for CFS channel sections with slits

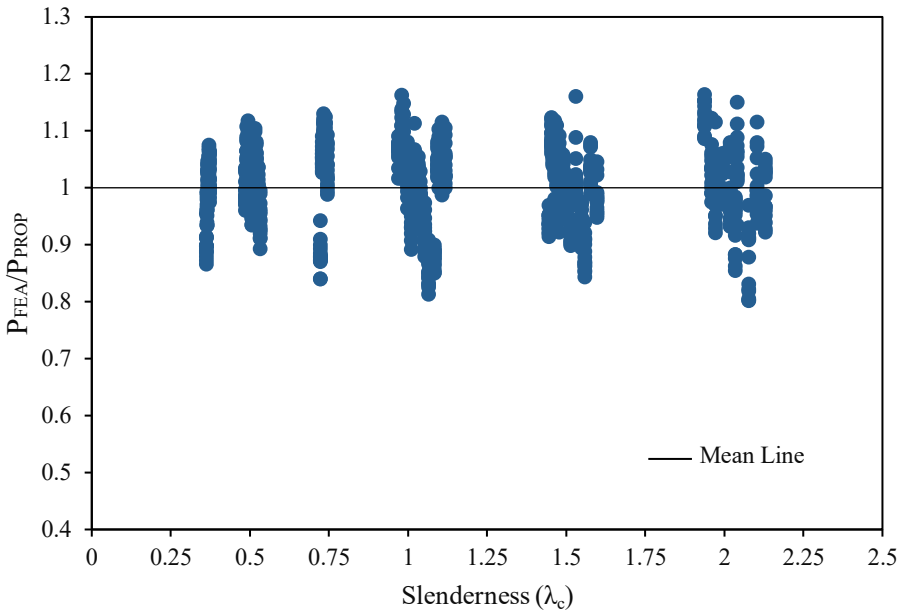

Fig.3- 18 Effect of Slenderness (λc) on the ratio of P_{FEA}/P_{PROP} of CFS section with slits

3.11 Reliability analysis

In the end, the accuracy of the suggested design equations for CFS channel sections with slits was evaluated by a reliability study. The parameters used in the study and their values are given in Table 3-10. The AISI specification [103] recommends a minimum target reliability index (β) of 2.5 for CFS structural members. Reliability studies showed that the DSM-based equations have reliability indices greater than 2.5 and correlation coefficients greater than 0.8 for CFS channel sections with slits (refer to Table 3-9). This shows that the axial capacity of CFS channel sections with slits can be predicted with accuracy using the suggested equations which are reliable. However, the above-mentioned dataset, although statistically reliable within the AISI S100 framework, is based on FEA-predicted axial capacities that were previously shown to overestimate experimentally measured strengths by approximately 8–12%. Consequently, the regression equations derived directly from this dataset inherently reflect the systematic overprediction associated with the numerical model. While this does not invalidate the statistical reliability assessment under the AISI methodology, it may introduce a slight unconservative bias

in the proposed design equations. To address this issue, a separate analysis was done by reducing the FEA-predicted axial capacities by 12%, corresponding to the upper bound of the observed overestimation. The regression calibration was subsequently repeated using the bias-adjusted dataset, and the reliability analysis was re-performed in accordance with the AISI S100 provisions. Accordingly, a revised set of prediction equations incorporating the model bias factor is proposed.

$$\varphi = 1.52 M_m F_m P_m e^{-\beta \sqrt{\{V_m^2 + V_f^2 + C_p V_p^2 + V_q^2\}}} \quad (17)$$

Table 3- 9 Reliability analysis of proposed DSM based equations

	Proposed equations for sections with slits					
	Eq. 11	Eq. 12	Eq. 13	Eq. 14	Eq. 15	Eq. 16
Number of data	225	225	180	120	90	60
Coefficient of variation, V_p	0.051	0.103	0.08	0.04	0.09	0.04
Mean, P_m	1.00	1.00	1.00	1.00	1.00	1.00
Resistance factor, φ	0.85	0.85	0.85	0.85	0.85	0.85
Correlation coefficient, C_c	0.99	0.97	0.99	0.99	0.98	0.97
Reliability index, β	2.8	2.6	2.7	2.8	2.6	2.8

Table 3- 10 Revised reliability analysis of proposed DSM based equations incorporating reduced FEA values

	Proposed equations for sections with slits					
	Eq. 17	Eq. 18	Eq. 19	Eq. 20	Eq. 21	Eq. 22
Number of data	225	225	180	120	90	60
Coefficient of variation, V_p	0.05	0.104	0.08	0.04	0.10	0.04
Mean, P_m	1.00	1.00	1.00	1.00	1.00	1.00
Resistance factor, φ	0.85	0.85	0.85	0.85	0.85	0.85
Correlation coefficient, C_c	0.99	0.97	0.99	0.99	0.98	0.97
Reliability index, β	2.8	2.6	2.71	2.8	2.6	2.8

For CFS channel sections with slits,

$$P_{Prop} = \left[0.668 - 0.00027\left(\frac{D}{t}\right) + 0.00328\left(\frac{Bf}{t}\right) - 0.00367\left(\frac{Wsl}{t}\right) + 0.002317\left(\frac{D}{Bf}\right) - 0.00026\left(\frac{Lsl}{Wsl}\right)\right] \times P_{DSM} \quad for\ 0.36 < \lambda_c < 0.53 \quad (17)$$

$$P_{Prop} = \left[0.301 - 0.0013\left(\frac{D}{t}\right) + 0.0067\left(\frac{Bf}{t}\right) + 0.0004\left(\frac{Wsl}{t}\right) + 0.081\left(\frac{D}{Bf}\right) + 0.0002\left(\frac{Lsl}{Wsl}\right)\right] \times P_{DSM} \quad for\ 0.72 < \lambda_c < 1.06 \quad (18)$$

$$P_{Prop} = \left[0.181 - 0.0009\left(\frac{D}{t}\right) + 0.0066\left(\frac{Bf}{t}\right) - 0.005\left(\frac{Wsl}{t}\right) + 0.104\left(\frac{D}{Bf}\right) - 0.0008\left(\frac{Lsl}{Wsl}\right)\right] \times P_{DSM} \quad for\ 1.08 < \lambda_c < 1.56\ and\ 0.6\,mm < t < 1.2\,mm \quad (19)$$

$$P_{Prop} = \left[0.54 - 0.0006\left(\frac{D}{t}\right) + 0.0141\left(\frac{Bf}{t}\right) - 0.071\left(\frac{Wsl}{t}\right) + 0.002\left(\frac{D}{Bf}\right) - 0.008\left(\frac{Lsl}{Wsl}\right)\right] \times P_{DSM} \quad for\ 1.08 < \lambda_c < 1.60\ and\ 1.6\,mm < t < 2\,mm \quad (20)$$

$$P_{Prop} = \left[0.185 - 0.0004\left(\frac{D}{t}\right) + 0.006\left(\frac{Bf}{t}\right) - 0.018\left(\frac{Wsl}{t}\right) + 0.104\left(\frac{D}{Bf}\right) - 0.0027\left(\frac{Lsl}{Wsl}\right)\right] \times P_{DSM} \quad for\ 1.94 < \lambda_c < 2.08\ and\ 0.6\,mm < t < 1.2\,mm \quad (21)$$

$$P_{Prop} = \left[0.46 - 0.0006\left(\frac{D}{t}\right) + 0.013\left(\frac{Bf}{t}\right) - 0.077\left(\frac{Wsl}{t}\right) + 0.002\left(\frac{D}{Bf}\right) - 0.008\left(\frac{Lsl}{Wsl}\right)\right] \times P_{DSM} \quad for\ 1.94 < \lambda_c < 2.13\ and\ 1.6\,mm < t < 2\,mm \quad (22)$$

Table 3- 11 Value of parameters used for calculating the reliability index as per AISI

$\mathbf{M_m}$	1.1
$\mathbf{F_m}$	1.0
$\mathbf{P_m}$	Mean
$\mathbf{V_m}$	0.1
$\mathbf{V_f}$	0.05
$\mathbf{V_q}$	0.21
$\mathbf{V_p}$	Coefficient of variation
$\mathbf{C_p}$	1.01
n	225
m	224
C	1.52
φ	0.85

3.12 Conclusion

This chapter assesses the axial capacity of CFS channel sections with slits using finite element (FE) analysis. To begin with, FE models were created and validated against the experimental results reported by Andreassen and Jönsson [3], showing a strong correlation in terms of ultimate axial capacity and failure behavior.

Subsequently, a comprehensive parametric study consisting of 960 FE models was carried out to examine the effects of D/t, B_f/t, W_{sl}/t, D/B_f, and L_{sl}/W_{sl} on the axial capacity of such CFS channel sections with both plain webs and slits.

The study's findings lead to the following conclusions:

(1) From parametric study results, the ratios of D/t, B_f/t, W_{sl}/t, D/B_f and L_{sl}/W_{sl} have an influence on the axial capacity of CFS channel sections with slits.

(2) The numerical simulation results revealed that the Direct Strength Method (DSM) equations from AISI 2016 and AS/NZS 2018 overestimated the axial strengths of CFS channel sections with slits by an average of 24.9%.

(3) Design equations incorporating capacity reduction factors were developed for DSM to estimate the axial capacity of CFS channel sections with slits. These equations are applicable within the ranges of $0.36< \lambda_c <0.53$, $0.72< \lambda_c <1.06$, $1.08< \lambda_c <1.60$ and $1.94< \lambda_c <2.13$, $241.67< D/t <416.67$, $75<B_f/t <108.33$, $5<W_{sl}/t <11.66$, $3.22< D/B_f <4.44$ and $20<L_{sl}/W_{sl}<30$.

(4) In conclusion, a reliability analysis was carried out, demonstrating that the proposed modified DSM equations are reliable, with β values of 2.5 or higher.

(5) The design equations are limited to local and global buckling and do not consider distortional buckling.

Chapter 4 Axial capacity of cold-formed steel channel sections with slits subjected to axial compressive load with eccentricity

4.1 Introduction

Eccentric loads in stud-based wall systems commonly result from ledger framing connections [15], [16]. Perimeter studs [4] and moment-resisting frame columns are typically subjected to combined axial compression and lateral pressure or bending [17], [18]. Most previous studies have focused on shear behaviour rather than axial strength under eccentric loading. Höglund [19] [1]proposed an analytical method, based on the Swedish Code, for estimating the shear strength of slitted webs. This approach was later validated through experimental studies by others [20], [21]. Salmi [22] also identified shear-related failure modes in perforated studs. However, neither study quantified axial capacity loss under eccentric loading using numerical or finite element methods.

Experimental studies on axial strength reductions due to web slits are scarce. Notable work includes that by Laboube [4], Andreassen and Jönsson [3], and Kesti [85], though all were limited to concentric loading. Laboube examined studs with both slits and service openings, while Andreassen, Jönsson, and Kesti focused on slit configurations.

Meanwhile, extensive research has been conducted on the general behaviour of CFS members under eccentric loading. Studies by Torabian et al. [104], [105] and Li et al. [106] found the AISI S100 (2012) [107] design provisions conservative for beam-columns. Hancock and Rasmussen [108] highlighted flexural-torsional buckling as a critical failure mode, and Cheng et al. [109] showed how bending moment direction affects compressive strength. Research by Ma et al. [110] and Li and Young [111], [112] found current standards conservative, particularly for high-strength elements and built-up open sections. Optimization studies have demonstrated that tailored cross-sectional shapes can yield significant strength gains [113], [114]. Hasanali et al.

[115], [116]also highlighted the conservative nature of the Direct Strength Method (DSM), especially under varying slenderness ratios and eccentricities. Öztürk et al. [117] found sigma channel profiles to exhibit higher strength, further underscoring the need to refine current design assumptions. In summary, despite numerous studies on CFS behaviour under eccentric loading, there remains a notable gap in understanding how web slits affect axial capacity in such conditions.

To address this critical research gap, particularly in slitted perforated sections under eccentric loading, a parametric investigation was undertaken. The current work extends the authors' earlier study in chapter 3 by addressing the influence of eccentric loading on axial strength. This study evaluated staggered slitted perforated sections with varying lengths, thicknesses, and cross-sectional dimensions subjected to six distinct load eccentricities. The axial load-carrying capacities derived from the analyses were evaluated against the DSM-based design provisions of AS/NZS 4600. The study subsequently proposes design recommendations through strength reduction factors, validated by a reliability analysis within the AISI-S100 framework to ensure adherence to established safety standards.

4.2 Summary of experimental results as reported by Andreassen and Jönsson [3] and Torabian et. al. [118]

Existing experimental research on the compressive performance of unstiffened cold-formed steel (CFS) studs with slits is limited to the work of Andreassen and Jönsson [3](see Fig. 4-1). Summary of the details regarding the experimental setup alongside the dimensional specifications of the tested sections can be found in chapter 3.

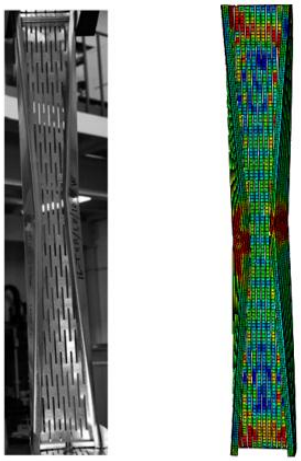

(i) Experimental test [3] (ii) FE model

Fig. 4- 1. Experimental (Andreassen and Jönsson [3]) vs. FEA failure modes

Torabian et al. [118] conducted experimental tests to investigate the structural behaviour of CFS-lipped plain channel sections under eccentric compression , including: (i) compression and a negative minor-axis bending moment; (ii) compression and a positive minor-axis bending moment; (iii) compression and a major-axis bending moment; and (iv) compression and bi-axial bending moments. The alignment of the axes is shown in Fig.4-2. In the investigation, proposed equations on the compressive strength for each limit state were developed. In the current study, 12 of the test results from Torabian et al. [118] were used for FE validation.

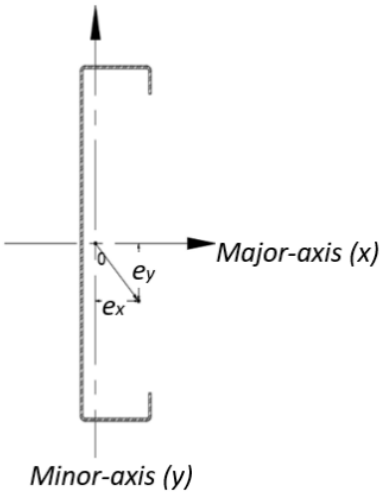

Fig. 4- 2. Definition of x- and y axis after Torabian et al. [118]

4.3 Finite element modelling methodology

4.3.1 General

The channel sections, both with and without slits, were modeled using an elasto-plastic

material model. The finite element analysis was carried out using ABAQUS [98], with particular attention given to capturing the influence of initial geometric imperfections inherent in the CFS sections. The modelling approach adopted in this study, including boundary conditions, meshing strategies, and imperfection modelling, is described in detail in the subsequent sections.

4.3.2 Material properties

The material properties used for validating the finite element models were adopted from Andreassen and Jönsson [3], with a yield strength of 360.8 MPa and a Young's modulus of 192 GPa. For the FEA models as per Torabian et al [118], the yield stress, and the ultimate stress of the CFS material are equal to Fy = 365 MPa and Fu = 560 MPa, respectively. The parametric analysis was carried out using a higher yield strength of 500 MPa to evaluate the performance of high-strength CFS sections. To accurately capture the stress–strain behaviour of the material, the nonlinear constitutive models proposed by Gardner and Yun [99] and Rossi et al. [100] were employed. The conversion of the engineering stress–strain curve into the true stress–strain curve was carried out using the following equations:

$$\sigma_{true} = \sigma(1 + \varepsilon) \quad (1)$$

$$\varepsilon_{true} = \ ln\ (1 + \varepsilon) - \frac{\sigma_{true}}{E} \quad (2)$$

Where E is the modulus of elasticity, σ is the engineering stress, ε is the engineering strain, σ_{true} is the true stress, and $\varepsilon_{\text{true}}$ is the true strain.

4.3.3 Meshing

The cold-formed steel (CFS) channel sections were modelled using S4R shell elements, each providing six degrees of freedom at each node. A mesh size of 1 mm × 1 mm was adopted (see Fig. 4-3) to accurately represent the complex geometry and stress distribution arising from the multiple slits present in the section. For comparison with the experimental results of Torabian et al. [118] involving plain CFS sections subjected to eccentric loads, a coarser mesh size of 5 mm × 5 mm was employed in the finite element simulations.

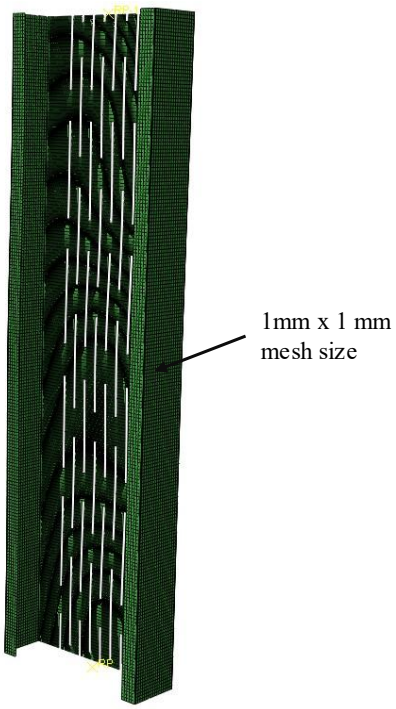

Fig. 4- 3. Finite element mesh details

4.3.4 Boundary and loading conditions

4.3.4.1 CFS sections under concentric loading

Reference points (RP-1 and RP-2) were defined at the column centroid on both ends of the channel sections, for both slit and plain configurations. The experimental boundary conditions were represented in the FE model using rigid body tie constraints.

Further details regarding the boundary and loading conditions can be found in chapter 3.

4.3.4.2 CFS sections under eccentric loading

The boundary conditions observed in the experimental test setup were replicated in the validated finite element (FE) models, as illustrated in Fig. 4-4. Two reference points were defined at the ends of the lipped channel sections using “Rigid” constraints to represent the supports and to apply eccentric axial loads. The nodal degrees of freedom at both ends were coupled to their respective reference points, which were pinned about both the minor and major axes. By adjusting the coordinates of these reference points, various eccentricities were introduced. A concentrated axial force was applied at one reference point (RP-2 in Fig. 4-4) under force control,

while the opposite reference point was restrained in the longitudinal (U_Z) direction to replicate the boundary support conditions. The physical test setup is depicted in Fig. 4-5. For the subsequent parametric investigation, an idealised pinned boundary condition consistent with the modelling framework developed for the slitted concentric models was adopted, and displacement control ensured continuity in representing slit-induced stiffness reduction and instability behaviour, while eccentricity was introduced through load offset.

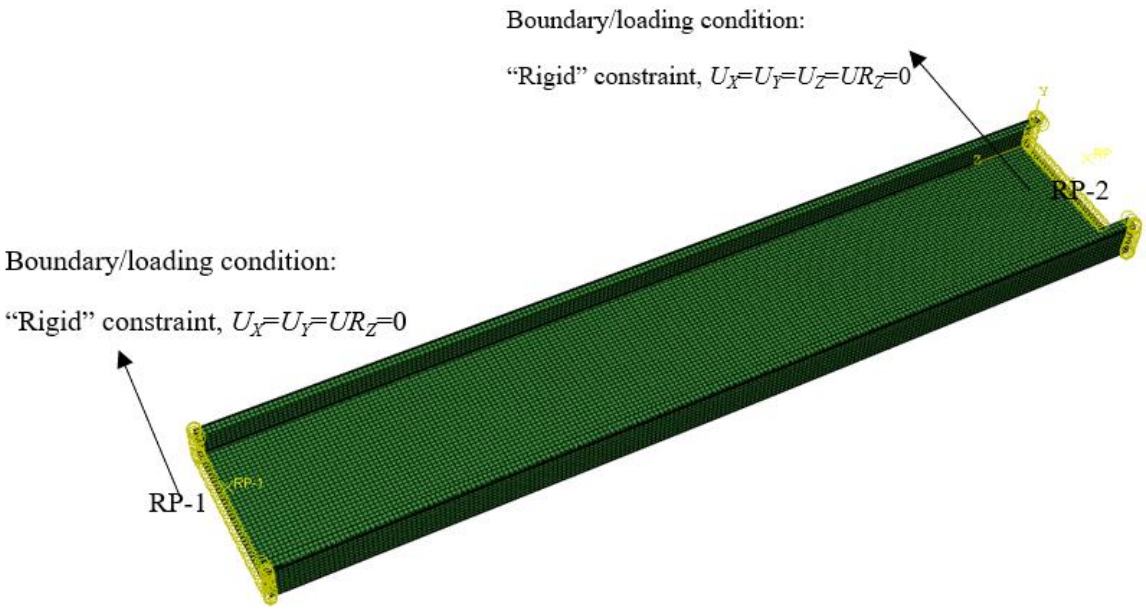

Fig. 4- 4. CFS element boundary conditions under eccentric compressive loads

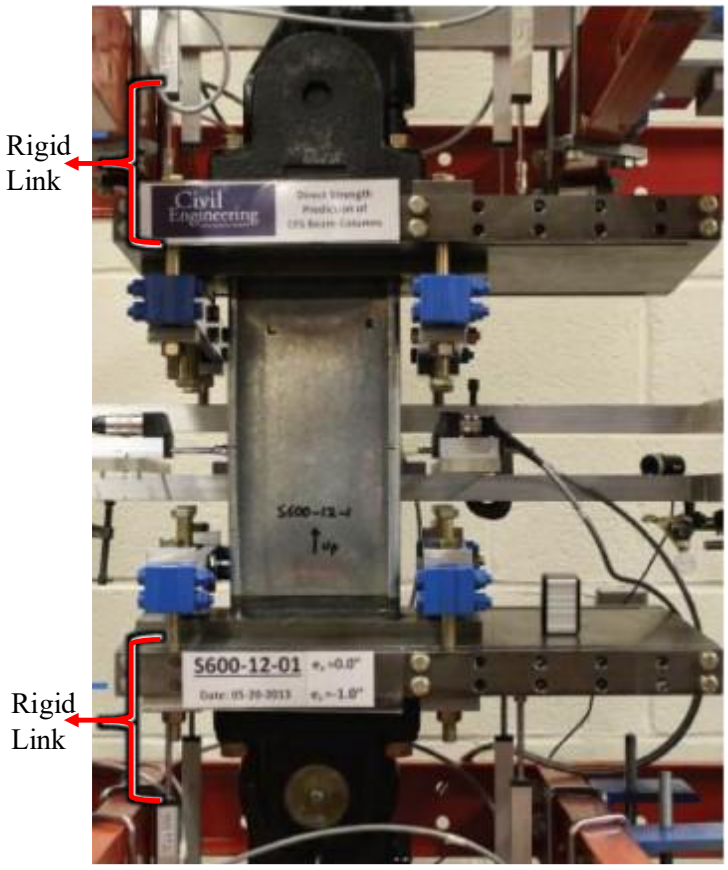

Fig. 4- 5. Lipped channel cross-section tested by Torabian et al. [118]

4.3.4.3 Geometrical imperfections

Cold-formed steel (CFS) sections are susceptible to geometric imperfections arising from manufacturing and handling processes. The finite element models included these imperfections to improve the reliability of the simulations. The imperfection magnitudes were determined in accordance with the guidelines specified in AS/NZS 4600. To define the imperfection shapes and amplitudes, eigenvalue buckling analyses were conducted.

4.4 Validation of finite element models

4.4.1 CFS sections under concentric loading

The FE analysis results showed strong correlation with the experimental data reported by Andreasson and Jönsson [3], particularly in terms of ultimate loads and failure modes. Comparison between the experimental results (P_{EXP}) with the numerical predictions (P_{FEA}) for C145 × 45 × 15 channel sections, yielded a mean P_{EXP}/P_{FEA} ratio of 0.92 and a coefficient of variation (COV) of 0.05. Additional details can be found in the authors' previous work on slitted

studs [119].

4.4.2 CFS sections under eccentric loading

The finite element (FE) models for the channel sections were validated against the experimental results of Torabian et al. [118]. Fig. 4-6 and Table 4-1 show the cross-sectional dimensions and lengths of the beam-column specimens tested under axial compression with nine eccentricities along both major (x) and minor (y) axes. These introduced combined loading conditions: (i) axial compression with negative minor-axis bending, (ii) axial compression with positive minor-axis bending, (iii) axial compression with major-axis bending, and (iv) axial compression with biaxial bending. The predicted capacities from FE models and experiments, compared in Table 4-1, showed a maximum deviation of 6.0%. Fig. 4-7 compares axial force–displacement responses of specimens S600-305-13, S600-610-15, and S600-1219-17, showing that the FE models accurately reproduced peak load, initial stiffness, maximum capacity, and post-buckling response. Stiffness deviations were attributed to separations between plates and movement in swivel joints during testing. Although the FE models accurately reproduced the ultimate capacity and post-buckling response, noticeable differences are observed in the initial stiffness of the load–displacement curves in Fig. 4-7. This discrepancy can be fundamentally attributed to boundary compliance inherent in physical test setups. In column and beam-column testing, even nominally pinned supports are realised using clevis or swivel joints, which introduce rotational clearance, local deformation of connection components, and minor slip or seating effects during load application. Such boundary flexibility influences the effective rotational restraint and end compliance, thereby effecting the measured initial stiffness. In contrast, the FE models adopt idealised rigid-body constraints with perfect geometric alignment and no mechanical clearance. Importantly, while boundary compliance affects the initial elastic stiffness, its influence on the ultimate buckling capacity is generally less pronounced when the global instability mode is correctly captured. The deformation modes observed in the

simulations, including local, distortional, and global buckling, closely matched experimental observations, as shown in Fig. 4-8 for specimen S600-610-8 under axial compression with major-axis bending.

Table 4- 1. Validated models' variables and results

Section name	Web	Flange	Lip	Thickness	R	Length	Eccentricities		P_{test}	P_{FEA}	Percentage difference (%)
	d	b_f	b_l	t	r	L	e_x	e_y			
S600-305-1	152.05	34.95	9.5	1.45	2.87	305	-25.4	0.0	25.4	25.7	-1.2
S600-305-9	152.05	34.95	9.5	1.45	2.87	305	0.0	-190.5	20.6	20.0	2.9
S600-305-10	152.05	34.95	9.5	1.45	2.87	305	2.6	-38.1	48.9	48.2	1.4
S600-305-13	152.05	34.95	9.5	1.45	2.87	305	-15.5	-76.2	25.0	25.4	-1.6
S600-305-15	152.05	34.95	9.5	1.45	2.87	305	-15.5	-76.2	26.5	25.4	4.2
S600-610-6	152.05	34.95	9.5	1.45	2.87	610	31.8	0.0	16.1	16.5	-2.5
S600-610-8	152.05	34.95	9.5	1.45	2.87	610	0.0	-76.2	34.8	33.3	4.3
S600-610-9	152.05	34.95	9.5	1.45	2.87	610	0.0	-165.1	21.5	21.1	1.9
S600-610-14	152.05	34.95	9.5	1.45	2.87	610	-3.8	-19.1	42.8	42.1	1.6
S600-610-15	152.05	34.95	9.5	1.45	2.87	610	-14.2	-69.9	25.0	24.4	2.4
S600-1219-14	152.05	34.95	9.5	1.45	2.87	1219	-3.6	-17.8	27.2	28.6	-5.1
S600-1219-17	152.05	34.95	9.5	1.45	2.87	1219	-6.9	-101.6	20.0	18.8	6.0

Negative eccentricity in the x direction means that web of the specimens is in compression.

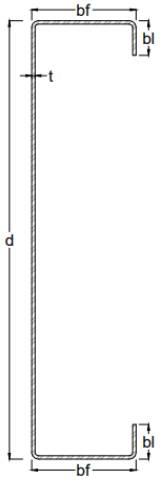

Fig. 4- 6. Nominal cross-sections of CFS channel sections

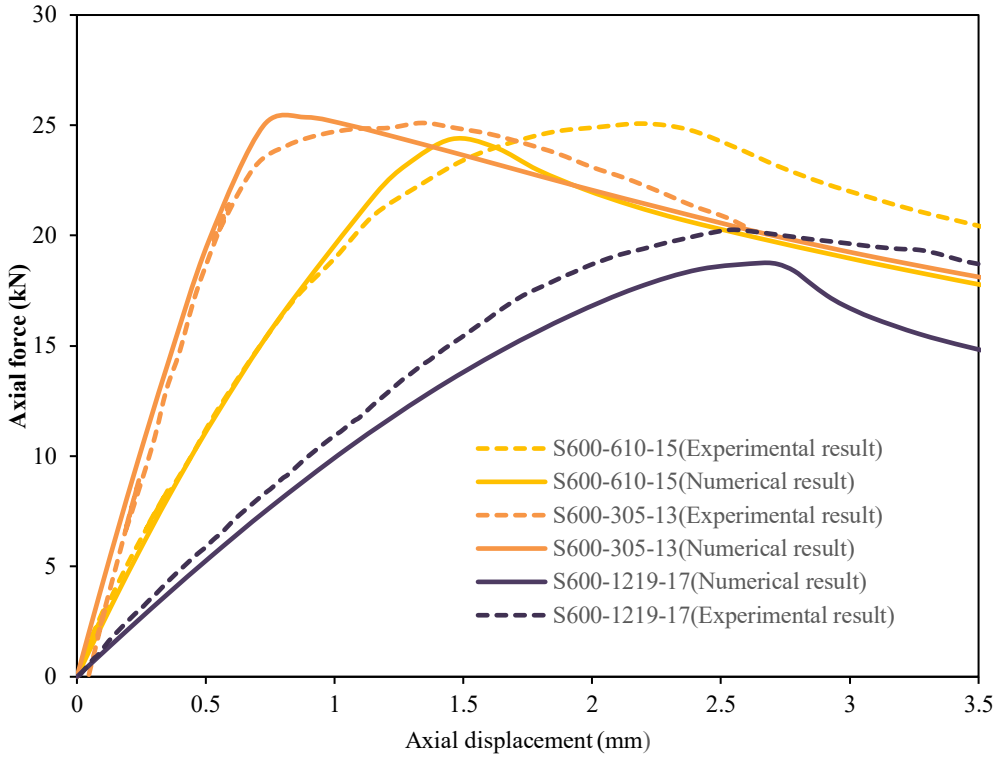

Fig. 4- 7. Axial force-displacement relationship resulting from experimental test against FE models for S600-305-13, S600-610-15 and S600-1219-17

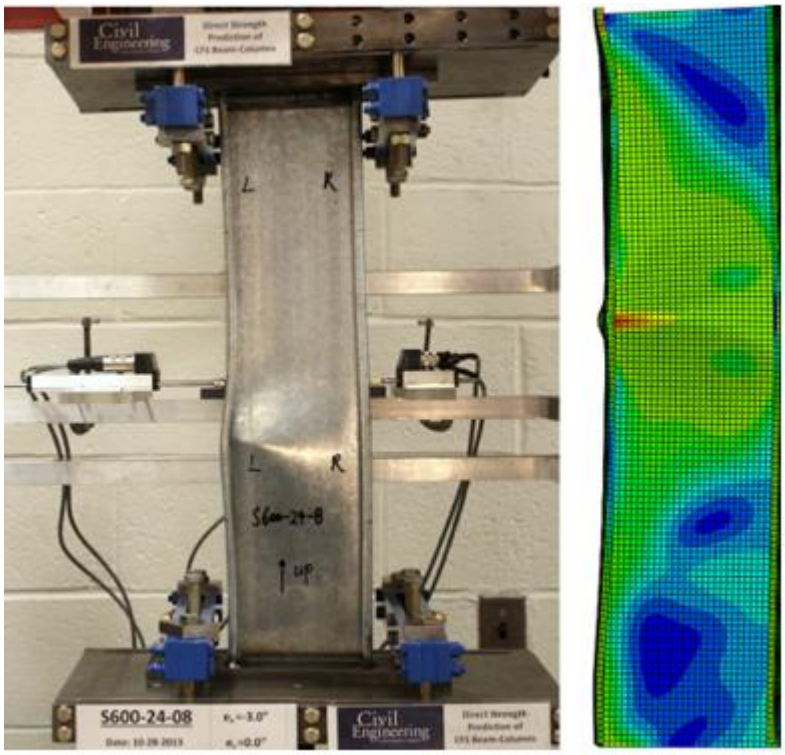

Fig. 4- 8. Failure mode determined by FE model versus experimental (S600-610-8) (test set-up adopted from [118])

4.5 Parametric investigation

4.5.1 General, selected parameters and specimen labelling

An extensive parametric analysis was conducted using the validated FE model. In total, 1134 FE simulations were conducted to examine the influence of various parameters on the axial load capacity of cold-formed steel (CFS) sections with slits under eccentric loading. The study evaluated the effects of several factors, including geometric properties of the channel, slit dimensions, wall thickness, stud length, and different eccentricity values.

The dimensional variables altered during the analyses comprised section depth (D), flange width (B_f), wall thickness (t), slit length (L_{sl}), slit width (W_{sl}), overall member length (L), and eccentricities (e), with detailed values provided in Table 4-2. For all models, the assigned material properties were a yield strength of 500 MPa, Young's modulus of 192 GPa, and Poisson's ratio of 0.3. The findings from the parametric study are summarized in Tables (4-3)–(4-5), while Fig. 4-9 illustrates the specimen labeling system.

Table 4- 2. Details of the parametric study

Axial Compression + Minor axis bending									
fy	D	B_f	B_l	t	L_{sl}	W_{sl}	L	Eccentricity	No of models
(MPa)	(mm)	(mm)	(mm)	(mm)	(mm)	(mm)	(mm)	(mm)	
500	145	45	15	0.6,1.2, 2	60, 90	3, 5,7	500,1000, 1500	10, -10,25, -25,50, -50	324
	200	45	15	0.6,1.2, 2	60, 90	3, 5,7	500,1000, 1500	10, -10,25, -25,50, -50	324
	250	65	15	0.6,1.2, 2	60, 90	3, 5,7	500,1000, 1500	10, -10,25, -25,50, -50	324
Pure Bending									
	145/200/ 250	45/65	15	0.6,1.2, 2	60,90	3,5,7	500,1000, 1500	0	162
							Total		**1134**

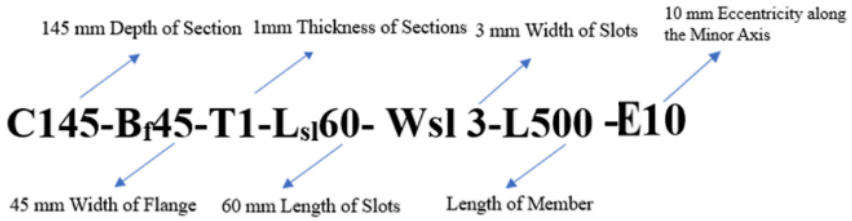

Fig. 4- 9. Labelling of specimens

Table 4- 3. Results from the parametric analysis of C145 slitted channel sections under eccentric loading

FEA results for axial capacity of slitted channel sections, P_{FEA} (kN)																		
L500																		
Specimen	L_{sl}60-E 10			Lsl60-E -10			Lsl60- E 25			Lsl60- E -25			Lsl60- E -50			Lsl60- E 50		
	W_{sl} 3	W_{sl} 5	W_{sl} 7	W_{sl} 3	W_{sl} 5	W_{sl} 7	W_{sl} 3	W_{sl} 5	W_{sl} 7	W_{sl} 3	W_{sl} 5	W_{sl} 7	W_{sl} 3	W_{sl} 5	W_{sl} 7	W_{sl} 3	W_{sl} 5	W_{sl} 7
C145-Bf45-T0.6	19.36	17.80	19.00	13.69	13.48	12.84	10.62	10.60	9.76	9.76	9.57	9.19	5.90	5.64	5.30	6.56	6.42	6.15
C145-Bf45-T1.2	59.68	58.91	62.00	40.34	39.06	37.95	32.34	32.73	33.04	28.32	27.43	26.28	18.28	17.99	17.78	18.99	18.26	17.39
C145-Bf45-T2.0	111.41	112.68	104.97	83.88	81.28	78.72	59.85	58.25	58.97	59.09	57.49	54.83	34.84	34.36	32.93	39.63	38.49	36.64
L1000																		
C145-Bf45-T0.6	13.16	12.62	12.32	10.99	10.85	10.84	7.12	6.89	6.69	8.18	8.12	7.90	4.43	4.16	3.91	5.58	5.47	5.34
C145-Bf45-T1.2	40.12	39.67	37.34	31.37	30.33	29.55	24.38	23.94	21.66	23.22	22.47	22.34	12.45	11.70	10.98	14.76	14.51	14.10
C145-Bf45-T2.0	81.46	79.504	79.956	64.01	61.81	59.07	49.48	47.94	45.20	47.88	45.83	44.21	28.70	27.63	26.26	28.39	26.98	25.24
L1500																		
C145-Bf45-T0.6	10.45	10.45	10.10	8.53	8.48	8.33	6.16	5.66	5.66	6.66	6.46	6.40	3.61	3.57	3.21	4.23	3.72	4.05
C145-Bf45-T1.2	29.36	28.75	28.63	15.55	21.20	20.31	20.27	18.50	17.62	16.57	15.25	15.44	12.07	12.16	10.57	10.82	10.58	9.93
C145-Bf45-T2.0	66.75	64.58	55.33	42.71	40.64	38.16	40.53	39.16	37.11	32.02	30.63	28.89	25.35	24.39	22.92	20.62	19.43	18.05
FEA results for axial capacity of slitted channel sections, P_{FEA} (kN)																		
L500																		
Specimen	L_{sl}90- E 10			Lsl90- E -10			Lsl90- E 25			Lsl90- E -25			Lsl90- E -50			Lsl90- E 50		
	W_{sl} 3	W_{sl} 5	W_{sl} 7	W_{sl} 3	W_{sl} 5	W_{sl} 7	W_{sl} 3	W_{sl} 5	W_{sl} 7	W_{sl} 3	W_{sl} 5	W_{sl} 7	W_{sl} 3	W_{sl} 5	W_{sl} 7	W_{sl} 3	W_{sl} 5	W_{sl} 7
C145-Bf45-T0.6	19.26	16.87	19.51	12.84	12.70	12.56	10.57	10.23	9.46	9.04	8.94	9.01	5.83	5.32	5.21	6.08	6.02	5.91
C145-Bf45-T1.2	56.935	56.12	62.52	38.37	36.86	35.25	31.93	31.57	31.42	26.52	25.68	24.75	17.95	17.72	17.57	17.57	17.00	16.56
C145-Bf45-T2.0	109.72	100.48	107.45	81.75	79.54	76.67	61.69	58.35	56.99	57.56	55.56	53.95	33.66	33.26	33.33	38.02	37.08	36.13
L1000																		
C145-Bf45-T0.6	12.35	11.36	11.53	10.80	10.69	10.15	6.94	6.55	6.28	7.95	7.76	7.32	4.30	4.11	3.73	5.37	5.28	5.03
C145-Bf45-T1.2	36.58	34.79	32.34	30.64	29.18	29.20	21.92	20.54	20.95	22.49	21.18	21.26	11.33	11.11	10.95	14.38	14.14	13.68
C145-Bf45-T2.0	78.40	74.76	74.83	61.46	59.78	56.56	46.89	46.68	42.59	45.57	44.26	42.22	27.14	25.90	24.51	26.55	25.41	24.01
L1500																		
C145-Bf45-T0.6	9.78	9.44	8.73	8.26	8.21	7.76	5.77	5.76	4.97	6.41	5.60	5.91	3.41	3.07	3.07	4.09	3.60	4.01
C145-Bf45-T1.2	29.55	28.45	27.28	20.93	20.23	19.04	17.65	16.70	14.17	16.05	15.53	14.87	11.41	10.25	8.83	11.64	10.17	9.59
C145-Bf45-T2.0	60.37	53.66	45.82	39.98	38.40	35.71	38.74	37.59	35.09	29.86	28.70	27.00	23.54	22.15	20.08	17.29	18.12	15.31

Table 4- 4. Results from the parametric analysis of C200 slitted channel sections under eccentric loading

FEA results for axial capacity of slitted channel sections, P_{FEA} (kN)																		
L500																		
Specimen	L_{sl}60- E 10			Lsl60- E -10			Lsl60- E 25			Lsl60- E -25			Lsl60- E -50			Lsl60- E 50		
	W_{sl} 3	W_{sl} 5	W_{sl} 7	W_{sl} 3	W_{sl} 5	W_{sl} 7	W_{sl} 3	W_{sl} 5	W_{sl} 7	W_{sl} 3	W_{sl} 5	W_{sl} 7	W_{sl} 3	W_{sl} 5	W_{sl} 7	W_{sl} 3	W_{sl} 5	W_{sl} 7
C200-Bf45-T0.6	19.35	19.19	19.11	12.34	12.26	12.31	10.63	10.37	10.25	9.10	9.03	9.12	6.93	6.87	5.71	6.32	6.28	6.32
C200-Bf45-T1.2	68.96	66.92	66.42	39.81	39.07	37.92	34.82	33.80	34.40	28.96	28.07	27.20	19.22	19.22	19.09	19.76	19.16	18.56
C200-Bf45-T2.0	119.7	119.35	121.54	82.95	80.88	78.33	68.12	67.70	67.19	59.59	58.13	56.55	36.60	36.27	35.88	40.14	39.38	38.53
L1000																		
C200-Bf45-T0.6	15.23	15.10	14.11	10.80	10.90	10.55	8.46	8.22	8.33	8.01	7.82	8.05	4.64	4.75	4.55	5.34	5.57	5.23
C200-Bf45-T1.2	48.73	48.01	49.89	31.98	31.28	29.82	29.92	27.67	27.96	23.51	22.96	22.46	15.27	15.00	14.67	14.49	14.25	13.99
C200-Bf45-T2.0	98.886	96.395	95.484	64.45	62.82	60.96	54.67	54.28	53.64	48.14	46.96	45.69	31.08	30.66	30.08	28.27	27.37	26.40
L1500																		
C200-Bf45-T0.6	14.61	13.29	14.05	8.55	8.40	8.17	6.63	6.67	6.63	6.53	6.51	6.32	4.40	4.08	3.84	4.15	4.52	3.58
C200-Bf45-T1.2	33.62	33.54	32.72	23.18	22.42	21.96	22.23	24.52	22.14	17.23	16.80	16.38	13.65	13.34	14.35	9.70	10.52	11.18
C200-Bf45-T2.0	68.804	68.605	68.344	48.06	43.37	42.13	44.87	44.03	43.27	32.66	31.59	30.47	27.43	27.02	26.68	20.58	18.21	17.38
FEA results for axial capacity of slitted channel sections, P_{FEA} (kN)																		
L500																		
Specimen	L_{sl}90- E 10			Lsl90- E -10			Lsl90- E 25			Lsl90- E -25			Lsl90- E -50			Lsl90- E 50		
	W_{sl} 3	W_{sl} 5	W_{sl} 7	W_{sl} 3	W_{sl} 5	W_{sl} 7	W_{sl} 3	W_{sl} 5	W_{sl} 7	W_{sl} 3	W_{sl} 5	W_{sl} 7	W_{sl} 3	W_{sl} 5	W_{sl} 7	W_{sl} 3	W_{sl} 5	W_{sl} 7
C200-Bf45-T0.6	18.90	19.14	19.02	12.16	12.29	11.92	9.83	10.00	9.80	8.87	9.00	8.81	6.88	6.86	5.61	6.40	6.27	6.14
C200-Bf45-T1.2	68.25	63.22	66.05	38.21	36.90	35.95	34.25	34.04	33.69	27.18	26.44	25.90	19.44	19.00	18.87	18.56	18.21	17.69
C200-Bf45-T2.0	115.52	110.51	114.29	77.23	75.72	73.84	68.16	65.35	64.70	55.44	54.35	53.07	35.92	35.63	35.30	37.69	37.03	35.89
L1000																		
C200-Bf45-T0.6	13.80	13.21	12.91	10.43	10.30	10.19	7.78	7.63	7.27	7.88	7.88	7.68	4.89	4.83	4.78	5.19	5.75	5.04
C200-Bf45-T1.2	46.83	46.66	46.25	30.02	30.04	29.30	24.93	25.09	23.80	22.59	22.42	21.81	14.31	13.89	13.90	13.89	13.74	13.42
C200-Bf45-T2.0	88.50	90.67	92.27	60.62	59.50	58.32	53.04	52.66	51.91	45.34	44.55	43.62	29.73	29.26	29.44	26.55	25.78	24.92
L1500																		
C200-Bf45-T0.6	13.97	13.79	13.56	8.25	8.13	7.99	6.65	6.52	7.26	6.32	6.25	6.11	4.11	3.78	3.95	4.04	3.51	3.46
C200-Bf45-T1.2	34.91	32.31	33.17	21.60	21.26	20.95	20.75	21.55	20.08	15.99	15.67	15.50	12.42	12.48	11.84	10.21	8.97	8.71
C200-Bf45-T2.0	75.89	75.22	72.94	41.93	40.08	39.09	43.42	42.76	41.45	30.50	29.60	28.64	27.45	27.44	25.03	19.13	16.81	17.86

Table 4- 5. Results from the parametric analysis of C250 slitted channel sections under eccentric loading

FEA results for axial capacity of slitted channel sections, P_{FEA} (kN)																		
L500																		
Specimen	L_{sl}60- E 10			Lsl60- E -10			Lsl60- E 25			Lsl60- E -25			Lsl60- E -50			Lsl60- E 50		
	W_{sl} 3	W_{sl} 5	W_{sl} 7	W_{sl} 3	W_{sl} 5	W_{sl} 7	W_{sl} 3	W_{sl} 5	W_{sl} 7	W_{sl} 3	W_{sl} 5	W_{sl} 7	W_{sl} 3	W_{sl} 5	W_{sl} 7	W_{sl} 3	W_{sl} 5	W_{sl} 7
C250-Bf65-T0.6	21.06	20.973	20.43	13.96	13.93	14.38	14.79	14.83	14.25	10.93	10.89	11.37	8.66	8.49	8.34	8.07	8.02	8.24
C250-Bf65-T1.2	77.65	76.59	76.29	49.97	48.93	48.30	48.95	48.87	48.88	38.66	37.90	38.14	32.57	32.48	32.49	27.90	27.28	27.62
C250-Bf65-T2.0	152.62	147.10	150.24	111.20	109.52	110.84	106.19	105.92	95.55	85.17	83.59	84.56	60.71	60.46	59.84	60.98	59.89	60.59
L1000																		
C250-Bf65-T0.6	19.81	18.62	18.28	12.94	12.87	12.96	10.10	10.43	10.66	10.18	10.12	10.30	6.85	6.85	7.50	7.56	7.51	7.61
C250-Bf65-T1.2	54.68	54.53	55.49	44.79	44.28	43.49	32.16	33.20	31.93	35.28	34.10	34.75	21.98	21.58	19.98	25.28	24.96	25.30
C250-Bf65-T2.0	122.27	122.78	125.00	96.55	94.49	95.71	78.14	76.47	79.32	74.73	73.42	74.36	46.09	45.78	45.47	53.06	51.72	52.19
L1500																		
C250-Bf65-T0.6	17.68	17.68	17.12	11.41	11.39	11.64	8.97	8.41	8.18	9.11	9.04	9.29	5.54	5.47	4.97	6.56	6.50	7.01
C250-Bf65-T1.2	54.74	53.30	59.86	38.07	37.57	37.33	30.43	28.01	27.98	30.28	29.78	29.71	17.52	17.19	15.59	20.41	20.18	18.55
C250-Bf65-T2.0	90.37	90.21	90.10	79.03	77.07	77.41	65.20	67.36	68.92	62.21	60.69	60.82	37.30	40.43	40.03	45.21	37.78	41.03
FEA results for axial capacity of slitted channel sections, P_{FEA} (kN)																		
L500																		
Specimen	L_{sl}90- E 10			Lsl90- E -10			Lsl90- E 25			Lsl90- E -25			Lsl90- E -50			Lsl90- E 50		
	W_{sl} 3	W_{sl} 5	W_{sl} 7	W_{sl} 3	W_{sl} 5	W_{sl} 7	W_{sl} 3	W_{sl} 5	W_{sl} 7	W_{sl} 3	W_{sl} 5	W_{sl} 7	W_{sl} 3	W_{sl} 5	W_{sl} 7	W_{sl} 3	W_{sl} 5	W_{sl} 7
C250-Bf65-T0.6	20.78	20.75	20.88	13.67	13.56	14.03	14.64	14.27	14.93	10.67	10.52	10.91	8.47	8.33	8.43	7.93	7.93	8.16
C250-Bf65-T1.2	74.93	73.51	74.78	47.73	47.19	47.56	48.92	48.90	48.74	36.98	36.53	36.07	32.49	32.43	32.18	26.79	26.44	26.63
C250-Bf65-T2.0	168.97	171.47	158.13	105.40	103.28	104.56	104.35	95.35	96.23	80.81	79.54	80.52	60.26	60.25	57.73	58.27	57.31	57.61
L1000																		
C250-Bf65-T0.6	18.71	16.12	16.92	12.31	12.34	12.78	10.28	10.49	10.19	9.79	9.78	9.98	6.75	6.71	6.27	7.29	7.41	7.61
C250-Bf65-T1.2	56.04	55.73	53.17	42.41	42.49	43.11	33.65	33.22	32.45	32.96	32.57	33.44	21.00	19.65	20.70	24.11	23.82	24.09
C250-Bf65-T2.0	116.92	117.90	116.27	90.05	89.09	91.06	71.24	70.52	70.38	69.95	69.01	70.58	45.65	43.87	41.39	49.13	48.07	49.45
L1500																		
C250-Bf65-T0.6	14.86	14.52	13.15	10.92	11.31	11.44	8.45	8.23	6.10	8.94	9.02	9.39	4.70	4.92	4.41	6.78	6.72	6.34
C250-Bf65-T1.2	52.96	56.26	59.06	35.99	35.45	35.81	26.66	25.64	25.84	28.61	28.32	29.13	15.85	15.51	13.95	17.48	17.28	17.91
C250-Bf65-T2.0	84.77	84.56	84.81	73.11	72.28	73.77	65.27	63.59	62.92	57.67	56.38	57.74	38.05	37.30	32.22	35.57	34.48	34.72

4.6 Results and discussion

Tables 4-3 to 4-5 present the axial load capacities of CFS channel sections with slitted webs, based on the results obtained from FEA. The axial load capacities of plain sections under eccentric loading is provided in the appendix. The subsequent sub-sections analyze the effects of various parameters, including eccentricity (e), column slenderness ratio (λ_c), depth-to-thickness ratio (D/t), flange width-to-thickness ratio (B_f/t), slit width-to-thickness ratio (W_{sl}/t), depth-to-flange width ratio (D/B_f), and the ratio of slit length to slit width (L_{sl}/W_{sl}), on the axial performance of the sections, as interpreted from the parametric study results.

4.6.1 Effect of eccentricity (E) on the axial capacity of slitted sections under eccentric loading

The eccentricity (E) with respect to the minor axis was varied between ±10 mm and ±50 mm to investigate its effect on the axial capacity of CFS channel sections with slits. As shown in Tables (4-3)–(4-5), the average reduction in axial capacity for eccentricity values of –10 mm, 25 mm, –25 mm, 50 mm, and –50 mm was 22.66%, 36.19%, 42.92%, 68.62%, and 62.24%, respectively. Notably, for an eccentricity of +10 mm, an average increase in axial capacity was observed for the CFS channel sections with slits.

4.6.2 Effect of column slenderness (λ_c) on the axial capacity of slitted sections under eccentric loading λ_c

The influence of column slenderness (λ_c) on the axial strength of slitted CFS channel sections was investigated over a range of 0.36–1.6. For simplicity, the slenderness values used correspond to those of the equivalent plain sections. As illustrated in Figs. 4-10 (a), (b), and (c), local buckling was observed as the predominant failure mode for specimens with lengths ranging from 500 mm to 1500 mm. Fig. 4-11 (a) shows that under a 10 mm eccentricity, axial capacity progressively decreased as λ_c increased from 0.48 to 1.45, with a 19.73% reduction observed between 0.48 and 0.97, and a further 22.44% reduction from 0.97 to 1.45. Under a 25 mm eccentricity, as shown in Fig. 4-11 (b), a similar trend was noted, with axial capacity reducing

by 13.78% as λ_c increased from 0.51 to 1.02, followed by a further 25.18% drop between 1.04 and 1.56. At a higher eccentricity of 50 mm (Fig. 4-11 (c)), axial capacity also declined with increasing slenderness; specifically, a 16.79% reduction occurred as λ_c increased from 0.36 to 0.72, and a further 19.09% drop was recorded from 0.72 to 1.08.

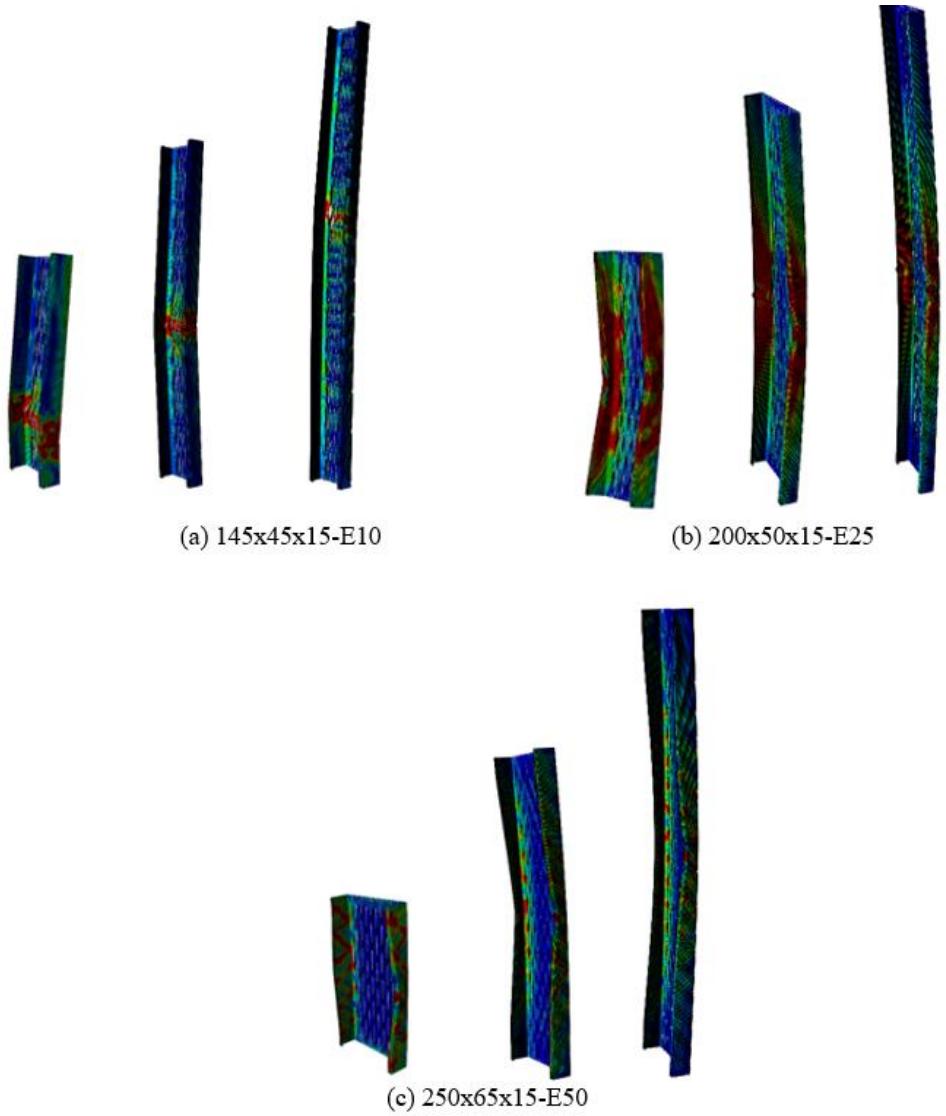

Fig. 4- 10. Failure modes of CFS channel sections with different lengths under varying eccentricities

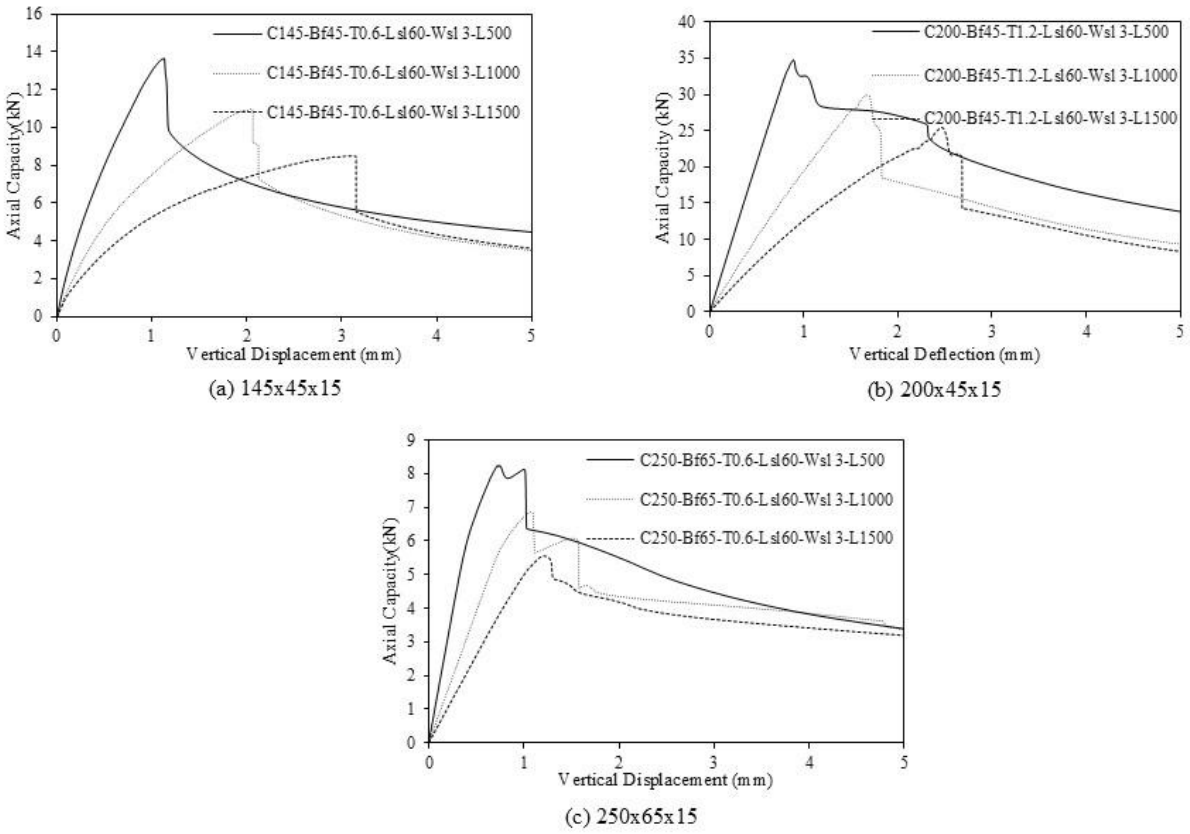

Fig. 4- 11. Axial capacity vs vertical displacement of slitted CFS channel sections

4.6.3 Effect of D/t on the axial capacity of slitted sections under eccentric loading

In Fig.4-12, the effect of the depth-to-thickness ratio (D/t) on the axial capacity of slitted CFS channel sections under minor axis eccentric loading (E = –10 mm) was evaluated for various slenderness ratios (λ_c). For λ_c values between 0.49 and 0.52, increasing the D/t ratio from 120.83 to 166.66 resulted in a 1.31% decrease in axial capacity. However, a further increase to 208.33 led to a 25.50% increase in axial capacity. For λ_c values between 0.99 and 1.04, raising the D/t ratio from 120.83 to 166.66 produced a 1.94% increase, while a subsequent increase to 208.33 resulted in a 40.06% gain in axial capacity. For higher slenderness ratios, λ_c between 1.48 and 1.56, the axial capacity increased by 48.99% as the D/t ratio rose from 120.83 to 166.66, with a further increase to 208.33 yielding a substantial 64.28% improvement. As per Fig. 4-12, the

average overall capacity reductions for the section with slits, compared to the plain section, are 28.59%, 16.41%, and 14.02% for D/t ratios of 120.83, 166.67, and 208.33, respectively

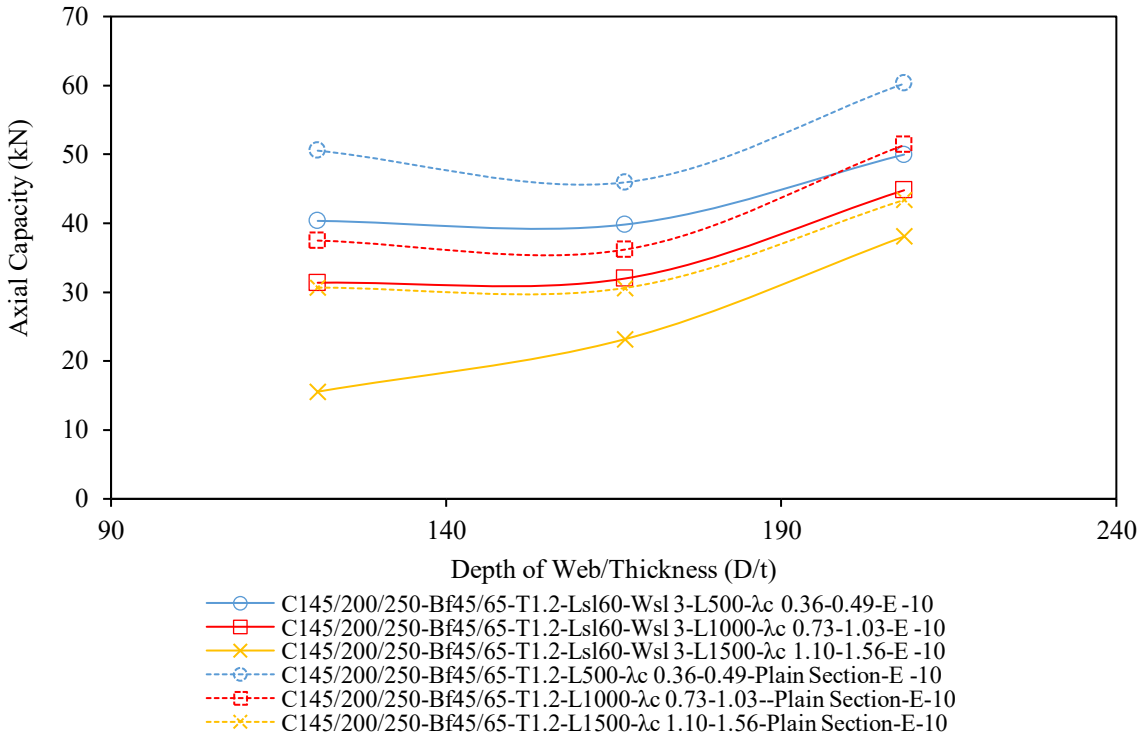

Fig. 4- 12. Influence of depth-to-thickness ratio (D/t) on the axial strength of slitted CFS channel sections

4.6.4 Effect of B_f/t on the axial capacity (P) of slitted sections under eccentric loading

The effect of the flange width-to-thickness ratio (B_f/t) on the axial capacity of CFS channel sections with slits under eccentric loading was investigated using finite element analysis (FEA), as summarised in Tables (4-3)–(4-5) and illustrated in Fig. 4-13. Across the range of column slenderness ratios (λ_c), axial capacity increases consistently as the B_f/t ratio rises from 37.5 to 54.16. For sections with λc between 0.36 and 0.49, a 23.85% increase in axial capacity was observed under minor-axis eccentricity of 10 mm. For λ_c values between 0.73 and 0.99, the axial capacity increased by 42.79%, while a substantial improvement of 144.77% was recorded for λ_c ranging from 1.09 to 1.48. These findings demonstrate the pronounced impact of the B_f/t ratio on the axial performance of slitted CFS channel sections subjected to eccentric loading. In

addition, it can be seen that as per Fig. 4-13, the average overall capacity reductions for the section with slits, compared to the plain section, are 28.58% and 14.02% for B_f/t ratios of 37.5 and 54.17, respectively.

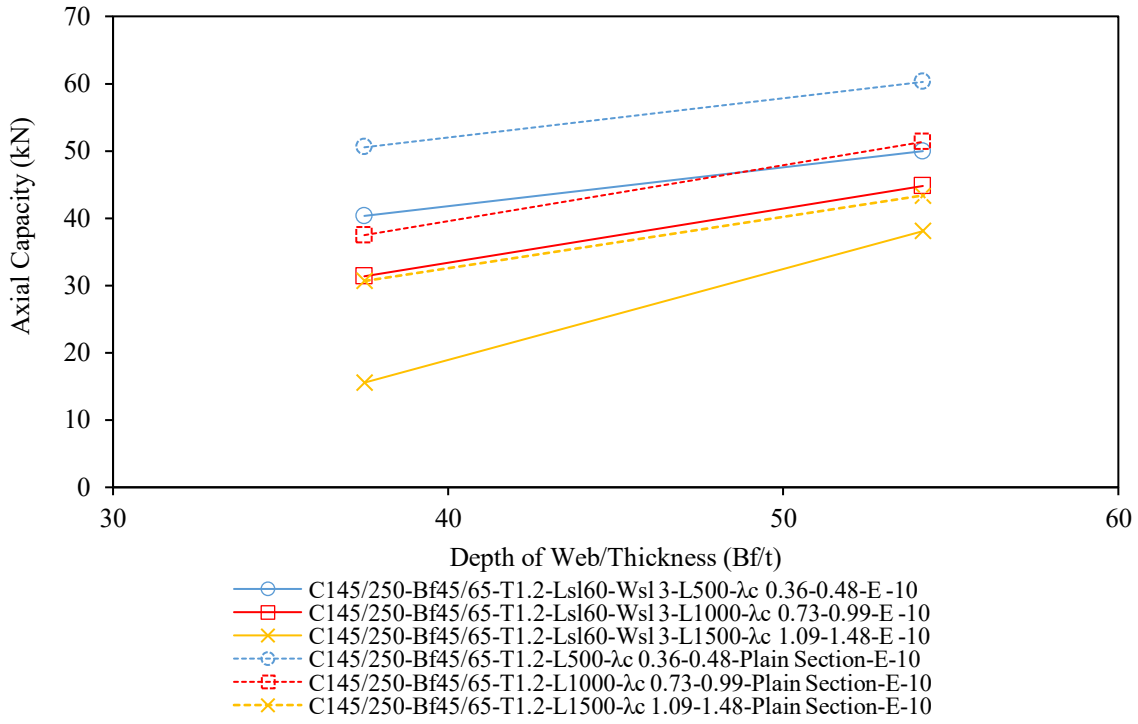

Fig. 4- 13. Influence of flange width-to-thickness ratio (B_f/t) on axial strength of slitted CFS sections under eccentric loading

4.6.5 Effect of D/B_f on the axial capacity (P) of slitted sections under eccentric loading

The effect of the depth-to-flange width ratio (D/B_f) on the axial capacity of CFS channel sections with slits is presented in Tables (4-3)–(4-5) and Fig. 4-14. When the D/B_f ratio increased from 3.22 to 3.85 for λ_c values between 0.49 and 0.37, the axial capacity increased by 23.85% under minor-axis eccentricity of −10 mm. However, a further increase in the D/B_f ratio from 3.85 to 4.44 for λ_c values between 0.52 and 0.37 led to a 20.32% reduction in axial capacity under the same loading condition. For λ_c values between 0.73 and 1.04, increasing the D/B_f ratio from 3.22 to 3.85 resulted in a 42.78% increase in axial capacity, followed by a 28.61% decrease when the ratio was further increased to 4.44. Similarly, for λ_c values between 1.47 and 1.09, the axial

capacity improved significantly by 144.77% as the D/B_f ratio rose from 3.22 to 3.85. However, a subsequent increase to 4.44 for λ_c values between 1.09 and 1.56 resulted in a sharp reduction of 39.12%. These findings indicate that while increasing the D/B_f ratio initially enhances axial performance, excessive increases may adversely affect the load-carrying capacity of slitted CFS channel sections under eccentric loading. In terms of overall capacity reduction for the section with slits compared to the plain section, the values are 28.59%, 14.02%, and 16.41% for D/B_f ratios of 3.22, 3.85, and 4.44, respectively.

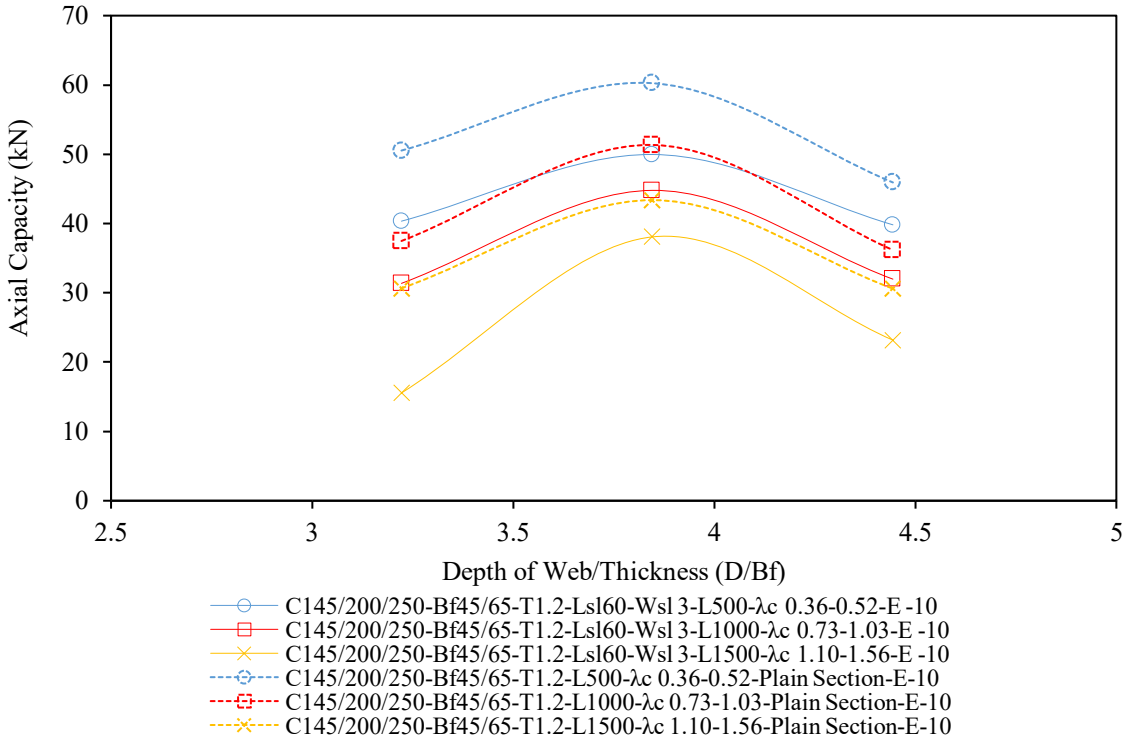

Fig. 4- 14. The influence of the flange width-to-thickness ratio (B_f/t) on axial performance of slitted CFS channel sections under eccentric loading

4.6.6 Effect of W_{sl}/t on the axial capacity (P) of slitted sections under eccentric loading

Tables (4-3)–(4-5) and Figs. 4-15 (a), (b), and (c) collectively present the effects of the slit width-to-thickness ratio (W_{sl}/t) on the axial capacity of different slitted CFS channel sections, based on FEA results. As shown in Fig. 4-15 (a), the C145×45×15 section exhibited reductions in axial capacity of 6.14%, 7.72%, and 10.65% corresponding to λ_c values of 0.504, 1.008, and

1.51, respectively, under minor-axis eccentricity of −10 mm, when the W_{sl}/t changes from 1.5 to 3.5. Similarly, for the C200×45×15 section (Fig. 4-15 (b)), variation of W_{sl}/t from 2.5 to 5.83 resulted in reductions of 4.75%, 6.73%, and 5.23% for λ_c values of 0.51, 1.04, and 1.56, respectively. Similarly, for the C250×45×15 section (Fig. 4-15 (c)), for variation of W_{sl}/t from 2.5 to 5.83, the axial capacity decreased by 3.32%, 2.88%, and 1.94% for λ_c values of 0.51, 1.04, and 1.56, respectively. These results indicate that an increase in the W_{sl}/t ratio generally leads to a reduction in axial capacity, with more pronounced effects observed in shorter sections and at higher slenderness levels, particularly for the C145×45×15 section. The overall capacity reduction for the section with slits compared to the plain section, for the C145X45X15 section, the reductions were 20.28%, 23.18%, and 32.35% for λ_c values of 0.504, 1.008, and 1.51, respectively. For the C200X45X15 section, the reductions were 15.22%, 14.24%, and 26.42% for λ_c values of 0.51, 1.04, and 1.56. Similarly, for the C250X65X15 section, the reductions were 18.56%, 13.94% and 13.18% for the corresponding λ_c values of 0.37, 0.73, and 1.09 respectively.

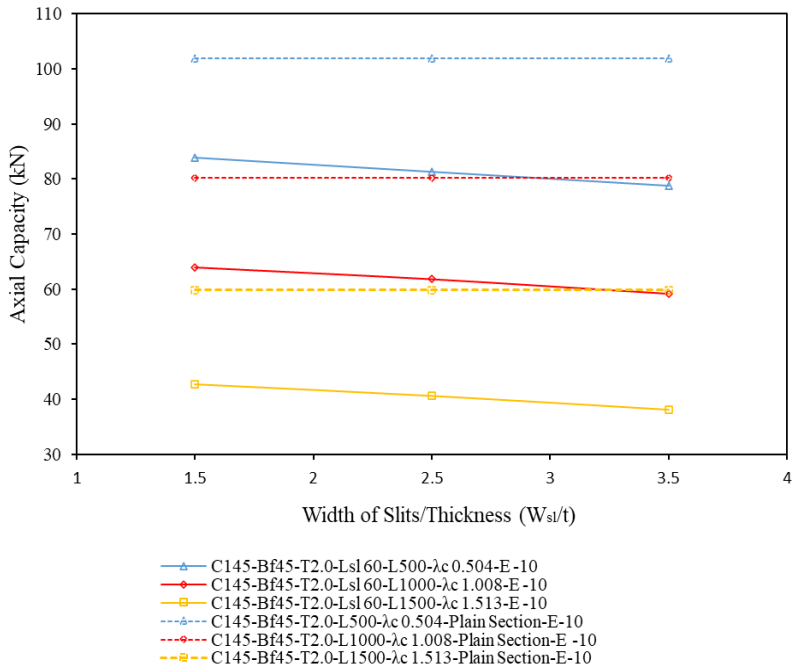

(a)

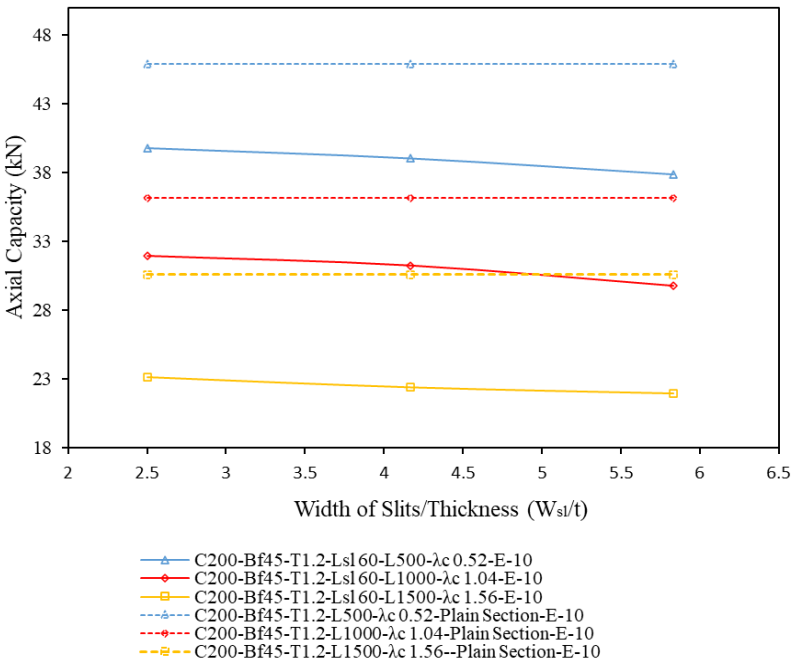

(b)

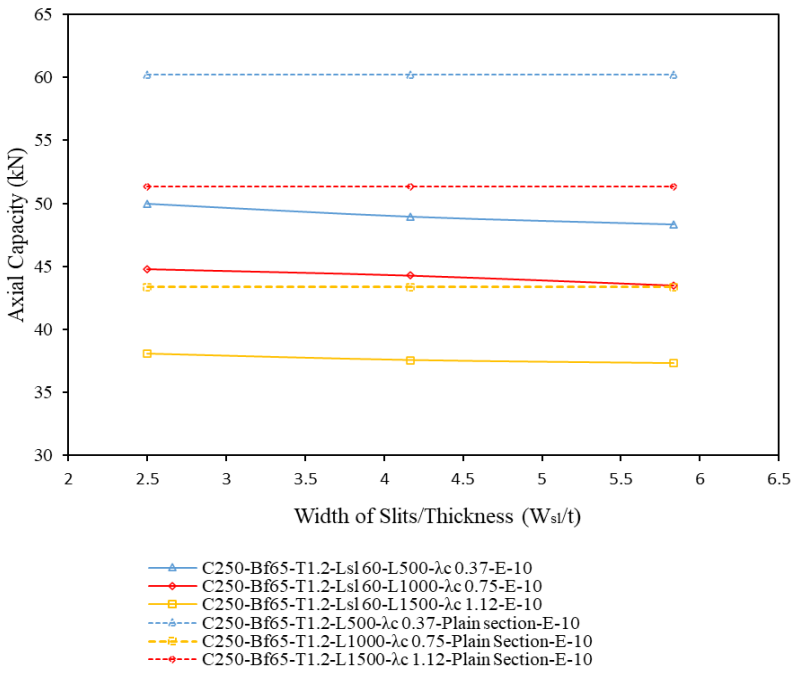

(c)

Fig. 4- 15. Influence of slit width-to-thickness ratio (W_{sl}/t) on axial strength of slitted CFS channel sections under eccentric loading

4.6.7 Effect of L_{sl}/W_{sl} on the axial capacity (P) of slitted sections under eccentric loading

Tables (4-3)–(4-5) and Figs. 4-16 (a)–(c) present the FEA-based axial capacity results of slitted CFS channel sections, showing the influence of the L_{sl}/W_{sl} ratio. For the C145X45X15 sections (Fig. 4-16 (a)),for λ_c value of 0.48,when the L_{sl}/W_{sl} changes from 20 to 30, the axial capacity decreased by 6.22% for minor axis eccentricity (E = -10 mm). For values of 0.97, when the L_{sl}/W_{sl} changes from 20 to 30, the axial capacity decreased by 1.76% for minor axis eccentricity (E = -10 mm). For values of 1.45, when the L_{sl}/W_{sl} changes from 20 to 30, the axial capacity decreased by 3.15% for minor axis eccentricity (E = -10 mm). For the C200X45X15 sections (Fig. 4-16 (b)),for λ_c value of 0.51, when the L_{sl}/W_{sl} changes from 20 to 30, the axial capacity decreased by 1.43% for minor axis eccentricity (Px = -10 mm). For values of 1.02, when the L_{sl}/W_{sl} changes from 20 to 30, the axial capacity decreased by 3.44% for minor axis eccentricity (E = -10 mm). For values of 1.53, when the L_{sl}/W_{sl} changes from 20 to 30, the axial capacity decreased by 3.50% for minor axis eccentricity (E = -10 mm).

C250X45X15 sections (Fig. 4-16 (c)),for λ_c value of 0.37, when the L_{sl}/W_{sl} changes from 20 to 30, the axial capacity decreased by 1.43% for minor axis eccentricity (E = -10 mm). For values of 0.75, when the L_{sl}/W_{sl} changes from 20 to 30, the axial capacity decreased by 2.48% for minor axis eccentricity (E = -10 mm). For values of 1.12, when the L_{sl}/W_{sl} changes from 20 to 30, the axial capacity decreased by 6.56% for minor axis eccentricity (E = -10 mm). The overall capacity reduction for the section with slits compared to the plain section, as the L_{sl}/W_{sl} ratio varied from 20 to 30, varied depending on the section type. For the C145X45X15 section, the reductions were 5.54%, 9.21% and 13.25% for λ_c values of 0.48, 0.96 and 1.45 respectively. In the case of the C200X45X15 section, the reductions were 7.14%, 9.41% and 12.56% for the λc values of 0.51, 1.02 and 1.53 respectively. Similarly, for the C250X65X15 section, the reductions were 18.72%, 20.94% and 20.31% for the corresponding λ_c values of of 0.37, 0.75 and 1.12 respectively.

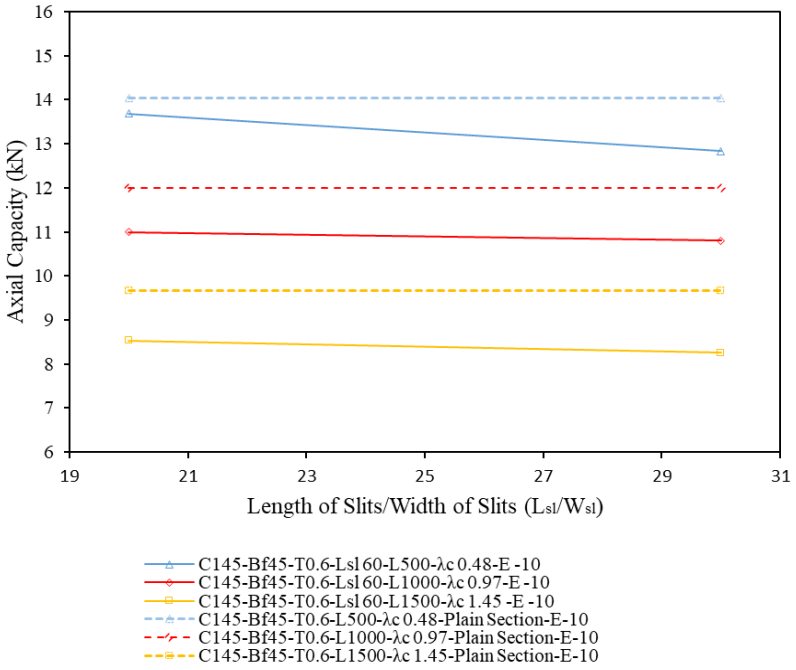
Axial Capacity (kN)
16
15
14
13
12
11
10
9
8
7
6
19
21
23
25
27
29
31
Length of Slits/Width of Slits (Lsl/Wsl)
C145-Bf45-T0.6-Lsl60-L500-λc 0.48-E-10
C145-Bf45-T0.6-Lsl60-L1000-λc 0.97-E-10
C145-Bf45-T0.6-Lsl60-L1500-λc 1.45-E-10
C145-Bf45-T0.6-L500-λc 0.48-Plain Section-E-10
C145-Bf45-T0.6-L1000-λc 0.97-Plain Section-E-10
C145-Bf45-T0.6-L1500-λc 1.45-Plain Section-E-10

(a)

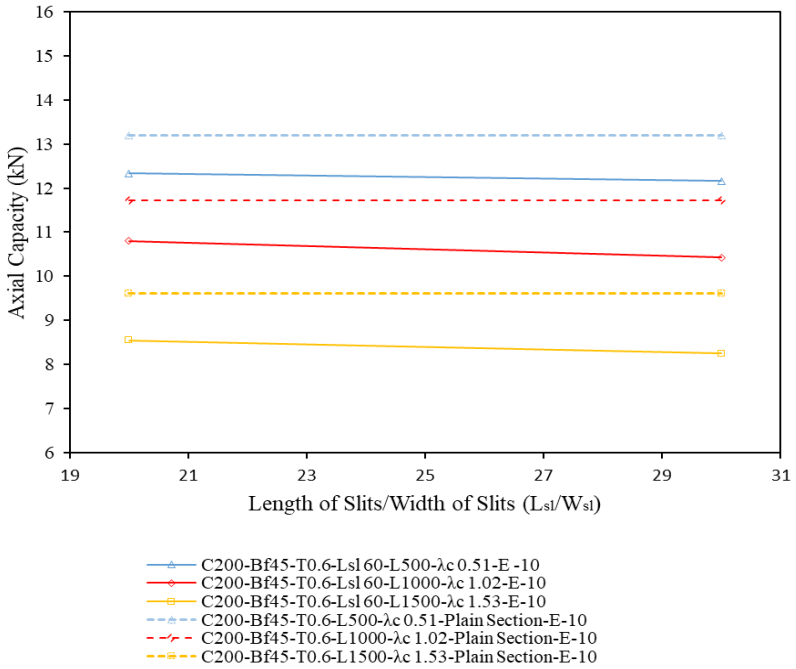
Axial Capacity (kN)
16
15
14
13
12
11
10
9
8
7
6
19
21
23
25
27
29
31
Length of Slits/Width of Slits (Lsl/Wsl)
C200-Bf45-T0.6-Lsl60-L500-λc 0.51-E-10
C200-Bf45-T0.6-Lsl60-L1000-λc 1.02-E-10
C200-Bf45-T0.6-Lsl60-L1500-λc 1.53-E-10
C200-Bf45-T0.6-L500-λc 0.51-Plain Section-E-10
C200-Bf45-T0.6-L1000-λc 1.02-Plain Section-E-10
C200-Bf45-T0.6-L1500-λc 1.53-Plain Section-E-10

(b)

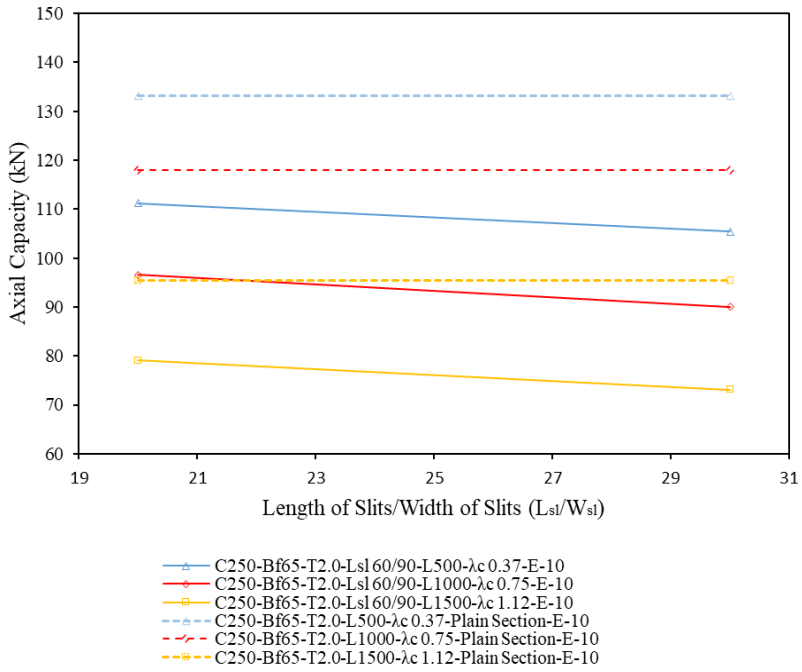

(c)

Fig. 4- 16. Influence slit length-to-width ratio (L_{sl}/W_{sl}) on axial strength of slitted CFS channel sections under eccentric loading

4.6.8 Assessment of beam–columns under minor-axis bending

The behaviour of CFS beam-columns under combined axial load and minor-axis bending was studied using validated FE models, with results shown in Figs. 4.17 (a)–(c). Specimens were grouped by cross-sectional slenderness (D/t) and column slenderness (λ_c). For low D/t sections, design equations were generally conservative at negative eccentricity but showed variability at positive eccentricity. Medium D/t sections exhibited mixed agreement, with tighter clustering near the interaction curve for moderate λ_c values. High D/t sections mostly aligned with design predictions under negative eccentricity but showed significant overestimation under positive eccentricity. Strength deviations ranged from -23.28% to +38.32%, with design equations underestimating strength by approximately 13% for 10–25 mm eccentricities and overestimating by approximately 20% at 50 mm. Results highlight reduced prediction accuracy with increasing slenderness and eccentricity.

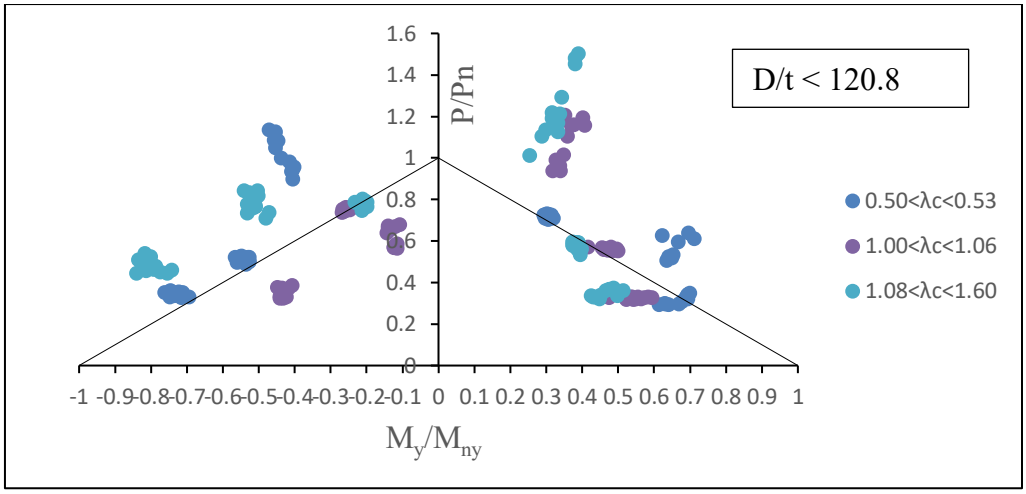

(a)

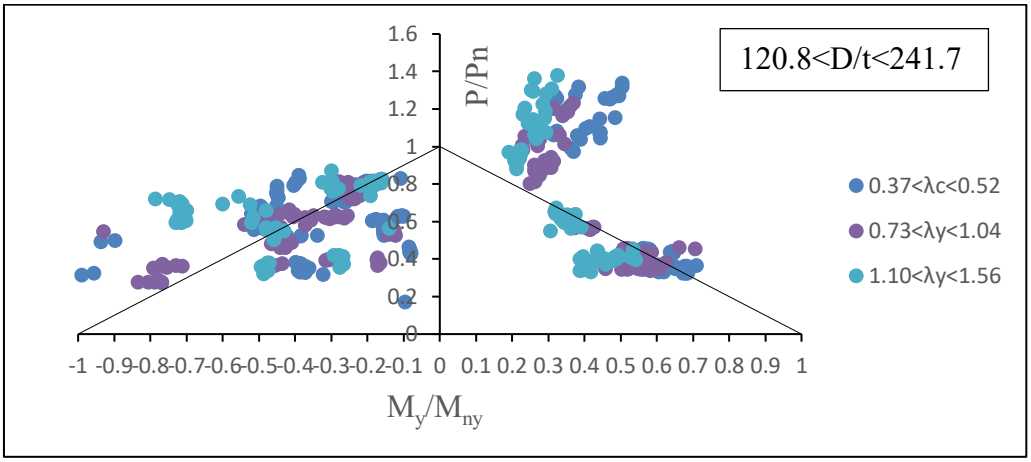

(b)

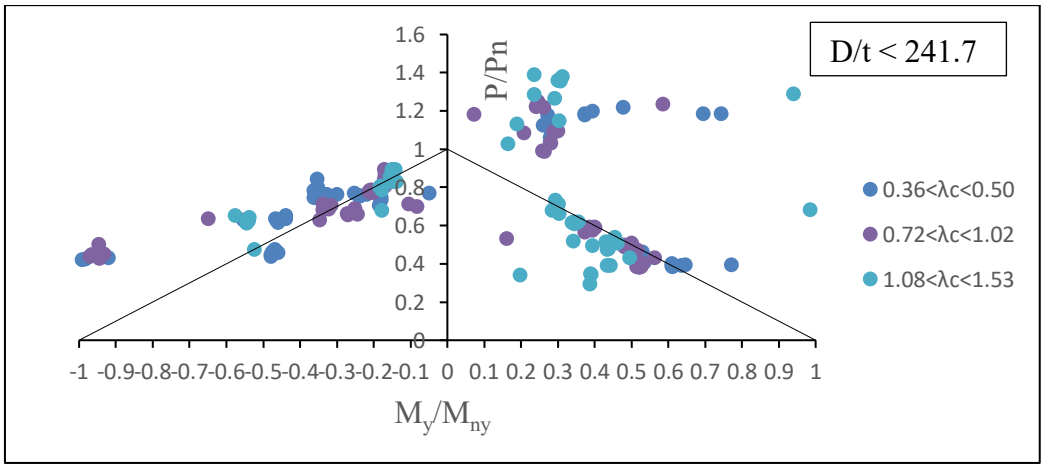

(c)

Fig. 4- 17. Interaction of P/P_n and M_y/M_{ny} for CFS beam–columns with low web slenderness ratio (D/t < 120.8), (120.8<D/t <241.7) and (D/t >241.7).

4.7 Proposed design equations

As noted earlier, the literature contains no design guidelines for evaluating the axial capacity of slitted CFS channels subjected to eccentric loading.

To determine the strength of a member subjected to multiple actions, the typical approach in steel design is to employ an interaction equation. For a CFS member under combined compression and bending actions, a simplified linear interactive equation recommended by AISI S100 [103] (Eq. (1)) and AS/NZS 4600 [101] (Eq. (2)) is generally employed:

$$\frac{P}{P_n} + \frac{M_x}{M_{nx}} + \frac{M_y}{M_{ny}} \leq 1.0 \quad [1]$$

For combined compression and minor axis bending, the equation is transformed to:

$$\frac{P}{P_n} + \frac{M_x}{M_{nx}} \leq 1.0 \quad [2]$$

In this study, a modified interaction equation was proposed to improve the strength predictions of cold-formed steel (CFS) beam–columns with slits. The equation incorporates the influence of key geometric parameters, including the ratios D/t, B_f/t,W_{sl}/t,D/B_f and L_{sl}/W_{sl} . The interaction equation introduces a variable exponent α, which is expressed as a function of these parameters and is tailored for different ranges of column slenderness (λ_c) and eccentricity-to-depth ratios (E/D).

For CFS channel sections with slits,

$$\left(\frac{P}{P_n}\right)^{\alpha} + \left(\frac{M_x}{M_{nx}}\right)^{\alpha} \leq 1.0$$

Where $\alpha = C_0 + C_1(L_{sl}/W_{sl}) + C_2(W_{sl}/t) + C_3(B_f/t) + C_4(D/t) + C_5(D/B_f)$ [3]

The coefficients C_0 to C_5 vary based on the ranges of the slenderness parameter (λ_c) and the eccentricity-to-depth ratio (E/D), as listed below in Table 4-6:

Table 4- 6. Coefficients (C_0, C_1, C_2, C_3, C_4, C_5) corresponding to the parametric equation of α for different ranges of λc

Equation No.	C0	C1	C2	C3	C4	C5	λc Range	E/D Range
4	0.2647	-0.0026	0.0202	-0.0064	-0.0026	0.2163	0.36 < λc < 0.51	-0.15 <E/D < -0.22
5	0.7764	-0.0004	-0.0072	-0.0015	0.0004	0.0563	0.52 < λc < 0.99	-0.15 < E/D < -0.22
6	0.8597	-0.0014	-0.0118	-0.0052	-0.0015	0.0236	1.09 < λc < 1.12	-0.15 < E/D < -0.22
7	0.6697	-0.001	-0.022	0.0047	-0.0013	0.0869	1.45 < λc < 1.60	-0.15 < E/D < -0.22
8	6.135	0.05516	0.00081	-0.1659	0.6	0.00108	0.36 < λc < 0.51	-0.15 < E/D < -0.22
9	7.2044	0.00349	0.024103	0.04348	0.0094	0.685	0.52 < λc < 0.99	-0.15 < E/D < -0.22
10	34.0403	-0.00341	-0.08551	-0.00042	0.03276	-0.00273	1.09 < λc < 1.12	0.15 < E/D < 0.22
11	22.2836	-0.00339	-0.02538	-0.00082	0.01647	-0.00473	1.45 < λc < 1.60	0.15 < E/D < 0.22
12	-1.6951	-0.0067	-0.0441	-0.0448	-0.0113	0.9133	0.36 < λc < 0.51	0.38 < E/D < 0.55
13	-0.8427	0.0008	0.0002	0.00002	-0.0003	0.5314	0.52 < λc < 0.99	0.38 < E/D < 0.55
14	0.3729	-0.0002	-0.0001	-0.00002	-0.0015	0.2522	1.09 < λc < 1.12	0.38 < E/D < 0.55
15	0.1847	-0.00003	-0.0001	-0.00005	-0.0037	0.4657	1.45 < λc < 1.60	0.38 < E/D < 0.55
16	1.15	-0.0049	-0.0188	-0.0031	0.0019	-0.0435	0.36 < λc < 0.51	-0.38 < E/D < -0.55
17	1.0185	-0.0006	0.0017	-0.0009	0.0003	-0.015	0.52 < λc < 0.99	-0.38 < E/D < -0.55
18	1.1509	-0.0049	-0.0188	-0.0031	0.0019	-0.0435	1.09 < λc < 1.12	-0.38 <E/D < -0.55
19	1.0185	-0.006	-0.0003	-0.0009	0.0003	-0.006	1.45 < λc < 1.60	-0.38 < E/D < -0.55
20	1.05	-0.003	-0.0144	-0.0024	0.00002	-0.00003	0.36 < λc < 0.51	-0.77 < E/D < -1.11
21	-0.167	-0.0074	-0.0268	-0.021	-0.0052	0.3544	0.52 < λc < 0.99	-0.77 < E/D < -1.11
22	0.8007	-0.00002	-0.00003	-0.0016	0.0006	-0.00004	1.09 < λc < 1.12	-0.77 < e/D < -1.11
23	1.0289	0.0011	0.0023	-0.0029	-0.0006	-0.0692	1.45 < λc < 1.60	-0.77 < E/D < -1.11
24	-0.2815	0.0005	-0.0083	0.0052	-0.0018	0.3927	0.36 < λc < 0.51	0.77 < E/D < 1.11
25	-0.2512	-0.0005	-0.0069	-0.0037	-0.0008	0.2943	0.52 < λc < 0.99	0.77 < E/D < 1.11
26	0.7067	0.00004	-0.0036	-0.0051	0.0006	-0.0594	1.1 < λc < 1.12	0.77 < E/D < 1.11
27	0.7642	-0.0054	-0.0232	-0.023	-0.001	0.1782	1.45 < λc < 1.60	0.77 < E/D < 1.11

The results of the parametric analysis indicate that the axial load capacity of cold-formed steel (CFS) channel sections with slits is primarily influenced by the geometric ratios D/t, B_f/t, W_{sl}/t, D/B_f, and L_{sl}/W_{sl}. Equations (4) through (14) present the revised design formulations for estimating the axial capacity (P_{prop}) of these slitted sections. According to the FEA results, CFS columns with slenderness ratios (λ_c) between 0.36 and 1.60 exhibited local and distortional buckling under compressive loads. To address these buckling behaviors, modified Direct Strength Method (DSM) equations, as outlined in Equations (4) through (27), were developed to determine the nominal axial strength (P_{prop}) of slitted CFS sections subjected to axial compression in combination with bending about the minor axis.

Fig. 4-18 presents a comparison between the FEA results and the axial capacities predicted by the proposed equations for cold-formed steel (CFS) channel sections with slits under minor-axis bending. The proposed equations align well with the FEA results in estimating the axial capacity of slitted CFS channel sections. Table 4-7 presents a comparison of the mean and COV of the FEA results with the proposed DSM-based design equations for slits. The use of these design equations is limited to the specific ranges, $0.36 < \lambda_c < 0.51$, $0.52 < \lambda_c < 0.99$, $1.08 < \lambda_c < 1.12$, $1.45 < \lambda_c < 1.60$ and $-1.11 < \frac{E}{D} < -0.77$, $-0.55 < \frac{E}{D} < -0.38$, $-0.22 < \frac{E}{D} < -0.15$, $0.15 < \frac{E}{D} < 0.22$, $0.38 < \frac{E}{D} < 0.55$ and $0.77 < \frac{E}{D} < 1.11$.

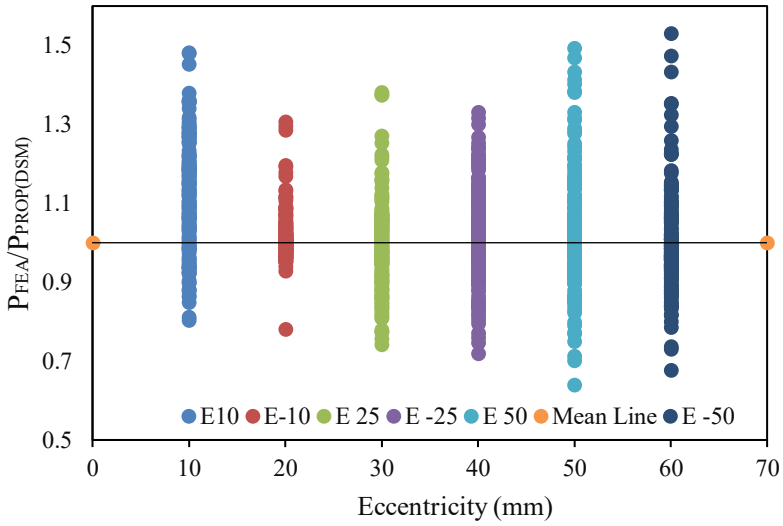

Fig. 4- 18. Comparison of finite element results with predictions from proposed DSM-based design equations for the axial capacity of slitted CFS channel sections

Table 4- 7. Reliability analysis of proposed DSM based equations

Eccentricity	λ_c	Number of data	Coefficient of variation, Vp	Mean, Pm	Resistance factor, φ	Reliability index, β
e-10 (-0.15<E/D<-0.22)	0.36-0.51	42	0.02	0.99	0.85	2.8
e-10 (-0.15<E/D<-0.22)	0.52-0.99	42	0.03	0.99	0.85	2.8
e-10 (-0.15<E/D<-0.22)	1.09-1.12	42	0.02	0.99	0.85	2.8
e-10 (-0.15<E/D<-0.22)	1.45-1.60	36	0.08	1.09	0.85	3.0
e 10(0.15<E/D<0.22)	0.36-0.51	42	0.09	1.12	0.85	3.1
e 10(0.15<E/D<0.22)	0.52-0.99	42	0.14	1.06	0.85	2.6
e 10(0.15<E/D<0.22)	1.09-1.12	42	0.12	1.09	0.85	2.9
e 10(0.15<E/D<0.22)	1.45-1.60	36	0.19	1.18	0.85	2.7
e-25(-0.38<E/D<-0.55)	0.36-0.51	42	0.13	1.02	0.85	2.6
e -25(-0.38<E/D<-0.55)	0.52-0.99	42	0.15	1.06	0.85	2.6
e -25(-0.38<E/D<-0.55)	1.09-1.12	42	0.12	0.98	0.85	2.5
e -25(-0.38<E/D<-0.55)	1.45-1.60	36	0.08	1.05	0.85	2.85
e25(0.38<E/D<0.55)	0.36-0.51	42	0.11	0.98	0.85	2.5
e25(0.38<E/D<0.55)	0.52-0.99	42	0.13	1.004	0.85	2.5
e25(0.38<E/D<0.55)	1.09-1.12	42	0.13	1.008	0.85	2.5
e25(0.38<E/D<0.55)	1.45-1.60	36	0.08	0.99	0.85	2.7
e50(0.77<E/D<1.11)	0.36-0.51	42	0.17	1.07	0.85	2.5
e50 (0.77<E/D<1.11)	0.52-0.99	42	0.11	0.99	0.85	2.5
e50 (0.77<E/D<1.11)	1.09-1.12	42	0.16	1.04	0.85	2.5
e50 (0.77<E/D<1.11)	1.45-1.60	36	0.13	1.01	0.85	2.5

Eccentricity	λ_c	Number of data	Coefficient of variation, Vp	Mean, Pm	Resistance factor, φ	Reliability index, β
e-50 (-0.77<E/D<-1.11)	0.36-0.51	42	0.11	0.98	0.85	2.5
e-50 (-0.77<E/D<-1.11)	0.52-0.99	42	0.13	0.99	0.85	2.5
e-50 (-0.77<E/D<-1.11)	1.09-1.12	42	0.12	1.006	0.85	2.6
e-50 (-0.77<E/D<-1.11)	1.45-1.60	36	0.15	1.04	0.85	2.5

4.8 Reliability analysis

Finally, the accuracy of the proposed design equations for slitted CFS channel sections was assessed through reliability analysis. According to AISI [103], a minimum reliability index (β) of 2.5 is required for CFS members. The parameters used for the analysis are given in Table 4-8. As shown in Table 4-7, the DSM-based formulations provide reliability indices meeting or surpassing the required limit. The reliability analysis conducted in this study follows the calibration procedure outlined in AISI S100 which provides recommended statistical parameters for material properties, fabrication effects, load effects, and model uncertainty and is consistent with approaches adopted in several previous studies [120], [121], [122] involving numerically generated resistance databases. In this framework, the statistical parameters of the proposed equations were derived using the finite element (FE) results as the primary resistance dataset. The parameters adopted for the reliability calculations are summarised in Table 4-8. The mean material factor $M_m = 1.1$accounts for the statistical variability between nominal and actual material strengths of cold-formed steel and reflects the typical ratio of mean yield strength to nominal yield strength reported in experimental studies. The fabrication factor $F_m = 1.0$ represents the mean effect of manufacturing imperfections such as geometric deviations and residual stresses on member strength. The parameter $P_m$represents the mean resistance ratio

obtained from the comparison between the predicted strengths from the proposed design equations and the corresponding finite element (FE) strengths. This parameter therefore captures the model bias associated with the proposed design formulation.

The coefficients of variation used in the reliability calculations represent the uncertainty associated with different sources of variability. Specifically, $V_m = 0.10$ represents the coefficient of variation of material properties, $V_f = 0.05$ represents the variability associated with fabrication and geometric imperfections, $V_q = 0.21$ represents the variability in load effects, and V_p represents the coefficient of variation of the resistance prediction obtained from the statistical analysis of the FE-to-predicted strength ratios. These values are consistent with those recommended in the AISI S100 calibration framework and have been widely adopted in previous reliability studies of cold-formed steel members.

The resistance reduction factor ϕ was calculated using the AISI reliability formulation, which incorporates the mean resistance ratio and the combined coefficient of variation of the governing uncertainties. In this formulation, the combined variability term accounts for the contributions from material variability, fabrication effects, load variability, and model uncertainty. The calibration constant $C = 1.52$ used in the equation corresponds to the reliability calibration factor adopted in the AISI specification for load and resistance factor design (LRFD) calibration. The parameters n and m represent the number of resistance and load data points used in the statistical calibration, respectively, and are included to account for the statistical confidence level of the estimated resistance parameters.

It is nevertheless recognised that the reliability calculations were performed using statistical parameters derived from the FE database without explicitly introducing a separate model bias factor to account for the observed P_{FE}-to-P_{test} deviation. Accordingly, the calculated reliability indices represent the reliability level relative to the validated numerical model rather than directly

to physical test data. While the computed reliability indices satisfy or exceed the AISI target reliability index of β = 2.5 under this formulation, it is acknowledged that incorporation of an explicit experimental model bias correction could influence the absolute reliability level. Further refinement of the reliability calibration using an expanded experimental database is recommended for future investigation.

Table 4- 8. Parameter values used for determination of reliability index as specified by AISI

M_m	F_m	P_m	V_m	V_f	V_q	V_p	C_p	n	m	C	φ
1.1	1	Mean	0.1	0.05	0.21	Coefficient of variation	1.01	42/36	41/35	1.52	0.85

$$\varphi = 1.52 M_m F_m P_m e^{-\beta \sqrt{\{V_m^2 + V_f^2 + C_p V_p^2 + V_q^2\}}} \quad (12)$$

4.8.1 Reliability assessment of worst case scenarios

To identify the most critical configurations, the entire dataset was first sorted in both ascending and descending order based on the strength ratio P_{FEA}/P_{prop}. A value of 1 indicates perfect agreement between the predicted and numerical strengths, values greater than unity correspond to conservative predictions where the design equation underestimates the capacity, and values less than unity represent unconservative predictions. Values on the lower end of the spectrum that is 0.63 to 0.85 and on the higher end of the spectrum 1.25 to 1.53 were taken. A total of 126 cases were included in this subset. The lower bound represents the most unconservative prediction observed in the database, while the upper bound corresponds to the most conservative prediction.

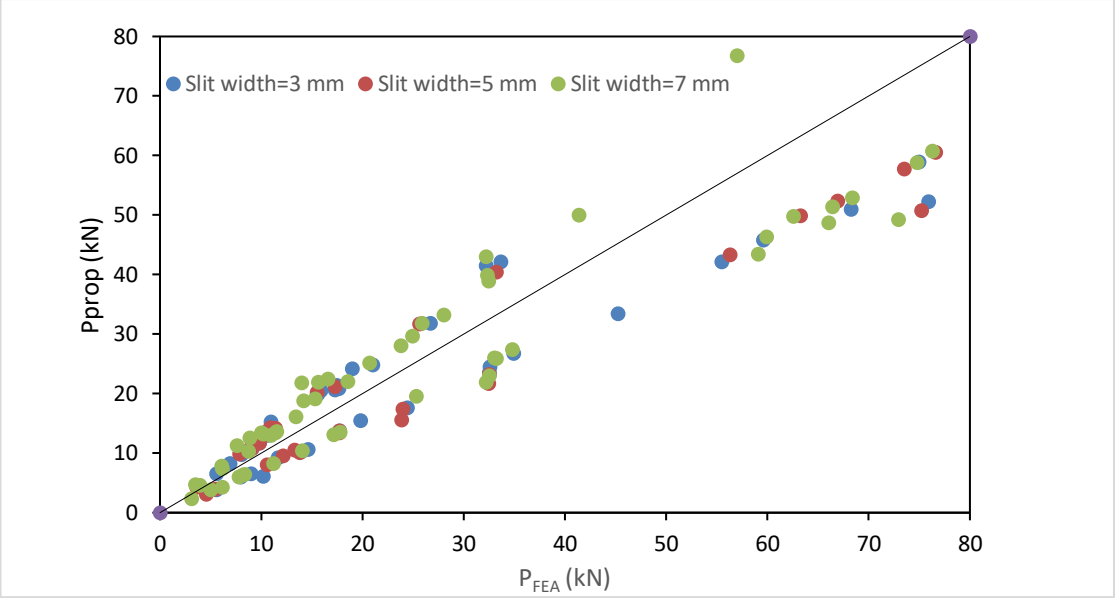

Fig. 4- 19. Comparison of finite element results with predictions from proposed DSM-based design equations for the axial capacity of slitted CFS channel sections using the worst-case dataset

As per Fig. 4-19, when the results are grouped according to slit width, it can be observed that the data points associated with larger slit widths exhibit slightly greater scatter. In particular, the specimens with a slit width of 7 mm tend to show larger deviations compared with those having slit widths of 3 mm and 5 mm. This behaviour is expected since wider slits reduce the effective stiffness of the web and increase stress concentrations around the openings, which may influence the interaction between different buckling modes.

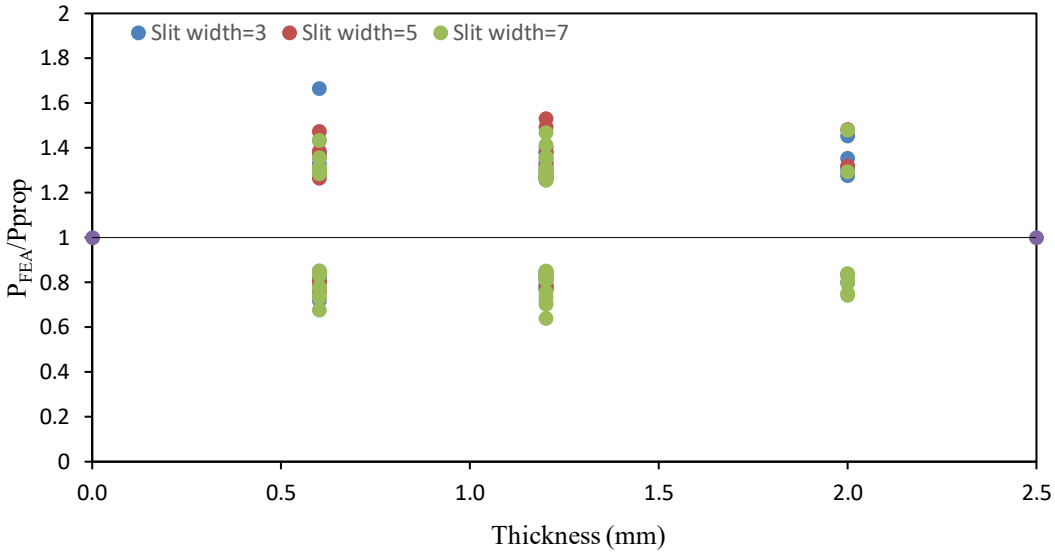

Fig. 4- 20. Comparison of finite element results with predictions from proposed DSM-based design equations for the axial capacity of slitted CFS channel sections using the worst-case dataset

The influence of section thickness on the strength ratio was also examined. The influence of section thickness on the strength ratio was also examined and is illustrated in Fig. 4-20, where the variation of the ratio P_{FEA}/P_{prop} is plotted against section thickness for different slit widths. As observed in the figure, the majority of the worst-case strength ratios are clustered around specimens with thicknesses of 0.6 mm and 1.2 mm, where a wider spread of data points is evident. In contrast, specimens with a thickness of 2.0 mm appear less frequently in the worst-case subset and show comparatively smaller scatter, indicating more predictable behaviour for thicker sections. The increased dispersion of the strength ratios for thinner sections can be attributed to the higher susceptibility of thin cold-formed steel members to local and distortional buckling effects, which intensify the interaction between web perforations and the overall structural response. Consequently, the presence of slits tends to have a

more pronounced influence on the strength predictions for thinner sections, resulting in a larger variation in the ratio P_{FEA}/P_{prop} .

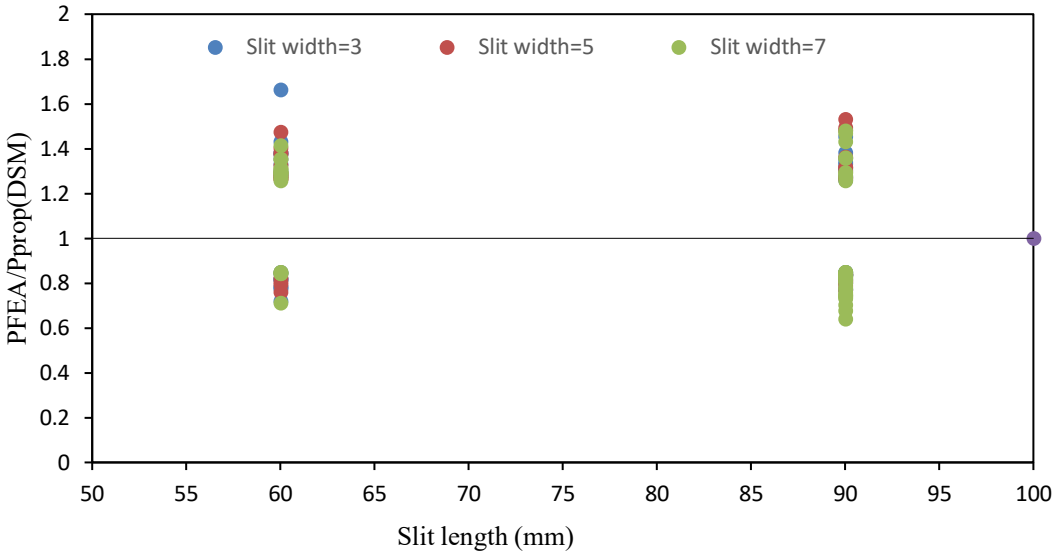

Fig. 4- 21. Comparison of finite element results with predictions from proposed DSM-based design equations for the axial capacity of slitted CFS channel sections using the worst-case dataset

The effect of slit length on the prediction accuracy was also investigated for the two slit lengths considered in the parametric study, namely 60 mm and 90 mm. The results show that both slit lengths produce similar ranges of strength ratios. However, slightly greater scatter is observed for members with a slit length of 90 mm. This behaviour can be attributed to the larger reduction in web stiffness associated with longer slits, which may increase the sensitivity of the structural response to buckling interactions.

4.9 Conclusion

This chapter investigates the axial capacity of slitted CFS channel sections subjected to axial compression and eccentric loading through minor axis bending with slits using FEA. Initially, FE models were developed and validated against the experimental results reported by Torabian

et al [118] and Andreassen and Jönsson [3], demonstrating close agreement in ultimate axial capacity and failure behavior.

Subsequently, a comprehensive parametric investigation involving 1134 FE models was carried out to assess how the geometric ratios as *D/t, B_f/t, W_{sl}/t, D/B_f, and L_{sl}/W_{sl}* influence the axial capacity of CFS channel sections with plain and slitted webs.

The following conclusions can be drawn from this study:

(1) The parametric study revealed that the ratios *D/t, B_f/t, W_{sl}/t, D/B_f, and L_{sl}/W_{sl}* significantly affect the axial capacity of slitted CFS channel sections under axial compression and minor-axis bending.

(2) When the numerical simulation results were compared with design strengths obtained from AISI (2016) [103] and AS/NZS (2018) [101], the results showed that, in the case of slitted CFS channel sections, the design equations underestimated the strengths by approximately 13% at eccentricities between 10 mm and 25 mm, whereas they overestimated the strengths by around 20% at 50 mm eccentricity.

(3) DSM-based design equations that include capacity-reduction factors were formulated to predict the axial capacity of slitted CFS channel sections, valid within the ranges of $0.36 < \lambda_c < 0.51$, $0.52 < \lambda_c < 0.99$, $1.08 < \lambda_c < 1.12$, $1.45 < \lambda_c < 1.60$ and $-1.11 < \frac{E}{D} < -0.77$, $-0.55 < \frac{E}{D} < -0.38$, $-0.22 < \frac{E}{D} < -0.15$, $0.15 < \frac{E}{D} < 0.22$, $0.38 < \frac{E}{D} < 0.55$ and $0.77 < \frac{E}{D} < 1.11$.

(4) The reliability analysis demonstrated that the proposed DSM modifications satisfy reliability requirements, with β values of 2.5 and above.

Chapter 5 Thermal performance of cold-formed steel channel sections with slits

5.1 Introduction

As discussed in the earlier chapters, the insertion of slits increases the heat-flow path, thereby enhancing thermal performance compared to solid-web sections. This chapter examines the influence of channel dimensions, slit sizes, section thicknesses, and stud lengths on the heat flux of cold-formed steel wall panels.

5.2 Description of the thermal modelling

5.2.1 General

A three-dimensional steady-state heat-transfer model was developed in COMSOL using the heat transfer in solids interface. The wall-panel assembly was represented as a layered 3D block and discretised with a fine free tetrahedral mesh to capture the geometry accurately. A uniform reference temperature was defined for the domain, while all non-exposed faces were assigned thermal insulation boundary conditions. On the exterior surface, an outdoor air temperature of $T_{ext} = -5°\text{C}$was prescribed with a natural-convection heat transfer coefficient of $h_{ext} = \frac{1}{0.03} = 33.33\ \text{W}/(\text{m}^2 \cdot \text{K})$., as recommended by ASHRAE [123] guidelines. On the interior surface, a constant indoor air temperature of $T_{int} = 20°\text{C}$ was applied with a corresponding convective heat transfer coefficient of $h_{int} = \frac{1}{0.12} = 8.33\ \text{W}/(\text{m}^2 \cdot \text{K})$. The coefficients are taken from Table 10 from chapter 26 of ASHRAE [123] guidelines. The exterior value corresponds to a winter wind condition (high external convection). The governing heat-conduction equation was solved under steady-state conditions to obtain the temperature distribution and through-panel heat flux, allowing comparison of thermal performance across different geometric and material configurations.

5.2.2 Material properties

The thermal properties of the wall assembly components were assigned in COMSOL Multiphysics based on tabulated values from ASHRAE[123]. Each material was defined by its density, thermal conductivity, and specific heat capacity, as summarised in Table 5-1. Configuration of the wall panel is shown in Fig 5-1.

Table 5- 1-Summary of material properties

Material	Density (kg/m^3)	Heat Capacity (J/(kg.k)	Thermal Conductivity
Cold formed steel	7850	460	50.4
Stucco	1858.15	837.36	0.72
Mineral wool (Exterior rigid board insulation)	160.19	837.36	0.04
Gypsum sheathing	656.76	879.23	0.16
Fiberglass Batt Insulation	8.17	837.6	0.05

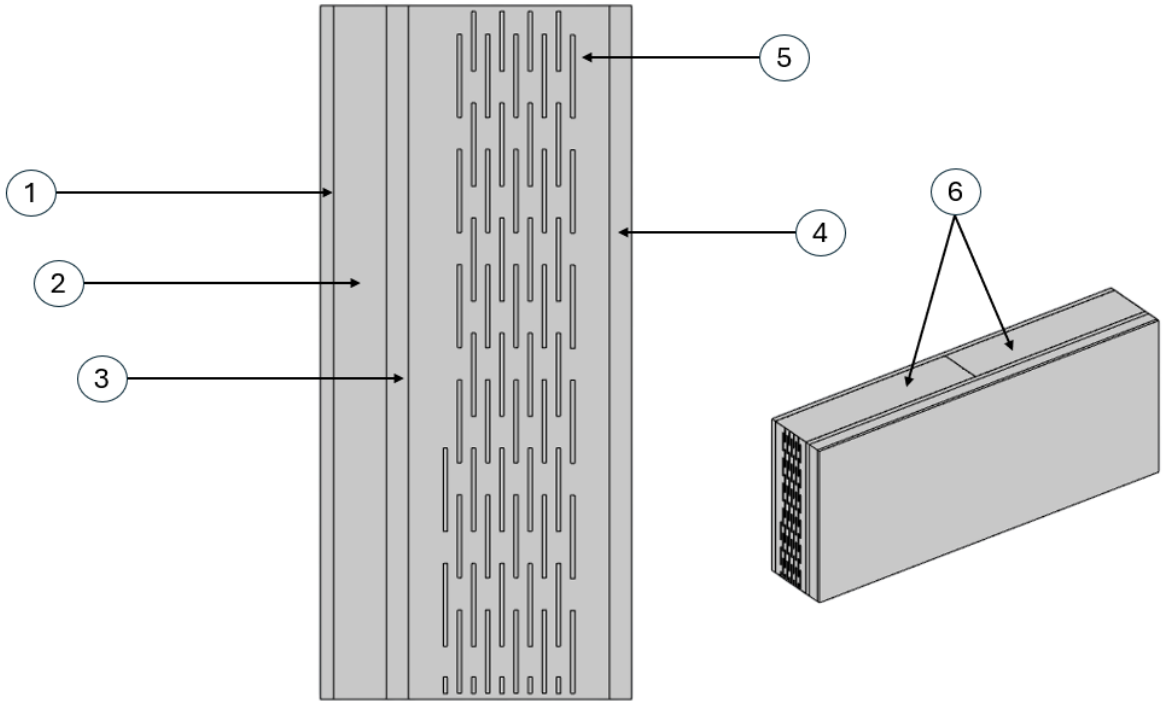

Fig. 5- 1 Configuration of wall panels with CFS sections with slits

5.2.3 Meshing

The finite element discretisation of the wall assembly was carried out using a tetrahedral

mesh generated in COMSOL as shown in Fig.5-2. A predefined fine mesh calibration was adopted to balance computational accuracy and efficiency. The mesh parameters were set with a maximum element size of approximately 100 mm and a minimum element size of 10 mm, with a growth rate below 1.5 to ensure smooth element transition. The curvature factor and resolution of narrow regions were adjusted to adequately capture the geometric details of the thin-walled steel sections and insulation interfaces.

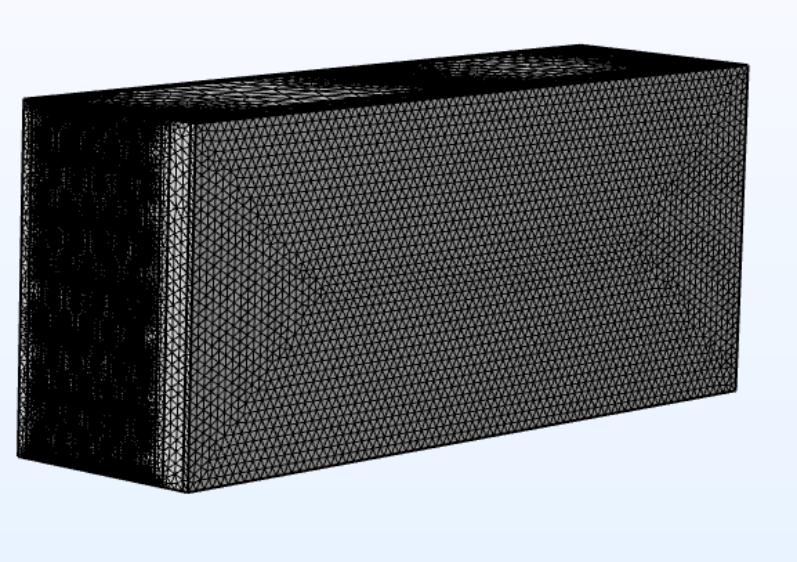

Fig. 5- 2 Details of the FE meshing

5.2.4 Boundary and loading conditions

The thermal performance of the cold-formed steel (CFS) wall assembly was investigated under steady-state conditions by applying appropriate boundary and loading parameters in COMSOL Multiphysics. A convective heat flux boundary condition was assigned to the exterior surface of the wall to simulate outdoor exposure. The lateral edges of the model were thermally insulated to ensure one-dimensional heat transfer through the thickness of the wall system.

The steady-state thermal analysis was conducted by solving the governing heat transfer equation across all domains, considering the interaction between different layers of materials (steel, insulation and sheathing). This boundary and loading configuration allowed for the evaluation of heat flux distribution and the effective thermal resistance of the CFS wall assembly with slits.

5.3 Parametric study

5.3.1 General and chosen parameters

A total of 63 steady-state heat-transfer models were developed in COMSOL to examine how geometry and material parameters influence the thermal performance of CFS wall studs with slits. The dimensional parameters varied during the analysis included section depth (D), flange width (B_f), thickness (t), slit length (L_{sl}), slit width (W_{sl}) and length (L), the details of which are given in Table 5-2.

Table 5- 2 Parametric study details

D	B_f	B_l	t	L_{sl}	W_{sl}	L	No of models
(mm)	(mm)	(mm)	(mm)	(mm)	(mm)	(mm)	
145	45	15	0.6	0,60, 90	0,3,5,7	500,1000, 1500	21
200	45	15	0.6	0,60, 90	0,3,5,7	500,1000, 1500	21
250	65	15	0.6	0,60, 90	0,3,5,7	500,1000, 1500	21
						Total	63

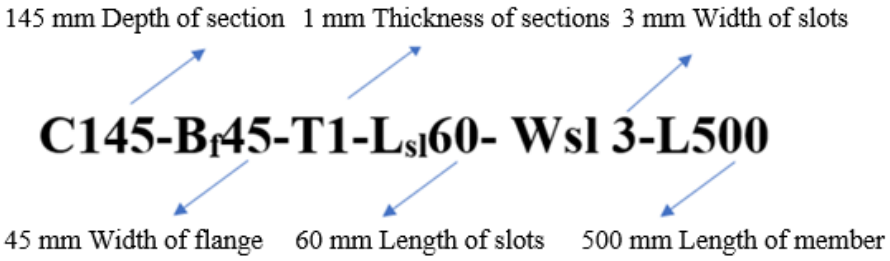

Fig. 5- 3 Specimen labelling

Table 5- 3 Heat Flux Values (W) of the Parametric Study for C145/200/250 Channel Sections with Slits

Specimen	Plain section	L_{sl} 60			L_{sl} 90		
		W_{sl} 3	W_{sl} 5	W_{sl} 7	W_{sl} 3	W_{sl} 5	W_{sl} 7
C145-B_f45-T0.6-L500	4.77	4.01	3.91	3.84	3.87	3.82	3.79
C145-B_f45-T0.6-L1000	9.52	7.99	7.79	7.60	7.61	7.59	7.51
C145-B_f45-T0.6-L1500	14.28	11.94	11.75	11.19	11.56	11.33	11.23
C200-B_f45-T0.6-L500	4.07	3.40	3.30	3.25	3.28	3.20	3.15
C200-B_f45-T0.6-L1000	8.16	6.72	6.61	6.46	6.45	6.33	6.25
C200-B_f45-T0.6-L1500	12.26	10.11	9.88	9.7	9.78	9.56	9.40
C250-B_f65-T0.6-L500	3.71	3.02	2.97	2.87	2.89	2.85	2.80
C250-B_f65-T0.6-L1000	7.4	6.05	5.90	5.81	5.68	5.60	5.54
C250-B_f65-T0.6-L1500	11.14	8.97	8.76	8.72	8.49	8.47	8.33

5.4 Results and discussion

Table 5-3 represents the heat flux of wall panels having CFS channel sections with slits, as obtained from the COMSOL simulations. The following subsections analyse the influence of the non-dimensional parameters including D/t, B_f/t, W_{sl}/t, D/B_f, and L_{sl}/W_{sl} on the heat flux of wall panels having CFS channel section with slits, with insights drawn from the results of the parametric study. Sections 5.4.1 to 5.4.5 examine the effects of the above parameters on the heat flux of specifically wall panels incorporating slitted CFS sections. Section 5.4.6 provides an overall comparison of how the introduction of slits influences the heat flux of these wall panels relative to panels with plain CFS channel sections. A representative 3-D COMSOL model of wall panels having C145 CFS channel sections with slits are shown in Fig. 5-4.

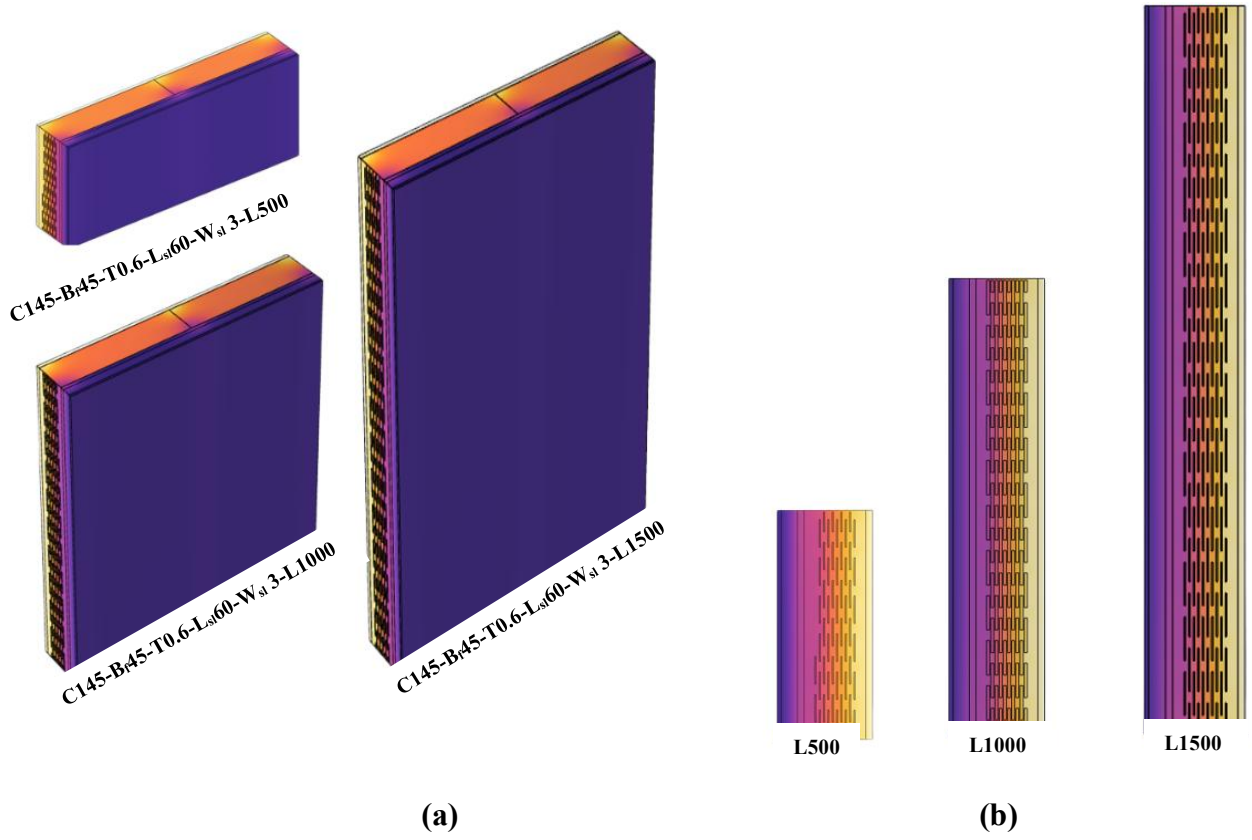

Fig. 5- 4 (a)3-D COMSOL model of wall panels having CFS channel sections with slits (b)Side Elevation of 3-D COMSOL model of wall panels having CFS channel sections with slits

5.4.1 Influence of D/t on the heat flux of wall panels consisting of sections with slits

The effect of the *D/t* ratio on the heat flux of wall panels having CFS channel sections with slits is detailed in Table 5-3 and results are depicted in Fig. 5-5. FEA (Fig. 5-5) revealed that the heat flux of the wall panels having CFS slitted sections with slit length of 60 mm as studs decreased by an average of 15.48% when the *D/t* ratio increased from 241.67 to 333.33. When the *D/t* ratio further increased from 333.33 to 416.67, heat flux of the wall panels with sections having slits saw an average decrease of 10.81%. For CFS slitted sections with slit length of 90 mm as studs, the heat flux decreased by an average of 15.25% when the *D/t* ratio increased from 241.67 to 333.33. When the *D/t* ratio further increased from 333.33 to 416.67, heat flux of the wall panels with sections having slits saw an average decrease of 11.71%.

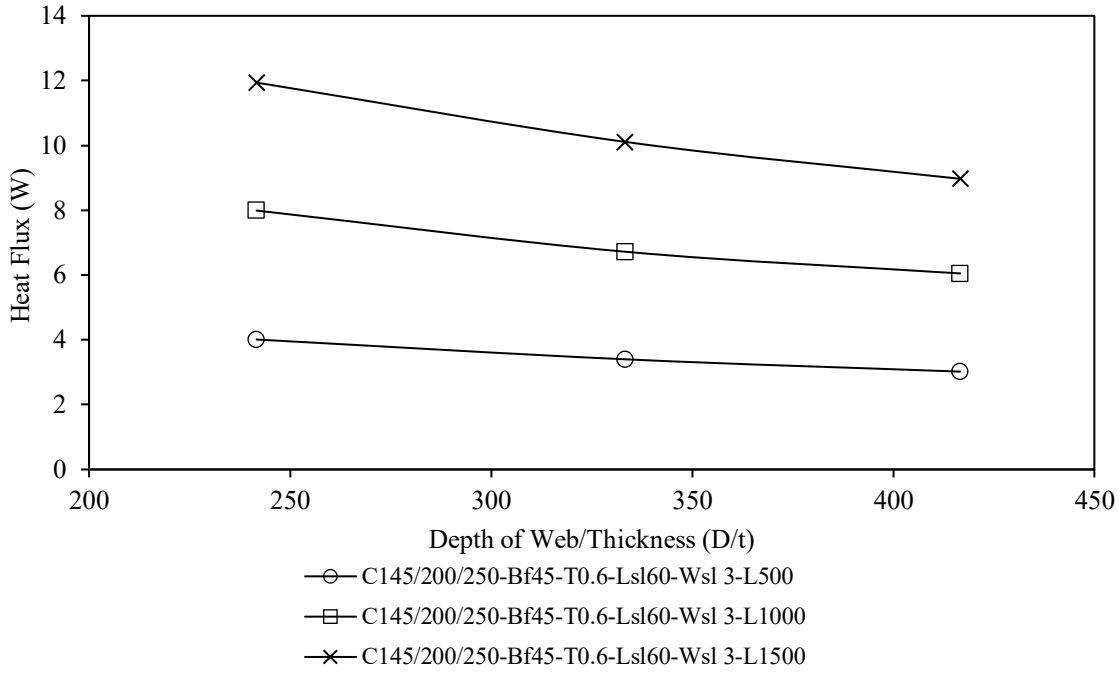

(a)

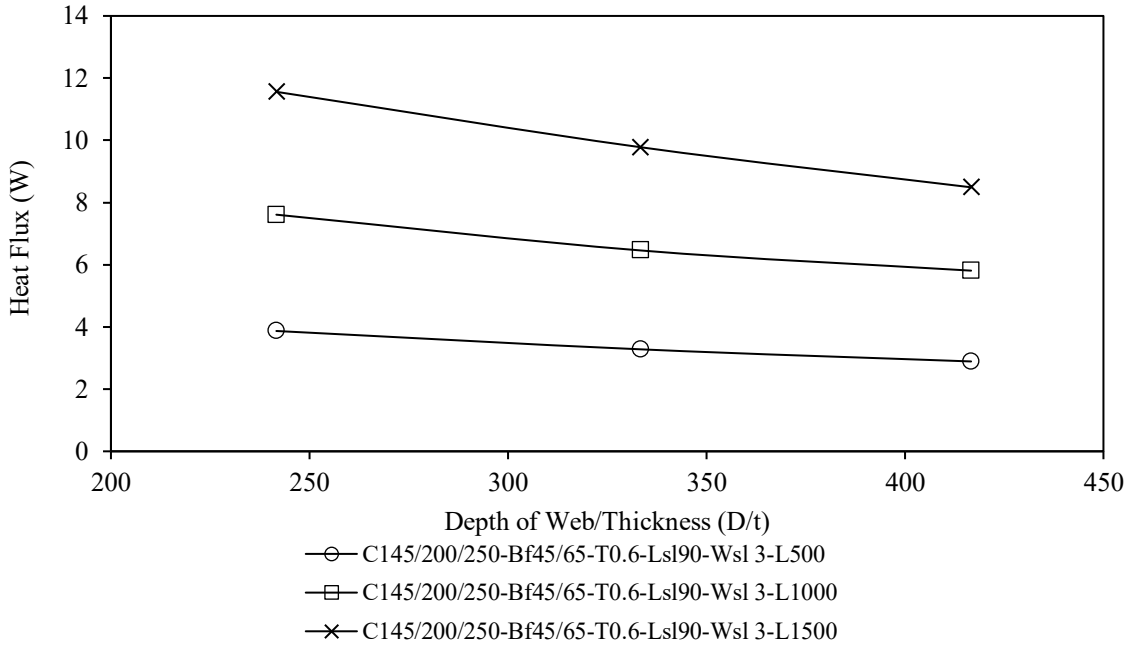

(b)

Fig. 5- 5 Effect of D/t on the heat flux of wall panels having CFS channel sections with slits for a) L_{sl} =60 and b) L_{sl}=90

5.4.2 Effect of B_f/t on the on the heat flux of wall panels consisting of sections with slits

The effect of the Bf/t on the heat flux of wall panels having CFS channel sections with slits is detailed in Tables 5-3 and results are shown in Fig. 5-6, according to results obtained from FEA. The data (Fig. 5-6) shows a reduction in heat flux associated with an increase in the B_f/t ratio from 75 to 108.33 across varying levels of slenderness (λ_c). For CFS slitted sections with a 60 mm slit length, heat flux decreased by 24.69%, 24.28%, and 24.87% for λ_c ranges of 0.36–0.48, 0.72–0.97, and 1.08–1.45, respectively. For sections with a 90 mm slit length, the corresponding decreases were 25.32%, 25.36%, and 26.56%.

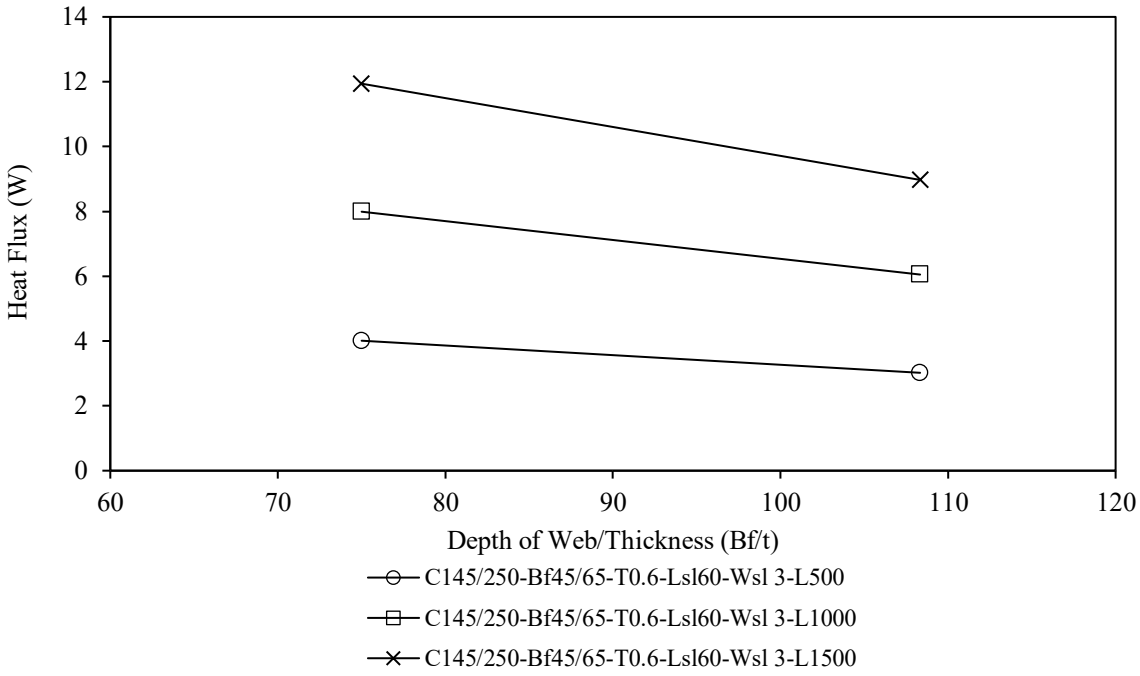

(a)

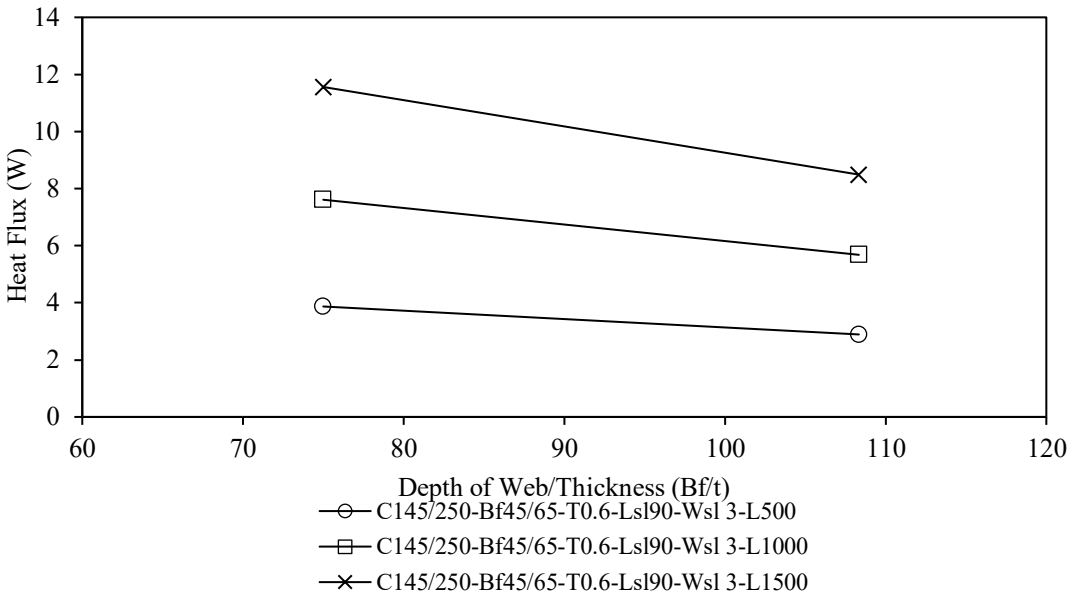

(b)

Fig. 5- 6 Effect of B_f/t on the of wall panels having CFS channel sections with slits for a) L_{sl} =60 and b) L_{sl}=90

5.4.3 Effect of D/Bf on the heat flux for sections with slits

The effect of the D/B_f ratio on the heat flux of wall panels having CFS channel sections with slits is shown in Tables 5-3 and depicted in Fig. 5-7. For CFS wall panels with 60 mm slits, heat flux decreased by an average of 24.61% as the D/B_f ratio rose from 3.22 to 3.85, but then increased by 12.12% when the ratio was further increased to 4.44. Similarly, for panels with 90 mm slits, heat flux decreased by 25.74% between D/B_f ratios of 3.22 and 3.85, followed by an 13.38% decrease when the ratio reached 4.44.

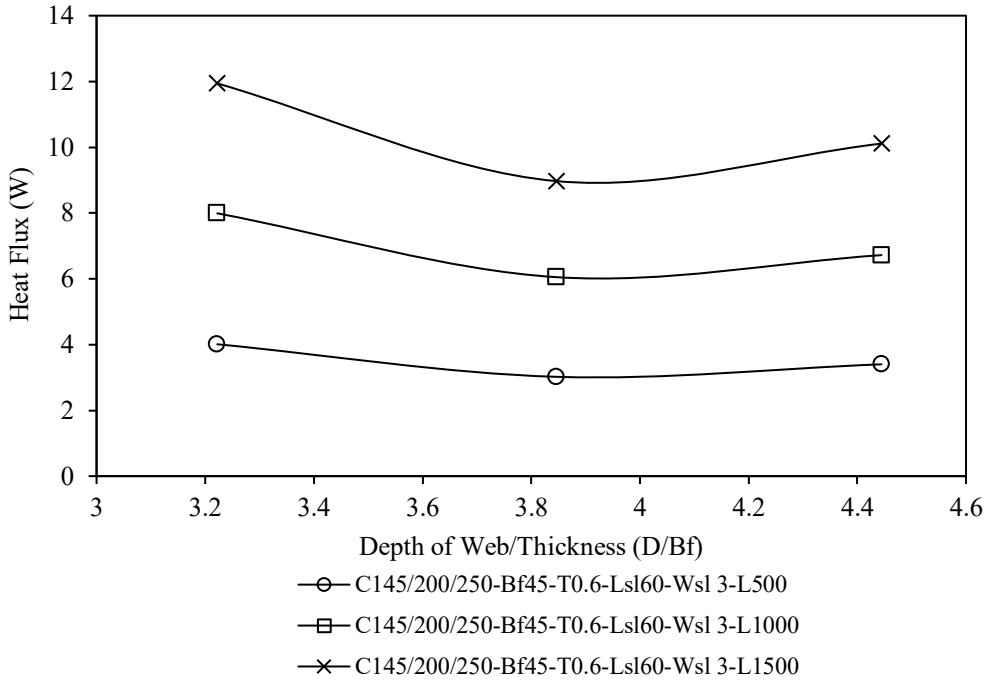

(a)

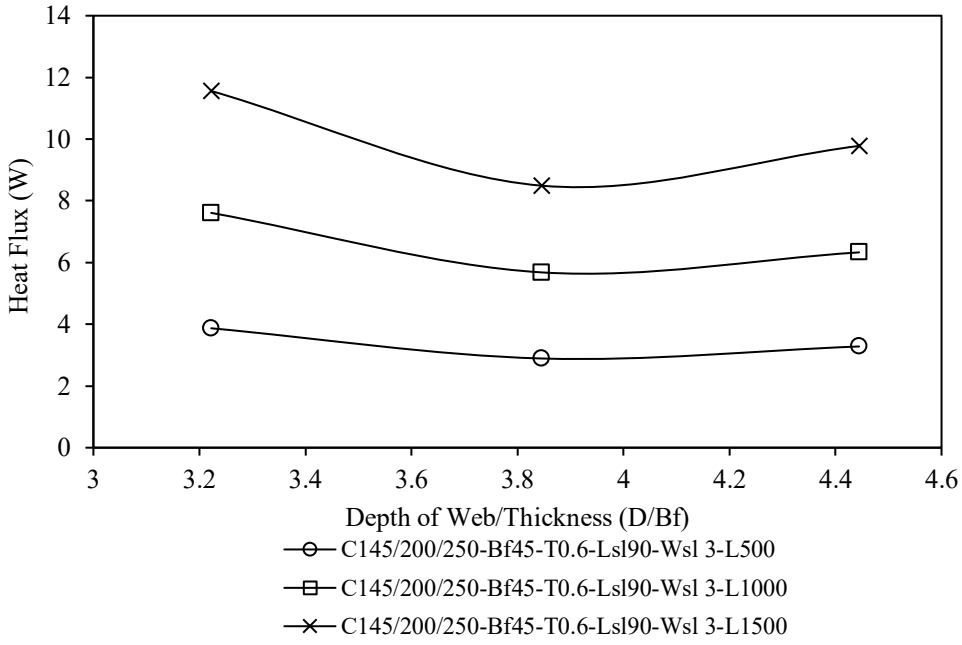

(b)

Fig. 5- 7. Effect of D/B_f on the heat flux of wall panels having CFS channel sections with slits for a) L_{sl} =60 and b) L_{sl}=90

5.4.4 Effect of width of slit W_{sl}/t on the heat flux for sections with slits

Table 5-3 and Figs. 5-8 (a), (b), (c), (d), (e) and (f) collectively depict the effects of the W_{sl}/t ratio on heat flux of wall panels having CFS channel sections with slits, as derived from FEA results. For the wall panels with C145X45X15 sections with slits of length 60 mm (Fig. 5-8 (a)), the heat flux decreased by 4.23% when the W_{sl}/t ratio varied from 5 to 11.66, for λ_c value of 0.48. The decrease in heat flux of wall panels was further observed as follows: by 4.88% for λ_c value of 0.97, and by 6.28% for λ_c value of 1.45. The C200X45X15 sections (Fig. 5-8 (c)) showed decrease of 4.41%, 3.87%, 4.06%, for λ_c values of 0.51, 1.02 and 1.53 respectively, as the W_{sl}/t ratio varied from 5 to 11.66. In contrast, the C250X65X15 sections (Fig. 5-8 (e)) experienced reductions of 4.97%, 3.97% and 2.79% for λ_c values of 0.36, 0.73 and 1.09, respectively, as the W_{sl}/t ratio varied from 5 to 11.66. These results highlight a decreasing trend of heat flux as the W_{sl}/t ratio increases across different levels of slenderness. For the wall panels with C145X45X15 sections with slits of length 90 mm (Fig. 5-8 (b)), the heat flux decreased by 4.24% when the W_{sl}/t ratio was varied from 5 to 11.66, for λ_c value of 0.48. The decrease in heat flux of wall panels was further observed as follows: by 4.88% for λ_c value of 0.97, by 6.28% for λ_c value of 1.46. The C200X45X15 sections (Fig. 5-8 (d)) showed a more gradual decrease, with reductions of 3.96%, 3.10%, 3.89%, for λ_c values of 0.51, 1.02 and 1.53 respectively, as the W_{sl}/t ratio varied from 5 to 11.66. In contrast, the C250X65X15 sections (Fig. 5-8 (f)) experienced reductions of 3.11%, 2.46% and 1.88% for λ_c values of 0.36, 0.73 and 1.09, respectively, as the W_{sl}/t ratio varied from 5 to 11.66. These results highlight a decreasing trend of heat flux as the W_{sl}/t ratio increases across different levels of slenderness.

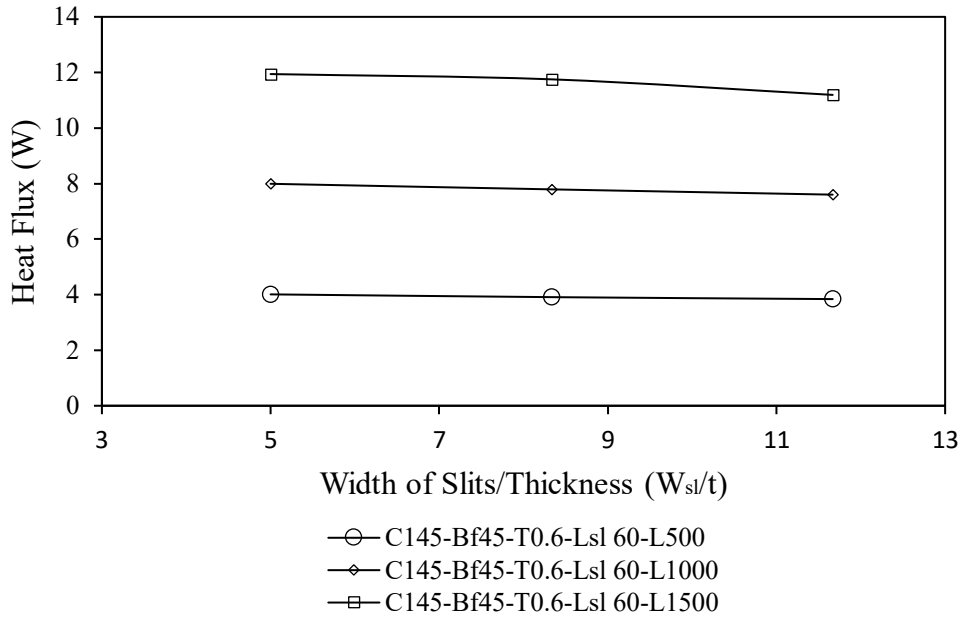
14
12
10
8
6
4
2
0
Heat Flux (W)
3
5
7
9
11
13
Width of Slits/Thickness (Wsl/t)
C145-Bf45-T0.6-Lsl 60-L500
C145-Bf45-T0.6-Lsl 60-L1000
C145-Bf45-T0.6-Lsl 60-L1500

(a)

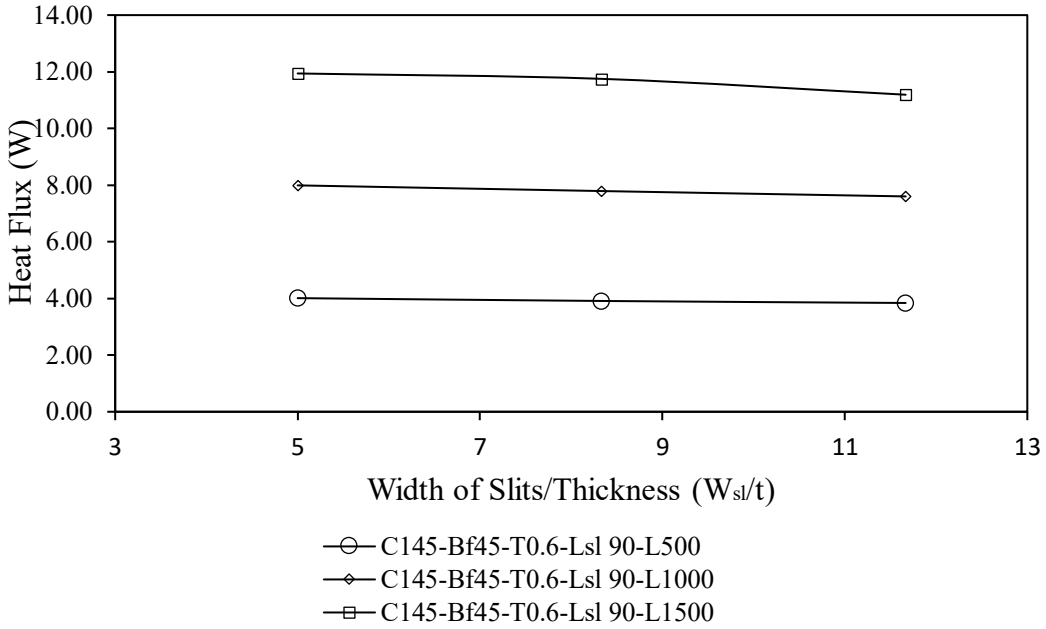
14.00
12.00
10.00
8.00
6.00
4.00
2.00
0.00
Heat Flux (W)
3
5
7
9
11
13
Width of Slits/Thickness (Wsl/t)
C145-Bf45-T0.6-Lsl 90-L500
C145-Bf45-T0.6-Lsl 90-L1000
C145-Bf45-T0.6-Lsl 90-L1500

(b)

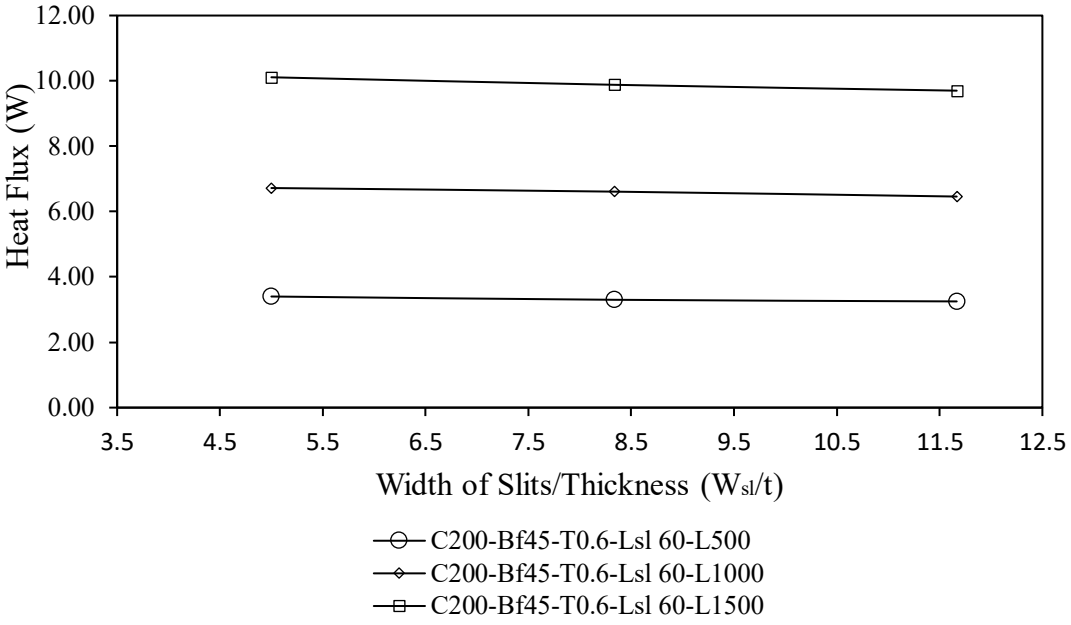
12.00
10.00
8.00
6.00
4.00
2.00
0.00
Heat Flux (W)
3.5
4.5
5.5
6.5
7.5
8.5
9.5
10.5
11.5
12.5
Width of Slits/Thickness (Wsl/t)
C200-Bf45-T0.6-Lsl 60-L500
C200-Bf45-T0.6-Lsl 60-L1000
C200-Bf45-T0.6-Lsl 60-L1500

(c)

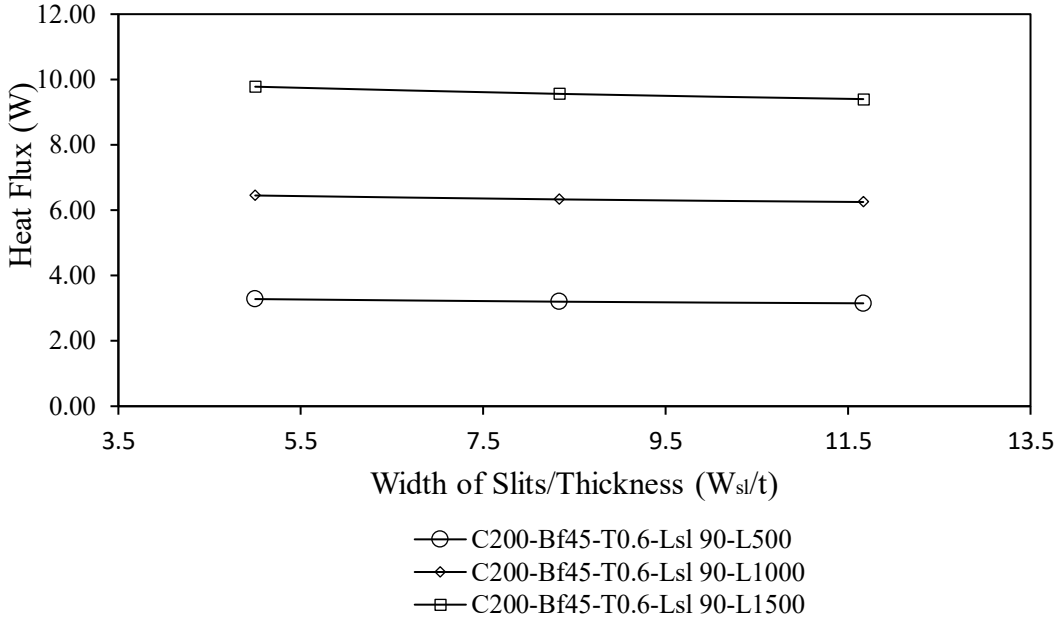
12.00
10.00
8.00
6.00
4.00
2.00
0.00
Heat Flux (W)
3.5
5.5
7.5
9.5
11.5
13.5
Width of Slits/Thickness (Wsl/t)
C200-Bf45-T0.6-Lsl 90-L500
C200-Bf45-T0.6-Lsl 90-L1000
C200-Bf45-T0.6-Lsl 90-L1500

(d)

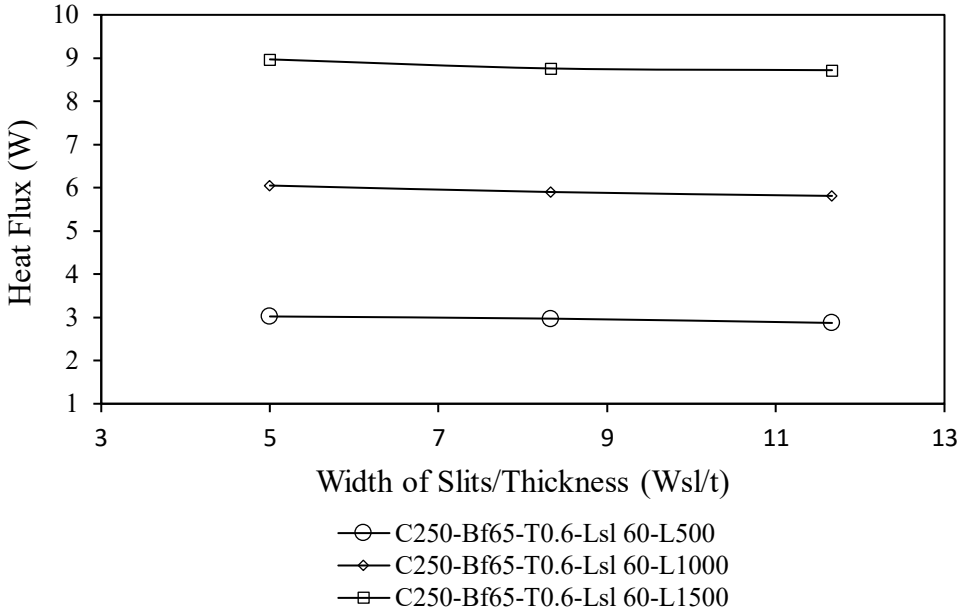

(e)

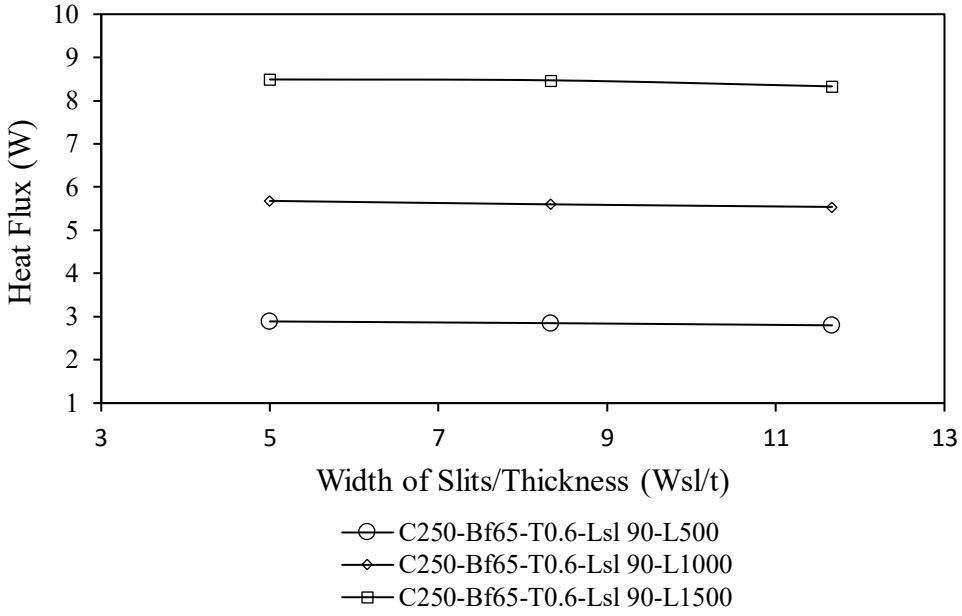

(f)

Fig. 5- 8. Effect of W_{sl}/t on the heat flux of wall panels having CFS channel sections with slits

5.4.5 Effect of L_{sl}/W_{sl} on the heat flux for sections with slits

Tables 5–3 and Figs. 5-9 (a), (b), and (c) collectively show the effects of the L_{sl}/W_{sl} ratio on heat flux of wall panels having CFS channel sections with slits of length 60 mm, according to FEA results. For the C145X45X15 sections (Fig. 5-9 (a)), heat flux decreased by 3.49% when

the L_{sl}/W_{sl} ratio increased from 20 to 30 for a λ_c value of 0.48, by 5.13% for 0.97 and by 3.18% for 1.45. The C200X45X15 sections (Fig. 5-9 (b)) experienced decreases of 3.53%, 4.01% and 3.26%, for λ_c values of 0.51, 1.02 and 1.53 respectively, as the L_{sl}/W_{sl} ratio increased from 20 to 30. In contrast, the reductions in the C250X65X15 sections (Fig. 5-9 (c)) were 4.3%, 6.12%, 5.35%, for λ_c values of 0.36, 0.97, and 1.08, respectively, as the L_{sl}/W_{sl} ratio increased from 20 to 30.

These results demonstrate a consistent trend of decreasing heat flux with increasing L_{sl}/W_{sl} ratios across different column section dimensions.

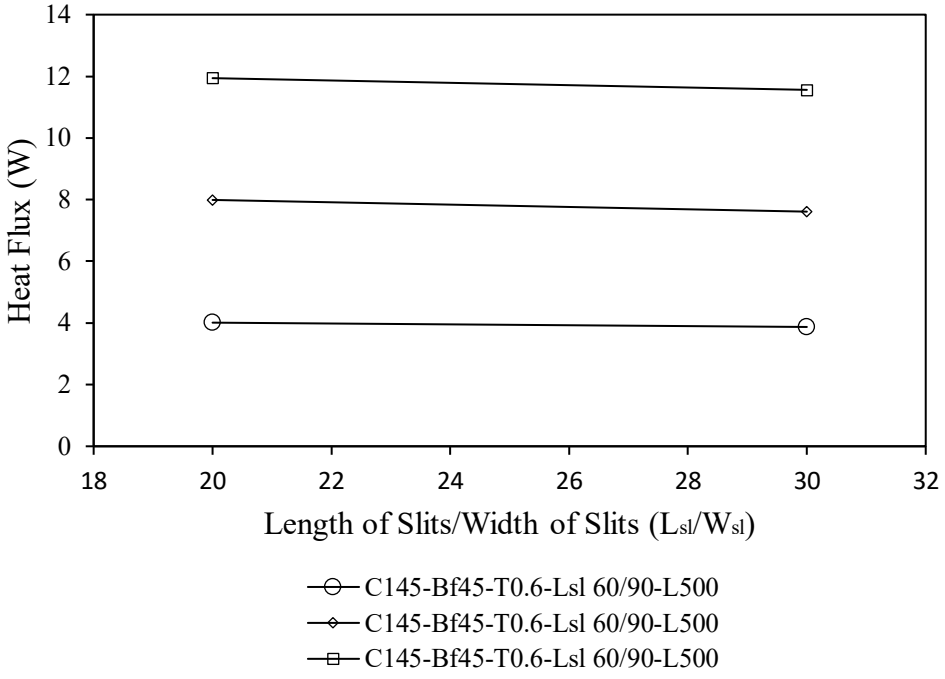

(a) 145x45x15

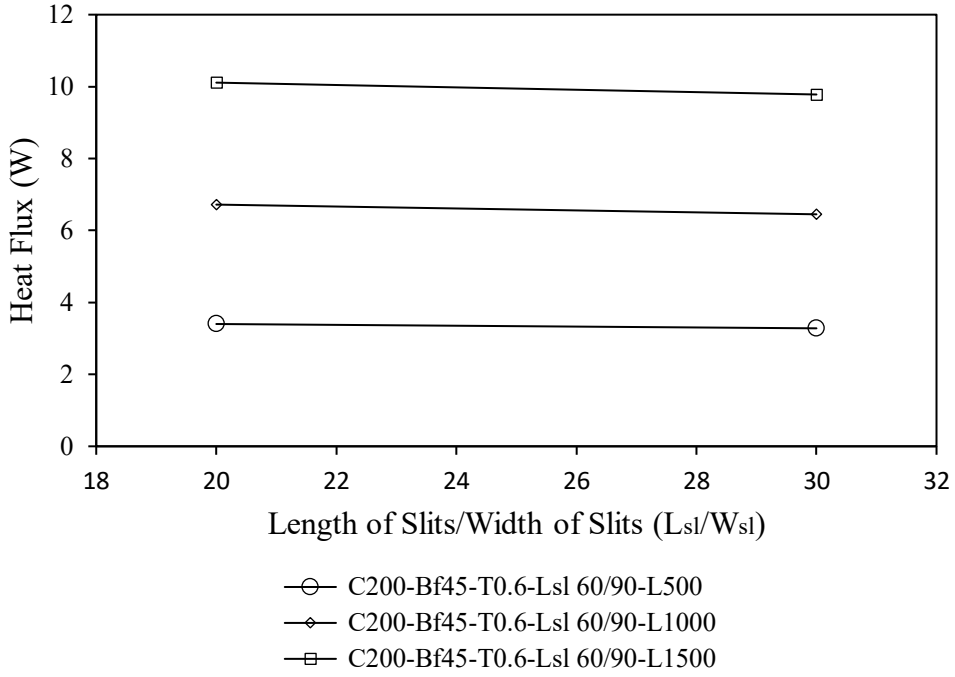

(b) 200x45x15

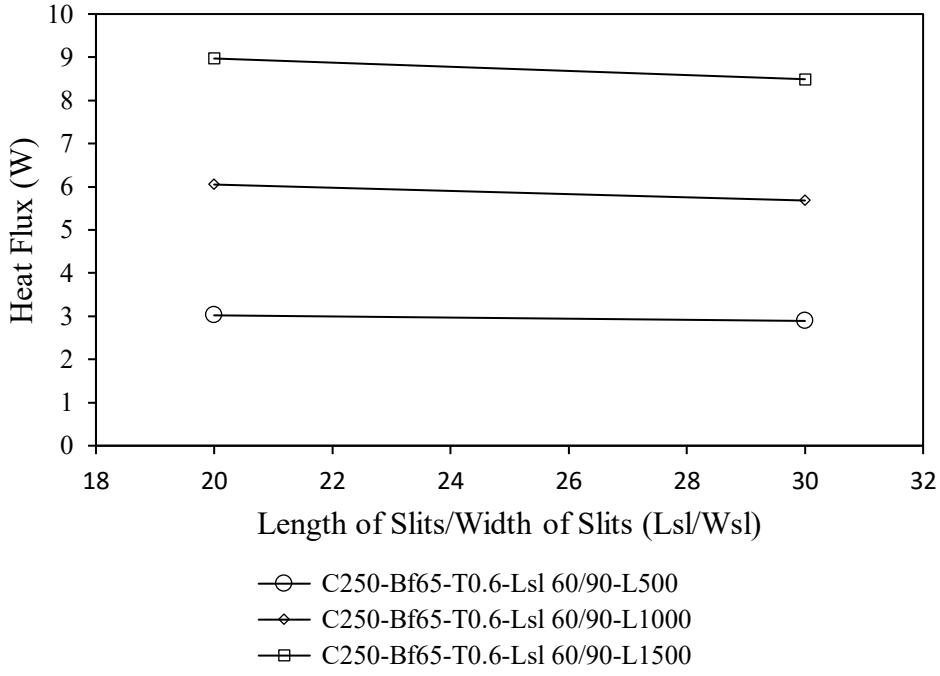

(c) 250x65x15

Fig. 5- 9. Effect of L_{sl}/W_{sl} on the heat flux of wall panels having CFS channel sections with slits

5.4.6 Influence of slits on the heat flux of wall panels with respect to plain sections

This section summarises the key findings on the reduction of heat flux in wall panels incorporating CFS sections with slits, relative to panels with plain CFS sections. The plain sections correspond to configurations where both the L_{sl}/W_{sl} ratio and the W_{sl}/t ratio are equal to zero. Tables 5-3 and Figs. 5-10(a)–(c) present the influence of the L_{sl}/W_{sl} ratio on heat flux for slitted CFS sections with a slit length of 60 mm, compared with corresponding plain sections, based on the FEA results. For the C145×45×15 sections (Fig. 5-10(a)), the heat flux decreased by 15.93% when the L_{sl}/W_{sl} ratio increased from 0 to 20, and by 18.86% for when the ratio increased from 20-30 at λ_c = 0.48. Reductions of 16.07% and 20.38% were recorded for λ_c = 0.97, and 16.39% and 19.05% for λ_c = 1.45. For the C200×45×15 sections (Fig. 5-10(b)), the heat flux decreased by 16.46% as the L_{sl}/W_{sl} ratio increased from 0 to 20, and by 19.41% when the ratio increased from 0 to 30 for λ_c = 0.51. Reductions of 17.65% and 20.96% were observed for λc = 1.02, and 17.54% and 20.23% for λ_c = 1.53. For the C250×65×15 sections (Fig. 5-10(c)), the heat flux decreased by 18.60% when the L_{sl}/W_{sl} ratio increased from 0 to 20, and by 22.10% when the ratio increased from 0 to 30 for λ_c = 0.36. Further reductions of 22.31% and 28.43% were observed for λ_c = 0.72, and 24.19% and 29.54% for λ_c = 1.08.

Table 5-3 and Figs. 5-11 (a), (b) and (c) collectively depict the effects of the W_{sl}/t ratio on heat flux of wall panels having CFS channel sections with slits with respect to wall panels having plain CFS channel sections, as derived from FEA results. For wall panels with C145×45×15 sections (Fig. 5-11(a)), the heat flux decreased by 15.93% as the W_{sl}/t ratio increased from 0 to 5, and by 19.49% as the ratio increased to 11.66 for λ_c = 0.48. Further reductions of 19.15% and 20.16% were observed for λ_c = 0.97, and 19.59% and 21.64% for λ_c = 1.45. For the C200×45×15 sections (Fig. 5-11(b)), decreases of 16.46% and 20.15% were observed for λ_c = 0.51, 17.65% and 20.83% for λc = 1.02, and 17.54% and 20.88% for λ_c = 1.53 as the W_{sl}/t ratio increased from 0 to 5 and from 0 to 11.66, respectively. For the C250×65×15 sections (Fig. 5-11(c)), heat flux reductions of 18.59% and 22.64% were observed for λ_c = 0.36, 18.24% and 21.49% for λ_c = 0.72,

and 17.54% and 20.88% for λ_c = 1.08 as the W_{sl}/t ratio increased from 0 to 5 and from 0 to 11.66, respectively.

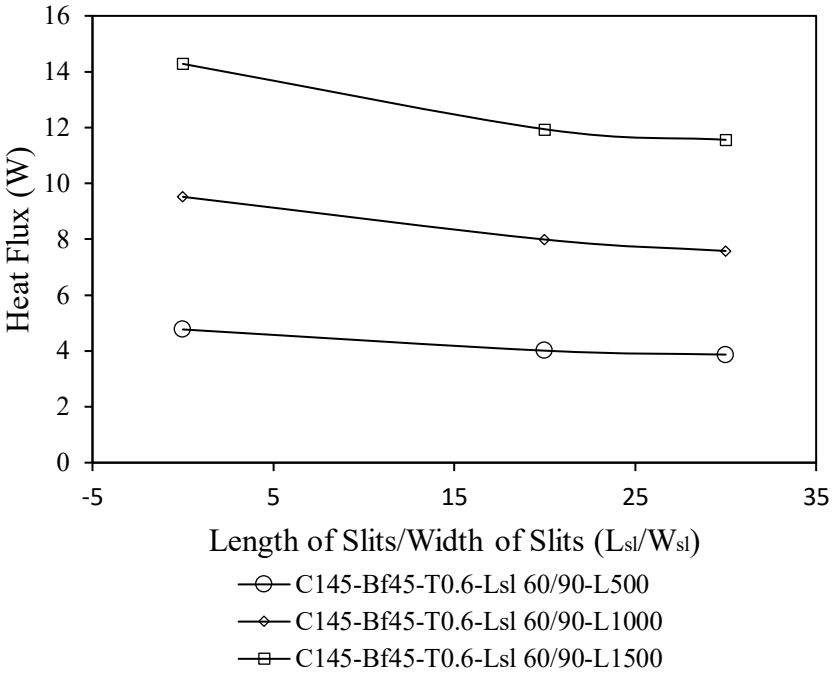

(a)

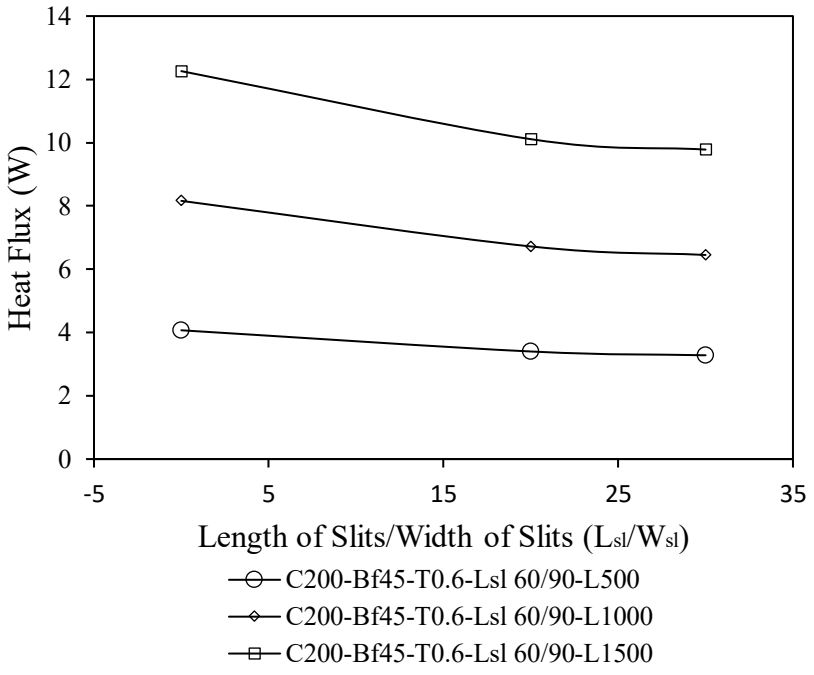

(b)

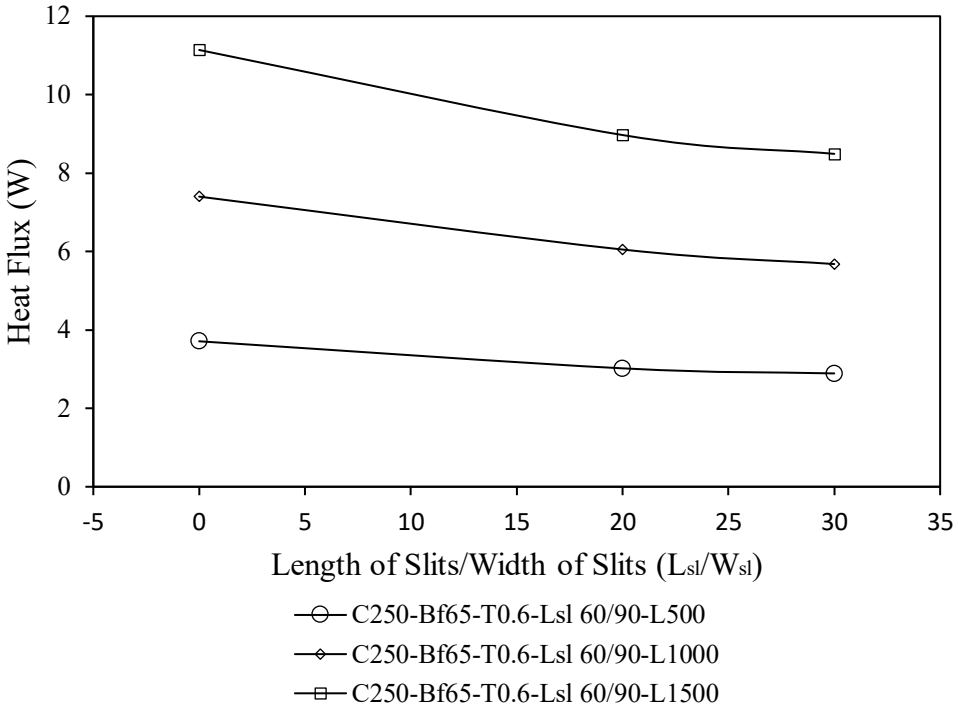

(c)

Fig. 5- 10. Effect of L_{sl}/W_{sl} on the heat flux of wall panels having CFS channel sections with slits with respect to wall panels having plain sections

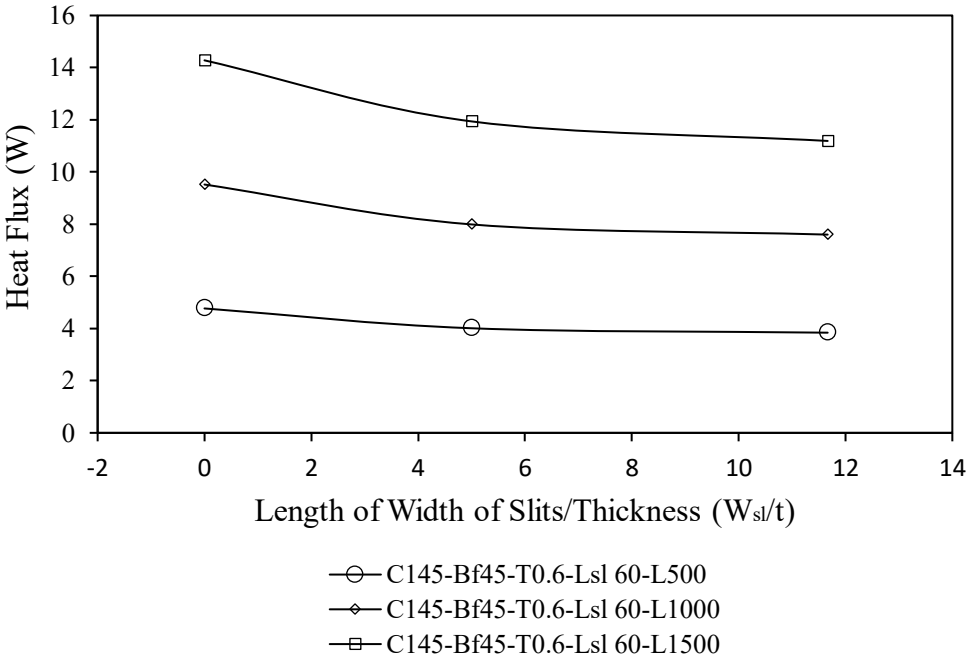

(a)

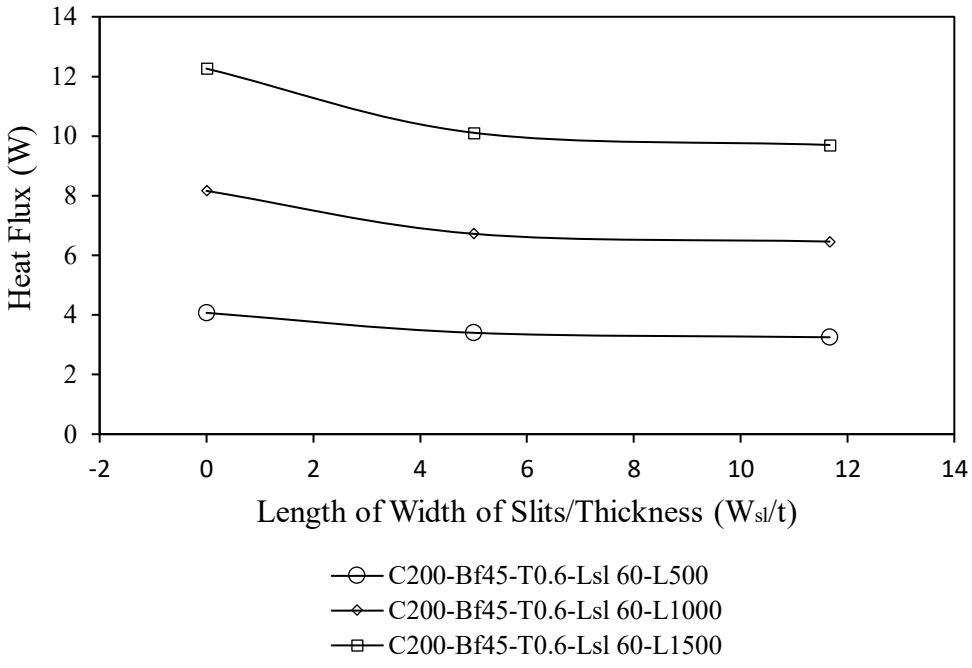

(b)

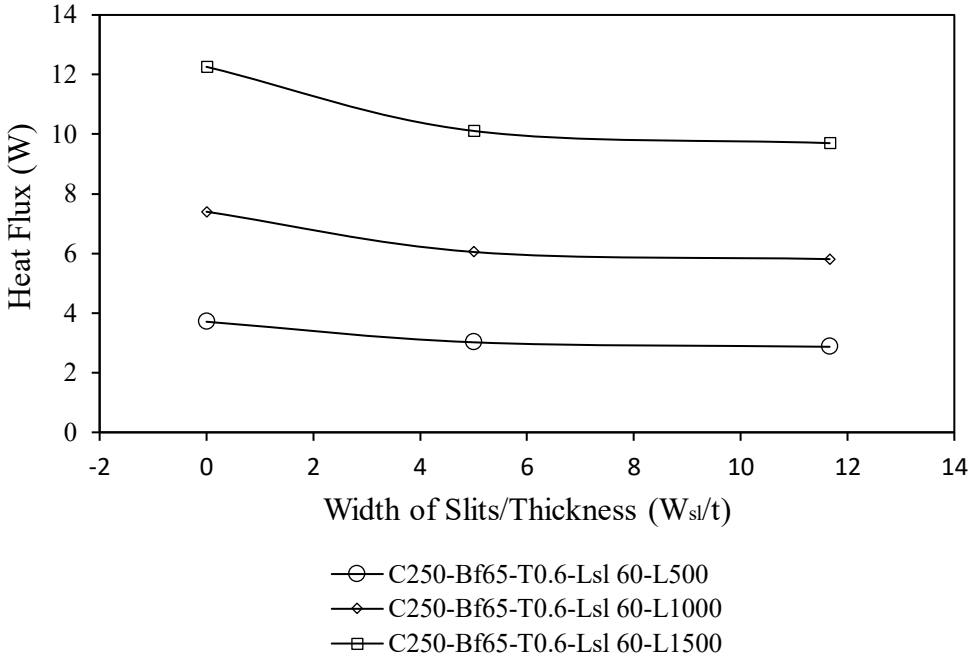

(c)

Fig. 5- 11. Effect of W_{sl}/t on the heat flux of wall panels having CFS channel sections with slits with respect to wall panels having plain sections

5.4.7 Performance Index Evaluation

To enable an assessment of the thermal–structural trade-off introduced by web slits, a dimensionless Performance Index (PI) was defined to quantify the thermal benefit achieved per unit of structural strength reduction. For each configuration, the percentage thermal gain relative to the corresponding reference section without slits was computed, along with the percentage reduction in axial capacity. The Performance Index was then defined as the ratio of thermal improvement to strength loss, thereby normalising performance across different section geometries and member lengths.

$$\mathrm{PI} = \frac{\Delta T}{\Delta S}$$

where ΔT represents the percentage increase in thermal resistance (or equivalent reduction in heat flux) and ΔS represents the percentage reduction in axial capacity relative to the reference section. This formulation allows direct comparison between configurations of different depths, slit widths and member lengths. A value greater than unity indicates that the thermal benefit outweighs the structural strength reduction, while higher values indicate more efficient thermal–structural optimisation. As shown in Table 5-4, the index was evaluated for three section groups (C145-B45, C200-B45, C250-B65), three member lengths (500, 1000 and 1500 mm), and slit widths of 3, 5 and 7 mm with a constant slit length of 60 mm.

Table 5- 4 Performance Index Values of the Parametric Study for C145/200/250 Channel Sections with Slits

Specimen	L_{sl} 60			L_{sl} 90		
	W_{sl} 3	W_{sl} 5	W_{sl} 7	W_{sl} 3	W_{sl} 5	W_{sl} 7
C145-B_f45-T0.6-L500	15.47	6.93	3.19	3.38	3.17	2.57
C145-B_f45-T0.6-L1000	1.7	1.67	1.75	1.62	1.68	1.36
C145-B_f45-T0.6-L1500	1.28	1.2	1.24	1.16	1.14	1.04
C200-B_f45-T0.6-L500	2.46	2.74	2.55	2.16	2.41	2.07
C200-B_f45-T0.6-L1000	2.04	2.1	2.03	1.69	1.79	1.67
C200-B_f45-T0.6-L1500	1.7	1.75	1.71	1.56	1.55	-
C250-B_f65-T0.6-L500	37.2	3.55	2.59	2.75	3.3	2.23
C250-B_f65-T0.6-L1000	3.58	2.15	1.9	2.05	2.03	1.65
C250-B_f65-T0.6-L1500	1.61	1.74	1.31	1.5	1.55	1.4

The Performance Index demonstrates a strong dependence on both member slenderness and section geometry. For the shortest members (L = 500 mm), the C145-B_f45 configuration with W_{sl} = 3 mm and the C250-B_f65 configuration with W_{sl} = 3 mm exhibited very high PI values (15.47 and 37.2, respectively). These results indicate that significant thermal gains were achieved with relatively small structural strength reductions. This behaviour is consistent with stockier members, where global instability effects are limited. As member length increases, the PI values decrease consistently across all section groups. At L = 1500 mm, PI values are within a narrow range of approximately 1.2 to 1.7. This trend indicates that for more slender members, the structural strength reduction associated with web discontinuities becomes proportionally more significant, thereby diminishing the relative efficiency of thermal improvement. In longer members, global buckling sensitivity amplifies the impact of local stiffness loss, reducing the

overall benefit of slit-induced thermal enhancement. The value for C200-B_f45 configuration with W_{sl} = 7 at L = 1500 mm is considered to be an outlier and has not been included in the discussion.

The influence of slit width varies with geometry. For the C145- B_f45 series at L = 500 mm, increasing slit width reduces PI substantially (from 15.47 at W_{sl} = 3 mm to 3.19 at W_{sl} = 7 mm), indicating that structural strength reduction improves more than thermal performance. In contrast, the C200- B_f45 series at L = 500 mm shows relatively stable PI values across slit widths (2.46–2.74–2.55), suggesting a more balanced thermal–structural interaction for this geometry. This confirms that the optimal slit width is not universal but depends on sectional dimensions and slenderness. The C250- B_f65 sections produce the highest peak PI values at short lengths but exhibit sharper reductions with increasing length. While larger sections can tolerate local web weakening under low slenderness conditions, their relative efficiency decreases as global instability effects start to show.

Overall, the Performance Index analysis confirms that slit optimisation must be evaluated through coupled thermal–structural metrics rather than isolated performance indicators. Thermal enhancement is most efficient in shorter members and in geometries where local loss of stiffness does not significantly accelerate global instability. For more slender members, the structural strength reduction increasingly offsets thermal gains, reducing overall efficiency. The proposed index therefore provides a rational framework for identifying configurations that achieve balanced system-level performance.

The steady-state thermal simulations indicate that, after normalising by panel area, the predicted heat flux across all parametric wall configurations ranges between approximately 4.6 and 8.0 W/m² for an imposed indoor–outdoor temperature difference of 25 K (20°C to −5°C). These values correspond to effective overall thermal transmittance values of 0.18–0.32 W/m²K, giving equivalent assembly thermal resistances in the range of 3.1–5.4 m²K/W. The lower end of this

range represents plain stud configurations with greater thermal bridging, whereas the higher resistance values correspond to slit configurations that interrupt the steel heat-flow path. For comparison, current New Zealand Building Code H1 requirements for external wall construction specify minimum construction R-values of approximately 1.9–2.0 m²K/W, which under the same 25 K temperature difference would correspond to heat fluxes of roughly 12.5–13.2 W/m². Therefore, all configurations investigated in this study demonstrate thermal resistances exceeding current minimum regulatory requirements, with several slit configurations achieving performance significantly above typical code-compliant insulated wall assemblies.

5.5 Conclusion

From the steady-state thermal analysis carried out in COMSOL, the following conclusions can be drawn regarding the influence of geometric parameters on the heat flux of wall panels incorporating CFS channel sections with slits.

The results clearly show that introducing slits into CFS channel sections leads to a substantial reduction in heat flux when compared with wall panels containing plain CFS sections. This effect is consistent across all section sizes and slenderness levels, indicating that the presence of slits alone provides the principal improvement in thermal performance.

Once slits are introduced, varying the slit parameters, such as the L_{sl}/W_{sl} ratio and the W_{sl}/t ratio, leads to more gradual and less pronounced reductions in heat flux. As shown in Table 5-3, increase of the area of slits offers additional enhancement, although the magnitude of improvement is smaller when compared with the initial reduction obtained by transitioning from plain to slitted sections. This indicates that while parameter refinement contributes to improved thermal behaviour, the dominant effect is achieved through the incorporation of slits themselves.

Chapter 6 Conclusion and future studies

6.1. Conclusion

This study investigated the structural and thermal behaviour of cold-formed steel channel sections incorporating web slits, with the objective of quantifying their influence on axial performance under concentric and eccentric loading and developing validated design methodologies suitable for practical implementation. Through validated non-linear elasto-plastic finite element modelling and extensive parametric studies, the research has demonstrated that the introduction of web slits fundamentally modifies the buckling behaviour of cold-formed steel studs and that these effects are not consistently captured by existing design provisions.

6.1.1. Numerical investigation

Non-linear elasto-plastic finite element (FE) models of CFS studs with and without slits were developed and validated against previously reported experimental tests. After validation, parametric studies were conducted to investigate the effects of section depth, flange width, thickness, slit length, slit width, and member length on axial capacity under concentric loading. The results showed that the presence of slits alters local and global buckling behaviour, leading to reductions in axial strength that are not fully captured by existing design equations.

The validated models were then extended to eccentric loading to simulate combined axial compression and minor-axis bending, as commonly observed in stud-based wall systems. A comprehensive parametric study revealed that eccentricity significantly amplifies the adverse effects of slits on structural performance, particularly by shifting the governing failure mode to local buckling. Comparison with the general interaction equation in AS/NZS 4600 showed that current provisions can be both conservative and unconservative, depending on the magnitude of eccentricity and slit geometry.

Under concentric compression, the presence of slits resulted in measurable reductions in axial capacity, typically ranging between 6% and 31% depending on column slenderness and

geometric proportions. The interaction between local and distortional buckling was found to be strongly influenced by sectional parameters, particularly the D/B_f ratio, with an optimal value observed near 3.85. Increasing D/Bf beyond this range reduced axial capacity by up to 22% due to diminished flange restraint and accelerated local instability. These findings establish that slit-induced discontinuities alter stiffness distribution and instability interaction in a manner not explicitly addressed in current Direct Strength Method formulations.

The investigation was extended to eccentric loading to simulate combined axial compression and minor-axis bending, conditions representative of stud behaviour in wall systems. A comprehensive parametric database comprising 1,134 validated finite element models showed that eccentricity significantly amplifies the structural sensitivity of slitted sections. Average axial capacity reductions of 22.66%, 36.19%, 42.92%, 68.62%, and 62.24% were observed for eccentricities of −10 mm, +10 mm, 25 mm, −25 mm, and ±50 mm, respectively. Increasing column slenderness from $\lambda c \approx 0.48$ to 1.45 resulted in additional reductions of up to 25%, confirming that global instability magnifies the effect of local stiffness loss introduced by slits. The parametric study further demonstrated that D/t, B_f/t, D/B_f, W_{sl}/t, and L_{sl}/W_{sl} ratios significantly influence axial performance, with increases in Bf/t producing strength gains of up to 144% within specific slenderness ranges, while excessive increases in D/B_f led to strength deterioration. Comparison with AS/NZS 4600 and AISI-S100 interaction equations revealed systematic discrepancies: strengths were underestimated by approximately 13% for moderate eccentricities (10–25 mm) and overestimated by approximately 20% at 50 mm eccentricity. These deviations increased with slenderness and eccentricity, indicating that existing interaction equations do not fully represent the instability mechanisms governing slitted members.

6.1.2. Development of modified design equations

To address the inadequacies of the current Direct Strength Method (DSM), the FE results were used to derive strength reduction factors and modified DSM-based equations for slitted CFS

studs under concentric loading. The proposed equations were limited to global and local buckling. For eccentric loading, a new interaction equation was developed that incorporates element slenderness, web slenderness, and slit configuration. Both modified design approaches were calibrated and validated through reliability analysis in accordance with the AISI-S100 framework, achieving reliability indices that satisfy code requirements.

6.1.3. Thermal performance

The thermal performance of wall panels incorporating slitted CFS studs was evaluated, demonstrating that slits increase the heat flow path and reduce thermal bridging. A parametric thermal analysis showed that slit length, width, and spacing significantly influence thermal efficiency. The thermal investigation demonstrated that web slits increase the heat flow path and reduce thermal bridging in wall panels. However, structural and thermal performance cannot be assessed independently. The introduction of a dimensionless Performance Index enabled quantitative evaluation of this trade-off by relating thermal improvement to structural strength reduction. Maximum Performance Index values of 15.47 and 37.2 were achieved for members with L = 500 mm, while values reduced to approximately 1.2–1.7 at L = 1500 mm. Thermal optimisation was most effective in low-slenderness members, where global instability effects were less dominant and the structural strength reduction associated with web slits remained limited.The results highlight the need for an optimal balance between thermal improvement and structural capacity, and the study provides guidance on selecting slit configurations that achieve both performance objectives.

6.2 Key contributions of the research are as follows:

1. Development and validation of detailed non-linear FE models for CFS studs with and without slits under concentric and eccentric loading.

2. Comprehensive parametric studies quantifying the effects of geometric and slit parameters on axial strength and buckling behaviour.

3. Evaluation of the applicability and limitations of existing DSM provisions for slitted members.

4. Proposal of modified DSM-based design equations for concentric loading and a new interaction equation for eccentric loading.

5. Reliability analysis of proposed design equations to satisfy AISI-S100 requirements.

6. Quantification of the influence of slit parameters on thermal performance of wall panels having CFS studs with slits.

6.3 Recommendations for Future Work

As an extension of this research, the following areas are recommended for further investigation:

1. The current study is primarily based on numerical analysis. Although the FE models were validated against available experimental data of CFS sections with slits under concentric loading and plain CFS sections under eccentric loading, full-scale physical tests on slitted members under combined axial–bending loads are required to verify the proposed design equations and validate the failure modes observed in the simulations.

2. This study primarily considered a single slit pattern. Future research could explore different slit orientations (diagonal, staggered) and spacing patterns to identify configurations that optimise the balance between strength and thermal performance..

3. This study focused on individual stud members. Future work should investigate the performance of slitted CFS studs within full wall assemblies, considering sheathing restraint, bracing, connection stiffness, and system-level load redistribution under wind or seismic actions.

4. Although this study quantified the effect of slit parameters on both strength and thermal performance, an optimisation framework that simultaneously maximises thermal efficiency while maintaining structural capacity would be valuable.

5. Slits may alter heat transfer and structural behaviour under fire exposure. Future work should investigate the response of slitted CFS studs at elevated temperatures.

6. With the extensive parametric FE database generated in this study, future research could develop machine-learning models to predict axial capacity or thermal performance as a function of slit geometry, material properties, and boundary conditions. Algorithms such as XGBoost, neural networks, random forests could identify nonlinear interactions that are difficult to capture using traditional regression or DSM formulations.

References

[1] T. Höglund and H. Burstrand, “Slotted steel studs to reduce thermal bridges in insulated walls,” *Thin-Walled Structures*, vol. 32, pp. 81–109, 1998.

[2] F. Liu, F. Fu, Y. Wang, and Q. Liu, “Fire performance of non-load-bearing light-gauge slotted steel stud walls,” *J. Constr. Steel Res.*, vol. 137, pp. 228–241, Oct. 2017, doi: 10.1016/j.jcsr.2017.06.034.

[3] M. J. Andreassen and J. Jönsson, “Joint and column behaviour of slotted cold-formed steel studs,” *Steel Construction*, vol. 8, no. 3, pp. 155–161, Sep. 2015, doi: 10.1002/stco.201510025.

[4] W.-W. Yu and R. A. Laboube, “Development of Cost-Effective, Energy Efficient Steel Framing: Thermal Performance of Slit-Web Steel Wall Studs,” 2006.

[5] American Iron and S. Institute, “North American Specification for the Design of Cold-Formed Steel Structural Members,” Washington, DC, 2004.

[6] Standards Australia, *Cold-Formed Steel Structures*. Sydney, Australia: Standards Australia, 2005.

[7] C. D. Moen and B. W. Schafer, “Direct Strength Method for Design of Cold-Formed Steel Columns with Holes,” *Journal of Structural Engineering*, vol. 137, no. 5, pp. 559–570, May 2011, doi: 10.1061/(asce)st.1943-541x.0000310.

[8] B. Chen, K. Roy, A. Uzzaman, G. M. Raftery, and J. B. P. Lim, “Parametric study and simplified design equations for cold-formed steel channels with edge-stiffened holes under axial compression,” *J. Constr. Steel Res.*, vol. 172, Sep. 2020, doi: 10.1016/j.jcsr.2020.106161.

[9] B. Chen, K. Roy, A. Uzzaman, G. Raftery, and J. B. P. Lim, “Axial strength of back-to-back cold-formed steel channels with edge-stiffened holes, un-stiffened holes and plain webs,” *J. Constr. Steel Res.*, vol. 174, Nov. 2020, doi: 10.1016/j.jcsr.2020.106313.

[10] D. L. Chandramohan, K. Roy, G. Beulah Gnana Ananthi, Z. Fang, and J. B. P. Lim, “Structural behaviour and capacity of cold-formed steel channel sections with elongated edge-stiffened and unstiffened web holes under compression,” *J. Constr. Steel Res.*, vol. 218, Jul. 2024, doi: 10.1016/j.jcsr.2024.108681.

[11] J. Zhao, J. Liu, C. Yu, and W. Zhang, “Test investigation and direct strength method on cold-formed steel compression members with web holes of different widths,” *Eng. Struct.*, vol. 272, Dec. 2022, doi: 10.1016/j.engstruct.2022.114979.

[12] J. Zhao, S. Liu, and B. Chen, “Axial Strength of Slotted Perforated Cold-Formed Steel Channels under Pinned-Pinned Boundary Conditions,” *J. Constr. Steel Res.*, vol. 200, p. 107673, 2023, doi: 10.1016/j.jcsr.2023.107673.

[13] Z. He, Y. Jian, X. Zhou, and S. Jin, “Local-distortional interactive behavior and design of cold-formed steel C-sections with & without slotted holes,” *Journal of Building Engineering*, vol. 79, Nov. 2023, doi: 10.1016/j.jobe.2023.107812.

[14] J. H. Zhang, J. Wang, S. Xu, and F. Wang, “Testing, Numerical Modeling and Design of Perforated Advanced High-Strength Steel Channel Section Columns,” *J. Constr. Steel Res.*, vol. 214, p. 108440, 2024, doi: 10.1016/j.jcsr.2023.108440.

[15] I. Papargyriou and I. Hajirasouliha, “More efficient design of CFS strap-braced frames under vertical and seismic loading,” *J. Constr. Steel Res.*, vol. 185, Oct. 2021, doi: 10.1016/j.jcsr.2021.106886.

[16] F. Yilmaz, S. M. Mojtabaei, I. Hajirasouliha, and J. Becque, “Behaviour and performance of OSB-sheathed cold-formed steel stud wall panels under combined vertical and seismic loading,” *Thin-Walled Structures*, vol. 183, Feb. 2023, doi: 10.1016/j.tws.2022.110419.

[17] S. M. Mojtabaei, J. Becque, and I. Hajirasouliha, “Local Buckling in Cold-Formed Steel Moment-Resisting Bolted Connections: Behavior, Capacity, and Design,” 2020, doi: 10.1061/(ASCE).

[18] S. M. Mojtabaei, J. Becque, and I. Hajirasouliha, “Behavior and Design of Cold-Formed Steel Bolted Connections Subjected to Combined Actions,” *Journal of Structural Engineering*, vol. 147, no. 4, Apr. 2021, doi: 10.1061/(asce)st.1943-541x.0002966.

[19] T. Höglund, “Design of Slotted Light Gauge Studs,” Stockholm, Sweden, 1998.

[20] J. Borglund and J. Jonsson, “Resistance of Slotted Steel Studs (In Swedish),” Royal Institute of

Technology, Department of Structural Engineering, Stockholm, Sweden, 1997.
[21] M. da Costa, “Support Strength of Walls with Slotted Studs,” KTH, Royal Institute of Technology, Department of Structural Engineering, Sweden, 1999.
[22] P. Salmi, “Design of Web-Perforated Steel Wall Studs (In Finnish),” in *4th Finnish Steel Structures R&D Days*, Lappeenranta, Finland, 1998.
[23] K. S. Sivakumaran and K. Sivakumaran, “Some Studies on Cold-formed Steel Sections with Web Openings,” in *9th International Specialty Conference on Cold-Formed Steel Structures*, 1988.
[24] C. D. Moen and B. W. Schafer, “Experiments on cold-formed steel columns with holes,” *Thin-Walled Structures*, vol. 46, no. 10, pp. 1164–1182, Oct. 2008, doi: 10.1016/j.tws.2008.01.021.
[25] M. P. Kulatunga and M. Macdonald, “Investigation of cold-formed steel structural members with perforations of different arrangements subjected to compression loading,” *Thin-Walled Structures*, vol. 67, pp. 78–87, 2013, doi: 10.1016/j.tws.2013.02.014.
[26] M. P. Kulatunga, M. Macdonald, J. Rhodes, and D. K. Harrison, “Load capacity of cold-formed column members of lipped channel cross-section with perforations subjected to compression loading - Part I: FE simulation and test results,” *Thin-Walled Structures*, vol. 80, pp. 1–12, 2014, doi: 10.1016/j.tws.2014.02.017.
[27] R. Loov, “Local buckling capacity of C-shaped cold-formed steel sections with punched webs,” *Canadian Journal of Civil Engineering*, vol. 11, no. 1, pp. 1–7, 1984.
[28] Y. Pu, M. H. R. Godley, R. G. Beale, and H. H. Lau, “Prediction of Ultimate Capacity of Perforated Lipped Channels,” *Journal of Structural Engineering*, vol. 125, no. 5, pp. 510–514, 1999, doi: 10.1061/(ASCE)0733-9445(1999)125:5(510).
[29] Z. Yao and K. J. R. Rasmussen, “Inelastic local buckling behaviour of perforated plates and sections under compression,” in *Thin-Walled Structures*, Dec. 2012, pp. 49–70. doi: 10.1016/j.tws.2012.07.002.
[30] Z. Yao and K. J. R. Rasmussen, “Perforated Cold-Formed Steel Members in Compression. II: Design,” *Journal of Structural Engineering*, vol. 143, no. 5, May 2017, doi: 10.1061/(asce)st.1943-541x.0001636.
[31] Z. Yao and K. J. R. Rasmussen, “Perforated Cold-Formed Steel Members in Compression. I: Parametric Studies,” *Journal of Structural Engineering*, vol. 143, no. 5, May 2017, doi: 10.1061/(asce)st.1943-541x.0001635.
[32] T. G. Singh and K. D. Singh, “Experimental investigation on performance of perforated cold–formed steel tubular stub columns,” *Thin-Walled Structures*, vol. 131, pp. 107–121, 2018.
[33] K. S. Sivakumaran, “Load capacity of uniformly compressed cold-formed steel section with punched web,” *Canadian journal of civil engineering*, vol. 14, no. 4, pp. 550–558, 1987, doi: 10.1139/l87-080.
[34] K. S. Sivakumaran, “Analysis for local buckling capacity of cold-formed steel sections with web opening,” *Comput. Struct.*, vol. 26, no. 1–2, pp. 275–282, 1987, doi: 10.1016/0045-7949(87)90257-4.
[35] X. Yao, “Experiment and Design Method on Cold-Formed Thin-Walled Steel Lipped Channel Columns with Slotted Web Holes Under Axial Compression,” *The Open Civil Engineering Journal*, vol. 11, no. 1, pp. 244–257, May 2017, doi: 10.2174/1874149501711010244.
[36] C. D. Moen, A. Schudlich, and A. von der Heyden, “Experiments on Cold-Formed Steel C-Section Joists with Unstiffened Web Holes,” *Journal of Structural Engineering*, vol. 139, no. 5, pp. 695–704, May 2013, doi: 10.1061/(asce)st.1943-541x.0000652.
[37] Y. Guo and X. Yao, “Experimental Study and Effective Width Method for Cold-Formed Steel Lipped Channel Stud Columns with Holes,” *Advances in Civil Engineering*, vol. 2021, 2021, doi: 10.1155/2021/9949199.
[38] Y. Guo and X. Yao, “Distortional buckling behavior and design method of cold-formed steel lipped channel with rectangular holes under axial compression,” *Mathematical Biosciences and Engineering*, vol. 18, no. 5, pp. 6239–6261, 2021, doi: 10.3934/mbe.2021312.
[39] B. Chen *et al.*, “Effects of edge-stiffened web openings on the behaviour of cold-formed steel channel sections under compression,” *Thin-Walled Structures*, vol. 144, Nov. 2019, doi: 10.1016/j.tws.2019.106307.
[40] A. Jameei Osgouei, Y. Hosseinzadeh, and H. Ahmadi, “Local buckling analysis of cold-formed

steel webs with stiffened rectangular openings," *J. Constr. Steel Res.*, vol. 167, Apr. 2020, doi: 10.1016/j.jcsr.2019.105824.
[41] F. M. F. Shaker, Z. Mamdooh, A. Deifalla, and M. M. Yehia, "Experimental Investigations of the Behavior of Stiffened Perforated Cold-Formed Steel Sections Subjected to Axial Compression," *Buildings*, vol. 12, no. 6, Jun. 2022, doi: 10.3390/buildings12060812.
[42] M. T. Chen, B. Young, A. D. Martins, D. Camotim, and P. B. Dinis, "Experimental investigation on cold-formed steel stiffened lipped channel columns undergoing local-distortional interaction," in *Proceedings of the Annual Stability Conference Structural Stability Research Council, SSRC 2020*, Structural Stability Research Council, 2020. doi: 10.1016/j.tws.2020.106682.
[43] B. Chen, K. Roy, Z. Fang, A. Uzzaman, G. Raftery, and J. B. P. Lim, "Moment capacity of back-to-back cold-formed steel channels with edge-stiffened holes, un-stiffened holes, and plain webs," *Eng. Struct.*, vol. 235, May 2021, doi: 10.1016/j.engstruct.2021.112042.
[44] Y. Dai, K. Roy, Z. Fang, B. Chen, G. M. Raftery, and J. B. P. Lim, "A novel machine learning model to predict the moment capacity of cold-formed steel channel beams with edge-stiffened and un-stiffened web holes," *Journal of Building Engineering*, vol. 53, Aug. 2022, doi: 10.1016/j.jobe.2022.104592.
[45] Y. Chi *et al.*, "Effect of web hole spacing on axial capacity of back-to-back cold-formed steel channels with edge-stiffened holes," *Steel and Composite Structures, An International Journal*, vol. 40, no. 2, pp. 287–305, 2021.
[46] N. Baldassino, C. Bernuzzi, A. di Gioia, and M. Simoncelli, "An experimental investigation on solid and perforated steel storage racks uprights," *J. Constr. Steel Res.*, vol. 155, pp. 409–425, Apr. 2019, doi: 10.1016/j.jcsr.2019.01.008.
[47] L. H. de A. Neiva, A. M. C. Sarmanho, V. O. Faria, F. T. de Souza, and J. A. B. Starlino, "Numerical and experimental analysis of perforated rack members under compression," *Thin-Walled Structures*, vol. 130, pp. 176–193, Sep. 2018, doi: 10.1016/j.tws.2018.05.024.
[48] J. P. de L. Miyazaki, A. S. de Carvalho, C. H. Martins, and A. Rossi, "Evaluation of the interaction between distortional–global buckling in perforated cold-formed steel rack sections," *Structures*, vol. 54, pp. 808–824, Aug. 2023, doi: 10.1016/j.istruc.2023.05.105.
[49] M. Casafont, M. Magdalena Pastor, F. Roure, and T. Peköz, "An experimental investigation of distortional buckling of steel storage rack columns," *Thin-Walled Structures*, vol. 49, no. 8, pp. 933–946, Aug. 2011, doi: 10.1016/j.tws.2011.03.016.
[50] L. Bertocci, D. Comparini, G. Lavacchini, M. Orlando, L. Salvatori, and P. Spinelli, "Experimental, numerical, and regulatory P-Mx-My domains for cold-formed perforated steel uprights of pallet-racks," *Thin-Walled Structures*, vol. 119, pp. 151–165, Oct. 2017, doi: 10.1016/j.tws.2017.06.001.
[51] J. Bonada, M. M. Pastor, F. Roure, and M. Casafont, "Distortional Influence of Pallet Rack Uprights Subject to Combined Compression and Bending," *Structures*, vol. 8, pp. 275–285, Nov. 2016, doi: 10.1016/j.istruc.2016.05.007.
[52] M. Orlando, G. Lavacchini, B. Ortolani, and P. Spinelli, "Experimental capacity of perforated cold-formed steel open sections under compression and bending," *Steel and Composite Structures, An International Journal*, vol. 24, no. 2, pp. 201–211, 2017.
[53] M. M. Pastor, J. Bonada, F. Roure, M. Casafont, and M. R. Somalo, "Rack uprights under combined compression and bi-axial bending: Experimental testing, numerical analysis and European standard approach," *ce/papers*, vol. 1, no. 2–3, pp. 1609–1616, Sep. 2017, doi: 10.1002/cepa.204.
[54] F. H. Smith and C. D. Moen, "Finite strip elastic buckling solutions for thin-walled metal columns with perforation patterns," *Thin-Walled Structures*, vol. 79, pp. 187–201, 2014, doi: 10.1016/j.tws.2014.02.009.
[55] L. Dai, Y. Chen, L. Cheng, and C. Ren, "Buckling behavior and design of cold-formed thin-walled steel storage rack upright frames," *Structures*, vol. 75, May 2025, doi: 10.1016/j.istruc.2025.108685.
[56] G. Taranu, S. Iacob, and N. Taranu, "Buckling Behavior of Perforated Cold-Formed Steel Uprights: Experimental Evaluation and Comparative Assessment Using FEM, EWM, and DSM," *Buildings*, vol. 15, no. 9, May 2025, doi: 10.3390/buildings15091561.

[57] C. Wang, Z. Zhang, D. Zhao, and Y. Bai, “Experimental and numerical study on perforated channel columns with complex edge stiffeners and web stiffeners,” *Advances in Structural Engineering*, vol. 18, no. 8, pp. 1303–1318, 2015.
[58] C. Wang, Y. Bai, Q. Liu, and D. Zhao, “Stability Behavior of Perforated Lipped Channel Columns,” in *MATEC Web of Conferences 67, 03011*, EDP Sciences. doi: 10.1051/03011.
[59] C. Wang, Q. Guo, Z. Zhang, and Y. Guo, “Experimental and numerical investigation of perforated cold-formed steel built-up I-section columns with web stiffeners and complex edge stiffeners,” *Advances in Structural Engineering*, vol. 22, no. 10, pp. 2205–2221, Jul. 2019, doi: 10.1177/1369433219836174.
[60] Y. Xiang, X. Zhou, Y. Shi, L. Xu, and Y. Xu, “Experimental investigation and finite element analysis of cold-formed steel channel columns with complex edge stiffeners,” *Thin-Walled Structures*, vol. 152, Jul. 2020, doi: 10.1016/j.tws.2020.106769.
[61] R. Feng, X. Mou, Z. Chen, K. Roy, B. Chen, and J. B. P. Lim, “Finite-element modelling and design guidelines for axial compressive capacity of aluminium alloy circular hollow sections with holes,” *Thin-Walled Structures*, vol. 157, Dec. 2020, doi: 10.1016/j.tws.2020.107027.
[62] Z. Fang, K. Roy, B. Chen, Z. Xie, and J. B. P. Lim, “Local and distortional buckling behaviour of aluminium alloy back-to-back channels with web holes under axial compression,” *Journal of Building Engineering*, vol. 47, Apr. 2022, doi: 10.1016/j.jobe.2021.103837.
[63] Z. Fang, K. Roy, B. Chen, Z. Xie, J. Ingham, and J. B. P. Lim, “Effect of the web hole size on the axial capacity of back-to-back aluminium alloy channel section columns,” *Eng. Struct.*, vol. 260, Jun. 2022, doi: 10.1016/j.engstruct.2022.114238.
[64] N. Abdel-Rahman and K. S. Sivakumaran, “Effective design width for perforated cold-formed steel compression members,” *Canadian Journal of Civil Engineering*, vol. 25, no. 2, pp. 319–330, 1998.
[65] W.-W. Yu, C. S. Davis, by Wei-Wen Yu, and C. S. Davis, “Buckling Behavior and Post-Buckling Strength of Perforated Stiffened Compression Elements,” in *Proceedings of the International Specialty Conference on Cold-Formed Steel Structures*, 1971.
[66] C. N. Grey and C. D. Moen, “Elastic Buckling Simplified Methods for Cold-Formed Columns and Beams with Edge-Stiffened Holes,” in *Proceedings of the Annual Stability Conference*, Pittsburgh, Pennsylvania: Structural Stability Research Council, 2011.
[67] Z. Yao and K. J. Rasmussen, “Design of perforated thin-walled steel columns research report R949,” 2014, [Online]. Available: http://sydney.edu.au/civil
[68] C. S. Davis, “The structural behavior of cold-formed steel members with perforated elements perforated elements,” 1972.
[69] C. D. Moen, “Direct Strength Design of Cold-Formed Steel Members with Perforations,” 2008.
[70] C. D. Moen and B. W. Schafer, “Impact of holes on the elastic buckling of cold-formed steel columns with application to the direct strength method,” 2006.
[71] Z. Yao and K. J. Rasmussen, “Finite element modelling and parametric studies of perforated thin-walled steel columns,” 2014. [Online]. Available: http://sydney.edu.au/civil
[72] B. W. Schafer and T. Pekoz, “Direct strength prediction of cold-formed steel members using numerical elastic buckling solutions,” *Thin-walled structures, research and developments*, pp. 127–144, 1998.
[73] C. Ren, Y. He, Z. Wu, W. He, and L. Dai, “Experiments and numerical predictions of cold-formed steel members with web perforations under combined compression and minor axis bending,” *Eng. Struct.*, vol. 256, Apr. 2022, doi: 10.1016/j.engstruct.2022.114022.
[74] J. M. Davies, P. Leach, and A. Tayloff, “The Design of Perforated Cold-Formed Steel Sections Subject to Axial Load and Bending,” 1997.
[75] N. H. Pham, “Effects of Hole Locations on the Elastic Global Buckling Loads of Cold-Formed Steel Channel Members with Perforations Under Compression or Bending,” in *International Conference on Civil Engineering*, Springer, 2021, pp. 57–69.
[76] M. Y. Shan, R. A. Laboube, and W. W. Yu, “Bending and shear behavior of web elements with openings,” *Journal of structural engineering*, vol. 122, no. 8, pp. 854–859, 1996.
[77] M. Y. Shan, R. LaBoube, and W. W. Yu, “Behavior of Web Elements with Openings Subjected to Bending,” *Shear and the Combination of Bending and Shear*, 1994.
[78] P. Keerthan and M. Mahendran, “Shear behaviour and strength of LiteSteel beams with web

openings," *Advances in Structural Engineering*, vol. 15, no. 2, pp. 171–184, 2012.
[79] P. Keerthan and M. Mahendran, "New design rules for the shear strength of LiteSteel beams with web openings," *Journal of Structural Engineering*, vol. 139, no. 5, pp. 640–656, 2013.
[80] P. Keerthan and M. Mahendran, "Experimental studies of the shear behaviour and strength of lipped channel beams with web openings," *Thin-Walled Structures*, vol. 73, pp. 131–144, 2013, doi: 10.1016/j.tws.2013.06.018.
[81] P. Keerthan and M. Mahendran, "Improved shear design rules for lipped channel beams with web openings," *J. Constr. Steel Res.*, vol. 97, pp. 127–142, 2014, doi: 10.1016/j.jcsr.2014.01.011.
[82] A. Uzzaman, J. B. P. Lim, D. Nash, and K. Roy, "Cold-formed steel channel sections under end-two-flange loading condition: Design for edge-stiffened holes, unstiffened holes and plain webs," *Thin-Walled Structures*, vol. 147, Feb. 2020, doi: 10.1016/j.tws.2019.106532.
[83] A. Uzzaman, J. B. P. Lim, D. Nash, and K. Roy, "Web crippling behaviour of cold-formed steel channel sections with edge-stiffened and unstiffened circular holes under interior-two-flange loading condition," *Thin-Walled Structures*, vol. 154, Sep. 2020, doi: 10.1016/j.tws.2020.106813.
[84] B. Chen, K. Roy, Z. Fang, A. Uzzaman, Y. Chi, and J. B. P. Lim, "Web crippling capacity of fastened cold-formed steel channels with edge-stiffened web holes, un-stiffened web holes and plain webs under two-flange loading," *Thin-Walled Structures*, vol. 163, Jun. 2021, doi: 10.1016/j.tws.2021.107666.
[85] J. Kesti, "Local and distortional buckling of perforated steel wall studs," Helsinki University of Technology, Laboratory of Steel Structures, 2000.
[86] V. V. Degtyarev and N. V. Degtyareva, "Finite element modeling of cold-formed steel channels with solid and slotted webs in shear," *Thin-Walled Structures*, vol. 103, pp. 183–198, Jun. 2016, doi: 10.1016/j.tws.2016.02.016.
[87] N. V. Degtyareva and V. V. Degtyarev, "Experimental investigation of cold-formed steel channels with slotted webs in shear," *Thin-Walled Structures*, vol. 102, pp. 30–42, May 2016, doi: 10.1016/j.tws.2016.01.012.
[88] N. Degtyareva, P. Gatheeshgar, K. Poologanathan, S. Gunalan, I. Shyha, and A. McIntosh, "Local buckling strength and design of cold-formed steel beams with slotted perforations," *Thin-Walled Structures*, vol. 156, Nov. 2020, doi: 10.1016/j.tws.2020.106951.
[89] N. Degtyareva, P. Gatheeshgar, K. Poologanathan, S. Gunalan, K. D. Tsavdaridis, and S. Napper, "New distortional buckling design rules for slotted perforated cold-formed steel beams," *J. Constr. Steel Res.*, vol. 168, May 2020, doi: 10.1016/j.jcsr.2020.106006.
[90] N. Degtyareva, P. Gatheeshgar, K. Poologanathan, S. Gunalan, M. Lawson, and P. Sunday, "Combined bending and shear behaviour of slotted perforated steel channels: Numerical studies," *J. Constr. Steel Res.*, vol. 161, pp. 369–384, Oct. 2019, doi: 10.1016/j.jcsr.2019.07.008.
[91] P. Gatheeshgar, H. Alsanat, K. Poologanathan, S. Gunalan, N. Degtyareva, and I. Hajirasouliha, "Web crippling behaviour of slotted perforated cold-formed steel channels: IOF load case," *J. Constr. Steel Res.*, vol. 188, Jan. 2022, doi: 10.1016/j.jcsr.2021.106974.
[92] P. Gatheeshgar *et al.*, "Web crippling of slotted perforated Cold-Formed Steel channels under EOF load case: Simulation and design," *Journal of Building Engineering*, vol. 44, Dec. 2021, doi: 10.1016/j.jobe.2021.103306.
[93] N. Degtyareva, K. Poologanathan, and M. Mahendran, "Web crippling tests of cold-formed steel channels with staggered web perforations," *Thin-Walled Structures*, vol. 159, Feb. 2021, doi: 10.1016/j.tws.2020.107314.
[94] J. Lipták-Váradi, "Equivalent thermal conductivity of steel girders with slotted web," *Periodica Polytechnica Civil Engineering*, vol. 54, no. 2, pp. 163–170, 2010, doi: 10.3311/pp.ci.2010-2.12.
[95] C. Martins, P. Santos, and L. S. da Silva, "Lightweight steel-framed thermal bridges mitigation strategies: A parametric study," *J. Build. Phys.*, vol. 39, no. 4, pp. 342–372, 2016.
[96] T. Li, J. Xia, C. S. Chin, and P. Song, "Investigation of the Thermal Performance of Lightweight Assembled Exterior Wall Panel (LAEWP) with Stud Connections," *Buildings*, vol. 12, no. 4, Apr. 2022, doi: 10.3390/buildings12040473.
[97] R. Alekperov and I. Aksenov, "Decrease of cold-formed slotted studs heat conductivity by slots shape modification," in *E3S Web of Conferences*, EDP Sciences, May 2019. doi:

10.1051/e3sconf/20199706009.
[98] ABAQUS Inc., “Analysis User’s Manual - Version,” 2020, *USA*.
[99] L. Gardner and X. Yun, “Description of stress-strain curves for cold-formed steels,” *Constr. Build. Mater.*, vol. 189, pp. 527–538, 2018.
[100] B. Rossi, S. Afshan, and L. Gardner, “Strength enhancements in cold-formed structural sections—Part II: Predictive models,” *J. Constr. Steel Res.*, vol. 83, pp. 189–196, 2013.
[101] AS/NZS (Australia/New Zealand Standard), *Cold-Formed Steel Structures*. Sydney, Australia: Standards Australia, 2018.
[102] K. Mitsui and K. Ikarashi, “Elastic Critical Local Buckling Load and Behavior of Local Buckling for Cold-Formed Lipped Channel Steel Member under Compression,” *Japan Architectural Review*, vol. 7, no. 1, p. e12432, 2024, doi: 10.1002/2475-8876.12432.
[103] AISI (American Iron and S. Institute), *North American Specification for the Design of Cold-Formed Steel Structural Members*. Washington, DC: American Iron and Steel Institute, 2016.
[104] S. Torabian, B. Zheng, and B. W. Schafer, “Experimental response of cold-formed steel lipped channel beam-columns,” *Thin-Walled Structures*, vol. 89, pp. 152–168, 2015, doi: 10.1016/j.tws.2014.12.003.
[105] S. Torabian, D. C. Fratamico, and B. W. Schafer, “Experimental response of cold-formed steel Zee-section beam-columns,” *Thin-Walled Structures*, vol. 98, pp. 496–517, Jan. 2016, doi: 10.1016/j.tws.2015.10.016.
[106] Y. Li, Y. Li, and Y. Song, “Experimental Investigation on Ultimate Capacity of Eccentrically-Compressed Cold-Formed Beam-Columns with Lipped Channel Sections.” [Online]. Available: https://scholarsmine.mst.edu/isccss
[107] American Iron and S. Institute, *Commentary on North American Specification for the Design of Cold-Formed Steel Structural Members*. Washington, DC: American Iron and Steel Institute, 2002.
[108] G. J. Hancock and K. J. R. Rasmussen, “Recent research on thin-walled beam-columns,” 1998.
[109] S. S. Cheng, B. Kim, and L. Y. Li, “Lateral–Torsional Buckling of Cold-Formed Channel Sections Subject to Combined Compression and Bending,” *J. Constr. Steel Res.*, vol. 80, pp. 174–180, 2013, doi: 10.1016/j.jcsr.2012.09.014.
[110] J.-L. Ma, T.-M. Chan, and B. Young, “Cold-Formed High-Strength Steel Rectangular and Square Hollow Sections under Combined Compression and Bending,” *Journal of Structural Engineering*, vol. 145, no. 12, Dec. 2019, doi: 10.1061/(asce)st.1943-541x.0002446.
[111] Q. Y. Li and B. Young, “Tests of cold-formed steel built-up open section members under eccentric compressive load,” *J. Constr. Steel Res.*, vol. 184, Sep. 2021, doi: 10.1016/j.jcsr.2021.106775.
[112] Q. Y. Li and B. Young, “Design of cold-formed steel built-up open section members under combined compression and bending,” *Thin-Walled Structures*, vol. 172, Mar. 2022, doi: 10.1016/j.tws.2022.108890.
[113] B. Wang, G. L. Bosco, B. P. Gilbert, H. Guan, and L. H. Teh, “Unconstrained shape optimisation of singly-symmetric and open cold-formed steel beams and beam-columns,” *Thin-Walled Structures*, vol. 104, pp. 54–61, Jul. 2016, doi: 10.1016/j.tws.2016.03.007.
[114] H. Parastesh, S. Mohammad Mojtabaei, H. Taji, I. Hajirasouliha, and A. Bagheri Sabbagh, “Constrained optimization of anti-symmetric cold-formed steel beam-column sections,” *Eng. Struct.*, vol. 228, Feb. 2021, doi: 10.1016/j.engstruct.2020.111452.
[115] M. Hasanali, S. M. Mojtabaei, G. C. Clifton, I. Hajirasouliha, S. Torabian, and J. B. P. Lim, “Capacity and design of cold-formed steel warping-restrained beam-column elements,” *J. Constr. Steel Res.*, vol. 190, Mar. 2022, doi: 10.1016/j.jcsr.2022.107139.
[116] M. Hasanali, S. M. Mojtabaei, I. Hajirasouliha, G. C. Clifton, and J. B. P. Lim, “More accurate design equations for cold-formed steel members subjected to combined axial compressive load and bending,” *Thin-Walled Structures*, vol. 185, Apr. 2023, doi: 10.1016/j.tws.2023.110588.
[117] F. Öztürk, S. M. Mojtabaei, M. Şentürk, S. Pul, and I. Hajirasouliha, “Buckling behaviour of cold-formed steel sigma and lipped channel beam–column members,” *Thin-Walled Structures*, vol. 173, Apr. 2022, doi: 10.1016/j.tws.2022.108963.
[118] S. Torabian, B. Zheng, and B. W. Schafer, “Direct Strength Prediction of Cold-Formed Steel Beam-Columns,Research Rep.RP-16-3,” Ithaca, NY, 2016.

[119] K. Ghosh, K. Roy, S. Tiwari, Z. Fang, B. Paul, and J. B. P. Lim, “Axial capacity of cold-formed steel channel sections with slits,” *Eng. Struct.*, vol. 322, Jan. 2025, doi: 10.1016/j.engstruct.2024.119094.
[120] B. W. Schafer, “Review: The Direct Strength Method of cold-formed steel member design,” *J. Constr. Steel Res.*, vol. 64, no. 7, pp. 766–778, 2008, doi: https://doi.org/10.1016/j.jcsr.2008.01.022.
[121] J. He and B. Young, “Behaviour of cold-formed steel built-up I-sections with perforated web under localized forces,” *J. Constr. Steel Res.*, vol. 190, p. 107129, 2022, doi: https://doi.org/10.1016/j.jcsr.2022.107129.
[122] R. Singh and A. Samanta, “Reliability assessment of an improved DSM design proposal for cold-formed steel beam, column and beam-column members at elevated temperature,” *Structures*, vol. 79, p. 109502, 2025, doi: https://doi.org/10.1016/j.istruc.2025.109502.
[123] ASHRAE, *2021 ASHRAE Handbook: Fundamentals, Inch-Pound Edition*. 2021.

APPENDIX

Table A- 1 Results from the parametric analysis of plain channel sections under eccentric loading

FEA results for axial capacity of plain channel sections under eccentricity, P_{FEA} (kN)																		
L500																		
Specimen	E 10			E -10			E 25			E -25			E -50			E 50		
	T0.6	T1.2	T2.0	T0.6	T1.2	T2.0	T0.6	T1.2	T2.0	T0.6	T1.2	T2.0	T0.6	T1.2	T2.0	T0.6	T1.2	T2.0
C145-Bf45	20.60	60.16	106.64	14.04	50.53	101.97	11.74	35.89	60.60	10.11	34.47	78.73	6.91	23.43	46.82	6.48	20.83	35.27
C200-Bf45	22.51	71.49	114.78	13.19	45.93	106.93	14.21	38.06	63.50	9.98	34.53	72.41	6.82	23.21	43.90	7.67	21.62	42.50
C250-Bf65	22.96	83.42	155.04	14.32	60.25	133.24	17.28	57.99	119.36	11.53	44.29	102.53	9.74	33.48	70.72	10.75	39.24	62.00
L1000																		
C145-Bf45	15.65	48.35	82.18	12.00	37.48	80.23	9.29	32.06	49.47	9.12	30.78	57.52	6.26	18.90	38.85	5.97	17.86	30.67
C200-Bf45	17.72	50.32	90.53	11.72	36.18	78.85	9.63	34.26	52.52	8.95	26.68	54.67	6.19	18.69	34.83	6.69	17.81	31.79
C250-Bf65	21.92	67.53	117.31	13.25	51.34	118.01	14.08	40.56	88.27	11.29	39.56	92.03	8.34	30.09	66.14	7.62	26.45	53.53
L1500																		
C145-Bf45	13.06	37.17	69.21	9.68	30.66	59.87	8.45	24.15	39.34	7.41	17.56	45.43	5.93	17.45	29.97	4.97	15.49	24.99
C200-Bf45	13.07	39.69	64.07	9.61	30.61	58.36	9.76	33.15	41.75	6.88	24.00	40.12	5.53	15.30	27.96	5.48	12.11	27.15
C250-Bf65	20.95	50.85	90.93	12.92	43.38	95.46	9.85	34.87	72.64	10.26	38.59	80.29	7.75	25.66	58.26	6.76	21.84	48.01

THE UNIVERSITY OF WAIKATO
Te Whare Wānanga o Waikato

School of Graduate Research
The University of Waikato
Private Bag 3105
Hamilton 3240, New Zealand
Phone +64 7 838 5096
Email: SGR@waikato.ac.nz
Website: http://www.waikato.ac.nz/students/research-degre

Co-Authorship Form

This form is to accompany the submission of any PhD that contains research reported in published or unpublished co-authored work. **Please include one copy of this form for each co-authored work**. Completed forms should be included in your appendices for all the copies of your thesis submitted for examination and library deposit (including digital deposit).

Chapter 3
Kushal Ghosh, Krishanu Roy, Shubham Tiwari, Zhiyuan Fang, Bikram Paul, and James BP Lim. "Axial capacity of cold-formed steel channel sections with slits." *Engineering Structures* 322 (2025): 119094.

Nature of contribution by PhD candidate	Writing –original draft, Methodology, Validation, Investigation, Data curation, Conceptualization
Extent of contribution by PhD candidate (%)	90

Name	Nature of Contribution
CO-AUTHORS	
Krishanu Roy	Writing – review & editing, Supervision, Investigation, Conceptualization.
Shubham Tiwari	Investigation, Data curation.
Zhiyuan Fang	Writing – review & editing
Bikram Paul	Validation
James B.P. Lim	Writing – review & editing, Supervision.

Certification by Co-Authors

The undersigned hereby certify that:

- the above statement correctly reflects the nature and extent of the PhD candidate's contribution to this work, and the nature of the contribution of each of the co-authors; and
- that the candidate wrote all or the majority of the text.

Name	Signature	Date
Krishanu Roy	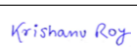	17.6.2025
Shubham Tiwari	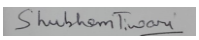	17.6.2025
Zhiyuan Fang	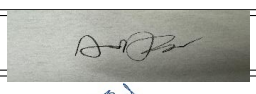	16.7.2025
Bikram Paul		21.6.2025
James B.P. Lim	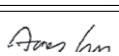	17.6.2025

THE UNIVERSITY OF WAIKATO
Te Whare Wānanga o Waikato

School of Graduate Research
The University of Waikato
Private Bag 3105
Hamilton 3240, New Zealand
Phone +64 7 838 5096
Email: SGR@waikato.ac.nz
Website: http://www.waikato.ac.nz/students/research-degre

Co-Authorship Form

This form is to accompany the submission of any PhD that contains research reported in published or unpublished co-authored work. **Please include one copy of this form for each co-authored work**. Completed forms should be included in your appendices for all the copies of your thesis submitted for examination and library deposit (including digital deposit).

Chapter 4 Kushal Ghosh, Shubham Tiwari, Krishanu Roy, Zhiyuan Fang, Bikram Paul, and James BP Lim. "Axial capacity of cold-formed steel channel sections with slits subjected to axial compressive load with eccentricity."	
Nature of contribution by PhD candidate	Writing –original draft, Methodology, Validation, Investigation, Data curation, Conceptualization
Extent of contribution by PhD candidate (%)	90

Name	Nature of Contribution
CO-AUTHORS	
Shubham Tiwari	Conceptualization, Validation, Data Curation, Methodology.
Krishanu Roy	Writing – review & editing, Supervision, Investigation, Conceptualization.
Bikram Paul	Validation
Zhiyuan Fang	Writing – review & editing
James B.P. Lim	Conceptualization, Supervision, Writing - Review & Editing.

Certification by Co-Authors

The undersigned hereby certify that:

- the above statement correctly reflects the nature and extent of the PhD candidate's contribution to this work, and the nature of the contribution of each of the co-authors; and
- that the candidate wrote all or the majority of the text.

Name	Signature	Date
Shubham Tiwari		17.6.2025
Krishanu Roy	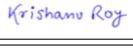	17.6.2025
Bikram Paul		21.6.2025
Zhiyuan Fang	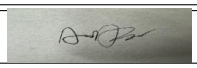	16.7.2025
James B.P. Lim	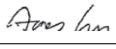	17.6.2025